

APPLICATION OF PARALLEL TIME-IMPLICIT DISCONTINUOUS GALERKIN FINITE
ELEMENT METHODS TO HYPERSONIC NONEQUILIBRIUM FLOW PROBLEMS

By
ANKUSH BHATIA

A DISSERTATION PRESENTED TO THE GRADUATE SCHOOL
OF THE UNIVERSITY OF FLORIDA IN PARTIAL FULFILLMENT
OF THE REQUIREMENTS FOR THE DEGREE OF
DOCTOR OF PHILOSOPHY

UNIVERSITY OF FLORIDA

2014

Report Documentation Page		Form Approved OMB No. 0704-0188
Public reporting burden for the collection of information is estimated to average 1 hour per response, including the time for reviewing instructions, searching existing data sources, gathering and maintaining the data needed, and completing and reviewing the collection of information. Send comments regarding this burden estimate or any other aspect of this collection of information, including suggestions for reducing this burden, to Washington Headquarters Services, Directorate for Information Operations and Reports, 1215 Jefferson Davis Highway, Suite 1204, Arlington VA 22202-4302. Respondents should be aware that notwithstanding any other provision of law, no person shall be subject to a penalty for failing to comply with a collection of information if it does not display a currently valid OMB control number.		
1. REPORT DATE MAY 2014	2. REPORT TYPE	3. DATES COVERED 00-00-2014 to 00-00-2014
4. TITLE AND SUBTITLE Application of Parallel Time-Implicit Discontinuous Galerkin Finite Element Methods to Hypersonic Nonequilibrium Flow Problems	5a. CONTRACT NUMBER	
	5b. GRANT NUMBER	
	5c. PROGRAM ELEMENT NUMBER	
6. AUTHOR(S)	5d. PROJECT NUMBER	
	5e. TASK NUMBER	
	5f. WORK UNIT NUMBER	
7. PERFORMING ORGANIZATION NAME(S) AND ADDRESS(ES) University of Florida, Applied Physics Research Group, Department of Mechanical and Aerospace Engineering, Gainesville, FL, 32611		8. PERFORMING ORGANIZATION REPORT NUMBER
9. SPONSORING/MONITORING AGENCY NAME(S) AND ADDRESS(ES)		10. SPONSOR/MONITOR'S ACRONYM(S)
		11. SPONSOR/MONITOR'S REPORT NUMBER(S)
12. DISTRIBUTION/AVAILABILITY STATEMENT Approved for public release; distribution unlimited		
13. SUPPLEMENTARY NOTES		
14. ABSTRACT <p>Discontinuous Galerkin (DG) methods are high-order accurate, compact-stencil methods, proven to possess favorable properties for highly efficient parallel systems complex geometries and unstructured meshes. Coding effort is significantly reduced for compact-stencil DG methods in comparison to main stream finite difference and finite volume methods. This work successfully introduces DG methods to thermal ablation and non-equilibrium hypersonic flows. In the state-of-the-art hypersonic flow codes, surface heating predictions are very sensitive to mesh resolution in the shock. A minor misalignment can cause major changes in the heating predictions. This is due to the lack of high-order accuracy in current streamline methods and numerical errors associated with the shock capturing approach. Shock capturing methods like slope limiter or artificial viscosity, being empirical have errors in the shock region. This work employs r-p adaptivity to accurately capture the shock with $p = 0$ elements (first order accuracy). Smooth flow regions are captured using p greater than 0. This method is stable. Implicit methods are developed for solution advancement with high CFL numbers. Error in the shock is reduced by redistributing the elements (outside of the shock) to within the shock (r adaptivity). Inviscid and viscous hypersonic flow problems, with same accuracy as in h-p adaptivity method, are simulated with one-third elements. This methodology requires no a priori knowledge of the shock's location, and is suitable for detached shock problems. r-p adaptivity method has allowed for successful prediction of surface heating rate for hypersonic flow over cylinder. Additionally, good comparisons are made, for non-equilibrium hypersonic flows, to the published results. This tool is also used to determine the effect of micro-second pulsed sinusoidal Dielectric Barrier Discharge (DBD) plasma actuators on the surface heating reduction for hypersonic flow over cylinder. A significant effect, of the plasma actuators, is found on the surface heating for hypersonic flows (with and without thermo-chemistry) and several designs are investigated for optimum heating reduction.</p>		
15. SUBJECT TERMS		

16. SECURITY CLASSIFICATION OF:			17. LIMITATION OF ABSTRACT Same as Report (SAR)	18. NUMBER OF PAGES 192	19a. NAME OF RESPONSIBLE PERSON
a REPORT unclassified	b ABSTRACT unclassified	c THIS PAGE unclassified			

© 2014 Ankush Bhatia

*Ishvarah paramah krsnah
sac-cid-ananda-vigraha
anadir adir govindah
sarva karana-karanam*

- Brahma Samhita 5.1

“Krsna who is known as Govinda is the Supreme Godhead. He has an eternal blissful spiritual body. He is the origin of all. He has no other origin and He is the prime cause of all causes.”

Source: <http://vedabase.net/bs/5/1/en>

I offer this dissertation at the lotus feet of my beloved spiritual master, His Grace Kalakantha Prabhu, who has very mercifully given me shelter at his lotus feet; His Divine Grace A. C. Bhaktivedanta Swami Srila Prabhupada, the dearest devotee of Lord Krishna, by whose mercy I have gotten the opportunity to practice Krishna consciousness along with my PhD work here, in Gainesville, Florida; and finally unto the Supreme Personality of Godhead, Sri Krishna, who is very favorably inclined towards his devotees and those who are trying to be devotees of his devotees.

ACKNOWLEDGMENTS

I especially thank all the devotees in Krishna House, for making this PhD a very memorable experience.

I am grateful towards my advisor, Dr. Subrata Roy, for providing me a platform to pursue my research interests and his consistent guidance in my PhD program. I also acknowledge the time and effort, the professors in my Ph.D. committee, Dr. S. Balachandar, Dr. R. Mei, Dr. S. Sinnott and Dr. R. Gosse, took to reviewing my dissertation and my defense presentation.

I am also grateful to Dr. R. Gosse and Dr. M. Parmar, who have put significant time and effort into guiding me for my PhD work. Dr. M. Parmar has specifically helped me in looking at the numerical problem in a more fundamental way, to debug the issues while attempting to solve tough problems. Dr. R. Gosse helped me look at the physics of these tough problems, and the numerical challenges in hypersonic flows and thermal ablation that are not yet resolved. Their help have been pivotal in my Ph.D. work.

I acknowledge the support of Air Force Research Laboratory (AFRL) and Mechanical Engineering Department to support this work.

I also thank all my labmates, including James, Dr. Singh, Richard, Navya, Tomas, Ryan, Ariel, Mark, Jignesh, Arnob, Moses, Pengfei, Thomas, Nick and Sam for their companionship during my Ph.D. sojourn.

I express my gratitude to all my spiritual mentors and teachers that I have had, at different phases of my life, who helped me to come at this point, where I am at right now.

Finally, I acknowledge the support of my family, including my parents, my brother, my sister-in-law and their sweet daughter, Ria, during this complete Ph.D. program. They always supported my decisions, and also guided when it was needed.

TABLE OF CONTENTS

	<u>page</u>
ACKNOWLEDGMENTS	4
LIST OF TABLES	8
LIST OF FIGURES	9
ABSTRACT	13
 CHAPTER	
1 INTRODUCTION	15
1.1 Motivation: Complex Physics of Thermal Ablation and Hypersonic Flow Problems	17
1.1.1 Flight Trajectory	18
1.1.2 Flow Environment	19
1.1.3 Thermal Response of Ablating Material	21
1.1.3.1 Thermal conduction	22
1.1.3.2 Material failure and thermal decomposition	22
1.1.3.3 Surface ablation	24
1.2 State of the Art of Numerical Simulations in Thermal Ablation	24
1.2.1 Past Development of Material Thermal Response Codes	25
1.2.1.1 Charring Material Ablation (CMA) code	26
1.2.1.2 Fully Implicit Thermal response and Ablation program (FIAT)	28
1.2.2 Recent Developments of Material Thermal Response Codes	29
1.2.2.1 Control Volume Finite Element Method (CVFEM)	29
1.2.2.2 Two-dimensional Implicit Thermal response and Ablation program (TITAN)	30
1.2.2.3 COYOTE/SACCARA fully coupled simulations	32
1.3 State of the Art of Numerical Simulations in Hypersonic Flow	36
1.4 Industrial Standard Numerical Tools	42
1.4.1 Finite Element Formulation for Thermal Ablation	42
1.4.2 Discontinuous Galerkin Method and Its Benefits	44
1.5 Contribution	48
1.6 Thesis Layout	48
2 GOVERNING EQUATIONS	50
2.1 Inviscid Euler Equations	50
2.2 Viscous Navier-Stokes Equations	51
2.3 Multi-species Navier-Stokes Equations	53
2.3.1 Thermo-Chemical Non-Equilibrium	53
2.3.2 Multispecies Navier Stokes Equations	56

2.3.3	Transport Properties	58
2.3.4	Source Term for Chemical Reactions	60
2.3.5	Source Term for Vibrational Energy	62
2.4	Thermal Ablation	63
3	NUMERICAL METHODS	66
3.1	Why Discontinuous Galerkin?	66
3.2	Inviscid Terms	67
3.3	Viscous Terms	69
3.3.1	BR1 vs BR2	72
3.3.2	Original Formulation of BR2	74
3.4	Source Terms	76
3.5	Time Integration	76
3.5.1	Explicit Time Integration	77
3.5.2	Implicit Time Integration	78
3.6	Parallelization	79
3.7	r-p Adaptive Methods	82
4	CODE VALIDATION EXAMPLES	86
4.1	Inviscid Flow	86
4.1.1	Potential Flow Around the Cylinder	87
4.1.2	Subsonic Flow Around the Cylinder	88
4.1.3	Transonic Flow Around the Cylinder	90
4.1.4	Double Mach Reflection	95
4.2	Viscous Flow	100
4.2.1	Taylor Vortex	101
4.2.2	Rayleigh Impulsively Started Flow	103
4.2.3	Flat Plate	105
5	THERMAL ABLATION TEST CASES	110
5.1	1D Arc Jet Cases from Ahn & Park	111
5.1.1	Material Properties of Carbon-Phenolic	112
5.1.2	A Comment on Governing Equations Used in This Work	113
5.1.3	Pyrolysis Gas Modeling	114
5.1.4	Boundary and Initial Conditions	116
5.1.5	Results	117
5.2	Ablation Workshop Cases	123
5.3	Langley Arc Jet Test Case	126
5.3.1	1-D Ablation Test Case with Fay Riddell Model	128
5.3.2	Simulation Results	129

6	HYPersonic FLOW CASES	133
6.1	Inviscid Hypersonic Flow	135
6.2	Viscous Hypersonic Flow	141
6.3	Hypersonic Flow with Thermo-Chemical Non-Equilibrium	144
7	EFFECT OF PLASMA DBD ACTUATORS ON HYPersonic FLOW CASES .	159
7.1	Effect of Plasma DBD Actuator on Surface Heating in Mach 17 Hypersonic Flow Over Cylinder	161
7.2	Effect of Plasma DBD Actuator on Surface Heating in Mach 17 Non-equilibrium Hypersonic Flow Over Cylinder	172
8	CONCLUSION	177
APPENDIX		
A	FLUID PROPERTIES	182
B	BASIS FUNCTIONS	183
REFERENCES		184
BIOGRAPHICAL SKETCH		192

LIST OF TABLES

<u>Table</u>	<u>page</u>
2-1 Vibrational temperatures for non-ionizing dissociating air	55
2-2 Electronic temperatures and degeneracies for non-ionizing dissociating air . .	55
3-1 Time taken for 1 processor GMRES for Double Mach Reflection	79
A-1 Blottner coefficients for species viscosity	182
A-2 Coefficients for forward reaction rates	182
A-3 Equilibrium constant coefficients	182
B-1 Basis functions for 2D discontinuous Galerkin	183

LIST OF FIGURES

<u>Figure</u>	<u>page</u>
1-1 Physical processes on the surface of the space vehicle in hypersonic re-entry .	17
1-2 Hypersonic shock-wave boundary layer interaction	21
1-3 Schematic showing three zones in the charring ablator	23
1-4 Comparison of net heating rates at the surface of Pioneer Venus probes	27
1-5 Comparison of temperature histories from flight data and numerical predictions	28
1-6 Effect of loosely coupled formulations on shape change simulations	31
1-7 Simulation of arc-jet test model using MARC/TITAN/GIANTS	32
1-8 Anomalous fall of stagnation point temperature using COYOTE/SACCARA coupling	33
1-9 Avoiding anomalous surface recession in COYOTE/SACCARA coupling	34
1-10 Oscillations in heat and mass flux due to perpendicularity assumptions	35
1-11 Sensitivity of heating prediction to grid alignment along the shock	36
1-12 Large variation in heating predictions for 3D hypersonic flow over cylinder . . .	37
1-13 Range of densities for hypersonic flow around re-entry capsule	38
1-14 Error in C_h profile at one of r-p adaptivity iterations	39
1-15 Carbuncle effect in hypersonic flow over cylinder	40
1-16 Asymmetry in C_h profile using PDE based artificial viscosity	41
1-17 Generic heat shield penetration concept	43
1-18 Grid points in finite difference for approximation of curved body shape.	43
1-19 Comparison of finite difference and finite element for a curved geometry	44
3-1 Parallel performance of Euclid+GMRES solver in Hypre	81
3-2 Parallel performance of DS + BiCGStab solver in Hypre	81
3-3 Locating shock using pressure based shock indicator.	83
3-4 Mesh before and after r-p adaptivity	85
4-1 Order of accuracy analysis for potential flow around a cylinder	88
4-2 Steady state velocity contours comparison for potential flow over cylinder . . .	89

4-3	Mesh comparison for Mach 0.38 flow around cylinder	90
4-4	Mach contours comparison for $M = 0.38$ flow around cylinder	91
4-5	Formation of separation region for Mach 0.5 transonic flow around the cylinder	92
4-6	Vortex shedding for Mach 0.5 transonic flow around the cylinder	94
4-7	Mach contours comparison for $M = 0.5$ flow over cylinder	95
4-8	Schematic of 2-D double mach reflection problem.	96
4-9	Results for double Mach reflection with $p = 0$ and 33,000 elements	97
4-10	Results for double Mach reflection with $p = 1$ and 33,000 elements	99
4-11	Density contours for $p = 1$ and five different meshes	100
4-12	Taylor Vortex problem	102
4-13	Taylor Vortex problem: 3D contour plots of x-momentum	103
4-14	Rayleigh problem: Effect of inviscid terms on BR1 solution	105
4-15	Rayleigh problem: Comparison of $p = 1$ and $p = 2$ using BR1 scheme	106
4-16	Rayleigh problem using BR2 and $p = 1$	106
4-17	Schematic of flat plate problem	107
4-18	Flat plate solution with BR1 scheme and incorrect boundary condition	108
4-19	Flat plate solution with BR1 and correct boundary conditions for inviscid terms	108
4-20	Flat plate solution with BR2 and correct boundary conditions for the inviscid terms	109
5-1	Advanced Entry Heating Simulator	111
5-2	Material properties of carbon phenolic	113
5-3	CANTERA plots for the pyrolysis gas	115
5-4	Second curve-fitting for internal energy of the pyrolysis gas	116
5-5	Results for thermal ablation with diffusion coefficient, $D = 0$	118
5-6	Temporal variation of surface temperature for $D = 0$	120
5-7	Results for thermal ablation and nonzero diffusion coefficient	121
5-8	Surface temperature and mass loss comparison for non zero diffusion	123

5-9	Material properties for TACOT	125
5-10	Boundary condition for TACOT	126
5-11	Simulation results for TACOT	127
5-12	Langley arc-jet test sample	128
5-13	Specific heat plots for Narmco 4028	130
5-14	Specific heat plot for pyrolysis gas from Sutton	130
5-15	Thermal conductivity plots for Narmco 4028 with perpendicular fibers	131
5-16	Thermal conductivity plots for Narmco 4028 with parallel fibers	131
5-17	Simulation results for Langley arc jet test case	132
6-1	Results for inviscid hypersonic case ($M = 6$) with $p = 0$	136
6-2	Shock indicator	138
6-3	3-D density contour plots for different shock indicator thresholds	139
6-4	Shock-based r-p adaptivity mesh refinement	139
6-5	Solution comparison for inviscid hypersonic flow with r-p adaptive method	140
6-6	Stagnation line pressure comparison for Mach 6 inviscid hypersonic flow	141
6-7	Mach 17 viscous hypersonic flow results	142
6-8	r-p adaptive solutions to viscous hypersonic flow	142
6-9	Viscous hypersonic flow result comparison	143
6-10	Surface heating coefficient profile for viscous hypersonic flow	143
6-11	Final r-p adapted meshes for non-equilibrium cases	144
6-12	Mass fraction of O_2 for MIG and US3D for only O_2 test case	146
6-13	Mass fraction of O for MIG and US3D for only O_2 test case	147
6-14	Contours for temperature, T for MIG and US3D for only O_2 test case	148
6-15	Contours for vibrational temperature, T_v for MIG and US3D for only O_2 test case	149
6-16	3D contours for temperature, T for MIG and US3D for only O_2 test case	150
6-17	Stagnation line plots for only O_2 case	150

6-18 Temperature contours for $N_2 + O_2$ case	151
6-19 Vibrational temperature contours for $N_2 + O_2$ case	152
6-20 Mass fraction contours of O_2 for $N_2 + O_2$ case	153
6-21 Mass fraction contours of O for $N_2 + O_2$ case	154
6-22 Mass fraction contours of NO for $N_2 + O_2$ case	155
6-23 Mass fraction contours of N for $N_2 + O_2$ case	156
6-24 Mass fraction contours of N_2 for $N_2 + O_2$ case	157
6-25 Stagnation line plots for $N_2 + O_2$ case	158
7-1 Mesh for plasma actuation of hypersonic flow	162
7-2 Plasma body force distribution in 'plasma1' configuration	163
7-3 Three configurations of plasma DBD actuators	164
7-4 Effect of plasma on C_h profile for hypersonic flow over cylinder	165
7-5 Effect of plasma actuator, in 'plasma1', on temperature contours	166
7-6 Temperature plots in 'plasma1' configuration	167
7-7 Velocity profiles in 'plasma1' configuration	168
7-8 Temperature contours for plasma2 and plasma3 configurations	168
7-9 Schematic of flow induced by plasma body force	169
7-10 Y-velocity profile in 'no plasma' and 'plasma1' configurations	170
7-11 Temperature profiles for 'plasma2' and 'plasma3' configurations	171
7-12 Y-velocity profiles for 'plasma2' and 'plasma3' configurations	172
7-13 Effect of plasma actuator on C_h profile for NEQ hypersonic flow	173
7-14 Effect of plasma3 configuration on stagnation line plots of T and T_v	173
7-15 Effect of plasma3 configuration on stagnation line plots of O_2 and O	174
7-16 Effect of plasma3 configuration on stagnation line plots of N and NO	175
7-17 Effect of plasma3 configuration on stagnation line plots of N_2	176

Abstract of Dissertation Presented to the Graduate School
of the University of Florida in Partial Fulfillment of the
Requirements for the Degree of Doctor of Philosophy

APPLICATION OF PARALLEL TIME-IMPLICIT DISCONTINUOUS GALERKIN FINITE
ELEMENT METHODS TO HYPERSONIC NONEQUILIBRIUM FLOW PROBLEMS

By

Ankush Bhatia

May 2014

Chair: Subrata Roy

Major: Mechanical Engineering

Discontinuous Galerkin (DG) methods are high-order accurate, compact-stencil methods, proven to possess favorable properties for highly efficient parallel systems, complex geometries and unstructured meshes. Coding effort is significantly reduced for compact-stencil DG methods in comparison to main stream finite difference and finite volume methods. This work successfully introduces DG methods to thermal ablation and non-equilibrium hypersonic flows.

In the state-of-the-art hypersonic flow codes, surface heating predictions are very sensitive to mesh resolution in the shock. A minor misalignment can cause major changes in the heating predictions. This is due to the lack of high-order accuracy in current streamline methods and numerical errors associated with the shock capturing approach. Shock capturing methods like slope limiter or artificial viscosity, being empirical have errors in the shock region.

This work employs r-p adaptivity to accurately capture the shock with $p = 0$ elements (first order accuracy). Smooth flow regions are captured using p greater than 0. This method is stable. Implicit methods are developed for solution advancement with high CFL numbers. Error in the shock is reduced by redistributing the elements (outside of the shock) to within the shock (r adaptivity). Inviscid and viscous hypersonic flow problems, with same accuracy as in h-p adaptivity method, are simulated with

one-third elements. This methodology requires no a priori knowledge of the shock's location, and is suitable for detached shock problems.

r-p adaptivity method has allowed for successful prediction of surface heating rate for hypersonic flow over cylinder. Additionally, good comparisons are made, for non-equilibrium hypersonic flows, to the published results. This tool is also used to determine the effect of micro-second pulsed sinusoidal Dielectric Barrier Discharge (DBD) plasma actuators on the surface heating reduction for hypersonic flow over cylinder. A significant effect, of the plasma actuators, is found on the surface heating for hypersonic flows (with and without thermo-chemistry) and several designs are investigated for optimum heating reduction.

CHAPTER 1 INTRODUCTION

Solving multi-physics problems is a daunting task. Specifically, our problems of interest include thermally ablative surface of a hypersonic vehicle (for example at re-entry condition) and simulation of thermo-chemical non-equilibrium flow field around this vehicle. We aim to simulate such problems using a high-order accurate, fully implicit method.

The current state of the art, for the Computational Fluid Dynamic or CFD simulations of these areas, includes using finite difference and finite volume codes, that are typically second order accurate. Moreover, their applications are more suitable for simple geometries [1]. For more complex shaped geometries and higher order accuracy (> 2), finite element methods are more appropriate. Additionally, with advance in CFD techniques and expanding computational resources, the complexity of the problems is also increasing. This puts a great deal of strain on mesh resolution requirements for second order accurate methods, as the error is of order, $O(h^2)$ [2, 3].

To remedy this, we introduce Discontinuous Galerkin (DG), a high fidelity finite element based, method to the fields of thermal ablation [4, 5] and hypersonic flows with thermo-chemical non-equilibrium [6]. We also demonstrate, the usefulness and convenience of using the DG method for these problems, in terms of solution accuracy. For polynomial basis function of order p , the error convergence in DG methods is given as $O(h^{p+1})$, where h is the mesh size. Hence, with improved convergence rates, the solution error drops more rapidly, obviating the need for increasingly mesh resolved solutions. For complex problems and geometries, improving mesh resolution is a much more demanding task than enhancing the order of accuracy of the CFD method.

Another challenge in the field of hypersonic flows is capturing shocks. It is a well known fact, that applying a CFD method, with order of accuracy greater than one, directly to such a problem results in Gibbs oscillations around the shock. These

oscillations result in unphysical values of negative pressure and density, thus spoiling either the complete solution or causing convergence problems. Typical approaches in the literature, to deal with this problem, are applying slope limiters at the shock regions to eliminate oscillations in the solution, processed after a time step; or using artificial viscosity methods to supplement the numerical damping of the method, that smears out oscillations in the shock. However, these approaches are empirical and require a great deal of trial and error or experience for optimum shock capturing. The goal of such efforts is to capture the shock as finely as possible without generating oscillations in the solution.

Numerical errors, generated in the shock, are associated with the shock capturing methods employed. These have been known to corrupt solution downstream of the shock, especially in the field of hypersonic flows. This significantly affects the heating predictions at the surface of the vehicle in a hypersonic flow [7, 8]. Significant difference in the heating prediction, have been reported, for less than 1 % change in the mesh around the shock. Even recent methods like PDE based artificial viscosity methods do not give completely accurate results for surface heating prediction for hypersonic flow over cylinder [9].

This work uses r-p adaptivity, in conjunction with DG methods, both with and without the use of slope limiters, to capture the shock. This methodology identifies the shock location, using a pressure based sensor and uses first order solution ($p = 0$) in the shock and higher order solution in the smooth flow region. This approach, called p-adaptivity was first used in [10], in conjunction with h-adaptivity to finely capture the shock. However, its application was restricted to inviscid flows. We extend this p-adaptivity, along with r-adaptivity, to viscous hypersonic flows with and without full thermo-chemistry. This work is compared to other similar efforts in using DG method for solution of viscous hypersonic flows (without chemistry). Development of this tool

opens up more opportunities for us, in utilizing this tool, for performing plasma simulation problems (main focus area of our group), another area with complex physics.

The remainder of this chapter is written as follows. We elaborate on our motivation, by highlighting the thermal ablation and hypersonic flow physics in section 1.1. Sections 1.2 and 1.3 point out some test cases, that specifically illustrate the challenges faced by the state of the art codes in the fields of thermal ablation and hypersonic flows respectively. Section 1.4 highlights limitations, in general, for finite difference and finite volume methods that the DG scheme overcomes. Our specific contributions to the fields of DG methods, thermal ablation and hypersonic flow applications are discussed in section 1.5. Section 1.6 draws out the structure of the rest of the thesis.

1.1 Motivation: Complex Physics of Thermal Ablation and Hypersonic Flow Problems

Problems of thermal ablation and hypersonic flow simulation deal with extreme physics of flow around the space vehicle and the thermal response of thermal protective system (TPS) on the vehicle's surface. These vehicles, mainly intended for inter-planetary missions, typically enter the atmosphere of a planet with very high speeds. The entry Mach numbers can vary between 20 and 50 [11].

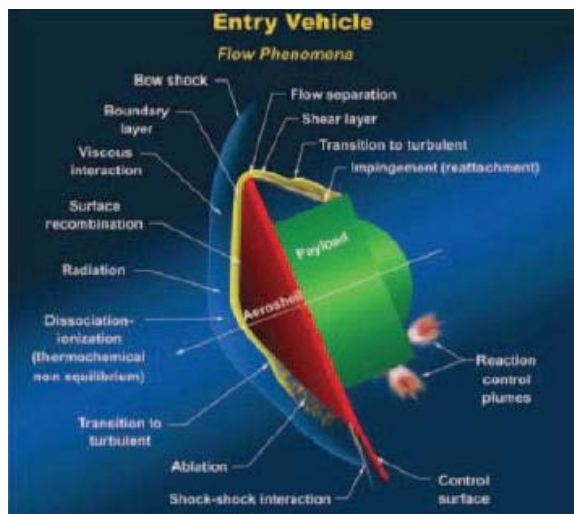


Figure 1-1. Physical processes on the surface of the space vehicle in hypersonic re-entry. All the relevant physical processes that contribute to the thermal ablation on the surface of the vehicle are shown.

Their body shape is designed to generate high drag forces so they can decelerate sufficiently either for landing purposes or to transfer to an orbit around the planet (aerobraking). Thus, they experience a large amount of viscous dissipation on the surface. Various mechanisms of heat transfer like radiation, convective heating, shock/boundary layer viscous interaction, and recombination of the dissociated and ionized species in gas flow, are responsible for excessive amount of heat transfer to the vehicle's surface that causes temperature rise of several thousand Kelvin. All these mechanisms are fully coupled to each other and complex in themselves. Thus their interaction is overwhelmingly difficult to accurately simulate the response of TPS to the given flow conditions.

Three main areas in analyzing the thermal ablation and hypersonic flow problem are the flight trajectory, the flow outside the space vehicle (interacting with the vehicle's body) and the thermal response of the ablating material on the surface of the vehicle [12]. As noted, all these mechanisms are complex and interact with each other in real time, and their proper understanding is essential to accurate modeling and numerical simulation of thermal ablation.

1.1.1 Flight Trajectory

Trajectory is the path of the vehicle during its flight with respect to Earth's or a planet's center. Flow environment around the vehicle can rapidly change as it descends. Gravitational, body and thrust forces acting on the vehicle's body can change its direction of motion thus changing the flow environment around the vehicle. Flow environment in turn affects the response of thermal protection system, and thermal response of TPS decides the mass, shape and Lift-to-Drag (L/D) ratio of the vehicle. So, both trajectory and TPS response can be strongly inter-coupled.

It is quite obvious that for a good design study, that aims to reduce extra mass on the vehicle, it's very essential to solve both flight trajectory and thermal response simultaneously. This is relevant for studies on design of TPS for future missions, and for

success of missions like Aero-assisted orbit transfer vehicles (AOTV), which are capable of on-orbit maneuvers [13, 14]. These studies focus on optimizing the solution space of trajectory for optimum mass, size and shape for TPS and fuel savings.

Studies aimed at understanding thermal ablation for an already made flight do not need to solve for flight trajectories in conjunction with thermal response of TPS and this can be calculated based on obtained data from the vehicle, during its flight, e.g. deceleration data sent from the accelerometer of Pioneer-Venus probes [15–18] was used to generate flight velocities during the entry of probes. Since, we focus on solving arc jet cases to establish solution capability for thermal ablation; solving for flight trajectory hence is not required in our work.

1.1.2 Flow Environment

As a space vehicle (on its entry) descends into atmosphere of increasing density, the flow around it makes a transition from free molecular to continuum flow. Collisions between impinging and reflected (from the surface) molecules are negligible in free molecular flow. This assumption is however not valid in transitional and continuum regime. A rapid rise in aerodynamic coefficient and heating rates are also observed at the end of transitional regime [11]. Free molecular and transitional flow regimes are a focus of DSMC (Direct Simulation Monte Carlo) schemes [19–21], we however focus on the continuum regime, where we can use the governing equations like Euler equations or Navier Stokes equations.

The flow chemistry can be characterized as frozen, non-equilibrium or equilibrium, depending on the intensity of collisions. Very few number of collisions ($K_{n,\infty} = \lambda_{\infty}/D \approx 100$) do not change the species distribution as the gas flows towards the surface (frozen chemistry). Moderate number of collisions ($K_{n,\infty} \approx 1$) cause the species distribution to be a function of collision history of the molecules (chemical non-equilibrium), and very large numbers of collisions ($K_{n,\infty} \approx 0.01$) overwhelm such dependence on previous collisions (chemical equilibrium), so that the distributions can be written as algebraic

functions of local temperature and pressure. Flows in general are chemically reactive and frozen or equilibrium models cannot be used.

Due to hypersonic flow velocities, a bow shock is formed in front of the vehicle and it can be either attached (at higher altitudes) or detached (at lower altitudes) from the surface of the vehicle. Flow away from vehicle surface is inviscid and there is a boundary layer formation, near the surface, due to the viscous nature of the flow. Boundary layer for the hypersonic flow can have large thickness, and a rapidly growing boundary layer interacts with the inviscid flow. If the inviscid flow is greatly affected by the boundary layer (due to large increase in pressure, skin friction and heating), then it may strongly feedback to the boundary layer itself [22], hence causing strong viscous interactions, which can cause severe local peaks in aerodynamic heating at the vehicle's surface.

In addition, shock wave may also impinge with boundary layer, due to its increasing thickness away from stagnation region (Figure 1-2). This results in adverse pressure gradient in that region of boundary layer, causing the boundary layer to separate. This in turn produces induced and reattachment shocks. Boundary layer becomes comparatively thin at the point of reattachment, and this again may cause severe local heating at the surface.

Due to strong shock, the gas species may also undergo dissociation and electronic excitation. Flow particles impinging on and also interacting with the vehicles surface (surface chemical reactions) cause convective heating. The dissociated species can also recombine (for high Damkohler numbers, or in other words chemical equilibrium) near the surface of the vehicle, due to lower temperatures, transferring their heat of formation to the surface, which results in additional convective heating. However since recombination is a three body reaction, Damkohler numbers usually tend to be small, and majority of the dissociated atoms flow into the wake and recombining far

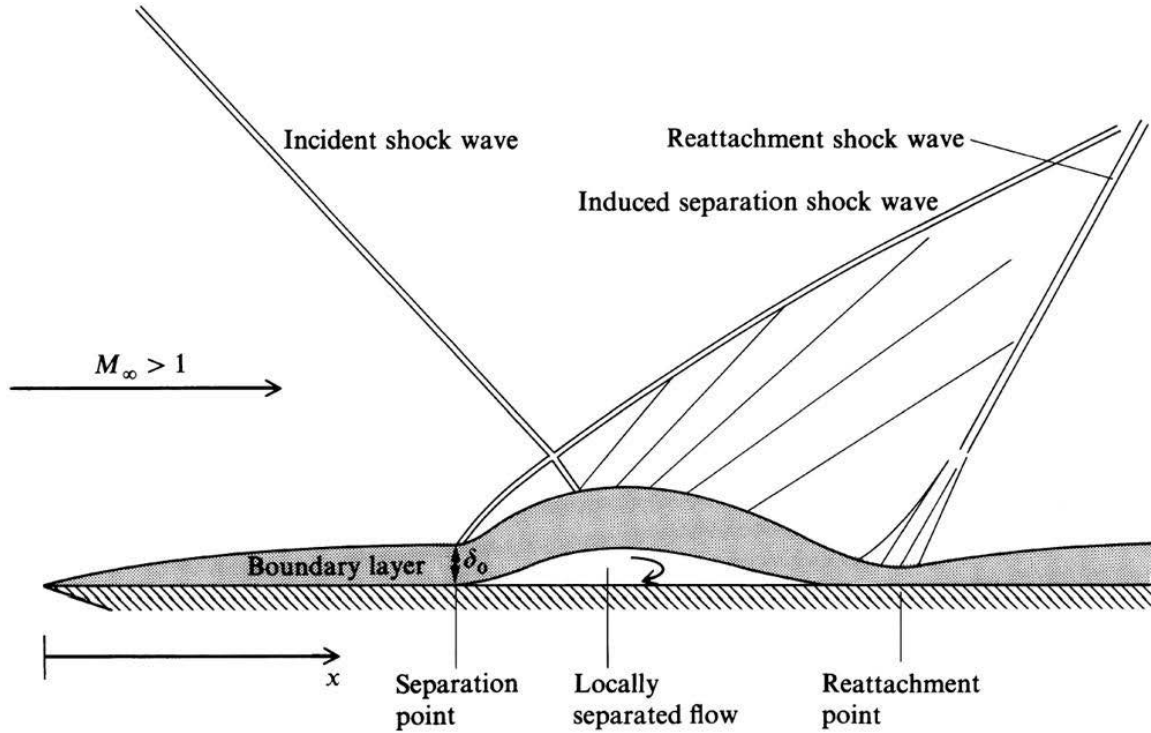


Figure 1-2. Hypersonic shock-wave boundary layer interaction. Adverse pressure gradient (due to interaction of shock and boundary layer) results in separation of boundary layer. Both induced separation shock and reattachment shock result from this interaction. Boundary layer especially tends to become thin at point of reattachment resulting in increased local heating at the surface [22].

downstream they reduce net heat transfer to the surface. However, surface acting as a catalyst for the recombination can also offset this advantage [11].

We consider dissociation reactions in our study. Since charged particles require different treatment than neutrals, for this study we omit out ionization reactions. Excited species also cause high amount of radiation heat flux to the surface of the vehicle (radiative heating). Since calculation of radiation requires solving integro-differential equations and is more complex than solving differential equations, we use emissivity and Stefan Boltzmann's law to incorporate radiation into the thermal ablation model.

1.1.3 Thermal Response of Ablating Material

Thermal protection systems are of two types, charring and non-charring [23]. Non-charring TPS (like carbon-carbon and silica) do not undergo chemical decomposition

at high temperatures. These materials may lose their mass by surface ablation, melting or fail mechanism. Surface ablation refers to removal of material from surface through chemical reactions, e.g. carbon in carbon-carbon may oxidize to form CO, or CO₂ and undergo nitridation to form CN [19].

Charring TPS like carbon phenolic is made of two components, fibrous component like graphitic carbon and a resin material. Resin component undergoes decomposition at high temperatures and releases mixture of gases called pyrolysis gas. Decomposition of resin material leads to formation of voids or pores in the material. Further gas generation and temperature rise leads to pressure build up in the pores, which causes the pyrolysis gas to leak out to the atmosphere. Leaking of pyrolysis gas into the boundary layer is called blowing phenomena and it acts to reduce the net amount of convective and radiative heat in flux to the surface [24]. Since, charring TPS provides better cooling mechanism, we will focus on these materials for our research. Important physics, that governs the thermal response of the material to the incoming heat flux, is described in the following sections.

1.1.3.1 Thermal conduction

Heat from hot gases is conducted into the TPS material. TPS material is a composite consisting of different materials. But still due to similar materials, thermal conductivity is fitted as one model for the overall material, by assuming that thermal conductivity is essentially isotropic [25]. These materials usually display low thermal conductivities and high specific heats, so that heat conduction process to inside material can be slowed down, and large amount of heat absorbed so that when some material is rejected at the surface it takes with itself substantial amount of thermal energy.

1.1.3.2 Material failure and thermal decomposition

The process of thermal decomposition was briefly mentioned in section 1.1.3. A charring TPS upon decomposition leads to formation of three zones in the ablating medium [26, 27]. These zones are shown in Figure 1-3. The zone with all the resin

intact is the virgin zone, the zone where material is undergoing decomposition is the pyrolysis zone and the last zone which has been depleted of all its resin content is the char zone.

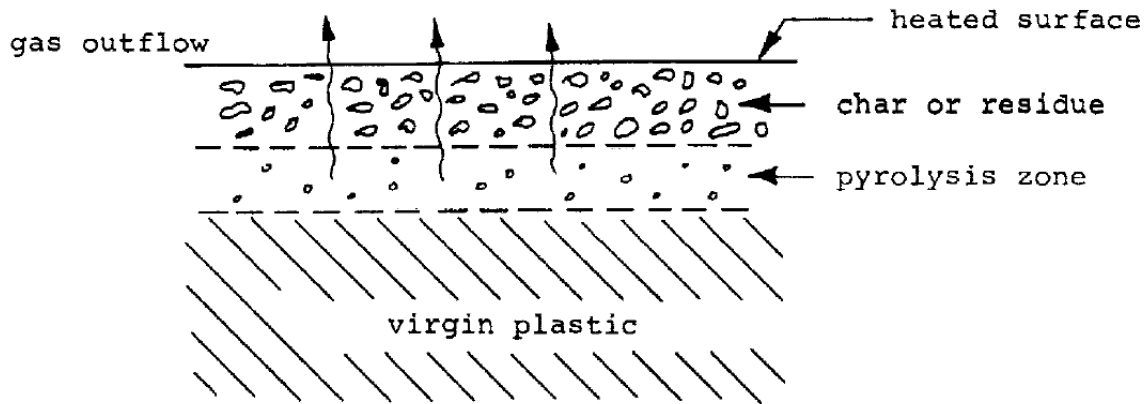


Figure 1-3. Schematic showing three zones in the charring ablator. Virgin zone has all its resin intact; pyrolysis zone undergoes thermal decomposition; and char zone, has all its resin content depleted. The released gas is called the pyrolysis gas, and it leaves the pores in the ablating zones. It also provides for the blowing effect at the surface [27].

Studies [16, 24, 28] have shown that the motion of pyrolysis gas through the porous media provides for extra cooling of the material, as it absorbs extra heat from the material, while exiting into the atmosphere. Some studies [15, 29–31] neglect this mechanism to avoid modeling of motion of pyrolysis gas through the porous media, but incorporating motion of pyrolysis gas is important for at least two reasons.

In low to moderate pressure and heating environment, thickness of both char and pyrolysis zone are substantial [16], so pyrolysis gas spends substantial amount of time traveling through this zone, hence absorbing sufficient energy from the solid. Second reason is to account for material failure due to development of high pressures within the porous media [16, 32, 33]. This phenomenon of material failure is referred to as spallation. In this work, we also include the modeling of the flow of the pyrolysis gases in our numerical simulations of thermal ablation problems presented in [4, 5, 34].

Additionally, these model equations are also employed for a Langley arcjet test case. These equations are taken from [16, 17, 35] and are presented in section 2.4.

1.1.3.3 Surface ablation

Degradation and recession of surface is referred to as surface ablation. Surface can recede due to chemical reaction of surface with incoming gases from the flow field, or surface may also melt or vaporize due to high temperature. This is referred to as thermo-chemical ablation. Shear stress and pressure of impinging fluid may also remove micro particles from the surface [12], and thermal expansion strains and mechanical loads (due to aerodynamics or high pressure inside) may also cause material to be removed from the surface.

1.2 State of the Art of Numerical Simulations in Thermal Ablation

Thermal ablation is governed by many complex and inter-dependent physical processes, as already discussed. Goal of TPS design study is to predict the performance of a TPS (both of its material and shape) under given flight conditions. Such flight conditions are either simulated in an entry simulation facility, like arc-jet test facility, or are available through data obtained from actual flight missions (or planetary missions). Success of the design study depends on our understanding of all processes relevant to thermal ablation and their interactions.

Experimental facility, being both cost and time intensive, is not sufficient on its own to carry out an effective design study. Also, it does not offer sufficient insight into the mechanisms involved in a thermal ablation process. Thermal ablation turns out to be too complex for an analytical approach to be useful. In contrast, numerical tools actually serve the purpose of testing out formulations that model the processes in thermal ablation. Data from actual flights and experiments are useful for validation of these numerical procedures, and thus the postulated models can be tested.

Numerical efforts in the past have focused on hypersonic flow environment and thermally ablating material which interact with each other in real time in actual flights.

Numerical models and simulations in both of these fields are very challenging and therefore developed independently as separate codes from the beginning. Later on, however, as the interdependence of both these codes was better understood, attempts were made to provide some kind of coupling between them.

The current state of the art in thermal ablation is that both the domains are coupled to each other through a surface boundary condition (for either mass balance or energy balance or both of them). They are not solved simultaneously with each other in an iterative fashion. They are only solved at discrete trajectory points, where only one of the two codes may be run for the whole time between two trajectory points, while the other one is called into operation, only at the trajectory point itself. This solver then provides for boundary conditions for the other solver, which remain constant for that solver till the next trajectory point. Reason for not simultaneously running both the thermal response code and the flow solver is that the flow solver simulations tend to be expensive to run at every timestep. Additionally, with the loose coupling, the number of iterations for convergence per time step is also large, further increasing the simulation cost. Fewer trajectory points result in accuracy and convergence issues and more trajectory points lead to increase in both time and cost of computations.

A brief overview of the past work, in the development of the material thermal response codes, highlighting their numerical and modeling aspects as well as the challenges that were overcome with time, is presented in sections [1.2.1](#) and [1.2.2](#).

1.2.1 Past Development of Material Thermal Response Codes

Since thermal ablation is itself a very complex problem, involving many complicated physical processes occurring simultaneously, past numerical efforts began with simplifying assumptions, and gradually level of complexity was increased with time. We look into major thermal response codes that brought some important change in the industry and were used to solve thermal ablation problems of known space missions.

1.2.1.1 Charring Material Ablation (CMA) code

Charring Materials Ablation code or CMA was developed in late 1960's by Moyer and Rindal [27]. It was developed as a one-dimensional finite difference based code with variable cross-section area, so it could be applied to 2-D geometries with 1-D energy flow. There are three important equations involved, internal energy equation that solves for thermal response of the ablating material; material decomposition equation that specifies rate at which material inside will decompose at the given temperature and surface energy balance equation, which applies to outside of the vehicle for balancing all incoming and outgoing heat fluxes at the receding surface. Pyrolysis gas formed due to decomposition of resin is assumed to be in thermal equilibrium with char, i.e. no chemical reaction with char material, and any gas formed is assumed to leave the char immediately, i.e. no residence time in the char.

Two main limitations of CMA [29, 33] are its explicit treatment of internal decomposition and surface energy balance (with implicitly solved internal energy equations). This causes convergence problems in the code for high decomposition or high surface recession rates. The complete treatment of one-dimensional finite difference is also very complex, due to node-dropping strategy employed for treating receding surfaces during ablation.

In one study [15], CMA was used to reconstruct the thermocouple data of 4 Pioneer-Venus probes that flew into the planet Venus in 1978. Both Wakefield heating [15] and Park heating [16] rate were used to assess the net heating rate at the surface of the probes during their flight. Comparison of their heating rates is given in Figure 1-4. Flight data from the probes provided for velocity and atmospheric pressure, and thus surface heating rates were calculated.

CMA does not account for the motion of the pyrolysis gas [36], which provides for the cooling phenomena in the ablator. Thus, Wakefield and Pitts [15] observed temperatures higher than the melting points of thermocouples (Figure 1-5). Neglecting

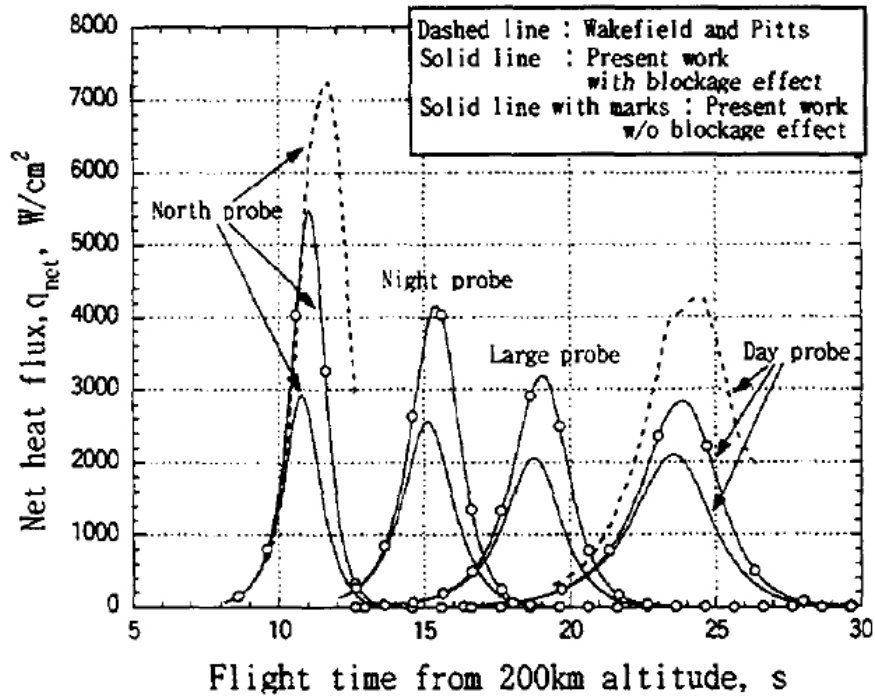


Figure 1-4. Comparison of net heating rates at the surface of Pioneer Venus probes. 'Present work' refers to Ahn et al. [36]. Comparison shows high heating prediction by Wakefield heating rate, which assumed thermo-chemical equilibrium assumption at the stagnation point, whereas heating rates predicted by Park's method, which assumes finite rate chemical reactions, are lower. Injection of the pyrolysis gas into the boundary layer is called the blowing phenomena and provides for convection blockage that further leads to lower heating rate predictions.

the flow of the pyrolysis gas, thus leads to unrealistically high temperature predictions. Also, by using finite-rate chemical reactions in both gas and gas-surface interactions, as opposed to Wakefield heating rate, which assumed thermo-chemical equilibrium at the surface, lower heating rates were predicted. The results of this simulation are shown in Figure 1-4. Lower temperature predictions, with and without the blockage effect, are found. Though the temperatures do not entirely match, the reason for this is difficult to ascertain, unless full CFD flow simulation is done with the material thermal response code. The methods used in this study are, in general, referred to as CFD approximation methods, which aim to find the heating rate profile with time. Hence, only the material thermal response code is run, with the heating rate provided as a function of time.

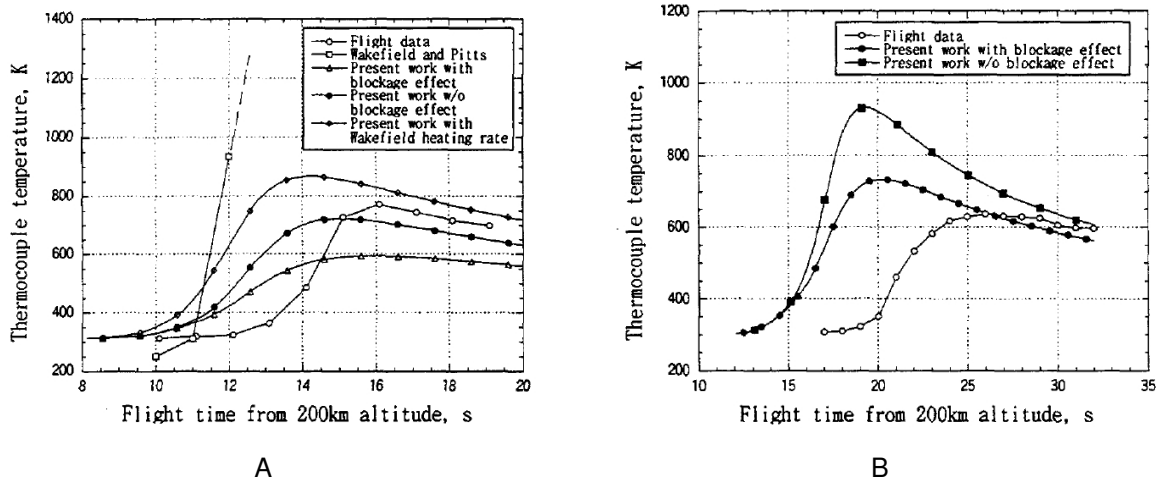


Figure 1-5. Comparison of the temperature histories from flight data and numerical predictions. A) Flight data and temperature predictions for the Day probe. B) Flight data and temperature predictions for the North probe. Numerical predictions are obtained from Wakefield and Pitts [15] and Ahn et al. [36] (referred to as 'Present work'). Wakefield and Park heating rates are used with and without the blockage effect. Results show that Wakefield heating rate predicts temperatures higher than the melting point temperatures of thermocouple. This is due to the neglect of the flow of the pyrolysis gas through the ablating material in CMA.

1.2.1.2 Fully Implicit Thermal response and Ablation program (FIAT)

Later on, to have more accurate TPS sizing programs, material thermal response code was coupled to flow solver code and both were iteratively solved. CMA due its numerical instabilities caused the iterations process to slow down. Therefore, FIAT, which is a fully implicit finite difference code based on the same governing equations as CMA, was developed by Chen and Milos [29] and was shown to be numerically stable for a wide range of TPS sizing problems. It also included other features like solving integro-differential equations (in explicit fashion, which did not cause any convergence issues, as internal radiation cools the surface) for internal radiation of the material, and coupling to CFD codes, like GIANTS [37, 38] and GASP [39, 40]. It was also used for thermal response analysis of materials like PICA (phenolic impregnated carbon ablator), and SIRCA (silicone-impregnated carbon ablator) for space missions like Stardust and

Mars pathfinder. Here grid compression, rather than node-dropping strategy in CMA, was used to represent receding surfaces.

1.2.2 Recent Developments of Material Thermal Response Codes

Here, we present some of the more recent thermal response codes and efforts, therein, to overcome the limitations of CMA and FIAT.

1.2.2.1 Control Volume Finite Element Method (CVFEM)

Moyer and Rindal [27] used upwind differencing scheme for apparent convection terms that appear due to translating grid (to account for surface recession) in CMA, and the same idea was also extended by Blackwell [41] in context of finite control volume using exponential differencing scheme by Spalding. The limitations with translating grids were that they were not easily applicable to multi-dimension problems. Therefore new concept of compressing grids was used in conjunction with Landau coordinates transformation by Blackwell and Hogan [42]. In comparison to CMA, where the last node at the ablating surface was dropped whenever the surface receded beyond the last node, total number of cells or elements remains constant in this method. Hence only the relative size of grid decreases. Therefore total number of elements or cells near the ablating surface always remains fixed.

Method of CVFEM in their initial publications was illustrated for one-dimensional problems, and later on in 1996 [43], it was extended to two-dimensional planar/axisymmetric geometries by assuming the mesh motion to be that of an elastic solid. This work, however did not consider effect of pyrolysis gas and coupling for both solid and fluid domains. In their recent works published in 2007 – 2010 [32, 33, 44], a code named MOPAR (Modeling of pyrolysis and ablation response), which is based on CVFEM, has been developed to deal with motion of pyrolysis gas flow within the ablating medium and also coupled [32] to a CFD flow solver, LeMANS [45, 46] developed for solving weakly ionized hypersonic flows with thermo-chemical non-equilibrium. They have enhanced

the explanation of effects of pyrolysis gas on the ablation response of a material, but have been restricted to one dimensional ablation problems.

1.2.2.2 Two-dimensional Implicit Thermal response and Ablation program (TITAN)

Capability to simulate thermal ablation for an actual two or three dimensional geometry is essential for shape-change simulations, where the goal is to predict shape change of the vehicle since that will affect the aerodynamics around the vehicle, and vice versa is also true. For this, a two dimensional thermal response code named TITAN was developed by Chen and Milos [47], which was solved in loose coupling with GIANTS, a CFD flow solver for simulating arc jet test models, and TITAN/MEIT, where MEIT [48] has engineering correlations developed for flow over slender body with small cone angles, and is thus less expensive as compared to GIANTS which is a full Navier Stokes solver. Here, they demonstrated how uncoupled simulations with TITAN and flow solvers would give unphysical results for their test cases of flat-faced cylinder test sample and slender body (Figure 1-6).

It has been identified in [49] that TITAN/GIANTS solver divides the complete mesh into two, external grid and internal grid, where external grid contains thermally ablating media is a moving grid and internal grid, the inside vehicle structure is fixed. With this, TITAN/GIANTS can only solve simplified two-dimensional geometries. To overcome this limitation, TITAN/GIANTS were coupled with a third finite element based code, MARC [50], that deals with thermal and structural analysis of inside material, where the temperatures rise to levels at which no ablation or any decomposition effects are observed. It is mentioned in [49], that MARC cannot handle pyrolysis and ablation phenomena. So, now they have three integrated coupling of TITAN/GIANTS/MARC, and this coupling is in no way trivial (Figure 1-7). Also, it is anticipated that such coupling will slow down computations and also present challenges for convergence.

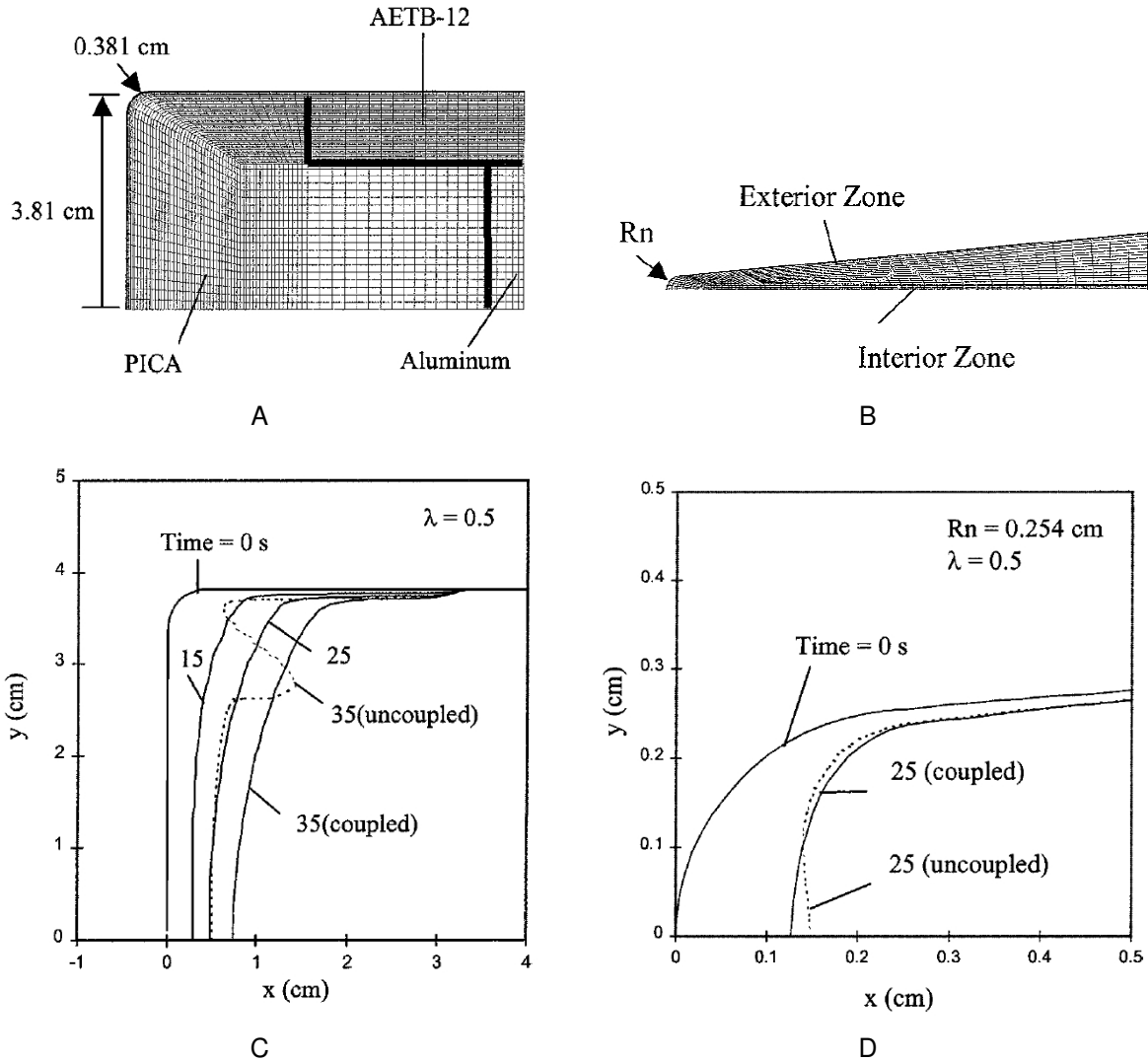


Figure 1-6. Effect of loosely coupled formulations on shape change simulations. A) Mesh for flat faced cylinder. B) Mesh for slender geometry. C) Shape change result for flat faced cylinder shown at 35 sec. D) Shape change result for slender geometry shown at 25 sec. TITAN/GIANTS are used [47] in loosely coupled as well as uncoupled simulation. Unphysical results are obtained by an uncoupled simulation.

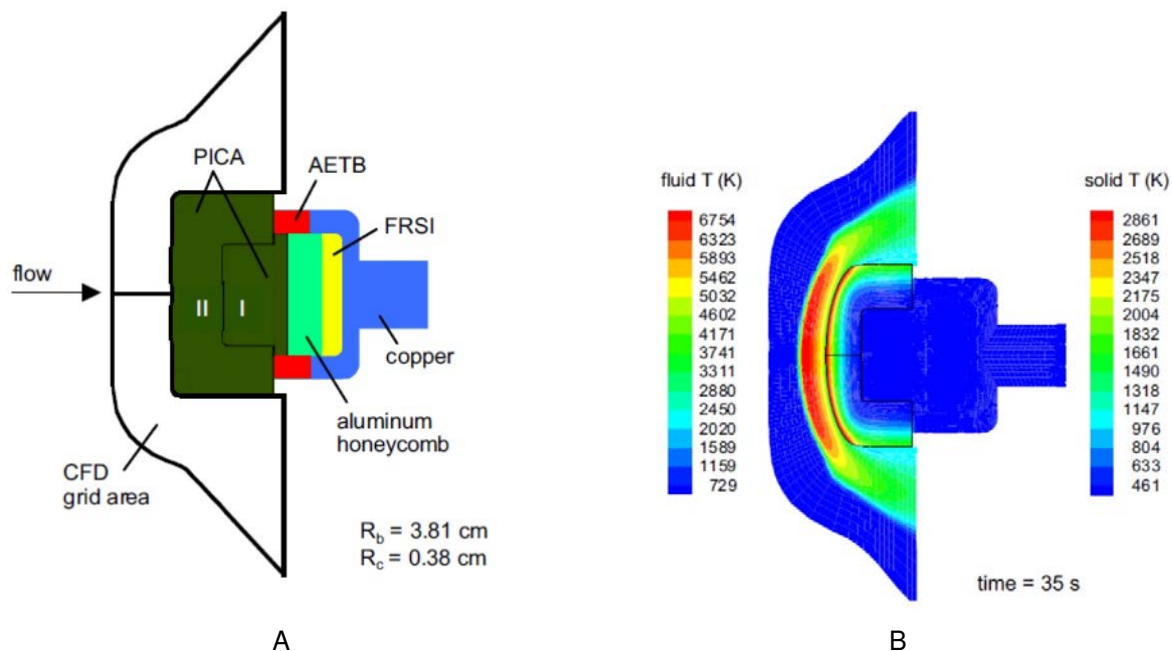


Figure 1-7. Simulation of arc-jet test model using MARC/TITAN/GIANTS. A) Different domains including fluid, ablating media (PICA) and other structural components holding PICA are shown. B) Simulation results for the arc jet test model are shown. Fluid domain is solved using GIANTS and solid domain is solved using TITAN for PICA material and MARC for rest of the structural components. Temperature distribution is shown at a time of 35 sec [49].

1.2.2.3 COYOTE/SACCARA fully coupled simulations

Flow solvers with chemically reacting flow are computationally intensive (due to extra equations from chemical reactions) and in coupling with a thermal response code, the requirements become excessive, therefore it is a general practice to solve only for discrete trajectory points of an actual flight, and solve flow solver only at the trajectory points, which then provide fixed boundary conditions to the thermal response codes. Such simulation was run by [51], where they assumed flow to be in thermo-chemical non-equilibrium, and simulation was performed through SACCARA (Sandia Advanced Code for Compressible Aerothermodynamics Research and Analysis), which is a finite volume parallel code and can solve full 3D Navier Stokes equations for flows in thermo-chemical non-equilibrium. The code was coupled to COYOTE, a finite element

based code developed to solve for heat conduction types of problems for complex geometries.

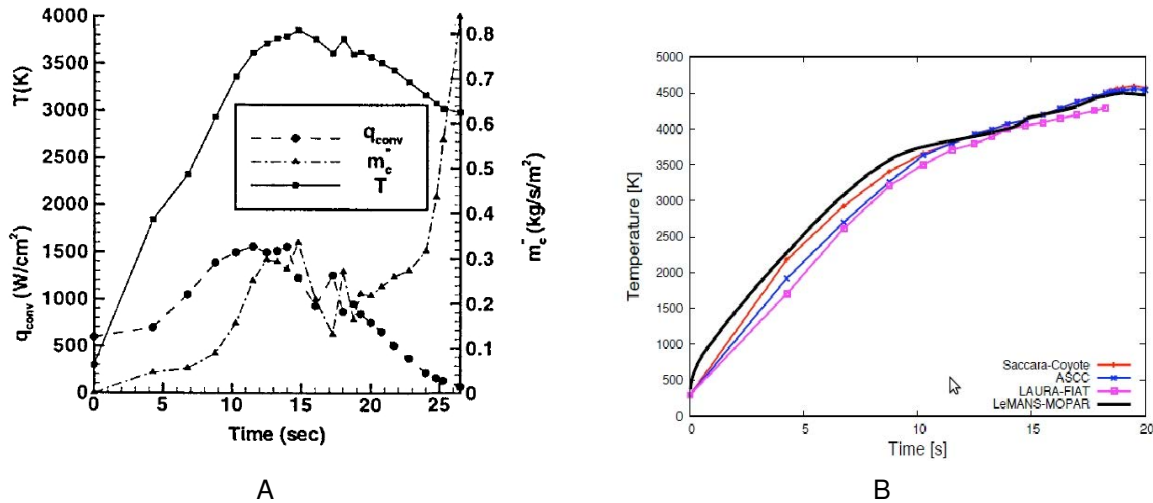


Figure 1-8. Anomalous fall of stagnation point temperature using COYOTE/SACCARA coupling. A) Results predict anomalous fall of stagnation point temperature after 14 seconds [51]. B) Improved results are shown for iterative coupling of COYOTE/SACCARA [52]. Lack of coupling resulted in temperature lag between the trajectory points (shown in dots). This imprecision leads to highly inaccurate predictions.

Both these codes are loosely coupled to each other. First, SACCARA code is run for a steady state flow at a trajectory point and it provides for convective heating rate, recovery enthalpy and pressure value at each surface node of the vehicle. These values are input to COYOTE, which then solves for temporal material response in and provides for ablation rate. Ablation rate and the pressure are used by ACE code to compute injected species mass fractions at the surface of the vehicle. Surface displacements from COYOTE are used to create new flow field mesh by a mesh generator, and the new mesh, surface species concentrations and surface temperatures (computed by COYOTE) are then fed in to SACCARA to for a new steady state simulation at the new trajectory point.

This coupling was tested out for an IRV-2 vehicle, and for its given trajectory its thermal response was studied. It was found in [51] that there were convergence

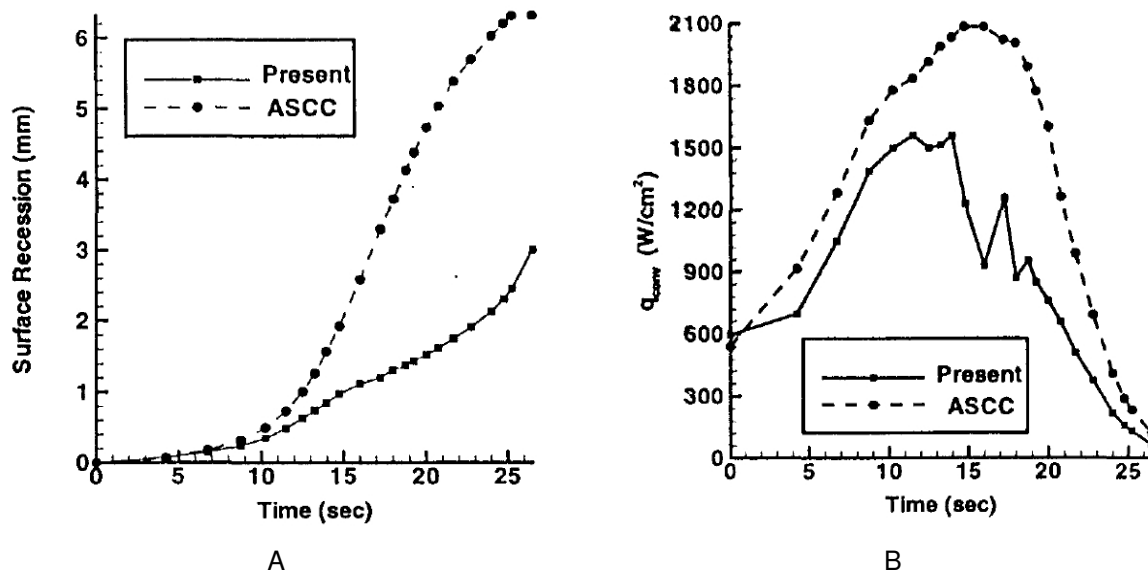


Figure 1-9. Avoiding anomalous surface recession in COYOTE/SACCARA coupling. A) Net surface recession comparison of COYOTE/SACCARA [51] and ASCC. B) Net heating rate comparison of COYOTE/SACCARA and ASCC. Heating flux value is updated every time step (10^{-3} sec) in ASCC and after every 0.5 sec in COYOTE/SACCARA. This results in ASCC heating prediction to be higher than COYOTE/SACCARA (denoted as 'Present'), causing anomaly in the surface recession observed.

problems in middle part of trajectory simulations, due to which a regular fall in stagnation point temperature was observed after nearly 14 seconds (Figure 1-8), due to which net surface recession predicted was almost half of as predicted by ASCC, which was used to validate their results. It was also noted that computed heating rate by the flow solver was sensitive to convergence; hence calculated heating rate was also lower than ASCC (Figure 1-9). In one of their papers [52] later on, they used iterative coupling between flow solver and thermal response code, and sufficiently accurate results were obtained (Figure 1-8 B).

Many test cases are available in thermal ablation literature, which show instability in numerical simulations due to some inconsistency in modeling. Another example is [53], in which MOPAR, a one-dimensional implicit material response code with surface ablation and pyrolysis, was coupled to LeMANS, a CFD solver, and results for IRV-2

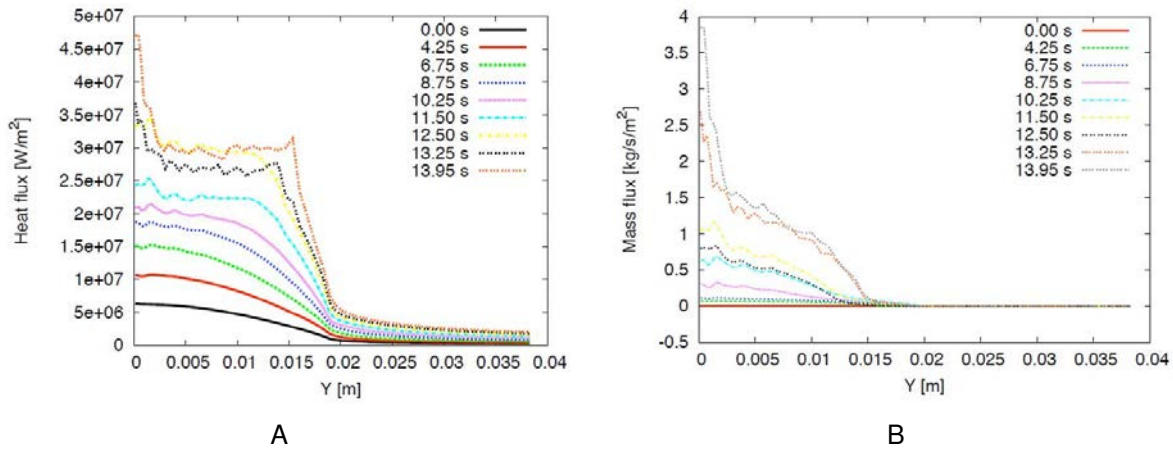


Figure 1-10. Oscillations in the heat and mass flux due to perpendicularity assumptions. A) Heat flux oscillations due to imprecision in modeling. B) Mass flux oscillations resulting from the loss of assumption of perpendicularity of mesh to the surface boundary as surface recedes. Imprecision is assumed to have been amplified at each discretized trajectory point, which can be attributed to the coupling between two domains. Such issues are not expected to occur where both problems are solved in one domain [53].

vehicle were shown. To implement a strong coupling between the material response code and the flow solver, modifications were made to the flow solver at the wall, where the ablated species were injected. This was done through adding blowing boundary conditions at the wall in flow solver by using first cell near the wall as a control volume.

In addition to this, mesh for the flow solver was also allowed to move as the surface the vehicle recedes for a complete strong coupling. For validation purposes, results were compared for IRV-2 vehicle. Both recession and stagnation point temperature was matched well to ASCC code and COYOTE/SACCARA, however their results for heat flux and blowing rate showed oscillations in the solution (Figure 1-10). This was attributed to the imprecision in the solution, which was amplified in later trajectory points in solution of heat flux and blowing rates, which are very critical to measure thermal response of the vehicle.

1.3 State of the Art of Numerical Simulations in Hypersonic Flow

Various challenges in the field of hypersonic flow simulation are complex geometries of space vehicles, e.g. capsule-based entry vehicles and air-breathing launch systems; accurate simulation of the roughness-induced transition of turbulence on the surface of the vehicle; new methods for coupling of radiation, chemistry and flow models; and need for automatic hybrid simulation methods for both continuum and rarefied flows [3].

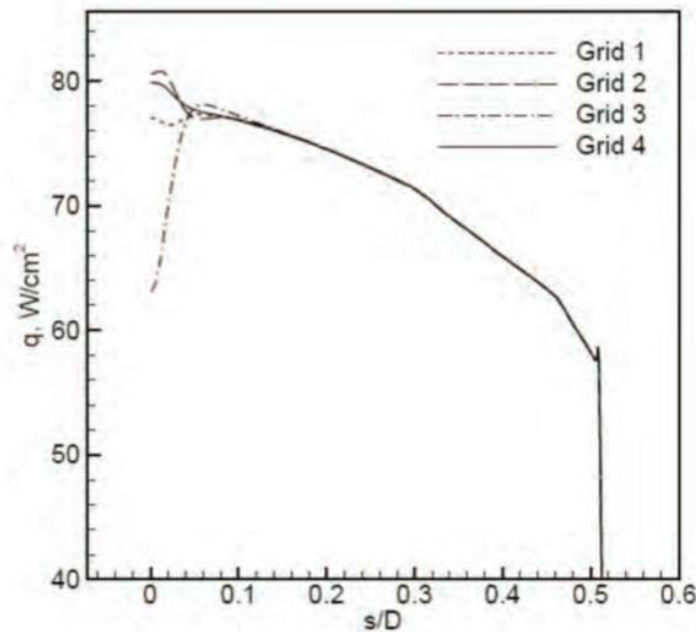


Figure 1-11. Sensitivity of heating prediction to grid alignment along the shock. Large variation in surface heat flux is observed for four different grids, with less than 1 % variation at the shock's location. Highest sensitivity is noticed at the stagnation point. The simulation results are shown for a capsule at an altitude of 70 km and with flow Mach number of 26.2 [7].

Toughest of all challenges in hypersonic flows has been accurate and robust prediction of aerodynamic heating or the heat transfer at the surface of the vehicle [3, 7–9, 54, 55]. Prediction of surface heat transfer coefficient is very sensitive to the mesh alignment along the shock. Even a slight misalignment of cells of a very small degree can cause tremendous changes in the surface heating prediction (Figure 1-11).

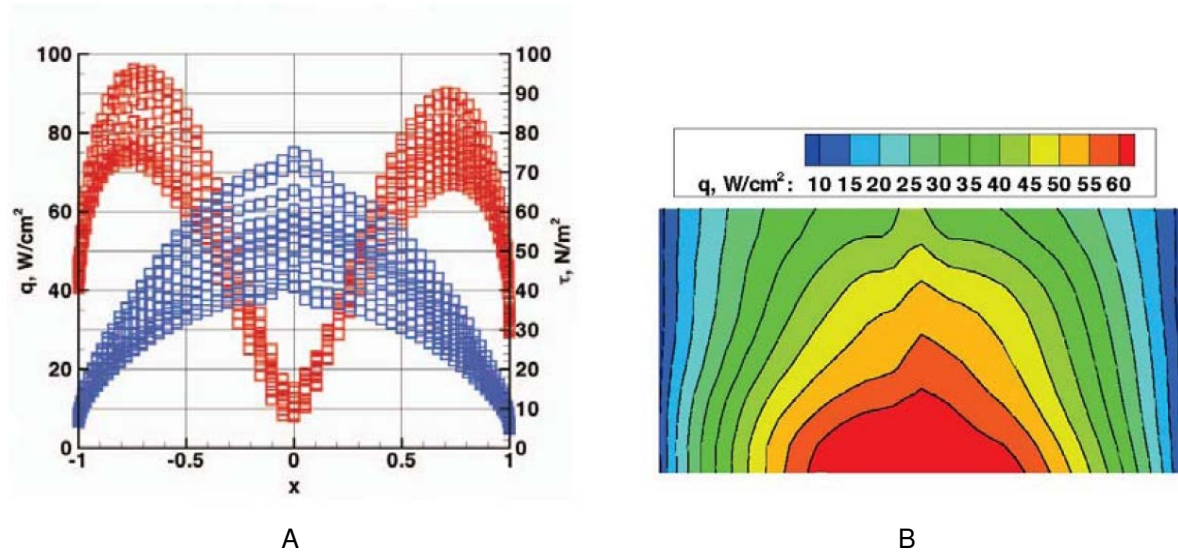


Figure 1-12. Large variation in heating predictions for 3D hypersonic flow over cylinder. A) Surface heat flux over ten spanwise elements, in the Z-direction. B) Heat flux contours over the cylinder's surface. Conventional reconstruction, for the tetrahedral grids, causes large variation in the spanwise direction for a problem of an essentially 2D nature [8].

The problem worsens for 3D simulations of an essentially 2D hypersonic flow over the cylinder (Figure 1-12), and large variations are seen to occur along the span-wise cells (in the z-direction, perpendicular to the plane of the flow) [8, 9].

Due to interest in the complex geometries, the use of unstructured meshes is desirable. Unstructured meshes are more convenient and less time-intensive to generate than the structured meshes. Furthermore, a lot of effort is still required, in the case of structured meshes, to align the elements along the shock and iterating for converged and accurate solutions.

To this end, solution adaptive methods are sought [2, 3, 9, 10] to enable output-guided grid adaptation, for accurate and efficient solutions. High-order methods are also essential for enhanced spatial accuracy to reduce the numerical error. In addition to all this, capturing complex physics further compounds the difficulty.

For more complex problems, there may also be multiple shock-shock interactions or shock-boundary layer interactions resulting in local flow separation and reattachment

thus generating complex flow features. Further challenges, to capture accurate solutions are dearth of hypersonic flow test facilities, approximated physical models based on limited experimental data, and numerical errors associated with capturing high gradient solution.

[7] points out additional complexities associated with the hypersonic flow simulations of re-entry vehicles. Temperatures in shock reach several thousand Kelvin, and hence the perfect gas model is no longer a valid assumption. Instead the flow is considered to be a mixture of ideal gases, and the flow chemistry accounts for production and destruction of all the species.

A wide range of density values varying almost by two orders of magnitude is encountered in the flow around a re-entry vehicle. Density increases by an order of magnitude across the shock and further even more significant increase is observed near the vehicle's cold surface (relative to high temperatures in the shock and shock layer). As the flow goes around the vehicle, the density value falls to values significantly lower than the free-stream value. Thus the flow field of a re-entry vehicle may span a wide range of chemical equilibrium (near cylinder surface or shock layer), non-equilibrium (in shock) and frozen chemistry (in the wake region) (Figure 1-13).

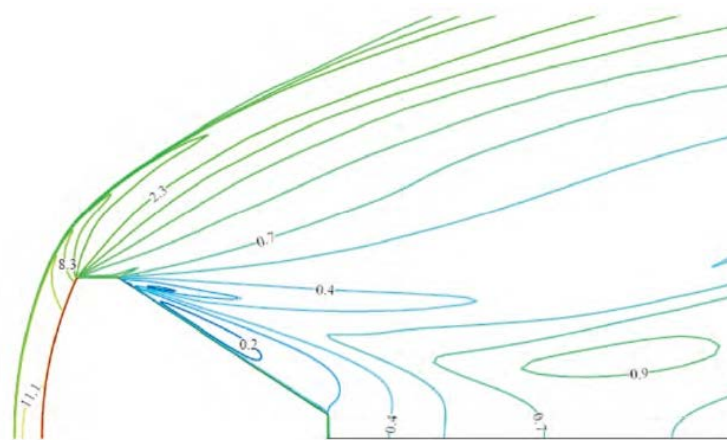


Figure 1-13. Range of densities for hypersonic flow around re-entry capsule. Contours of density show large variation of density values in the flow field. Flow Mach number is 16 [7].

Prediction of heat transfer is very sensitive, due to very high convective heat loads. For example, we found in our calculations for Mach 17 flow over cylinder, that a small error in temperature at the surface of the vehicle can cause significant differences in the heating predictions. If the temperature at the wall is fixed at 500°C , and the element next to the wall has 0.45°C error. Then this, apparently small error in the temperature, which is equal to 0.09 % error, will cause 3.125 % error in surface heating coefficient, C_h , at the stagnation point. Thus, the value of C_h at the stagnation point may vary from 0.008, the desired value, to be 0.00825. This error is significantly visible in Figure 1-14.

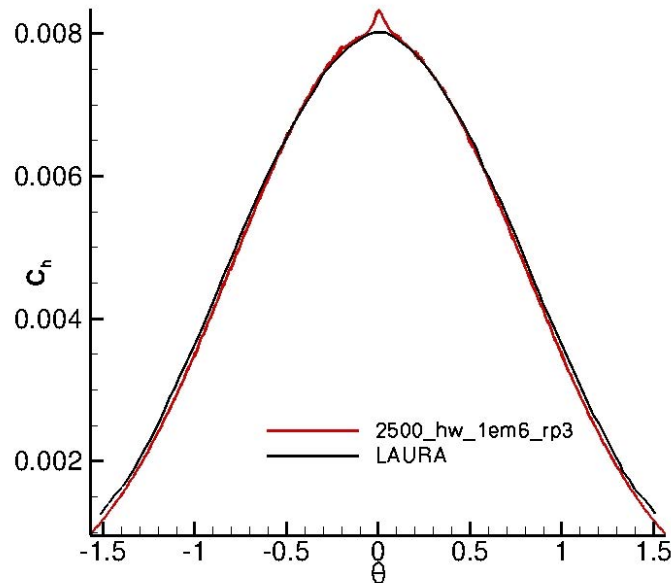


Figure 1-14. Error in C_h profile at one of r-p adaptivity iterations. 3.125 % error in C_h profile (shown in red color, in reference to LAURA solution, shown in black) can come due to a small 0.09 % error in temperature prediction near the wall. This is our result, from one of the r-p adaptive simulation, that needed one more iteration of r-adaptivity to remove the bump visible in C_h profile.

So, any amount of error in the prediction of the gas temperature close to the surface, will significantly affect the calculation of the net heat flux near the wall. This is dependent on few factors. Due to the cold wall, atomic gas species recombine at the wall (recombination is exothermic), thus releasing heat to the wall. Hence accuracy

of gas temperatures predicted near the wall depends on the uncertainty and errors associated with the modeling of chemical reactions rates. Additionally net thermal conductivity of the mixture also depends on its constituent gases, again affecting the net heat flux at the wall.

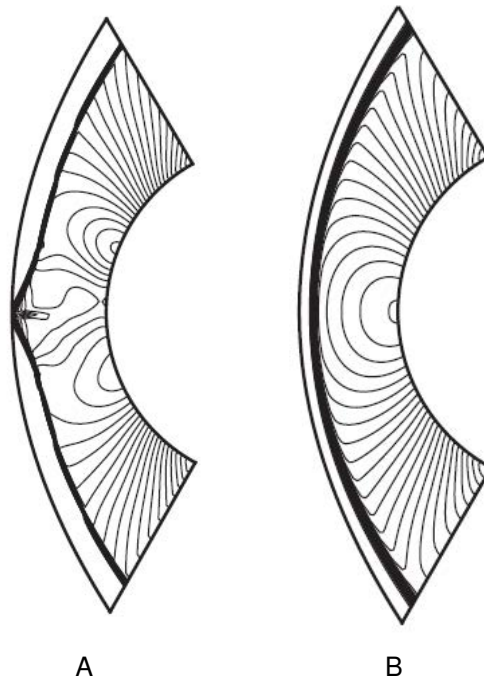


Figure 1-15. Carbuncle effect in hypersonic flow over cylinder. A) Solution with carbuncle. B) Solution without carbuncle [54].

Strong shock wave forming in front of the vehicle is also prone to numerical errors thus causing that error to propagate downstream and affecting net surface heat prediction. A fine grid is required to capture the shock to reduce the error, and the one set of grid has to be perfectly aligned with the shock to obtain accurate solution. Otherwise small misalignment can cause drastic differences in heating predictions as shown in Figure 1-11. It is interesting to note that the main sensitivity arises at the stagnation point rather than elsewhere on the body.

Carbuncle effects frequently plague many CFD methods on very fine mesh close to the shock (Figure 1-15). It is easy to identify such anomalies on simple geometries, but not so obvious in the case of complex geometries. In case of simple geometries, like

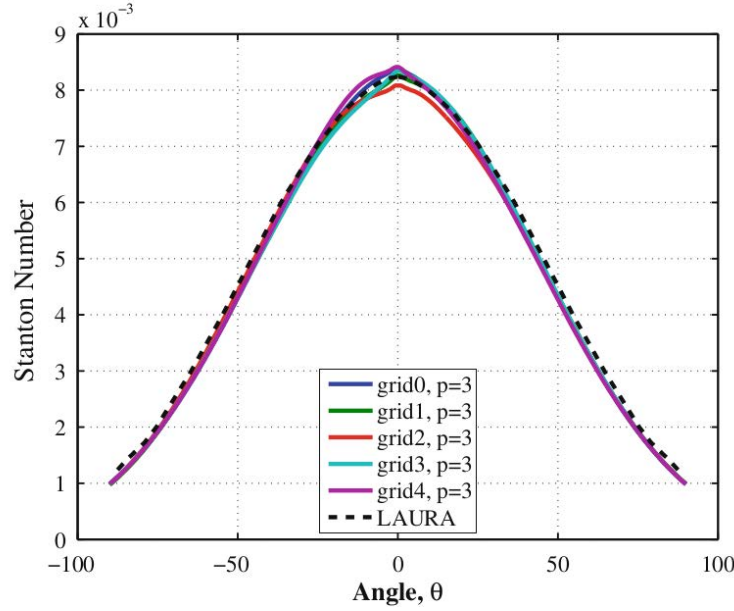


Figure 1-16. Asymmetry in C_h profile using PDE based artificial viscosity. A 4th order accurate DG method is used [54]. C_h profiles with different meshes are compared to the standard solution from LAURA. Minor asymmetry and small bumps in C_h plots are seen even for well resolved finest grid solutions. 'grid4' corresponds the finest grid used.

cylinder, it will be obvious to identify the carbuncle effect as non-physical, but the same is not true for complex geometries [54].

In the field of DG methods, the PDE based artificial viscosity is applied to the shock region, to capture the shock in one element [9]. The use of PDE based artificial viscosity instead of a piecewise constant one, reduces the amount of numerical errors propagating downstream due to cells around shock not being completely aligned with the shock, thus minimizing the effect on surface heat transfer prediction. The problems in heat transfer prediction arises not only for unstructured meshes but also for symmetric meshes, producing incorrect and asymmetric heating profiles.

Element to element jumps in artificial viscosity causes oscillations in state gradients and hence corrupts the smoothness and accuracy of the downstream solution. By using the smooth PDE based artificial viscosity along with the high order accuracy, the dependence of shock capturing on grid orientation is significantly reduced. But, to

illustrate the difficulty of getting accurate heating predictions, we can notice even in the well resolved case, with 4th order accuracy and the finest mesh used in [9], the results for C_h do not exactly fall on the standard expected results (Figure 1-16).

1.4 Industrial Standard Numerical Tools

Finite Difference (F.D.) and Finite Volume (F.V.) are industry standard methods used to solve both thermal ablation and hypersonic flow problems. These approaches have developed since 1960's and are robust methods to solve both these problems of our interest. However there are certain limitations associated with these methods when it comes to higher order accuracy ($> 2^{\text{nd}}$ order) and complex geometries. A suitable alternative for handling complex geometries is Finite Element, F.E. method.

1.4.1 Finite Element Formulation for Thermal Ablation

[1] compares advantages of both finite element and finite difference procedures for thermal ablation problem. All the previous approaches to solve thermal ablation problem are briefly presented, and it is identified, therein that all of them used finite difference scheme. It is mentioned that finite difference is suitable to one-dimensional and two-dimensional simple geometry problems.

For complex geometry (Figure 1-17) or complex/multifaceted boundary conditions, the scheme is no longer lucrative. It poses problems for a curved geometry, as the nodes which are supposed to be orthogonal to each other do not precisely lie on the curved boundary (Figure 1-18), and hence an accurate boundary condition can no longer be applied to curved boundary. We have seen earlier that an imprecision leads to numerical instability and solution inaccuracy.

In finite element, use of elements however provide for curved edges which can exactly represent any complex, curved shapes. An example [1], shown in Figure 1-19, compares the two meshes of finite difference and finite element discretizations of a turbine blade profile.

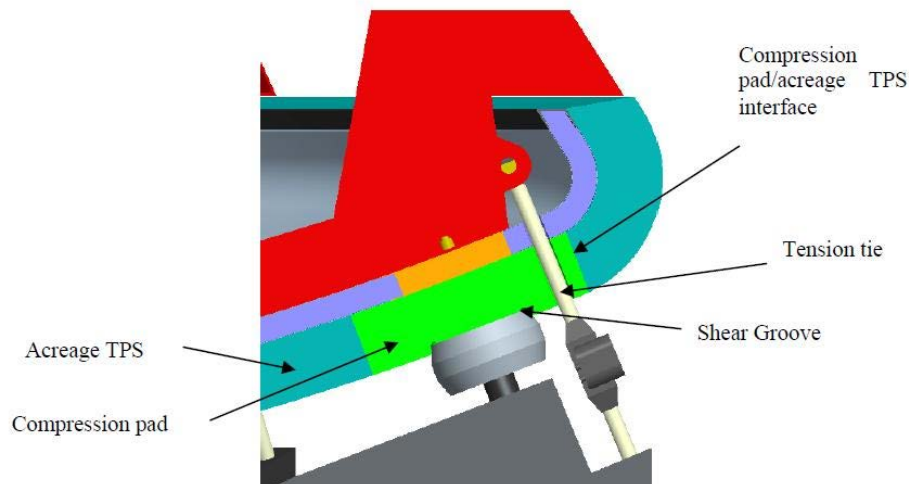


Figure 1-17. Generic heat shield penetration concept. Larger payloads increase the size and complexity of the entry vehicles. One single continuous piece of TPS can no longer serve as a heat shield material, thus isotropic material properties like thermal conductivity can no longer be assumed. To attach the launch load to primary vehicle or entry vehicle, tension tie rod penetrated through forebody TPS. This also consists of compression pad, which is inserted into acreage TPS. For such complex geometries, 1-D thermal response assumption will no longer work, and finite element will serve to analyze thermal response of such complicated structure of TPS [1].

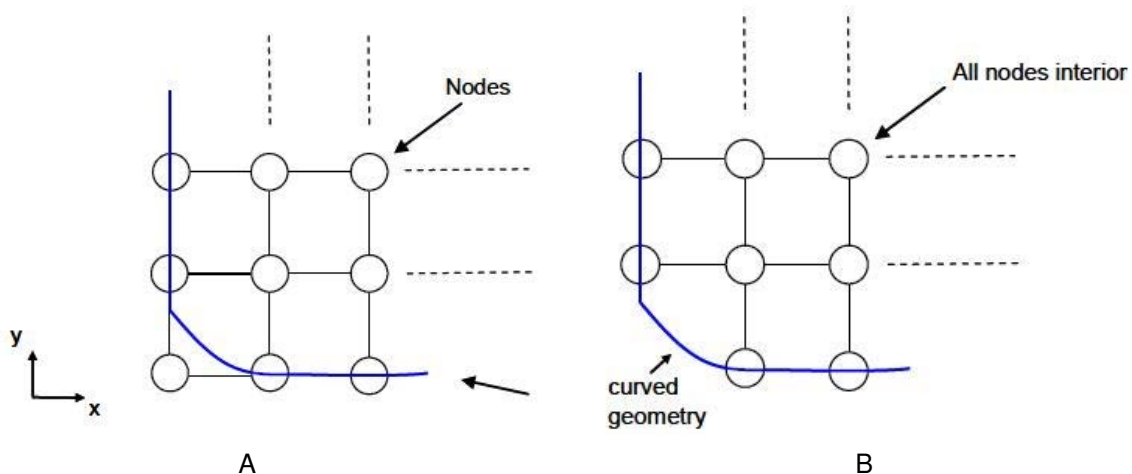


Figure 1-18. Grid points in finite difference for approximation of curved body shape. A) Node outside the boundary leads to incorrect boundary representation. B) Node inside the boundary also leads to incorrect boundary representation. Due to orthogonal nature of the grid points, curved boundary cannot be correctly approximated in finite difference [1].

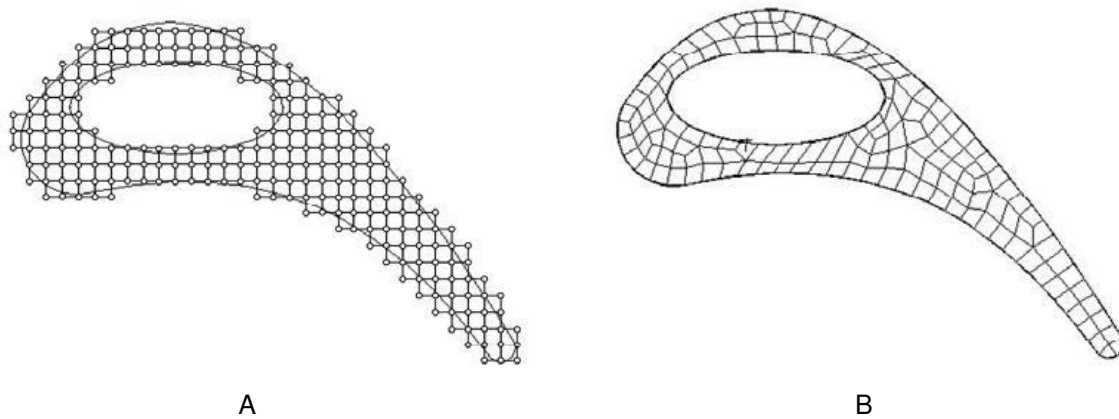


Figure 1-19. Comparison of finite difference and finite element methods for a curved geometry. A) Finite difference discretization of a curved geometry (a turbine blade). B) Finite element discretization of a curved geometry (a turbine blade). Boundary is correctly represented in finite element, since the elements with curved edges are represented with reference square elements in the parametric space [1].

1.4.2 Discontinuous Galerkin Method and Its Benefits

Despite the important advantages of using Finite Element (FE) method with regard to the handling of complex geometries and curved boundaries, finite element method is still not widely used for thermal ablation or high speed flow simulation. Its serious limitation is handling high speed flows or convection dominated problems associated with it. It is very well known that finite element method will give spurious oscillations when solving a convection dominated problem, just like a central difference scheme in finite difference.

To overcome this limitation of finite element method, at the same time using its leverage for complex geometries, we turn to discontinuous Galerkin methods. Discontinuous Galerkin methods or DG methods are high order accurate methods, and this accuracy is afforded without any additional code complexity. All the advantages of DG method stem from the fact that it combines benefits of both finite volume and finite element methods. Being based in a finite element framework, it very conveniently allows for the increment of the polynomial accuracy without requiring any stencil support from

the neighboring elements. This additional stencil support from the neighboring elements makes high order finite volume techniques (order of accuracy > 2) difficult to generalize for arbitrary meshes.

DG method also uses numerical fluxes for the inviscid terms in the governing equations, that gives it the capability to solve for the high speed or shock flow problems with the high order resolution. These fluxes are approximations to Riemann solver and were originally developed for finite volume method, and later applied by Cockburn and Shu to DG methods.

Discontinuous Galerkin or DG method was first applied by Reed and Hill [56] in 1973 to solve neutron transport equation. Later on, it was developed in a series of papers by [57–61], Cockburn and Shu, into what came to be known in research community as Total Variation Diminishing Runge-Kutta Discontinuous Galerkin method (TVD RKDG). They presented a formal development of the method for hyperbolic system of equations for multidimensional systems. This used unstructured or triangular meshes for 2-D and tetrahedral meshes for 3-D.

Discontinuous Galerkin method differs from (continuous) Galerkin finite element method in that it allows solution to be discontinuous across the element boundaries. Therefore, the solution is local to its element alone, and hence formulation is compact overall and also near boundaries without any special treatment at the boundaries. Due to this, application of the boundary condition is more robust in DG method for any kind of boundary condition. In finite difference methods, high order accuracy for the internal nodes can be easily ruined by low order accuracy at the boundary nodes. So for this purpose one-sided and biased finite difference formulations are applied at the boundary and inside (close to boundary) nodes respectively. This is quite complex to deal with even for 1-D problems for high order accuracy (> 2), and also when discretizing higher order derivatives in governing equation, and situation further worsens for higher dimensions.

One price however that has to be paid is of computational cost, but because of its amenability to easy parallelization this cost can be overcome. We will now describe recent developments in DG methods.

Brief history of recent developments in discontinuous Galerkin methods.

Extensive work has been done on discontinuous Galerkin (DG) methods to apply them to a variety of class of problems. Being first introduced in 1973, work was undertaken to develop these methods for linear and non linear hyperbolic systems. Major part of work was done by Cockburn and Shu for development of Runge-Kutta discontinuous Galerkin (RKDG) schemes. These were proven to be non-linearly stable for multi-dimensional hyperbolic systems, and shown later on to have favorable characteristics like high-order accuracy, high parallelizability and easy application to complicated geometries.

RKDG scheme was extended specifically to compressible Navier Stokes equations by Bassi and Rebay [62], where they rewrote second order governing equations as a set of first order equations by introducing new variables for first order derivative term. A simple average of viscous flux terms was taken from inside and outside of element at element boundaries. An important achievement of this work was that they used curved boundary and resolved the boundary layer within only a few elements. Their scheme became known as BR1 scheme in literature.

This caused the shift of focus of development of DG methods to convection-diffusion problems. Inspired by work of Bassi and Rebay, Cockburn and Shu applied RKDG methods to convection-diffusion problems and generalized the method of Bassi and Rebay into what came to be known as so called local discontinuous Galerkin methods (LDG) [63] in the literature. They showed that by proper choice of inter-element fluxes, additional variable could be eliminated locally and hence final discretization is solved only for original variable. But the problem with LDG method was that for multidimensional systems, the degree of freedoms for an element was connected to its

neighbors neighbors. Hence the compactness which was afforded by DG methods for hyperbolic systems was lost in LDG for multidimensional systems.

Other two popular works in solving elliptic problems using discontinuous finite elements include BR2 scheme [64], which was extension of work on BR1 scheme by Bassi and Rebay and Interior Penalty or IP schemes [65] developed in 1970s and 1980s independent of work on DG methods. Both these schemes directly discretize the second order derivative terms and add an explicit stabilization term. Both these schemes are compact for elliptic problems unlike LDG for multidimensional problems. So, these schemes are useful for implicit solution of a problem. Peraire and Persson [66] derived a variant of LDG method, named CDG or Compact discontinuous Galerkin method, where the difference lies in how the derivative term across element boundaries is approximated. This scheme enables to achieve compactness for multidimensions, and is at par with LDG method in all respects, and even excelling in some, like stability.

Time-implicit DG methods are used where explicit methods pose very restrictive time-step limitation, e.g. high Reynolds number flows using spatially varying mesh, where CFL limit is decided by smallest spatial scale, and low Mach number flows, where time scales of wave propagation and fluid flows differ by orders of magnitude. Implicit DG methods for non-linear problems will give rise to a system of equations, by use of Newtons method and the matrix arising out has to be most probably solved by iterative solution techniques. Since, the matrices arising out of application of DG methods to thermal ablation problem can be highly ill-conditioned and in general block-wise structured, it is useful to look at previous works on preconditioners and parallelization for discretizations arising from DG method.

As mentioned in [67], the block structure of DG methods has been used in designing the block preconditioners which are more efficient than regular preconditioners. Here a multigrid method is used in conjunction with a block preconditioner as a smoother. They refer to use of various preconditioners as smoothers like block Jacobi

smoother [68], block Gauss-Siedel (GS) smoother [68, 69], smoother based on solution of block tridiagonal systems [70] etc. In [67] itself, a new preconditioner approach is proposed, called ILU0, where post-smoothing is performed based on block incomplete LU factorization with zero fill-in. The use of multigrid strategies in combination with block preconditioners mainly finds its use in elliptic problems; for convection dominated problems, there is not much to be gained by use of multigrid methods.

1.5 Contribution

- Solved wide range of problems from thermal ablation, high speed flows to hypersonic flows with thermo-chemistry
- Found r-p adaptivity approach to obtain same accuracy as h-p adaptivity methods for hypersonic flows solution, with lesser number of elements.
- Employed $p = 0$ solution in shock along with r-adaptivity to eliminate errors encountered with other methods like PDE based artificial viscosity methods.
- Introduced DG methods to the field of thermal ablation, opening avenues for high-order accurate simulations for complex geometries in thermal ablation.
- Successfully solved hypersonic flow problem with thermo-chemical non-equilibrium with DG methods, not yet done in published literature.
- Developed generalized approach for implicit methods, bringing the capability to solve any new physics without much effort. Used numerical approach to evaluate jacobians that evades the need and tediousness of evaluating analytical jacobians for a full implicit problem.
- Combined rp adaptivity + slope limiter for high order solution in shock.
- Found the effect of plasma DBD actuators on the reduction of surface heating for hypersonic flow over cylinder.

1.6 Thesis Layout

In Chapter 1, we have described our motivation behind our work. We have pointed out several limitations of the current state of the art for numerical simulations in the field of thermal ablation and hypersonic flows. In addition, limitations and challenges associated with industry standard finite difference and finite volume codes were also pointed for complex geometries and high order solution. This laid the foundation for

using DG methods to open avenues for future work with more complex geometries and high order accurate solution.

In Chapter 2, we layout governing equations for inviscid, viscous flows along with hypersonic flows with thermo-chemical non-equilibrium and thermal ablation problem. We present discontinuous Galerkin methods in Chapter 3 along with our work on identifying the differences in BR1 and BR2 schemes. We also highlight our work on parallelization, implicit time integration and r-p adaptive methods to capture shock in Chapter 3. We present some validation examples in the field of inviscid and viscous flows in Chapter 4. Chapter 5 presents three test cases for thermal ablation, chosen to solve using DG methods developed. Chapter 6 shows validation cases for inviscid, viscous hypersonic flows and hypersonic flows with thermo-chemical non-equilibrium. The effect of a DBD plasma actuator on surface heating for hypersonic flows over a cylinder is discussed in Chapter 7. Finally, we conclude with Chapter 8 highlighting our achievements and future work.

CHAPTER 2 GOVERNING EQUATIONS

In this chapter, we describe all important governing equations for different physics studied in this work. These include inviscid Euler equations (section 2.1), viscous Navier-Stokes equations (section 2.2), thermo-chemical non-equilibrium for a multi-species Navier Stokes equations (section 2.3) and thermal ablation (section 2.4).

2.1 Inviscid Euler Equations

Neglecting both the viscous and thermal conduction effects, we can derive inviscid Euler equations, which can be written in following general form,

$$\frac{\partial \mathbf{U}}{\partial t} + \nabla \cdot \mathbf{F}_i = 0 \quad (2-1)$$

Here, \mathbf{U} is a conservative state vector given by,

$$\mathbf{U} = \begin{pmatrix} \rho \\ \rho u \\ \rho v \\ \rho w \\ \rho E \end{pmatrix} \quad (2-2)$$

and the inviscid flux tensor, $\mathbf{F}_i = (\mathbf{F}_i^x, \mathbf{F}_i^y, \mathbf{F}_i^z)$ is given by,

$$\mathbf{F}_i^x = \begin{pmatrix} \rho u \\ \rho u^2 + P \\ \rho uv \\ \rho uw \\ u(\rho E + P) \end{pmatrix}; \quad \mathbf{F}_i^y = \begin{pmatrix} \rho v \\ \rho uv \\ \rho v^2 + P \\ \rho vw \\ v(\rho E + P) \end{pmatrix}; \quad \mathbf{F}_i^z = \begin{pmatrix} \rho w \\ \rho uw \\ \rho vw \\ \rho w^2 + P \\ w(\rho E + P) \end{pmatrix} \quad (2-3)$$

ρE is the total energy which is the sum of the internal energy and the kinetic energy,

$$\rho E = \rho e + \frac{1}{2} \rho (u^2 + v^2 + w^2) \quad (2-4)$$

Pressure is constructed from the internal energy, and thus can be found from the conservative variables in Eq. (2-2), in following way,

$$P = (\gamma - 1) \left(\rho E - \frac{1}{2} \rho (u^2 + v^2 + w^2) \right) \quad (2-5)$$

Here γ is the specific heat ratio and is set equal to a constant value of 1.4 in this work.

2.2 Viscous Navier-Stokes Equations

With viscous effects and thermal conduction included, Eq. (2-1) become Navier-Stokes equations, which can be written in following general notation,

$$\frac{\partial U}{\partial t} + \nabla \cdot F_i = \nabla \cdot F_v \quad (2-6)$$

$F_v = (F_v^x, F_v^y, F_v^z)$ is the viscous flux term, given by,

$$F_v^x = \begin{pmatrix} 0 \\ \tau_{xx} \\ \tau_{xy} \\ \tau_{xz} \\ u\tau_{xx} + v\tau_{xy} + w\tau_{xz} + q_x \end{pmatrix}; \quad F_v^y = \begin{pmatrix} 0 \\ \tau_{yx} \\ \tau_{yy} \\ \tau_{yz} \\ u\tau_{yx} + v\tau_{yy} + w\tau_{yz} + q_y \end{pmatrix}; \quad (2-7)$$

$$F_v^z = \begin{pmatrix} 0 \\ \tau_{zx} \\ \tau_{zy} \\ \tau_{zz} \\ u\tau_{zx} + v\tau_{zy} + w\tau_{zz} + q_z \end{pmatrix} \quad (2-8)$$

where τ is the viscous stress tensor given as follows,

$$\tau = \begin{bmatrix} \tau_{xx} & \tau_{xy} & \tau_{xz} \\ \tau_{yx} & \tau_{yy} & \tau_{yz} \\ \tau_{zx} & \tau_{zy} & \tau_{zz} \end{bmatrix} \quad (2-9)$$

For flows with single species and without any thermo-chemical non-equilibrium we consider the working gas to be air. The viscous stress for air (being a Newtonian fluid) is given from Stokes hypothesis,

$$\tau_{ij} = \mu \left(\frac{\partial u_i}{\partial x_j} + \frac{\partial u_j}{\partial x_i} - \frac{2}{3} \frac{\partial u_k}{\partial x_k} \delta_{ij} \right) \quad (2-10)$$

μ is the viscosity of the fluid and is given for a monoatomic gas by the semi-empirical Sutherland's Law. In this, μ is a function of temperature.

$$\frac{\mu}{\mu_o} = \left(\frac{T}{T_o} \right)^{3/2} \frac{T_o + S}{T + S} \quad (2-11)$$

Here, the constants are defined as follows,

$$\mu_o = 1.716 \cdot 10^{-5} \frac{\text{kg}}{\text{ms}} \quad (2-12)$$

$$T_o = 273.15\text{K} \quad (2-13)$$

$$S = 110.55\text{K} \quad (2-14)$$

In addition to the viscous stress tensor, the heat flux vector, q in the viscous flux tensor, F_v is given by Fourier's law,

$$q_j = -\lambda \frac{\partial T}{\partial x_j} \quad (2-15)$$

λ is thermal conductivity coefficient given by molecular viscosity, μ , specific heat, C_p and Prandlt number, Pr ,

$$\lambda = \frac{\mu C_p}{Pr} \quad (2-16)$$

For all cases considered in this thesis, wherever we use Navier-Stokes equations, Pr is chosen to be 0.72.

2.3 Multi-species Navier-Stokes Equations

Temperatures in a hypersonic flow field are typically few thousand Kelvin, up to 10,000 K or higher. Thus, Navier Stokes equations, described in section 2.2, for a monoatomic gas can no longer be used. The gas at such high temperatures undergoes chemical reactions and vibrational-electronic excitation. Thus, we consider multi-species Navier-Stokes equations for solving hypersonic flow with thermo-chemical non-equilibrium. Before giving the equations, we discuss the physics of the thermo-chemical non-equilibrium.

2.3.1 Thermo-Chemical Non-Equilibrium

A gas at very high temperature can undergo excitation of internal energy modes, molecular dissociation and thermal non-equilibrium wherein the gas state can no longer be specified by one single temperature. Total energy, e of a gas molecule can be considered to consist of four components namely translational, rotational, vibrational and electronic excitation.

$$e = e_t + e_r + e_v + e_e \quad (2-17)$$

Translational and rotational modes exist at room temperatures. Vibrational and electronic excitation modes are only significant contributors at high temperatures. The translational and rotational modes are given by,

$$e_t = \frac{3}{2}k_bT, \quad (2-18)$$

$$e_r = \begin{cases} 0 & \text{for atoms,} \\ k_bT & \text{for diatomic molecules.} \end{cases} \quad (2-19)$$

Translational mode for a molecule or an atom stands for the kinetic energy due to its linear momentum and is same for both the atomic and polyatomic species. Rotational modes, on the other hand, represent kinetic energy due to the angular momentum of the molecule, and are thus zero for atoms and k_bT for diatomic molecules.

Vibrational energy mode is only relevant for polyatomic molecules, since it corresponds to the vibration of atoms within the molecule. In this work, we consider diatomic molecules (in addition to monoatomic molecules) which have two degrees of freedom. Since, this vibrational energy is not always fully excited, the molecule is represented by a harmonic oscillator and the vibrational energy of a (diatomic) molecule is given by,

$$e_v(T) = \frac{k_b\theta_v}{e^{\frac{\theta_v}{T}} - 1} \quad (2-20)$$

θ_v is the characteristic temperature for vibration and is unique for each molecule. It is given in Table 2-1.

Electronic mode is the energy associated with excitation of electrons from ground state to higher energy states. This is valid for all species. The expression for electronic energy is given by,

Table 2-1. Vibrational temperatures for non-ionizing dissociating air

Species	θ_v
O ₂	2239.0
NO	2817.0
N	0.0
O	0.0
N ₂	3395.0

$$e_{el} = k_b \frac{\sum_{i=1}^{\infty} g_i \theta_{el,i} e^{-\frac{\theta_{el,i}}{T}}}{g_0 + \sum_{i=1}^{\infty} g_i \theta_{el,i} e^{-\frac{\theta_{el,i}}{T}}} \quad (2-21)$$

$\theta_{el,i}$ is the characteristic temperature and g_i is the degeneracy for each electronic transition. Table 2-2 gives the values for first and second electronic transitions. As can be noted from Table 2-2, the characteristic temperatures for electronic transitions are much higher than those for vibrational modes. Hence, electronic transitions are only significant at very high temperatures, typically above 10,000 K.

Table 2-2. Electronic temperatures and degeneracies for non-ionizing dissociating air

Species	$\theta_{el,1}$	$\theta_{el,2}$	g_0	g_1	g_2
O ₂	11,392.0	18,985.0	3	2	1
NO	55,835.0	63,258.0	4	8	2
N	27,665.0	41,495.0	4	10	6
O	22,831.0	48,620.0	9	5	1
N ₂	72,233.0	85,744.0	1	3	6

So far, we discussed thermal non-equilibrium, which uses definitions of two temperatures namely, T , for translational and rotational modes and T_v for vibrational and electronic modes. For chemical non-equilibrium, we consider 5 species model in this work, consisting of O₂, NO, N, O and N₂. These 5 species undergo 5 chemical reactions, namely three dissociation reactions of N₂, O₂ and NO and two exchange reactions described in detail in section 2.3.4 in this chapter. Finite rate chemistry models are used for simulating chemical non-equilibrium.

2.3.2 Multispecies Navier Stokes Equations

Fluid flow in thermo-chemical non-equilibrium is represented by multi-species Navier Stokes equations. The gas undergoes molecular dissociation and exchange reactions between different species present. No ionization is considered in this model. We also assume the gas to be in equilibrium with itself. This means that every species can be described using its own species density, velocity and temperature for all energy modes. The equations can be written in following simple form,

$$\frac{\partial \mathbf{U}}{\partial t} + \nabla \cdot \mathbf{F}_i = \nabla \cdot \mathbf{F}_v + \mathbf{S} \quad (2-22)$$

\mathbf{U} again denotes the solution vector, \mathbf{F}_i and \mathbf{F}_v inviscid and viscous flux terms and \mathbf{S} is the source term vector, and are given as follows,

$$\mathbf{U} = \begin{pmatrix} \rho_s \\ \rho \vec{u} \\ \rho e_t \\ \rho e_v \end{pmatrix}; \quad \vec{\mathbf{F}}_i = \begin{pmatrix} \rho_s \vec{u} \\ \rho \vec{u} \otimes \vec{u} + P \\ \rho \vec{u} h_t \\ \rho \vec{u} h_v \end{pmatrix}; \quad \vec{\mathbf{F}}_v = \begin{pmatrix} -\rho_s \tilde{V}_s \\ \tau \\ \tau \cdot \vec{u} - \vec{q} - \vec{q}_v - \sum_s h_{t,s} \rho_s \tilde{V}_s \\ -\vec{q}_v - \sum_s h_{v,s} \rho_s \tilde{V}_s \end{pmatrix}$$

$$\mathbf{S} = \begin{pmatrix} \omega_s \\ 0 \\ 0 \\ \sum_s \omega_s \hat{e}_{v,s} + Q_{T-V} \end{pmatrix} \quad (2-23)$$

In this work, we consider 2-D form of Eq. (2-23) and thus we have total of 9 equations, considering 5 species. ρ_s is the species density, with $s = 1, 2, \dots, 5$ and ρ is the total density which is the sum of all species density. $\rho \vec{u}$ is the bulk momentum, ρe_t and ρe_v are the total energy and vibrational energy respectively. ρe_t is equal to the sum

of ρe_v , translational rotational energy, kinetic energy and heat of formation of present species and h_t is the total enthalpy, the sum of internal energy and pressure.

$$\rho e_t = \rho e_v + \sum_s \rho_s C_{V, \text{tr}} T + \sum_s \rho_s h_s^0 + \frac{1}{2} \rho (u^2 + v^2) \quad (2-24)$$

$$h_t = e_t + \frac{P}{\rho} \quad (2-25)$$

For vibrational energy equation, h_v is considered equal to e_v , since there is no consideration of pressure term in the vibrational energy equation (for ρe_v), since kinetic energy is considered only in the total energy equation, for ρe_t .

$$h_v = e_v \quad (2-26)$$

Considering viscous flux term in continuity equation for 5 species density, ρ_s , we note that that \tilde{V}_s is the diffusion velocity of species and is determined using Fick's law,

$$\rho_s \tilde{V}_s = -\rho D_s \nabla c_s \quad (2-27)$$

Shear stress, $\underline{\tau}$, and heat fluxes, \vec{q} and \vec{q}_v for translation-rotational modes and vibrational-electronic modes respectively are given by following formulas,

$$\underline{\tau} = \mu (\nabla \vec{u} + \vec{u} \nabla) - \frac{2}{3} \mu \nabla \cdot \vec{u} \underline{I} \quad (2-28)$$

$$\vec{q} = -k \nabla T \quad (2-29)$$

$$\vec{q}_v = -k_v \nabla T_v \quad (2-30)$$

Formulas for constants of diffusion, D_s , viscosity, μ , conductivities k and k_v is given in section 2.3.3. The terms, $\sum_s h_{t,s} \rho_s \tilde{V}_s$, and $\sum_s h_{v,s} \rho_s \tilde{V}_s$ in the viscous flux term (Eq. (2–23)) denote the transport of total and vibrational energies respectively, due to mass diffusion of the different species present. Finally, ω_s is the production rate of different species due to the chemical reactions between different species. $\sum_s \omega_s \hat{e}_{v,s}$ and Q_{T-V} in the source term, S in Eq. (2–23) are respectively, the production/destruction of vibrational energy (due to production/destruction of species) and energy exchange between translational-rotational and vibrational modes. The energy first of all is transferred to translational and rotational modes, where from it is transferred to vibrational modes depending on the translational-rotational temperature, T and the pressure, P .

2.3.3 Transport Properties

Fluid viscosity, μ is found from the species viscosities, μ_s using Wilke's semi-empirical mixing rule [71],

$$\mu = \sum_{s=1}^{ns} \frac{X_s \mu_s}{\phi_s} \quad (2-31)$$

where,

$$X_s = \frac{c_s M}{M_s} \quad (2-32)$$

$$M = \left(\sum_{s=1}^{ns} \frac{c_s}{M_s} \right)^{-1} \quad (2-33)$$

$$\phi_s = \sum_{r=1}^{ns} X_r \left[1 + \sqrt{\frac{\mu_s}{\mu_r}} \left(\frac{M_r}{M_s} \right)^{\frac{1}{4}} \right]^2 \left[\sqrt{8 \left(1 + \frac{M_s}{M_r} \right)} \right]^{-1} \quad (2-34)$$

Here, c_s is the mass fraction of each species, s ,

$$c_s = \frac{\rho_s}{\rho} \quad (2-35)$$

The individual species viscosities can be found from Blottner's model [72], which assumes the species viscosities to be a function of the translational-rotational temperatures, T,

$$\mu_s = 0.1 \exp [(A_s \ln T + B_s) \ln T + C_s] \quad (2-36)$$

Values of A_s , B_s and C_s are given in Appendix A. Model is valid for temperatures up to 30,000 K and is sufficient for our work.

The conductivities required for heat fluxes given in Eq. (2-30) are determined from Eucken relation [73],

$$k_t = \frac{5}{2} \mu_s C_{Vs}^{tr} \quad (2-37)$$

$$k_{rot} = \mu_s C_{Vs}^{rot} \quad (2-38)$$

$$k_{vib} = \mu_s C_{Vs}^{vib} \quad (2-39)$$

All the required specific heats in this section can be calculated by differentiation of the respective internal energies w.r.t. particular temperature, i.e.

$$C_{Vs} = \frac{\partial e_s}{\partial T} \quad (2-40)$$

Diffusion velocities are given by Fick's law, and depend upon gradients of concentration, pressure and temperature.

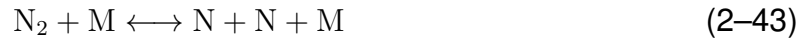
$$\rho_s \tilde{V}_s = -\rho D_s \nabla \left(\frac{\rho_s}{\rho} \right) \quad (2-41)$$

Here, D_s is the multi-component diffusion coefficient. In this work, D_s is replaced by single binary diffusion coefficient D , which is found using Lewis number, Le of 1.4 for all species,

$$Le = D \frac{\rho C_p}{\kappa} \quad (2-42)$$

2.3.4 Source Term for Chemical Reactions

We are using 5 species model in this work, for the hypersonic flow simulation, consisting of N_2 , O_2 , NO , N and O . These species undergo following 5 chemical reactions, consisting of 3 dissociation reactions and 2 exchange reactions,



First three reactions are dissociation of N_2 , O_2 and NO into their atomic species. M denotes the third body that can be any of the 5 species present, used to collide with the dissociating molecule that is required to conserve the energy of collision. These reactions are also known as third body reactions in the literature. Last two reactions are basically oxidation of N_2 and NO species, resulting in formation of atomic Nitrogen species.

These reactions are governed by the forward and backward reaction rates. Forward reactions rate is given in Arrhenius form,

$$k_{f,r,m} = C_{f,r,m} T_{\text{eff}}^{\eta_{f,r,m}} \exp\left(\frac{\theta_{f,r,m}}{T_a}\right) \quad (2-48)$$

Values of $C_{f,r,m}$, $\eta_{f,r,m}$ and $\theta_{f,r,m}$ are given in Appendix A. T_{eff} is equal to following from Park's TT_v model, [74]

$$T_{\text{eff}} = \sqrt{TT_v} \quad (2-49)$$

The backward rate constant, $k_{b,m}$, is determined from the equilibrium constant which is determined through curve fits to equilibrium experimental data given by McBride et al (2002) [75], and is in following form,

$$K_{\text{eq},m} = C_m \exp(A_{1,m} + A_{2,m}Z + A_{3,m}Z^2 + A_{4,m}Z^3 + A_{5,m}Z^4) \quad (2-50)$$

Here,

$$Z = \frac{10,000K}{T} \quad (2-51)$$

The constants $A_{1,m}$, $A_{2,m}$, $A_{3,m}$, $A_{4,m}$ and $A_{5,m}$ are also given in the Appendix A. These curve fits have been taken from [12].

The rates of each dissociation reaction is given by

$$R_c = \sum_{m=1}^{ns} \left[-k_{f,c,m} \frac{\rho_r}{M_r} \frac{\rho_m}{M_m} + k_{b,c,m} \frac{\rho_{P1}}{M_{P1}} \frac{\rho_{P2}}{M_{P2}} \frac{\rho_m}{M_m} \right] \quad (2-52)$$

Here, c is the reaction number, m is the collision partner, r is the reactant and P_1 and P_2 are products. For exchange reactions, the rates can be written in following manner,

$$R_c = -k_{f,c} \frac{\rho_{r1}}{M_{r1}} \frac{\rho_{r2}}{M_{r2}} + k_{b,c} \frac{\rho_{P1}}{M_{P1}} \frac{\rho_{P2}}{M_{P2}} \quad (2-53)$$

Finally the reaction rates of all species can be combined, to give production rates of all species, as follows,

$$\omega_{O_2} = M_{O_2} (R_2 - R_5) \quad (2-54)$$

$$\omega_{NO} = M_{NO} (R_3 - R_4 + R_5) \quad (2-55)$$

$$\omega_N = M_N (-2R_1 - R_3 - R_4 - R_5) \quad (2-56)$$

$$\omega_O = M_O (-2R_2 - R_3 + R_4 + R_5) \quad (2-57)$$

$$\omega_{N_2} = M_{N_2} (R_1 + R_4) \quad (2-58)$$

2.3.5 Source Term for Vibrational Energy

Two terms in Eq. (2-23) that appear in the source term, S for the vibrational energy equation are respectively, $\sum_s \omega_s \hat{e}_{v,s}$, production and dissociation of polyatomic species that also affects total vibrational energy, and Q_{T-V} , energy exchange between translational-rotational and vibrational modes of the gas. All different molecules are in vibrational equilibrium and thus a single vibrational temperature accounts for vibrational energy of all species. These exchange rates are combined into one single rate, Q_{T-V} . Landau-Teller model is used and is given as follows,

$$Q_{T-V} = \sum_s \rho_s \frac{e_{vs}^* - e_{vs}}{\langle \tau_s \rangle} \quad (2-59)$$

where e_{vs}^* is the vibrational energy at thermal equilibrium ($T_v = T$) and $\langle \tau_s \rangle$ is the molar averaged Landau-Teller relaxation time given by,

$$\langle \tau_s \rangle = \frac{\sum_{r=1}^{nd} X_r}{\sum_{r=1}^{nd} \frac{X_r}{\tau_{sr}}} \quad (2-60)$$

τ_{sr} is the Landau-Teller inter-species relaxation time given by Millikan and White (1953) [76],

$$\tau_{sr} = \frac{101,325}{P} \exp [A_{sr} (T^{-1/3} - 0.015\mu_{sr}^{1/4}) - 18.42] \quad (2-61)$$

$$A_{sr} = 1.16 \times 10^{-3} \mu_{sr}^{1/2} \theta_{vs}^{4/3} \quad (2-62)$$

$$\mu_{sr} = \frac{M_s M_r}{M_s + M_r} \quad (2-63)$$

2.4 Thermal Ablation

The governing equations for thermal ablation are taken from [16, 17] and are given as follows,

$$\frac{\partial \rho_r}{\partial t} = -R \quad (2-64)$$

$$\frac{\partial \epsilon \rho_g}{\partial t} + \frac{\partial \epsilon \rho_g u}{\partial x} = R + D \quad (2-65)$$

$$\frac{\partial \epsilon \rho_g u}{\partial t} + \frac{\partial \epsilon \rho_g u^2 + \epsilon P}{\partial x} = -\epsilon f + I \quad (2-66)$$

$$\frac{\partial \rho_c e_c + \rho_r e_r + \epsilon \rho_g e_g + \frac{1}{2} \epsilon \rho_g u^2}{\partial t} + \frac{\partial \epsilon u (\rho_g e_g + \frac{1}{2} \rho_g u^2 + P)}{\partial x} = \frac{\partial}{\partial x} \left(k \frac{\partial T}{\partial x} \right) \quad (2-67)$$

Eq. (2-64) describes the decomposition of resin material and Eq. (2-65) solves for conservation of mass for gas density. Here, ϵ is the void fraction and is given by,

$$\epsilon = \epsilon_{\max} - \frac{\rho_r}{\rho_p} \quad (2-68)$$

ϵ_{\max} is the maximum void fraction that happens in the char state, and ρ_p is the intrinsic density of resin and both of their values are equal to 0.1788 and 1763.6 kg/m³ respectively. Term R appears in the gas and solid equations with opposite signs, indicating that resin decomposes to release the pyrolysis gas. Second term, D, appearing in the gas continuity equation, is the diffusion term that represents the rate of change of gas density due to the spatial variation of pressure, and is given by,

$$D = \frac{K}{\mu} (\epsilon \rho_g) \frac{\partial^2 P}{\partial x^2} \quad (2-69)$$

Here, K is the permeability of gas, and μ is the gas viscosity. Momentum conservation in Eq. (2-66) for the gas, describes that the flow of gas is pressure driven. Here u is the gas velocity and $\epsilon \rho_g u$ is the gas momentum. Since, the gas is flowing through the porous media, the resistance to the gas motion are given through f, friction and I, inertia terms. These terms relate to the pyrolysis gas motion in the ablating media. Eq. (2-67) solves for the combined energy conservation of both the solid (resin + char) and the gas. e_g , e_c , and e_r are internal energies of the gas, char and resin material respectively. Terms e_c and e_r are evaluated using specific heats of char and resin materials respectively. Eq. (2-71) gives the expressions for e_c and e_r .

$$e_c = \rho_c C_{p_c} T \quad (2-70)$$

$$e_r = \rho_r C_{p_r} T + \rho_r h_r^o \quad (2-71)$$

Second term in energy equation is the derivative of the energy flux, similar to Euler equations, where the flux is decided by internal energy, kinetic energy and pressure flow energy of gas. These terms were neglected in most thermal response codes since the gas was supposed to leave the material as soon as it was generated. Last term in

energy equation is heat conduction within the material, through which we also apply net heat flux boundary condition at the surface.

CHAPTER 3

NUMERICAL METHODS

This chapter presents key ideas of DG formulation of all the terms presented in Chapter 2. These aid in better appreciation of the numerical tool, being used in this work, and also gain good understanding of some essential details for the numerics to be time and computationally cost effective.

3.1 Why Discontinuous Galerkin?

In this work, we focus on the discontinuous Galerkin methods to solve all the problems. Several methods generally used for solving the computational fluid dynamics problems are finite difference, finite volume and finite element. There has been main focus on the use of finite difference and finite volume for problems of fluid flow. Even though, finite element has a strong mathematical basis, its application to the fluid flow problems has rather been limited. Galerkin based finite element method, using same interpolation functions for both the test function and the solution vector, which are both continuous over the whole domain, is similar to a central difference method in its numerical properties. Thus it is very suitable for elliptic problems, like most problems in the solid mechanics, fluid flows with low Reynolds number and plasma. However, this method is not well suited for the high speed flow problems, which is a primary focus of this work.

Discontinuous Galerkin methods relax the requirement of solution continuity over the elements, and allows the solution to be piecewise continuous. This allows the problem within each element to be treated as a finite element domain in itself. Since the solution is discontinuous across the element's faces, the fluxes are no longer uniquely defined on the element faces. This is similar to the case of finite volume method, and hence by extending the Riemann solvers, developed in the context of finite volume method, to the discontinuous Galerkin method, provides for the upwind mechanism in DG scheme. This provides an additional advantage for DG methods, that by increasing

the polynomial approximation within the element, high order accuracy can be achieved in the solution, without extending the stencil to more and more neighbor elements. This advantage specifically comes from finite element framework used for DG method.

With compact stencil, discontinuous Galerkin method is a very suitable candidate for high order accurate methods, since a compact stencil lends itself easily to convenient coding and parallel efficiency. These two advantages, however, come at the cost of increased computational resources required for discontinuous Galerkin method.

3.2 Inviscid Terms

Discontinuous Galerkin method was first applied to the first order systems, or inviscid systems. It was primarily brought into the field of research by Cockburn and Shu [57–61]. Later on, this method was applied to elliptic problems as well. In this section, we focus on describing implementation of DG methods to inviscid systems.

Inviscid terms as presented in Eq. (2–1), can be multiplied with the basis function, ϕ and integrated over the element domain, Ω ,

$$\int_{\Omega} \phi \left(\frac{\partial U}{\partial t} + \nabla \cdot \mathbf{F}_i \right) d\Omega = 0 \quad (3-1)$$

Spatial integral term in Eq. (3–1) can be split into two by using integration by parts. Thus we get,

$$\int_{\Omega} \phi \frac{\partial U}{\partial t} d\Omega - \int_{\Omega} \nabla \phi \cdot \mathbf{F}_i d\Omega + \oint_{\partial\Omega} \phi \mathbf{F}_i \cdot \vec{n} d\sigma = 0 \quad (3-2)$$

In Eq. (3–2), $\partial\Omega$ denotes the boundary of the element's solution domain, Ω and \vec{n} is the outward going normal to the edge, $d\sigma$.

We can split the whole domain, Ω into non-overlapping elements, E , consisting of lines in 1-D and quadrilaterals (linear or curvilinear) in 2-D.

$$\tau_h = E \quad (3-3)$$

Then, Eq. (3-2) can be written as follows,

$$\sum_E \left[\int_E \phi \frac{\partial U}{\partial t} d\Omega - \int_E \nabla \phi \cdot F_i d\Omega + \oint_{\partial E} \phi F_i \cdot \vec{n} d\sigma \right] = 0 \quad (3-4)$$

Here, we choose the basis functions which are piecewise continuous within the element and discontinuous across the elements. These basis functions are given in Appendix B. The solution vector, U is also defined in terms of the same basis function, ϕ (Galerkin approach).

$$U = \sum_{k=0}^p \phi_k U_k^h \quad (3-5)$$

Here, p denotes the polynomial order of approximation and ϕ_k and U_k^h denote k^{th} order basis functions and degrees of freedom respectively. For overall p degrees of freedom, we get $(p+1)^{th}$ order of accuracy in DG method for inviscid terms.

Since the solution is discontinuous across element interfaces, we need numerical fluxes to uniquely define inviscid fluxes at the element interfaces. For our work, we use Local Lax-Friedrichs (LLF) solver [77] for the inviscid fluxes.

$$F_i \cdot \vec{n} = H(U_n, U_p) = \frac{1}{2} (F_{in} \cdot \vec{n} + F_{ip} \cdot \vec{n} - \alpha (U_p - U_n)) \quad (3-6)$$

U_n , U_p and F_{in} , F_{ip} are respectively the solution vectors and inviscid fluxes belonging to the current element (n), being considered, and the neighboring element (p). \vec{n} is the normal pointing outside to a face of an element. α is the bigger of maximum

absolute eigenvalue of the jacobian matrices $\frac{\partial F_{in}}{\partial U}$ and $\frac{\partial F_{ip}}{\partial U}$ evaluated at the face of an element.

As can be seen in Eq. (3–6), for two neighboring elements, the normal to the common face is reversed in direction, and term $(U_p - U_n)$ also changes sign. Hence, the numerical flux defined at the face of an element is conservative, i.e. the contribution is of opposite signs in the adjacent elements. This conserves the net flux going from one element into the neighboring one.

$$H_L(U_n, U_p) = -H_R(U_p, U_n) \quad (3-7)$$

α for both the elements retains same positive value, which is equivalent to the speed of wave propagation.

3.3 Viscous Terms

For the second order derivative terms, which are the viscous terms in Navier-Stokes equations, we present the numerical methodology in this section. Since, discontinuous Galerkin method was primarily developed for the first order systems, a common approach is to define an auxiliary variable for the second order derivative term. This gives rise to an additional auxiliary equation in addition to already existing governing equations. E.g., a discontinuous Galerkin formulation for 2-D Navier Stokes with 4 governing equations gives rise to 6 additional equations for x and y derivatives of x and y velocities and temperature, numbering a total of 10 equations.

Consider Eq. (2–6),

$$\frac{\partial U}{\partial t} + \nabla \cdot F_i = \nabla \cdot F_v$$

$F_v = F_v(U, \nabla U)$ is the viscous flux term. Here, ∇U can be replaced by auxiliary variable, θ , giving rise to the auxiliary equation,

$$\theta = \nabla U \quad (3-8)$$

So, now Eq. (3-8) will be solved along with Eq. (2-6). As in section 3.2, we multiply both Eq. (2-6) and Eq. (3-8) with the basis function, ϕ and apply integration by parts to both the inviscid and viscous flux terms. We thus get,

$$\int_{\Omega} \phi \frac{\partial U}{\partial t} d\Omega - \int_{\Omega} \nabla \phi \cdot F_i d\Omega + \oint_{\partial\Omega} \phi F_i \cdot \vec{n} d\sigma - \int_{\Omega} \nabla \phi \cdot F_v d\Omega + \oint_{\partial\Omega} \phi F_v \cdot \vec{n} d\sigma = 0 \quad (3-9)$$

Since, we already dealt with the inviscid terms in section 3.2, we only focus on the viscous terms. Viscous flux vector in the surface integral term is not uniquely defined on the element interface, therefore we define numerical flux which is the average of fluxes from both sides of the element's interface.

$$H_v = F_v \cdot \vec{n} = \frac{(F_v^-(U^-, \theta^-) + F_v^+(U^+, \theta^+)) \cdot \vec{n}}{2} \quad (3-10)$$

F_v^- and F_v^+ belong to the current element and the neighboring element respectively. In a similar fashion, we also formulate the weak form of Eq. (3-8) by multiplying with basis function, ϕ , applying integration by parts and central averaging for the numerical flux.

$$\int_{\Omega} \phi \theta d\Omega + \int_{\Omega} \nabla \phi \cdot U d\Omega - \oint_{\partial\Omega} \phi U \cdot \vec{n} d\sigma = 0 \quad (3-11)$$

Numerical flux for the surface integral term will be averaged from both sides of the element,

$$\mathbf{U} \cdot \vec{n} = \frac{\mathbf{U}^- + \mathbf{U}^+}{2} \quad (3-12)$$

This scheme in the literature is known as BR1 method and was first implemented by Bassi & Rebay [62]. This is a very simple and convenient method to use and implement, however it is computationally very intensive, due to extra auxiliary equations being solved. This increases the size of the matrix, to be solved for an implicit method, and hence hampers its speed considerably.

There are two ways to solve BR1 method in an implicit fashion. First is to solve the auxiliary equation in a coupled fashion along with the solution vector, \mathbf{U} . This approach is computationally intensive, as already discussed, due to the size of the matrix. Other faster alternative is to first explicitly solve for the degrees of freedom of auxiliary variable, θ , in terms of \mathbf{U} at a given time step and then substitute that in Eq. (3-9), so that \mathbf{U} is then explicitly dependent on itself only and not on θ .

As can be seen from Eq. (3-11) and Eq. (3-12), θ of the current element depends on \mathbf{U} from the current element as well as its neighbors.

$$\theta = \theta(\mathbf{U}^-, \mathbf{U}^+) \quad (3-13)$$

Through Eq. (3-9) and Eq. (3-13), we can see that since \mathbf{U} is connected to θ of the immediate neighbors, it is also connected to \mathbf{U} of neighbors' neighbors. Hence the coupling in BR1 scheme is not compact, i.e. it extends beyond just the immediate neighbors. This has its ramifications on second alternative to BR1, to make the method faster. Second method (for implicit treatment), although with smaller matrix consisting only of the original governing equations, is more complicated to code because of extended stencil. This complication is discussed, in more detail in section 3.3.1.

The limitation to second method of BR1 (for faster implementation) is actually overcome by another method, which was also introduced by Bassi & Rebay, [62] called BR2 method.

3.3.1 BR1 vs BR2

In this section, we first discuss implementation of second alternative to solve BR1 method faster, followed by BR2 method.

For second alternative to solve BR1 method faster, we first express θ in terms of U , using the weak form of the auxiliary equation, Eq. (3–11), which can be modified using the following expression [62],

$$U \cdot \vec{n} = \left(\frac{U^- + U^+}{2} \right) \cdot \vec{n} = \left(\frac{U^+ - U^-}{2} \right) \cdot \vec{n} + U^- \cdot \vec{n} \quad (3-14)$$

Substitute this expression in Eq. (3–11), we get

$$\int_{\Omega} \phi \theta d\Omega + \int_{\Omega} \nabla \phi \cdot U d\Omega - \oint_{\partial\Omega} \phi \left(\frac{U^+ - U^-}{2} + U^- \right) \cdot \vec{n} d\sigma = 0 \quad (3-15)$$

$$\int_{\Omega} \phi \theta d\Omega + \int_{\Omega} \nabla \phi \cdot U d\Omega - \oint_{\partial\Omega} \phi U^- \cdot \vec{n} d\sigma - \oint_{\partial\Omega} \phi \left(\frac{U^+ - U^-}{2} \right) \cdot \vec{n} d\sigma = 0 \quad (3-16)$$

First surface integral term can be combined with second domain integral term,

$$\int_{\Omega} \phi \theta d\Omega - \int_{\Omega} \phi \cdot \nabla U d\Omega - \oint_{\partial\Omega} \phi \left(\frac{U^+ - U^-}{2} \right) \cdot \vec{n} d\sigma = 0 \quad (3-17)$$

$$\int_{\Omega} \phi \theta d\Omega = \int_{\Omega} \phi \cdot \nabla U d\Omega + \oint_{\partial\Omega} \phi \left(\frac{U^+ - U^-}{2} \right) \cdot \vec{n} d\sigma \quad (3-18)$$

To speed up the BR1 method, Eq. (3–18) can be solved explicitly for θ within every element. More specifically, degrees of freedom of θ can be expressed directly in terms of the degrees of freedom of U .

Let, θ be defined using the same basis functions as for U ,

$$\theta = \phi^T \{\theta\} \quad (3-19)$$

Then Eq. (3–18) becomes,

$$\left[\int_{\Omega} \phi \phi^T d\Omega \right] \{\theta\} = \left[\int_{\Omega} \phi \cdot \nabla \phi^T d\Omega \right] \{U\} + \left[\oint_{\partial\Omega} \frac{\phi \phi^{+T}}{2} \vec{n} d\sigma \right] \{U\}_{nb} - \left[\oint_{\partial\Omega} \frac{\phi \phi^T}{2} \vec{n} d\sigma \right] \{U\} \quad (3-20)$$

Hence, degrees of freedom of θ are expressed in terms of degrees of freedom of U . This is useful in finding θ and also for finding the derivative of θ w.r.t. U , which is useful for implicit methods.

Another important point, to save computational time, is to find θ as a derivative of the conservative variable rather than the primitive variable. It is important to note that all the integrals, in Eq. (3–20), are constants throughout the whole computation (for a given mesh) and not dependent on the solution, U . This advantage is not available if we choose θ as derivative of primitive variable.

This advantage adds on for implicit methods, since the jacobian matrices are also constant, and hence will not need to be re-evaluated, therefore saving computational time. The derivative of $\{\theta\}$ w.r.t. $\{U\}$ (of current element) is given as,

$$\left[\int_{\Omega} \phi \phi^T d\Omega \right] \frac{\partial \{\theta\}}{\partial \{U\}} = \left[\int_{\Omega} \phi \cdot \nabla \phi^T d\Omega \right] - \left[\oint_{\partial\Omega} \frac{\phi \phi^T}{2} \vec{n} d\sigma \right] \quad (3-21)$$

and the derivative of $\{\theta\}$ w.r.t. $\{U\}_{nb}$ (of neighboring element) is given as,

$$\left[\int_{\Omega} \phi \phi^T d\Omega \right] \frac{\partial \{\theta\}}{\partial \{U\}_{nb}} = \left[\oint_{\partial\Omega} \frac{\phi \phi_{nb}^T}{2} \vec{n} d\sigma \right] \quad (3-22)$$

The disadvantage of faster version of BR1 method is that the matrix is no more compact (see section 3.5.2 for more detail). This complicates the implementation of this method. The alternative to this is BR2 method. Original formulation of BR2 method is exactly same as the BR1 method. This was used in our code to debug implementation of BR2 method by comparing it to BR1 method. Both should perform exactly same, since the BR2 in its original formulation is derived from BR1 scheme. After this first variant of BR1 method, other variations were introduced to improve the performance of BR2 method and also to make it a compact scheme.

3.3.2 Original Formulation of BR2

Taken from [62], BR2 formulation defines θ being equal to (from Eq. (3-18)) a sum of ∇U and a correction factor, R_h ,

$$\theta = \nabla U + R_h \quad (3-23)$$

where, R_h is defined by,

$$\int_{\Omega} \phi R_h d\Omega = \oint_{\partial\Omega} \phi \left(\frac{U^+ - U^-}{2} \right) \vec{n} d\sigma \quad (3-24)$$

R_h is expressed again in terms of the basis function, ϕ and the degrees of freedom of R_h ,

$$R_h = \phi^T \{R_h\} \quad (3-25)$$

Substituting Eq. (3-25) in Eq. (3-24),

$$\left[\int_{\Omega} \phi \phi^T d\Omega \right] \{R_h\} = \left[\oint_{\partial\Omega} \frac{\phi \phi_{nb}^T}{2} \vec{n} d\sigma \right] \{U\}_{nb} - \left[\oint_{\partial\Omega} \frac{\phi \phi^T}{2} \vec{n} d\sigma \right] \{U\} \quad (3-26)$$

So, in the original formulation of BR2, R_h is defined for every element, and right hand side being the surface integral is summed over all the edges of the element. This R_h is then input into Eq. (3-9) (excluding inviscid terms for space constraint),

$$\int_{\Omega} \phi \frac{\partial U}{\partial t} d\Omega - \int_{\Omega} \nabla \phi \cdot F_v(U_h, \nabla U_h, R_h) d\Omega + \oint_{\partial\Omega} \phi F_v(U_h, U_h^{nb}, \nabla U_h, \nabla U_h^{nb}, R_h, R_h^{nb}) \cdot \vec{n} d\sigma = 0 \quad (3-27)$$

It is easily seen that an implicit method for Eq. (3-27) will need derivatives w.r.t. $\{U\}$ from neighbors' neighbors as well, just as in faster version of BR1 method. This is because, R_h^{nb} depends on the immediate neighbors of the neighbor of current element.

This is the problem with the original formulation of BR2 method. It also does not reduce the jumps in the solution, in between the elements, as shown in the Chapter 4. Solution to this problem comes, by replacing the global correction factor, R_h in the surface integrals in Eq. (3-27), with local correction factors, r_h , which are defined only on their respective edges, i.e.,

$$\left[\int_{\Omega} \phi \phi^T d\Omega \right] \{r_h\} = \left[\oint_{\partial\Omega} \frac{\phi \phi_{nb}^T}{2} \vec{n} d\sigma \right] \{U\}_{nb} - \left[\oint_{\partial\Omega} \frac{\phi \phi^T}{2} \vec{n} d\sigma \right] \{U\} \quad (3-28)$$

In Eq. (3-28), the surface integrals are not circular integrals, but line integrals on one edge at a time. There is local r_h defined for every edge, rather than one global R_h for all the edges. Hence, r_h for a particular edge depends only on the current element and its immediate neighbor sharing the concerned edge, whereas R_h depends on current element and all its immediate neighbors. This way, first variation of BR2 can be written as,

$$\int_{\Omega} \phi \frac{\partial U}{\partial t} d\Omega - \int_{\Omega} \nabla \phi \cdot F_v (U_h, \nabla U_h, R_h) d\Omega \quad (3-29)$$

$$+ \oint_{\partial\Omega} \phi F_v (U_h, U_h^{nb}, \nabla U_h, \nabla U_h^{nb}, r_h, r_h^{nb}) \cdot \vec{n} d\sigma = 0 \quad (3-30)$$

The main advantage is that the scheme in Eq. (3-30) is compact, depending only on the current element and its immediate neighbors. This scheme is also more stable and it reduces the inter-element jumps. As for BR1 method, we can also define derivatives of $\{r_h\}$ w.r.t. $\{U\}$ and $\{U\}_{nb}$ respectively,

$$\left[\int_{\Omega} \phi \phi^T d\Omega \right] \frac{\partial \{r_h\}}{\partial \{U\}} = - \left[\oint_{\partial\Omega} \frac{\phi \phi^T}{2} \vec{n} d\sigma \right] \quad (3-31)$$

$$\left[\int_{\Omega} \phi \phi^T d\Omega \right] \frac{\partial \{r_h\}}{\partial \{U\}_{nb}} = \left[\oint_{\partial\Omega} \frac{\phi \phi_{nb}^T}{2} \vec{n} d\sigma \right] \quad (3-32)$$

3.4 Source Terms

For hypersonic flow, we have source terms corresponding to both chemical and thermal non-equilibrium. We can treat these source terms, with a source vector, S as in Eq. (2-22). Multiplying this equation with the basis function, ϕ and integrating over the element domain, we get (ignoring the inviscid and viscous flux terms, which were discussed in sections 3.2 and 3.3 respectively),

$$\int_{\Omega} \phi \frac{\partial U}{\partial t} d\Omega = \int_{\Omega} \phi S d\Omega \quad (3-33)$$

For the problems of our interest, S is a function of U alone, hence its implementation is straightforward for our work.

3.5 Time Integration

We have already discussed the discretization of all the spatial derivative terms in Eq. (2-22). Now, we present the time discretization for the unsteady term in Eq. (2-22).

We have considered two approaches in this work, namely explicit and implicit time integrations methods.

3.5.1 Explicit Time Integration

For explicit time integration, first order accurate forward Euler method is used,

$$\left[\int_{\Omega} \phi \phi^T d\Omega \right] \frac{\partial \{U\}}{\partial t} = \left[\int_{\Omega} \phi \phi^T d\Omega \right] \left(\frac{(\{U\}^{n+1} - \{U\}^n)}{\Delta t} + O(\Delta t) \right) = R(\{U\}^n) \quad (3-34)$$

Here, $R(\{U\}^n)$ denotes all the spatial terms moved to the right hand side of Eq. (2-22). For explicit method, $R(\{U\}^n)$ is known at previous time step, t^n , and hence solution procedure for explicit method is very easy and straightforward. Inviscid methods however, face time step restriction with CFL number restricted to $\frac{1}{2p+1}$, where p is the polynomial order of the basis function [60]. Thus, for a fine mesh and higher order accuracy, the time step is severely restricted for the explicit method for the inviscid terms.

Source terms, as in the chemistry terms in the hypersonic flows with thermo-chemical non-equilibrium, add on to the CFL time step restriction, which can be even more severe than the inviscid CFL restriction. This can be resolved by treating the source terms implicitly and the inviscid and the viscous terms explicitly.

For example, for one of the hypersonic flow problems over the cylinder (with $M = 17.65$), CFL was restricted to 0.005, with both thermal and chemical non-equilibrium on and a complete explicit method. However, with implicit treatment of only the source terms, we were able to come up to an inviscid time step restriction with CFL number of 0.5. As another example of the importance of implicit time integration methods, for the hypersonic and thermal ablation problems, Δt was restricted, for the thermal ablation problem, to 10^{-8} sec with an explicit method, however with a fully implicit method, we were able to run the code at a time step of $10^{-3} - 10^{-2}$ sec. Total solution time for the thermal ablation problems can be typically few seconds and the presence of high source

terms (for dealing with unsteady momentum equation of pyrolysis gas), makes explicit method very restrictive in its application. Implicit methods are thus very useful for the problems of our interest, namely thermal ablation and hypersonic flows.

3.5.2 Implicit Time Integration

Implicit methods overcome the severe time step restriction, by evaluating R at a current time step, i.e. $R(\{U\}^{n+1})$. Thus, the scheme can be written as,

$$\left[\int_{\Omega} \phi \phi^T d\Omega \right] \frac{\partial \{U\}}{\partial t} = \left[\int_{\Omega} \phi \phi^T d\Omega \right] \left(\frac{(\{U\}^{n+1} - \{U\}^n)}{\Delta t} + O(\Delta t) \right) = R(\{U\}^{n+1}) \quad (3-35)$$

Since the problems of our interest are non-linear, we need to use Newton method to obtain the solution of Eq. (3-35). With the Newton method, we want to drive $F(\{U\}^{n+1}, \{U\}^n)$ in Eq. (3-36) to zero,

$$F(\{U\}^{n+1}, \{U\}^n) = \left[\int_{\Omega} \phi \phi^T d\Omega \right] \left(\frac{(\{U\}^{n+1} - \{U\}^n)}{\Delta t} \right) - R(\{U\}^{n+1}) = 0 \quad (3-36)$$

For this, we need to evaluate jacobian matrices of $F(\{U\}^{n+1}, \{U\}^n)$ w. r. t. $\{U\}^{n+1}$,

$$J(\{U\}^{n+1}, \{U\}^n) = \frac{\partial F(\{U\}^{n+1}, \{U\}^n)}{\partial (\{U\}^{n+1})} = \frac{[\int_{\Omega} \phi \phi^T d\Omega]}{\Delta t} - \frac{\partial R(\{U\}^{n+1})}{\partial \{U\}^{n+1}} \quad (3-37)$$

The term, $\frac{\partial R(\{U\}^{n+1})}{\partial \{U\}^{n+1}}$ includes derivative of all the terms, inviscid, viscous and source term w.r.t $\{U\}^{n+1}$. These derivatives include terms on domain and element interfaces.

An element interface can either be inside the domain or on the boundary. In either case, finding the jacobians for all terms is a non-trivial task, and requires lot of careful attention for the Jacobian matrices to work correctly for a good performance of the implicit method.

After finding this jacobian, J , the solution can be iterated for by finding the change in the solution vector, $\{\delta U\}^{n+1,p}$ at the p^{th} iteration of the $(n + 1)^{\text{th}}$ timestep,

$$[J(\{U\}^{n+1,p}, \{U\}^n)] \{\delta U\}^{n+1,p} = -F(\{U\}^{n+1,p}, \{U\}^n) \quad (3-38)$$

At every iteration, this change is added to the initial guess ($p = 0$) for $\{U\}^{n+1}$, which is set equal to solution from previous timestep,

$$\{U\}^{n+1,0} = \{U\}^n \quad (3-39)$$

$$\{U\}^{n+1,p} = \{U\}^{n+1,p-1} + \{\delta U\}^{n+1,p}, \quad p \geq 1 \quad (3-40)$$

3.6 Parallelization

For solution with a single processor, we use a serial-processor ILU-preconditioned GMRES solver. This is a very robust solver, for almost all the problems we have worked with in our lab including plasma, high speed fluid flow, hypersonic flow and thermal ablation. As an example, let us consider double Mach reflection (DMR) problem solved using 1 processor GMRES.

Table 3-1. Time taken for 1 processor GMRES for Double Mach Reflection

Mesh Details	Time for forming matrix (sec)	Time for solving global matrix, using 1 processor GMRES (sec)
330 X 100	18	62
660 X 200	72	242

As we see in Table 3-1, MIG takes large time to solve for one iteration. For convergence in 5 iterations/time-step, and a time-step value of 10^{-3} sec for a total solution time of 0.2 sec, the program runs nearly 1000 iterations to give the final solution. This results in 22 hours run time for mesh 1 (330×100) and 3.6 days for mesh 2 (660×200). This necessitates the need for parallelization, which saves tremendous amount of time with more number of processors.

There are two components of the code, as shown in Table 3-1, that need parallelization. First part of the code assembles the global matrix and the second part solves the global system.

For the parallelization of the assembly of the global matrix, we have implemented domain decomposition. Herein, the total number of elements are divided almost equally amongst the total number of processors. This distribution is done based on element numbers. Thus, each processor forms only its own part of the global matrix. Currently to avoid any communication between the processors during the assembly part, we make complete domain's solution available to all the processors. This way, even the terms, which come from jacobian of the flux terms w. r. t. the elements from other processors, are formed by the processors without any need of communication from other processors.

Price is paid, however, at the end of the solution process, when the solution values are passed from all processors to processor with rank zero, and then broadcasted from processor with rank zero to the rest of the processors. Time taken in this step can become a bottleneck for larger problems, and hence will need attention in future.

For solution process, we use HYPRE [78], a high performance parallel solver, to solve the matrix in parallel. Two methods have been implemented into MIG from HYPRE, DS (Diagonal scaling) + BiCGStab and Euclid (ILU preconditioner) + GMRES. Since the matrices for high speed flow problems and thermal ablation can be highly ill conditioned, hence a good preconditioner is required along with the use of Krylov iterative solvers. Curves for the performance of the solver, in terms of the time taken vs. the number of processors for two meshes containing 2780 and 33,000 elements (used for double Mach reflection problem) respectively are shown in Figure 3-1.

Figure 3-1 A shows the performance plot of Euclid + GMRES for 2780 elements with different levels of fill for ILU preconditioner. Matrix size is $66,720 \times 66,720$. It can be seen that although level of fill '0' takes the lowest setup time (for ILU factorization), it

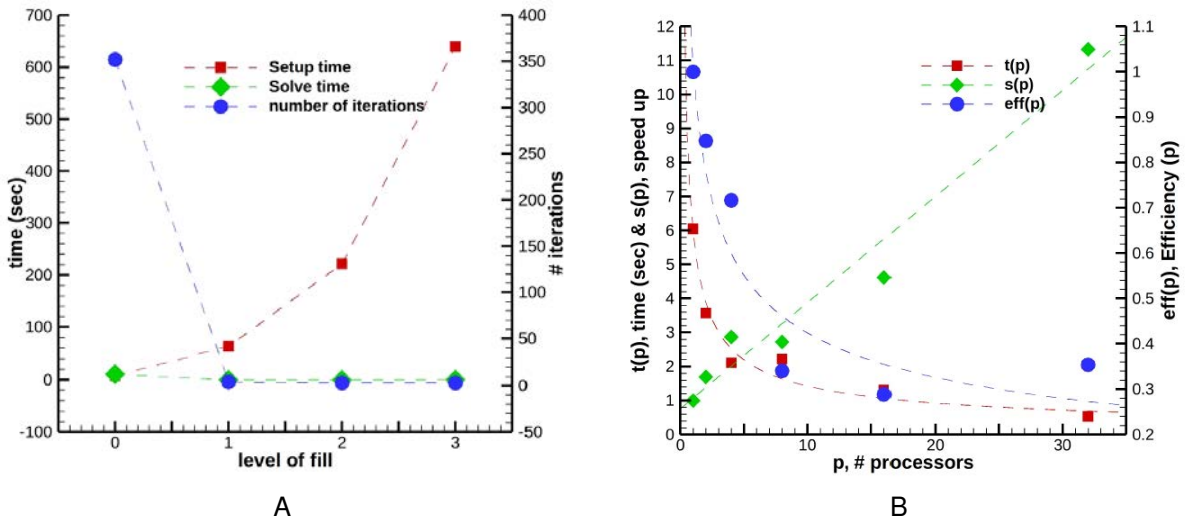


Figure 3-1. Parallel performance of Euclid+GMRES solver in HyPre. A) Performance plot of Euclid + GMRES for 2780 elements with different levels of fill for ILU preconditioner. B) Performance plot with 0 level of fill showing linear speed up.

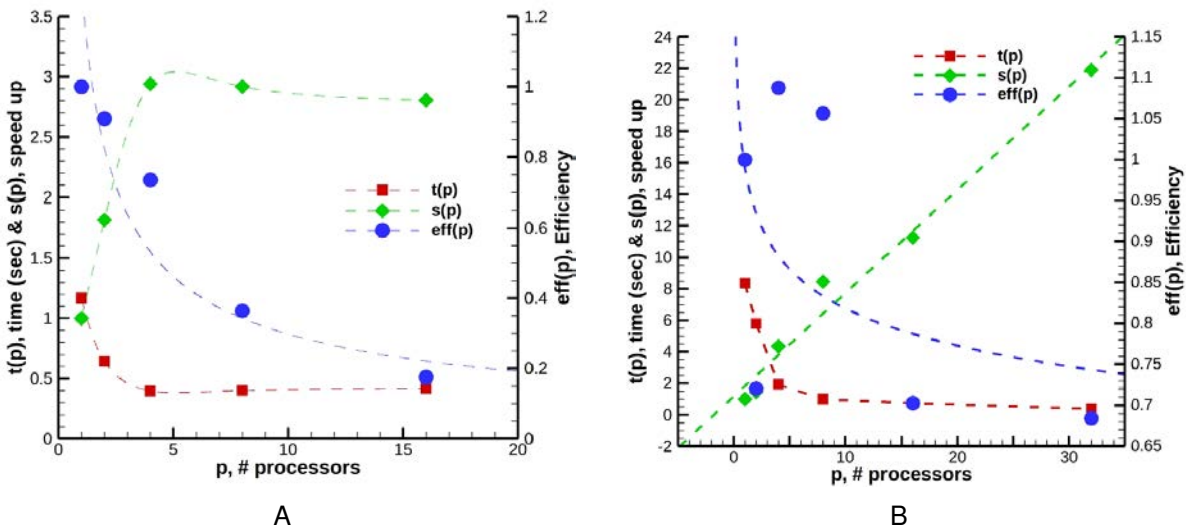


Figure 3-2. Parallel performance of DS + BiCGStab solver in HyPre. A) Performance plot of DS + BiCGStab for 2780 elements with different number of processors. B) Performance plot of DS + BiCGStab for 33000 elements with linear speed up.

also takes the largest number of iterations in solving the preconditioned system. This is probably due to ineffective factorization at the '0' level. This results in 6 sec solve time, which is very significant, given the smaller size of the matrix. With increase in level of fill, setup time increases tremendously hence making this method impractical for our use.

Figure 3-1 B shows the performance plot of Euclid + GMRES for 2780 elements with 0 level of fill. We can see linear speed up (green curve). Use of 32 processors results in approximately 10 times speed up in comparison to 1 processor performance.

More useful method, so far for our purpose, has been DS + BiCGStab, another solver available in HYPRE. Figure 3-2 shows performance plot of this method with different number of processors for A) 2780 elements and B) 33000 elements respectively. Matrices for these cases are of size $(66,720 \times 66,720)$ and (792000×792000) respectively. We notice saturation of speed up at a value of 3 for case A) for number of processors being more than 4. However DS + BiCGStab shows a promising performance with 33000 elements. Speed up is linear w. r. t. number of processors and a total 21 times speedup is achieved with 32 processors. Hence the performance improves with larger number of elements in the domain, which makes sense, since smaller number of elements will reach saturation faster.

3.7 r-p Adaptive Methods

Hypersonic flows have shocks which need to be captured with a given numerical method. Presence of the shocks is challenging for any high-order accurate method, since presence of shock like discontinuities leads to Gibbs oscillations. Naturally, amount of dissipation present in high order method is not sufficient to curtail these spurious oscillations. Therefore, a strategy is required for capturing the shock. Approaches, in the literature, used for capturing the shocks focus primarily on methods of artificial dissipation [2, 79] and slope limiters [59]. However, we focus on a different approach in this work.

This method is called p-adaptivity and was first used in [10]. Since, it is well known that $p = 0$ (corresponding to first order accurate method) is sufficient to capture shock of any strength. So using an effective shock indicator technique, we can use $p = 0$ in the shock regions and higher order polynomial accuracy ($p \geq 1$) in smooth flow regions. This approach avoids any use of slope limiters or artificial dissipation along with their complexities, and is thus more useful and convenient to use, especially in the case of DG methods. So far, this has been applied to only inviscid hypersonic flows [10], but in this work we further explore its application to viscous and thermo-chemical nonequilibrium hypersonic flows.

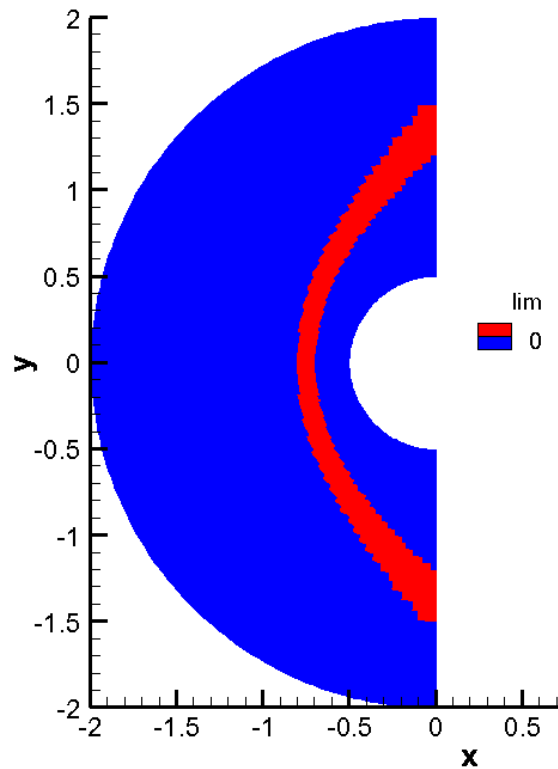


Figure 3-3. Locating shock using pressure based shock indicator. Shock indicator, defined by Eq. (3-41), is used to identify shock region (shown in red) from smooth flow regions (shown in blue). This is an example of using p-adaptivity to capture shocks for inviscid hypersonic flow over cylinder with $M = 17$. As can be seen the shock indicator is very effective.

Shock indicator, used in this work, is taken from [10], and is given as,

$$s_k = \log_{10} \left(\frac{1}{|\partial\Omega_k|} \int_{\partial\Omega_k} \left| \frac{[P_h] \cdot \vec{n}}{\{P_h\}} \right| ds \right) \quad (3-41)$$

$[P_h]$ in Eq. (3-41) denotes the jump in the pressure across the edges of an element, Ω_k , and $\{P_h\}$ denotes the average of pressure across the edge. s_k is evaluated for all the elements in the domain, and the following criteria is used to identify the regions of the shock from the smooth flow regions,

$$\begin{cases} s_k > 0.3, & p = 0 & (\text{shock region}) \\ s_k < 0.3, & p \geq 1 & (\text{smooth flow region}) \end{cases} \quad (3-42)$$

This shock indicator is very effective in identifying regions of shock from smooth flow regions. This can be used for transient problems, where the location of shock may change with time, or for problems where the hypersonic flow, starting with a uniform flow solution, develops into a steady state solution. A switch, 'lim' is used to identify the shock regions, and an example is shown in Figure 3-4 for hypersonic flow around a cylinder. $p = 0$ corresponds to red regions indicating shock and $p \geq 1$ corresponds to blue regions indicating smooth flow regions.

Solution accuracy in smooth flow regions can be improved by increasing the order of polynomial approximation, p in those regions, without changing the mesh resolution there. This is the advantage afforded by DG method. But, the shock region is limited to $p = 0$ and hence first order accurate only. Only possibility to improve solution accuracy in the shock is to refine the mesh in the shock. One approach taken in [10] is applying h-refinement in shock regions. This improves solution accuracy in shock regions. However, this also results in large number of elements in the region around the shock, which may not lie in the shock. For this purpose, we use r-adaptivity approach, where

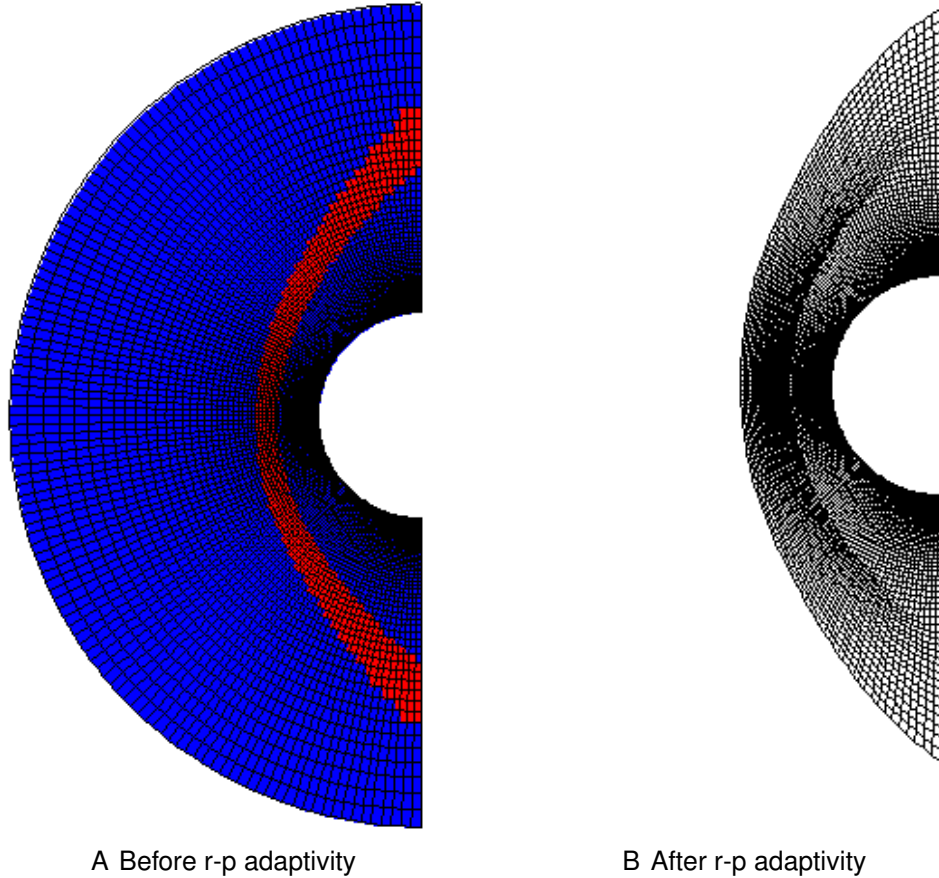


Figure 3-4. Mesh before and after r-p adaptivity. A) Mesh before r-p adaptivity. B) Mesh after r-p adaptivity. Elements outside the shock are brought closer to the shock, hence packing more elements in the shock. Thus, the mesh resolution in the shock is improved without increasing total number of elements.

we cluster the elements in the domain outside of the shock, to region very close to shock. An example of this is shown in Figure 3-4.

This application is also not dependent on the shape of the body, but is the shock based refinement, hence applies to all body shapes.

CHAPTER 4

CODE VALIDATION EXAMPLES

In this chapter, we present some example problems to test the inviscid and viscous sections of the code. In each section, a simple example problem leads to more and more complex ones. Each of these problem, tests the basic machinery of the code to see if the correct physics is captured in every section. This is a very effective way to solve a tough problem like non-equilibrium hypersonic flow or thermal ablation, i.e. to test the smaller sections of the code by isolating them in a sample problem.

Along with presenting the results, we will also show solution capability for high order polynomial accuracy.

4.1 Inviscid Flow

In this section, we isolate the inviscid phenomena that primarily deals with the pressure variation resulting in flow features. First problem is the potential flow around a cylinder (at very low Mach number of 0.01) where in the beginning, there develops a high pressure and low pressure regions in front and back of cylinder respectively, causing acceleration of fluid close to cylinder from front to back of cylinder. This effect is also connected to Bernoulli's equation (defined for incompressible and inviscid flow). As the flow speed increases, the flow at the top of the cylinder reaches sonic condition ($M = 1$) for free stream Mach number, M_∞ of 0.38 approximately.

As the flow speed further increases, we get what we call transonic flows, with flow Mach numbers increasing above unity at the top of cylinder. Presence of higher pressure downstream causes the shock to appear on the surface of the cylinder. Shocks move from back of the cylinder to the front, and weaken in strength since they can not sustain for Mach numbers below unity. A more complex problem of steady, but moving shock is then solved. This is double Mach reflection problem having is a Mach 10 flow that hits the wedge at an angle α . Complex inviscid interactions of shock with Mach stem giving rise to complex features is also noticed in this case.

4.1.1 Potential Flow Around the Cylinder

At very low Mach numbers, for the potential flow problem, only the inviscid effects are important. The problem of 2-D uniform flow, being suddenly exposed to the cylinder, is equivalent to a cylindrical particle being impulsively started in a quiescent flow field. The forces acting on the particle, till the flow achieves a steady state behavior, have been theoretically derived in [80].

Hence, we can test our inviscid part of the code for the transient effects, as the flow develops from initial uniform flow solution to the potential flow solution. We consider Mach number of 0.01, that tests our code for the unsteady forces, the convection and the pressure terms. Important details for the problem setup are as follows,

$$M = 0.01 \quad (4-1)$$

$$\rho = 1.17659 \text{ kg/m}^3 \quad (4-2)$$

$$u = 3.47224 \text{ m/s} \quad (4-3)$$

$$P = 101325 \text{ Pa} \quad (4-4)$$

$$\text{Radius} = R = 0.1 \text{ m} \quad (4-5)$$

$$\text{Domain size} = 20 (R) = 2 \text{ m} \quad (4-6)$$

$$\text{Acoustic time scale} = \tau = \frac{R}{a_o} = \frac{0.1 \text{ m}}{347 \text{ m/s}} = 2.88 \times 10^{-4} \text{ s} \quad (4-7)$$

The drag force on the cylindrical case for the inviscid problem is calculated from,

$$D = \int P n_x d\Gamma \quad (4-8)$$

The values for this drag force are compared to the exact solution from [80] and the code was tested for different orders of accuracy.

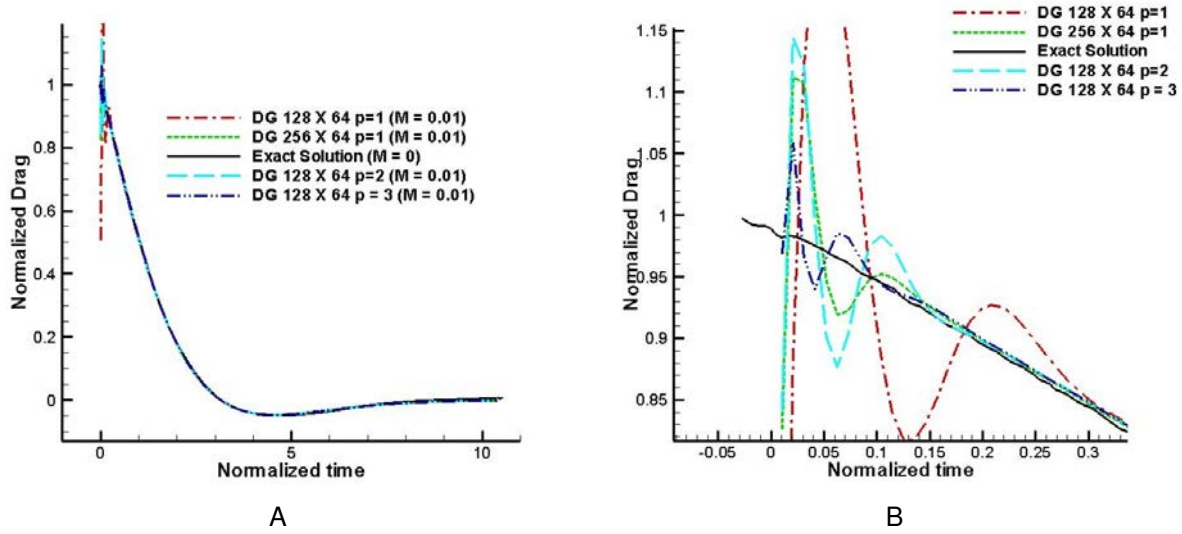


Figure 4-1. Order of accuracy analysis for potential flow around a cylinder. A) Normalized drag vs. normalized time response of fluid, to a sudden presence of cylindrical particle. B) Zoomed-in section of the initial transients.

We show the comparison of the exact solution to the results obtained using DG method in Figure 4-1. The solution is obtained with polynomial order of accuracy, $p = 1$, 2 and 3 for 128 X 64 mesh and $p = 1$ for 256 X 64 mesh. We see a good comparison of drag with the exact solution, and the more subtle differences for initial transients are also showed in a zoomed in section. We notice, that $p = 3$ and 128 X 64 mesh gives the best comparison for the initial transient prediction of the drag.

After comparing the transient solution, for the drag prediction of the potential flow, we also compare the steady state solution given by our code, MIG to the potential flow solution in Figure 4-2.

4.1.2 Subsonic Flow Around the Cylinder

Now we consider the case of subsonic flow around the cylinder, with $M = 0.38$. The viscous effects are ignored in this case, which shall be true for high Reynolds number cases, away from the wall. The Mach number of 0.38 is close to the critical Mach number (of 0.4) for the flow over cylinder. The flow Mach number (for critical Mach number) reaches unity at the top of the cylinder. There are no shocks in the solution

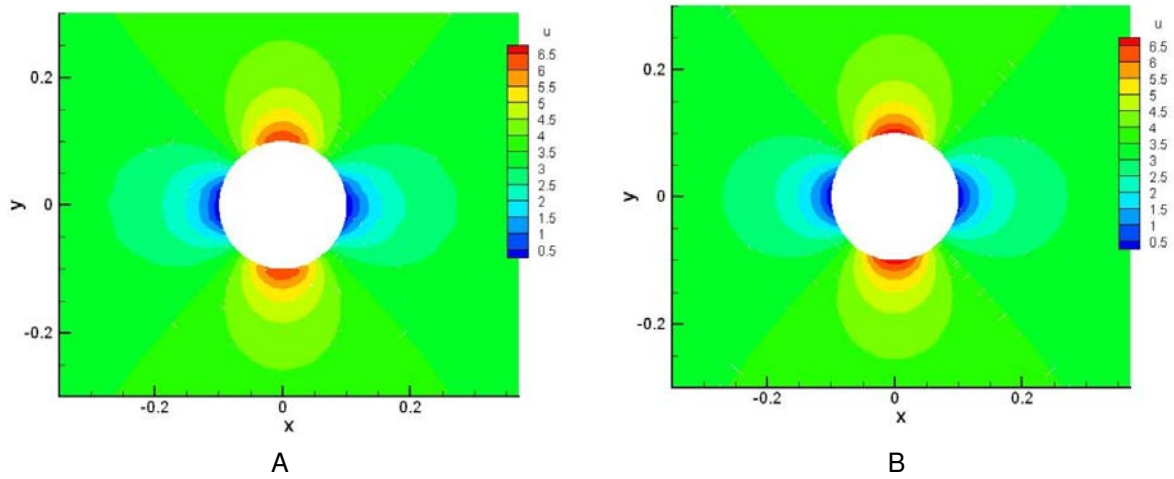


Figure 4-2. Steady state velocity contours comparison for potential flow over cylinder. A) Steady state solution for x-velocity contours, obtained using P1Q2 approximation in MIG. B) Steady state potential flow solution.

for critical Mach number. For Mach numbers greater than 0.4 (called transonic flows, presented in section 4.1.3), there is a shock that develops in the rear of the cylinder and travels towards the front. Thus we get some interesting flow physics, which is discussed in section 4.1.3.

For all the inviscid flow simulations presented, we choose a circular domain around the cylinder and use the quadrilateral mesh elements. Curved boundaries, with quadratic geometric interpolation function, are used at the circular body of the cylinder, giving an exact fit. For this purpose, we use Gordon Hall transformation, which gives the mapping of the complete physical element from the reference square element, by mapping the edges.

For the boundary conditions for all inviscid cylinder flow cases, we use slip boundary condition for the wall, and far-field boundary condition at the outflow domain. Left side of this domain uses inlet boundary condition, and right side interpolates the boundary from inside, except we make sure that pressure is 1 atm at the right side of outside domain. We show a comparison of these meshes in Figure 4-3. Bassi & Rebay

[81] use 128 x 32 triangular elements mesh, and we use 64 x 50 quadrilateral elements mesh.

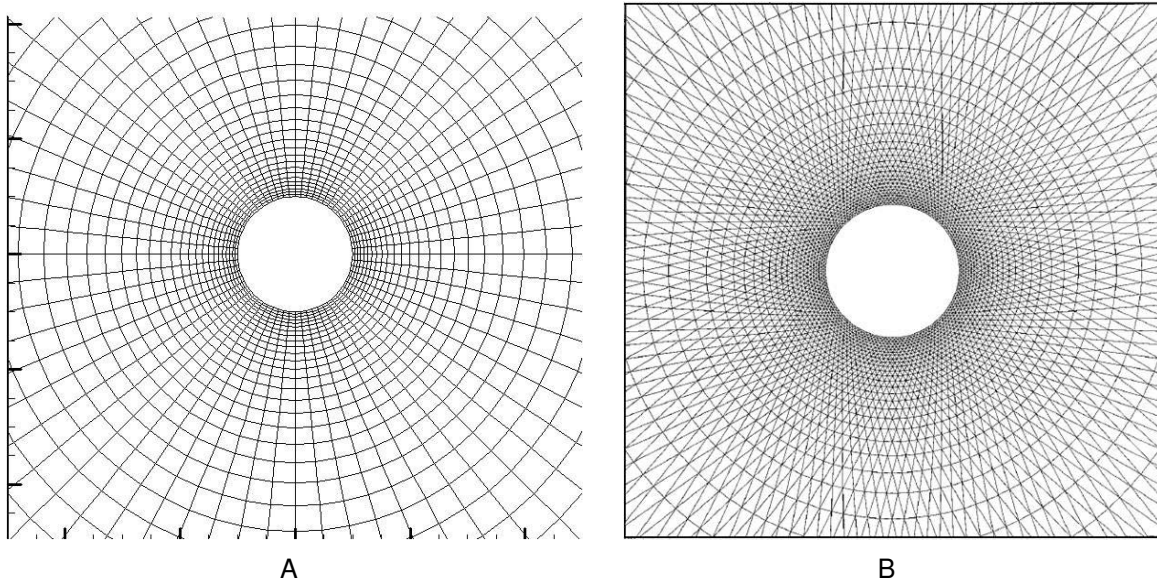


Figure 4-3. Mesh comparison for Mach 0.38 flow around cylinder. A) 64x50 mesh used in MIG. Quadrilateral elements and P1Q2 approximation are used in MIG. B) 128x32 mesh used in Bassi & Rebay [81]. Triangular elements and P1Q2 approximation are used in [81].

The steady state solution is compared by matching Mach number contours provided in [81] and these comparisons are given in Figure 4-4. Our results match well to their result, except behind the cylinder. This asymmetry, for front and back of the cylinder, was also noticed by Bassi & Rebay [81] for coarser meshes.

The asymmetry in the flow, behind the cylinder is due to use of coarser meshes behind the cylinder. Also, the number of triangular elements are higher in [81] than compared to the number of the quadrilateral elements used in MIG.

4.1.3 Transonic Flow Around the Cylinder

Subsonic flows with free stream Mach numbers being lower than the critical value of 0.38, can be captured without the use of limiters, as there are no shocks developed in the flow. But for flows with $M > 0.4$, the flow achieves Mach numbers greater than 1, over the cylinder top, and hence the solution develops transient radial shocks. Ideal

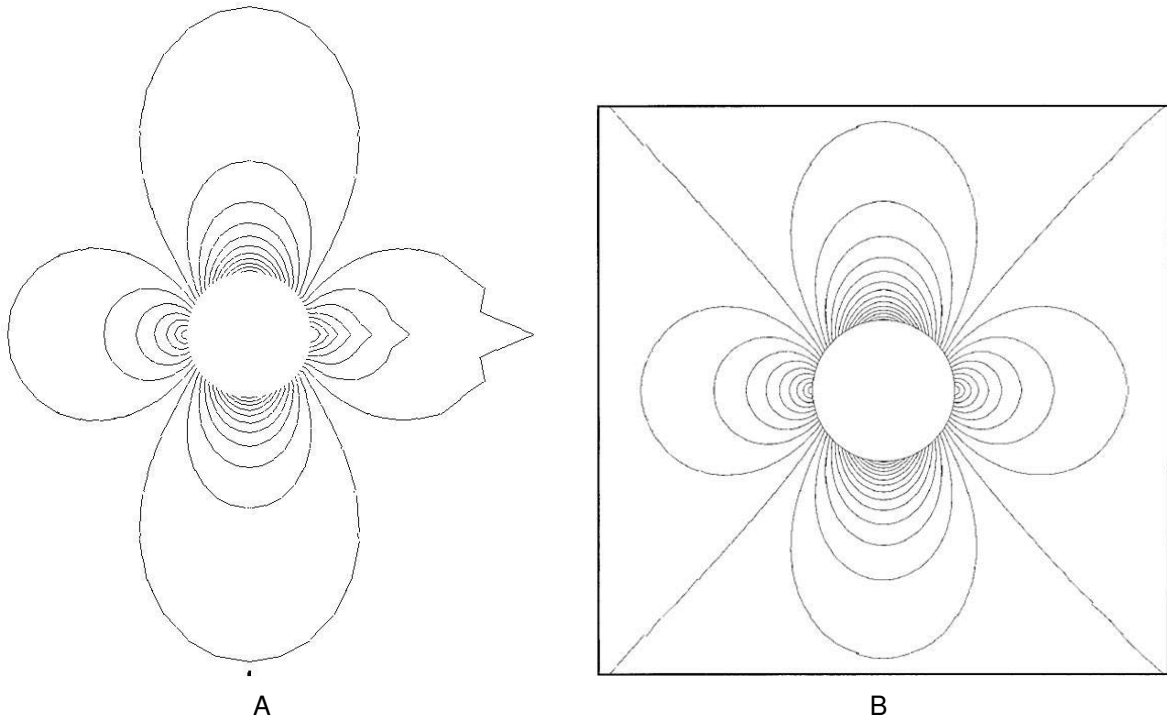


Figure 4-4. Mach contours comparison for $M = 0.38$ flow around cylinder. A) Results from MIG using 64×50 quadrilateral mesh elements. B) Results from Bassi & Rebay [81] using 128×32 triangular mesh elements. Results differ at the back of the cylinder, where the mesh is coarser for MIG in comparison to Bassi & Rebay.

handling of these flows requires the use of a good limiter. However, in our simulations we have attempted the solution without employing the limiters.

The fluid accelerates to a maximum velocity over the cylinder top. Seeing an adverse pressure gradient, downstream of the cylinder top, the flow develops a transient radial shock that propagates upstream. As the shock propagates upstream the shock weakens in strengths and hence eventually fades away. The complete mechanism of shock development, its propagation upstream along the cylinder surface, formation of the recirculation zone subsequently leading to vortex shedding phenomena, behind the cylinder is explained in Figure 4-5.

This case was run for P1Q2 i.e. linear basis function and quadratic approximation for the circular cylinder boundary. Time step of 10^{-5} sec was used along with the mesh

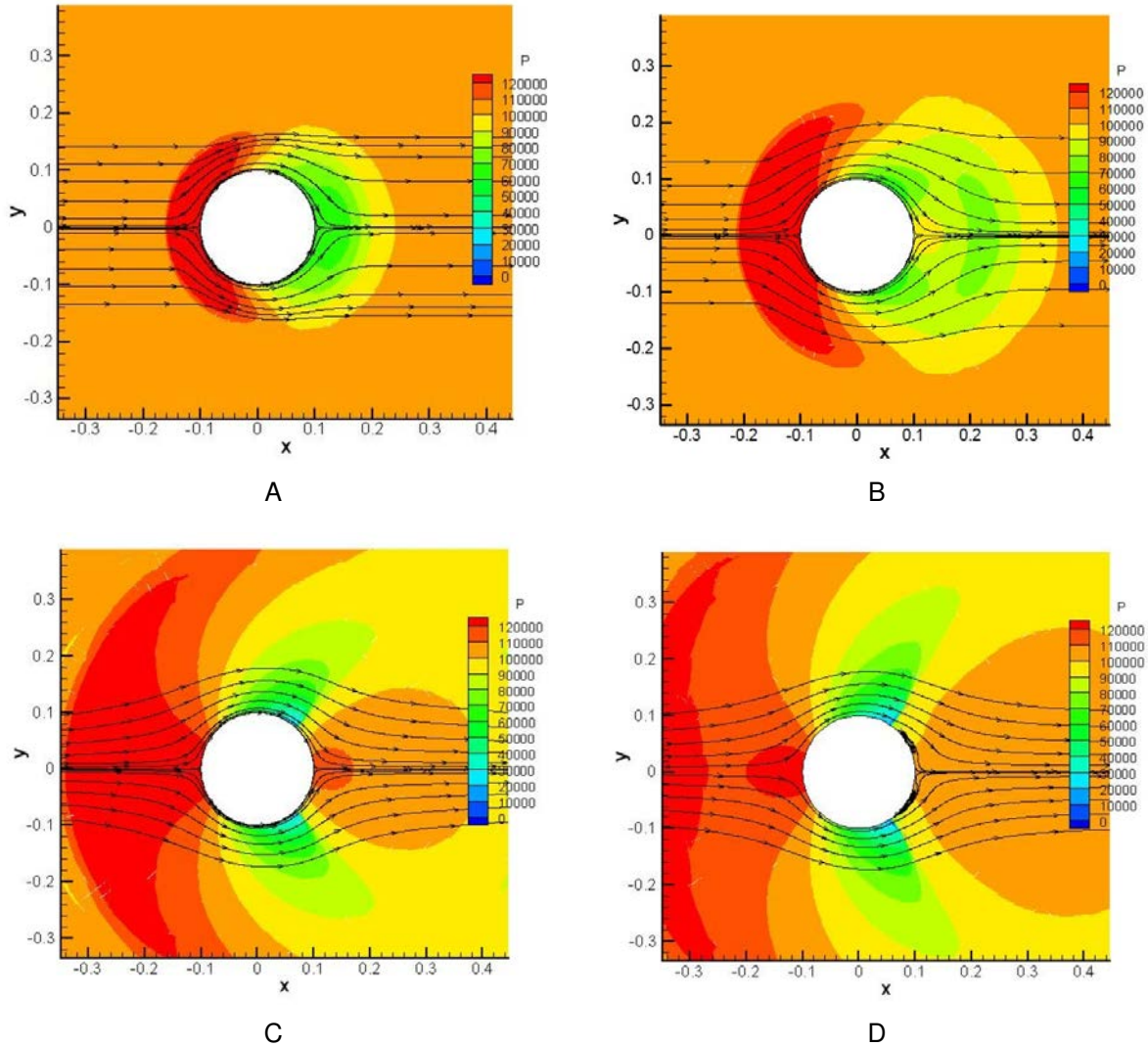


Figure 4-5. Formation of separation region for Mach 0.5 transonic flow around the cylinder. A) Initial development of high and low pressures across the front and back of the cylinder respectively. B) Further development of high and low pressure regions causing flow acceleration from the front of the cylinder to the back of the cylinder. C) Development of radial shock and its motion towards the front end of the cylinder. D) Adverse pressure gradient is formed after the shock, that causes recirculation and flow separation after the shock.

of 128 x 50 elements. 128 elements were used along the circumferential direction and 50 along the radial direction. For this case as mentioned, no limiters were used, but since the density and energy values can become zero or negative; to avoid the solution to either diverge or crash, we have limited density to not fall below the value of 0.1 kg/m^3 (the freestream value of density being 1.17659 kg/m^3). We see initial development of high and low pressure zones on the front and back portions of the cylinder respectively (Figure 4-5 A and B). This leads to the fluid accelerating from front to the back portion of cylinder hence resulting in the formation of radial shocks (two shocks in Figure 4-5 C and D are symmetric to the x-axis). These shocks move towards the front portion of the cylinder. They weaken as they move and fade away before reaching the front portion of the cylinder.

These shocks reappear again as the flow conditions again develop similar to the initial phase, causing acceleration of fluid from front portion to the end. The recirculation zone that is formed due to flow separation behind the shocks, creates two prominent counter-rotating vortices behind the cylinder (Figure 4-6 A and B). These vortices are stretched in the front direction and eventually leads to vortex shedding phenomena (Figure 4-6 C and D). The simulation is run for a total time of 7 ms.

There is a sudden pressure increase after the shock, which causes the shock to move more towards the front portion of the cylinder. We also see that after the shock, the pressure increases along the direction of the flow. This is adverse pressure gradient and causes the flow to decelerate after the shock. This is also referred to as the rotational effect produced by the shock, or isentropy deviation. Due to this deceleration, close to the surface of the cylinder, the flow starts to recirculate and separate from the cylinder surface.

As the radial shock moves towards the front portion of the cylinder, recirculation zone increases in size. But, then the pressure again increases in the front of the

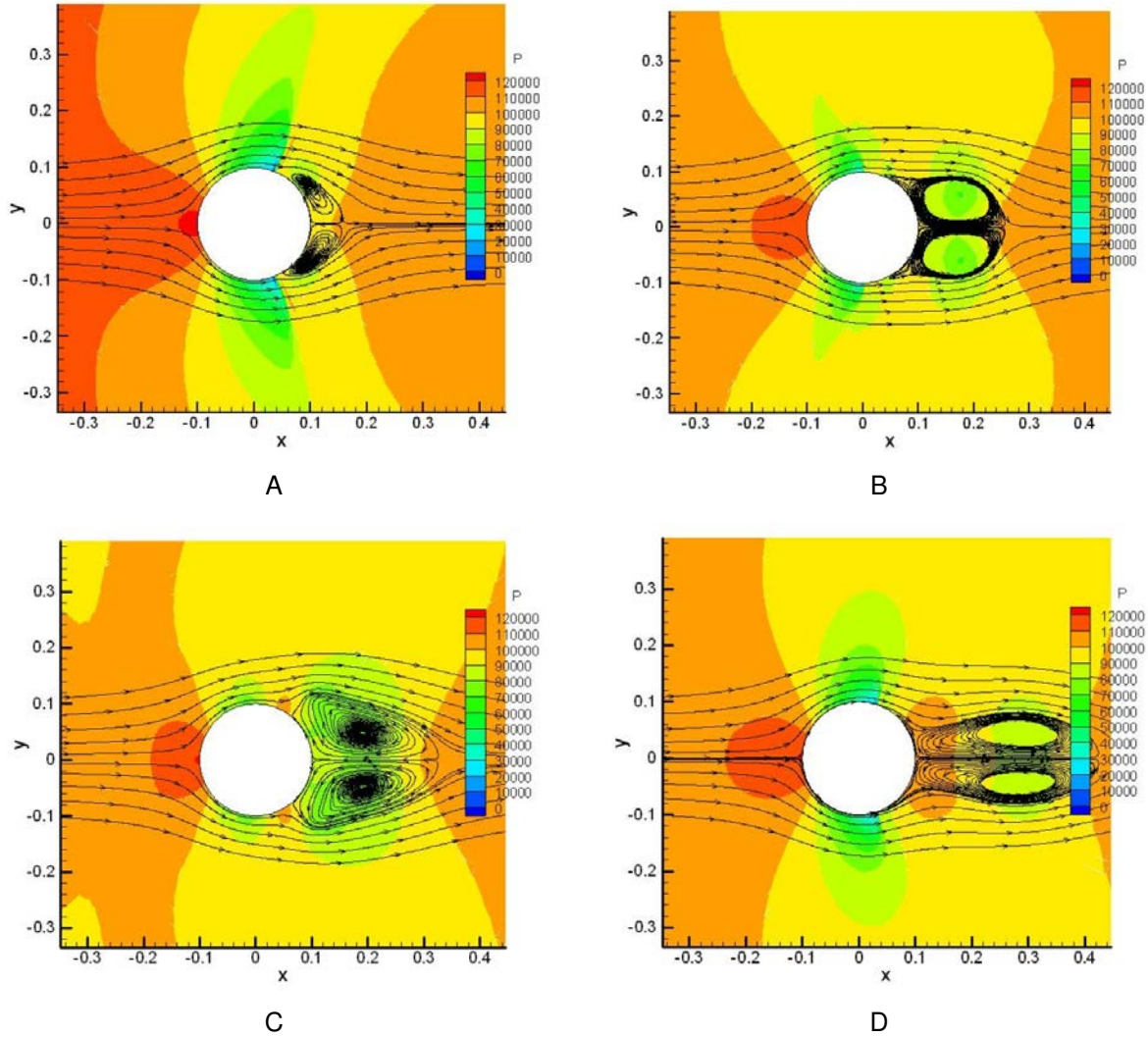


Figure 4-6. Vortex shedding for Mach 0.5 transonic flow around the cylinder. A) Motion of radial shocks towards the front of the cylinder. B) Formation of recirculation region behind the shock due to flow separation. C) Increase in the size of recirculation zone behind the cylinder causing higher pressure in the front of the cylinder. D) Redevelopment of radial shock and stretching of the recirculation zone. Higher pressure in the front of the cylinder leads to higher velocities over the cylinder. Stretching of the recirculation zone eventually leads to the vortex shedding phenomena.

cylinder, resulting in appearance of one more shock, and high velocities result in convection or stretching of the vortex. This, then causes the shedding of the vortices.

We also show comparison of Mach contours structure (Figure 4-7), with the published result from [82] at a time of 100 ms.

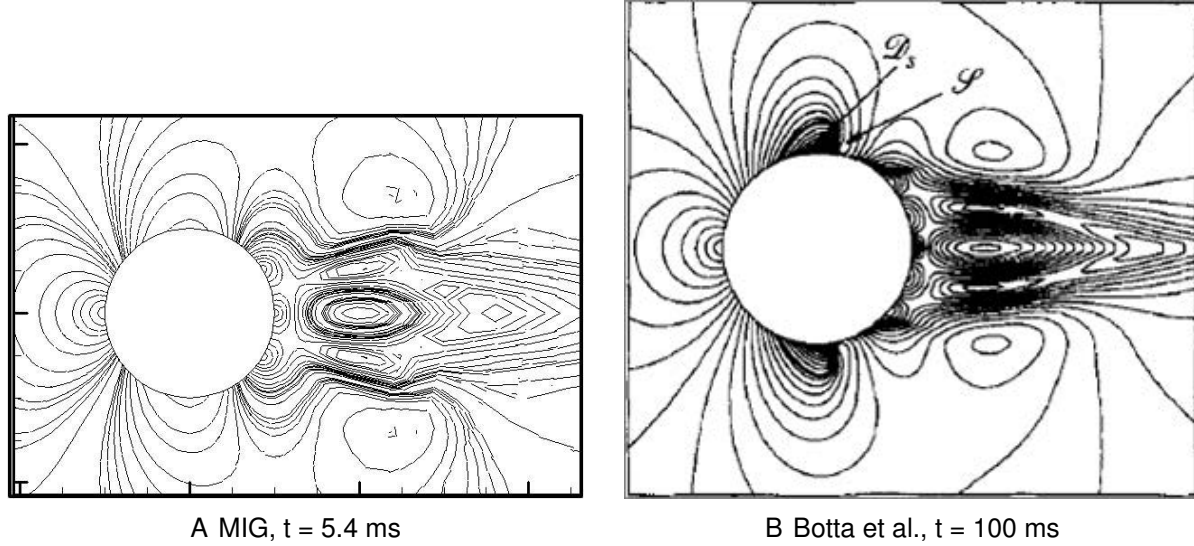


Figure 4-7. Mach contours comparison for $M = 0.5$ flow over cylinder. A) MIG results at $t = 5.4$ ms. B) Results from Botta et al. [82] at $t = 100$ ms.

In Figure 4-7, we use DG method for our results and Botta et al. uses Finite Volume or FV method, which is DG method with $p = 0$ (or first order approximation). Mesh used in [82] is also finer than ours close to the cylinder. Botta et al. shows a solution at 100 ms in comparison to our solution at 5.4 ms. The features are closest to the reported results at this time, though not exactly the same. Contours on front portion are similar, but at the back end, we see some differences in the solution.

4.1.4 Double Mach Reflection

So far we have tested the code for weak shocks of Mach number less than 2. To test the code for a strong shock problem, we choose double Mach reflection problem. In this problem, the Mach number of the traveling shock is 10. This shock hits a wedge inclined at an angle, α , with the x-axis. The wedge acting as a reflecting wall, causes the

shock to reflect off the leading edge of the wedge, resulting in a complex interaction of Mach stem, reflected shock and the incident shock.

The cartesian grid can be fixed to the wedge, and hence in rectangular domain (Figure 4-8), the shock is now at an angle of α with the x-axis. Thus, the incoming flow hits the wedge also at an angle of $-\alpha$ and will reflect off at the incident point.

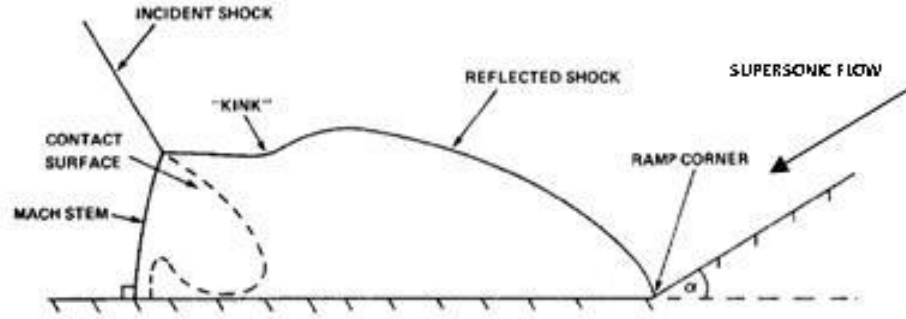


Figure 4-8. Schematic of 2-D double mach reflection problem.

For boundary conditions, and domain information please refer to [83]. Since this problem has a strong shock, and we are not using artificial dissipation in our scheme, we get overshoots and undershoots across the shock; this causes the density and total energy to take negative values near shock. In our code, we limit values of density and total energy to their minimum (physically) possible values. By this, we have been able to get results for $p = 1$ (linear polynomial approximation) for DG method. For higher p (≥ 2), the jumps across shock become steeper and causes convergence problems.

We show results obtained with $p = 0$ and 33,000 element in Figure 4-9. This gives us a good physical understanding of different flow features in this problem. The domain size considered is $3.3 \text{ m} \times 1 \text{ m}$, and the solution is seen at $t = 0.2 \text{ sec}$. Details of this problem can also be found in [4].

Looking at contour plots in Figure 4-9, we find that the high speed flow is highly compressed at the intersection of reflected shock and the reflecting wall. This is seen in Figure 4-9 A with higher density of nearly 18 units in comparison to 8 units. This density slowly merges into free-stream density value at the region between contact discontinuity

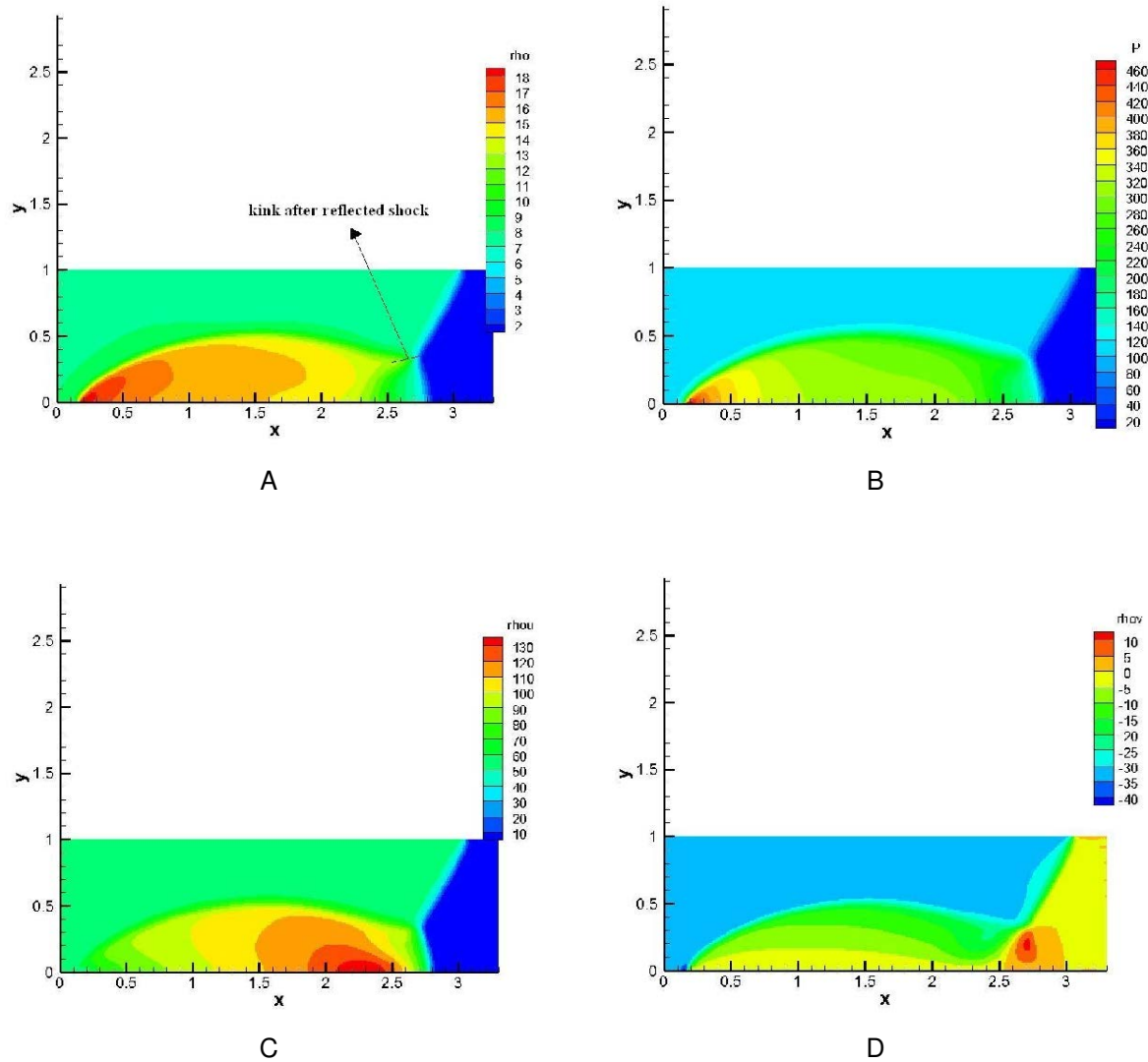


Figure 4-9. Results for double Mach reflection with $p = 0$ and 33,000 elements. A) Density contours at $t = 0.2$ sec shows that density is compressed when high speed flow hits the reflecting wall. B) High pressure region is thus, created at the intersection of the reflected shock with the wall. C) A jet is formed due to the high pressure zone, with velocity higher than the shock speed. This jet impinges the Mach stem, resulting in the convexly shaped Mach stem. D) The high speed jet impinging on the fluid at rest, after the Mach stem, leads to a recirculation of fluid in reference to the incident shock. These results give basic insight into the physics of DMR problem.

and Mach stem. This high compression is also seen in the pressure contour in Figure 4-9 B, where the pressure value is nearly 460 units compared to 116.5 units in the free stream. Uniformly decreasing pressure in the x-direction causes a wall jet in the fluid (Figure 4-9 C) with maximum speed of nearly 13 units. This is higher than the speed of the shock in line with the bottom boundary, which is equal to 11.547 units. Thus, we see that the high speed fluid is impinging the Mach stem, resulting in a convex Mach stem.

The recirculation region (Figure 4-9 D) results from the lifting of the fluid, close to the wall, by the wall jet hitting the fluid at rest. The recirculation region is defined in relation to the fluid velocity in the free stream. We also note that the results for $p = 0$ have large numerical diffusion, as can be noticed from the results in Figure 4-9. The kink after the reflected shock in Figure 4-9 A is also not finely resolved. In addition, the contact discontinuity between the kink and the Mach stem is also not clearly visible. These results are improved with $p = 1$ method, which has low numerical diffusion in relation to the case with $p = 0$. In Figure 4-10, we show zoomed-in sections of density and pressure contours noticing the clearly visible and well resolved kink and contact discontinuity.

We also found during the simulations of this problem for $p \geq 1$, that the order of Gaussian quadrature for performing area integration of a 2-D elements has to be the same to the order of Gaussian quadrature for doing the edge integration of the same 2-D element. If this is not followed, then the error in integration can cause the solution to grow unbounded and cause unphysical features that can destroy the solution.

Contact discontinuity is identified by the discontinuity in the density and continuity in in pressure. Whether the feature seen in Figure 4-10 is purely numerical or has some physical significance has to be further investigated. This feature is due to higher x-velocity produced (Figure 4-10 C), with value around 16 units higher than 13 units for fluid close to the wall (where jet velocity is maximum) for $p = 0$ case.

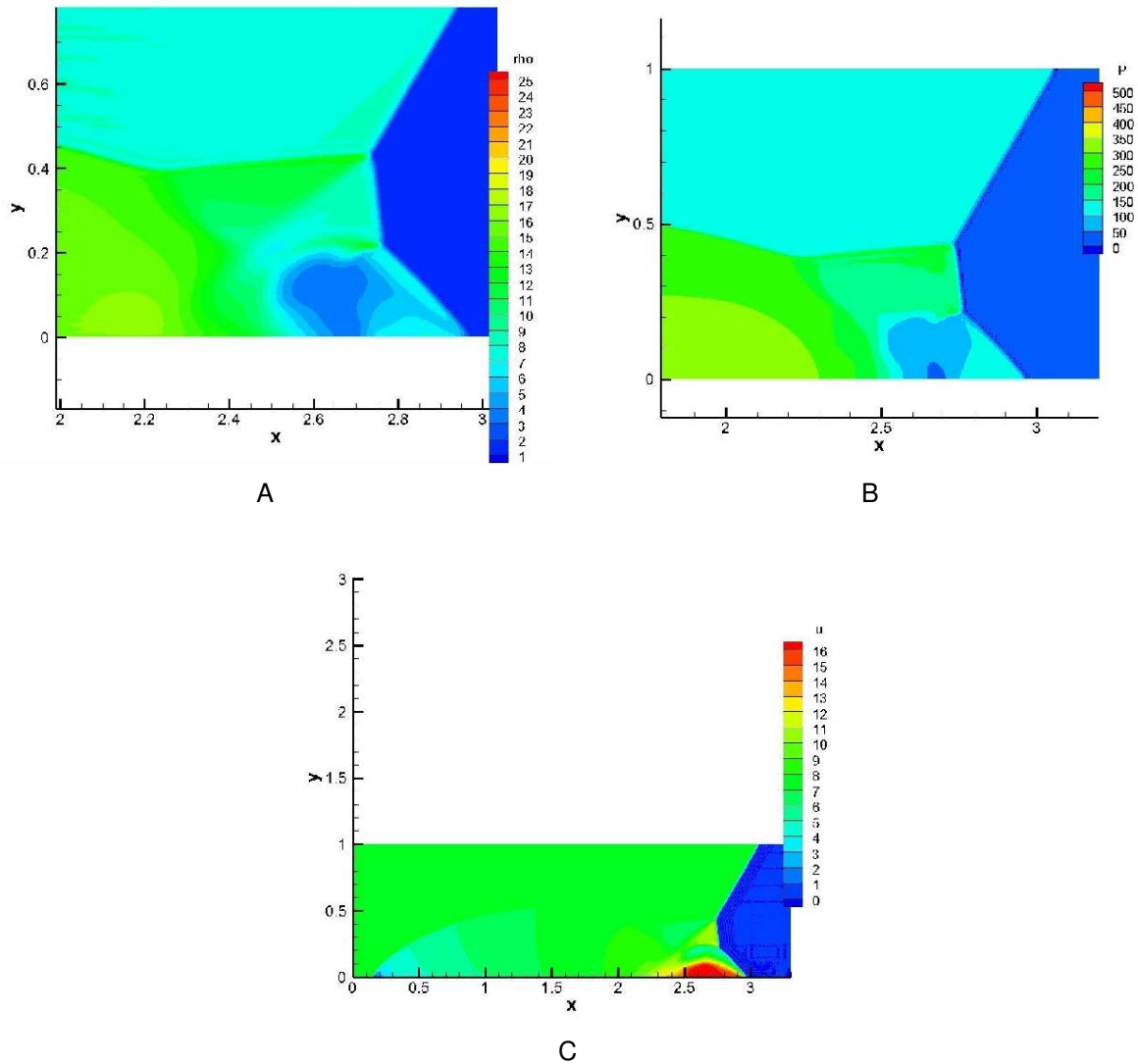


Figure 4-10. Results for double Mach reflection with $p = 1$ and 33,000 elements. A) Zoomed-in section of density contours at $t = 0.2$ sec. B) Zoomed-in section of pressure contours at $t = 0.2$ sec. Contact discontinuity is identified by seeing the discontinuity in density in the region between the kink (after reflected shock) and the Mach stem, and continuity in pressure in that region. Mach stem is convexly curved close to the incident shock. C) High speed fluid impinges the Mach stem producing a convexly curved Mach stem. The maximum velocity in the region of fluid jet is nearly 16 units, which is higher than the case with $p = 0$.

Improvement of our results with finer mesh resolution is shown in Figure 4-11. Density contours are shown for five different meshes, 40×10 , 80×20 , 160×40 , 330×100 and 660×200 elements. The features of reflected and incident shock, Mach stem and especially the region between kink after reflected shock and Mach stem are very well resolved with the finer mesh of 132,000 elements and $p = 1$.

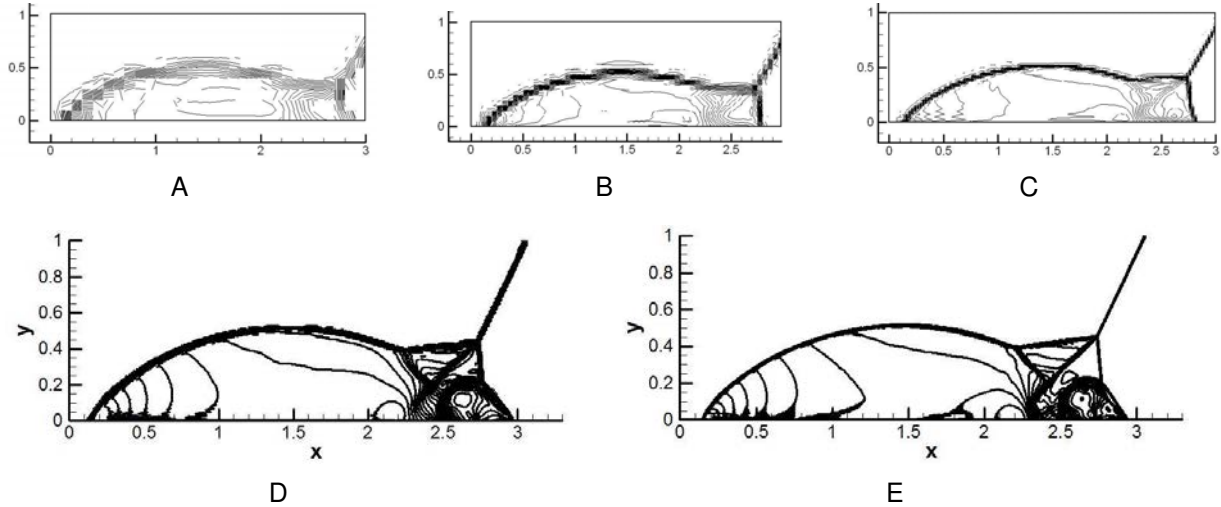


Figure 4-11. Density contours for $p = 1$ and five different meshes. A) 40×10 , B) 80×20 , C) 160×40 , D) 330×100 and E) 660×200 meshes. The regions of reflected and incident shock, Mach stem, and the region between kink and Mach stem becomes better resolved as the mesh is made finer. Total 30 levels of contours are shown. They are equally spaced between density values of 2 and 20 units.

4.2 Viscous Flow

After testing the inviscid cases with some of the standard problems, we now test viscous terms in this section. Our first problem deals with the dampening of the amplitude of two counter-rotating vortices. Here the inviscid terms have no role to play and hence the whole shear effect has to come from viscous terms. So, this is the basic testing for the viscous terms.

After this, we test our code for problems with gradually increasing complexity. Next problem is Rayleigh flow in an impulsively started plate. This problem reduces to a very simple diffusion equation (which has an exact solution) and hence tests the

code for viscous terms in the x and y directions separately. This problem has solution variation only in one direction, i.e. y. Flat plate flow, is more complex in that it has solution variation in both x and y directions, and hence tests the capability to capture the phenomena correctly in x and y directions. This problem also has an exact solution.

4.2.1 Taylor Vortex

This is a problem of counter rotating vortices present everywhere. It has periodic boundary conditions and thus we can avoid boundary conditions. So, we simply test the basic scheme of the DG method for the viscous terms.

Domain for this problem is 1×1 . Initial condition for this problem is as follows,

$$U = \begin{pmatrix} \rho \\ \rho u \\ \rho v \\ \rho E \end{pmatrix} = \begin{pmatrix} 1 \\ -\cos(2\pi(x + 0.25)) \sin(2\pi(y + 0.25)) \\ \sin(2\pi(x + 0.25)) \cos(2\pi(y + 0.25)) \\ \frac{P}{\gamma-1} + \frac{1}{2}\rho(u^2 + v^2) \end{pmatrix} \quad (4-9)$$

Here, P is given by,

$$P = 101325 \text{ Pa} - 0.25\rho \cos(4\pi(x + 0.25)) \cos(4\pi(y + 0.25)) \quad (4-10)$$

and, γ is 1.4. From this problem, we found that explicit treatment of correction terms in BR2 is not effective for running the problems at a high timestep. Hence we worked on making our BR2 code totally implicit, which required good amount of work. With earlier explicit treatment of correction terms, r_h , when we ran the Taylor vortex problem with viscosity coefficient of 0.1 (for heavier damping of the vortex amplitudes), we ran into divergence issues for the code. In order to check the BR2 scheme in the code, without the implicit jacobian terms, we first ran this problem explicitly with $\Delta t = 10^{-6}$ sec. Figure 4-12 shows the result at a total time of 0.1 sec, compared to initial solution at $t = 0$ sec,

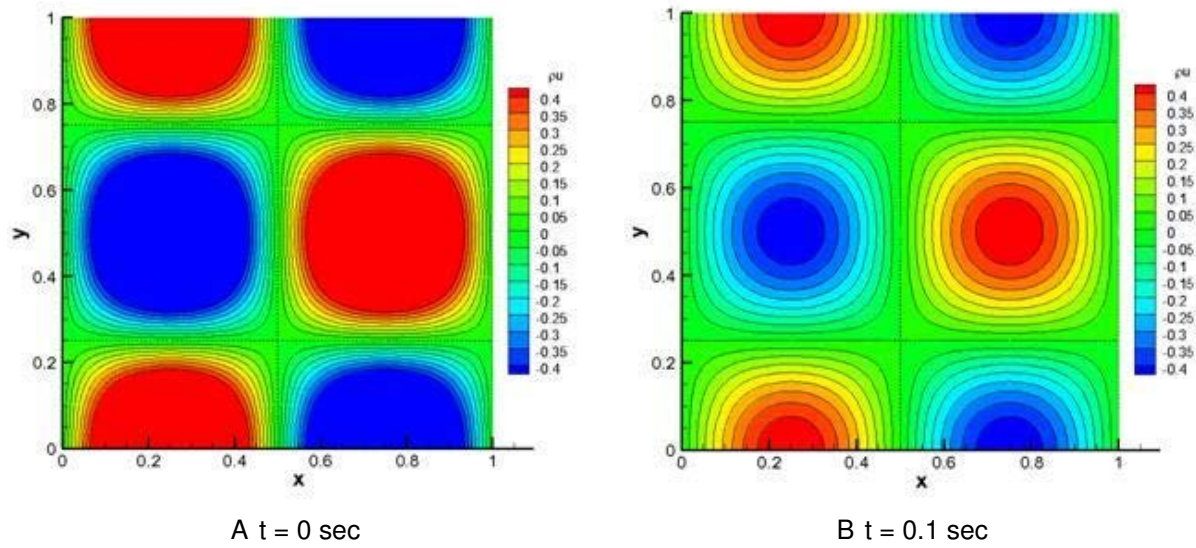


Figure 4-12. Taylor Vortex problem. A) Contours of ρu , shown at $t = 0$ sec (initial solution). B) Contours of ρu shown at $t = 0.1$ sec. These results are obtained using explicit time integration scheme with $\Delta t = 1.0 \times 10^{-6}$ sec.

The mesh for Taylor vortex problem shown in Figure 4-12, uses 100×100 elements. No dispersion effect is seen. Based on net analytical dissipation, velocity amplitude should be $\exp(-8\pi^2\nu t) = 0.45404$, and our amplitude is 0.451324. Additional amplitude damping can be attributed to numerical dissipation of the scheme. It is to be noted that this BR2 scheme is with global corrections, hence is exactly same as BR1 scheme, only with a faster performance. We can also see small effect that inviscid terms have on the solution.

By running the simulations without the inviscid terms, and seeing the 3D plots for solution of ρu with and without inviscid terms (Figure 4-13), we understand that inviscid terms are acting in this problem, and without inviscid terms, there are jumps in the solution in between the elements.

Also amplitude of ρu in Figure 4-13 A is 0.453815, as opposed to 0.451324 in comparison to the exact solution of 0.45404. Thus, we find there is very minimal numerical dissipation of viscous terms themselves, and the BR2 scheme as proposed is very similar to BR1 scheme.

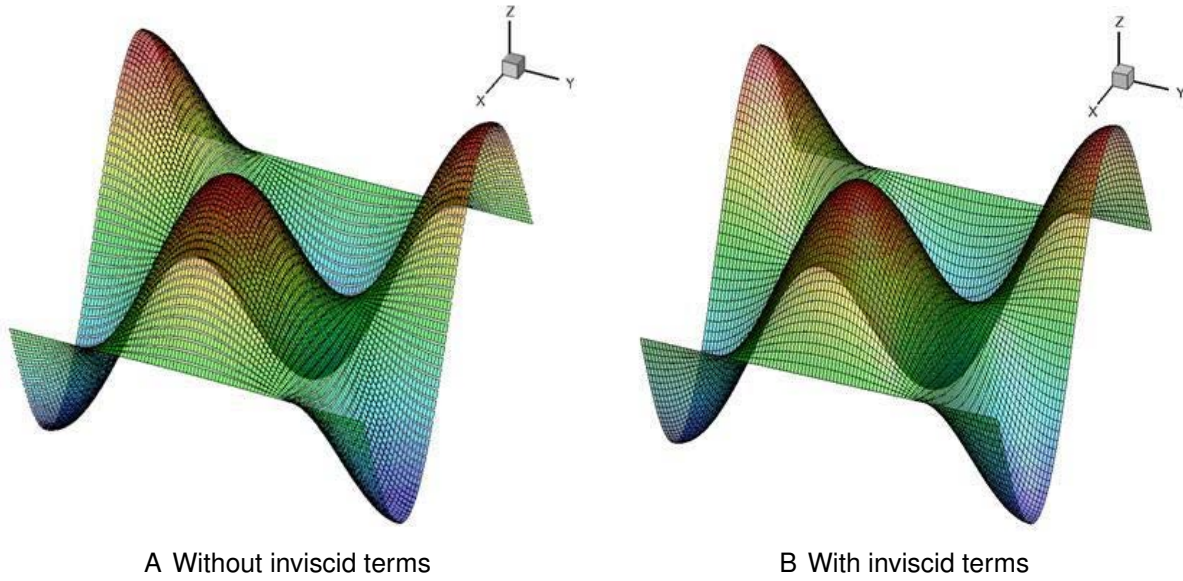


Figure 4-13. Taylor Vortex problem: 3D contour plots of x-momentum. A) Results with no inviscid terms activated. B) Results with inviscid terms activated. Without the inviscid terms, the inter-element jumps (seen as gaps) are visible in the solution. These jumps are no longer visible, however, when the inviscid terms are activated.

Dissipation error of viscous terms is very minimal, close to the central difference scheme in finite difference, and the dispersion error is not visible. For running the simulations with higher time step, fully implicit BR2 with local corrections are implemented that gives much better performance than the BR1 scheme.

4.2.2 Rayleigh Impulsively Started Flow

This problem tests the code for viscous terms in the presence of the inviscid terms. An impulsively started plate in a quiescent viscous fluid causes fluid particles near the plate, at $t = 0$, to accelerate under the effect of shear forces. With time, this effect is felt farther and farther away from the plate, which induces more and more fluid to move along with the plate.

As the plate moves at $t = 0$, the fluid (being ideal), next to the wall, also moves along with the plate at the speed of the wall. Assumption of incompressible fluid and no dependence of fluid motion on the x direction, leads to $v = 0$ (i.e. no y -velocity). Thus

examining y-momentum equations, we find that the pressure is not a function of the y direction. Hence the pressure is a constant. Under these conditions, the fluid equations simplify to the following parabolic equations.

$$\frac{\partial u}{\partial t} = \nu \frac{\partial^2 u}{\partial y^2} \quad (4-11)$$

The exact solution for this problem is a self similar solution given by,

$$\frac{u}{U} = \text{erf}(\eta) \quad (4-12)$$

$$\eta = \frac{y}{\delta} \quad (4-13)$$

$$\delta = 2\sqrt{\nu t} \quad (4-14)$$

For the simulation purpose, we consider the plate to be a stationary wall at $y = 0$. The fluid is considered to be uniformly moving at a given velocity, U at $t = 0$. We choose a rectangular domain, with left and right sides having periodic boundary conditions. Bottom wall has no slip boundary conditions (i.e. $u = v = 0$) and the top edge of the domain is considered to have floating boundary condition (i.e. no gradient in the y-direction at the top edge). Thus, this problem is exactly the Rayleigh impulsively started flat plate problem, where the frame of reference is attached to the moving plate.

We examine our results with BR1 and BR2 schemes for the viscous terms, and also do a convergence study with different orders of accuracy. The flow Mach number is 0.3.

For starting mesh, we consider 3×60 elements, with finest mesh at the wall having 10^{-5} m thickness. Having a coarser element at the wall leads to convergence problems at the start of the solution. Flow solution ($u = U$) immediately sees the wall ($u = 0$) and develops strong discontinuity, that causes convergence problems in the beginning of the simulations. Results for BR1 scheme, with and without the inviscid terms, are shown in Figure 4-14.

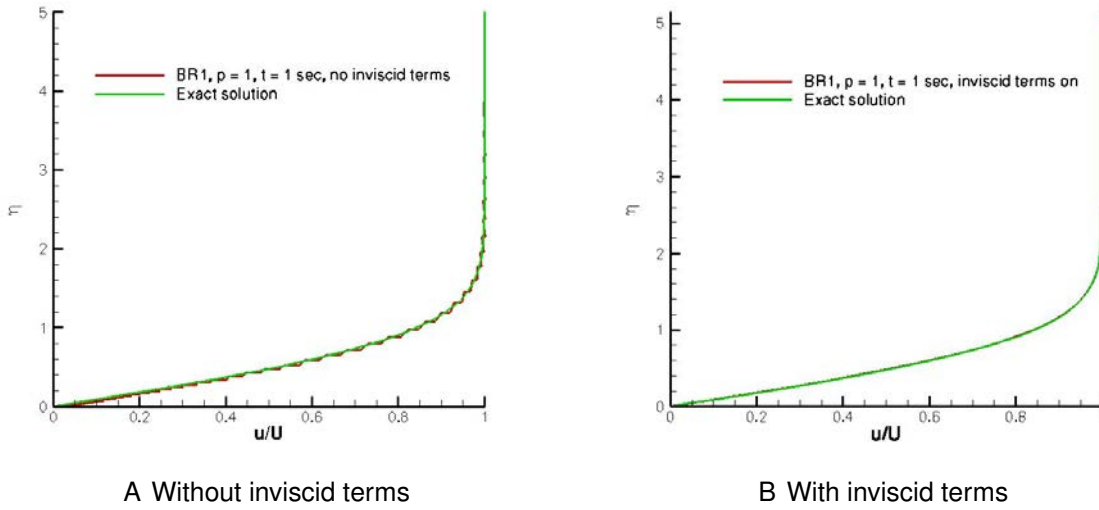


Figure 4-14. Rayleigh problem: Effect of inviscid terms on BR1 solution. A) Simulation result with no inviscid terms activated, shows inter-element jumps. B) Simulation result with inviscid terms activated show no inter-element jumps. These results are shown at a total time of 1 sec.

It is seen in Figure 4-14, that BR1 scheme with $p = 1$ is not able to remove inter-element jumps, which are incorrectly taken care of by the inviscid terms. Rayleigh problem is a purely viscous problem. Hence inviscid terms have no role, and their effect on the solution is inconsistent with the governing physics. This affects the inside solution and the solution at the boundary. This problem is taken care of by using the pressure normal contribution at the boundary, but at the inside domain, the viscous scheme is expected to smooth out such inter-element jumps. These inter-element jumps are found to disappear when using BR2 scheme (with local contribution for r_h) and $p = 1$ (Figure 4-16). For BR1 scheme, this happens when using $p = 2$ or quadratic basis function (Figure 4-15).

4.2.3 Flat Plate

Flat plate is a typical problem to check the viscous part of the code. The problem details are given in Figure 4-17,

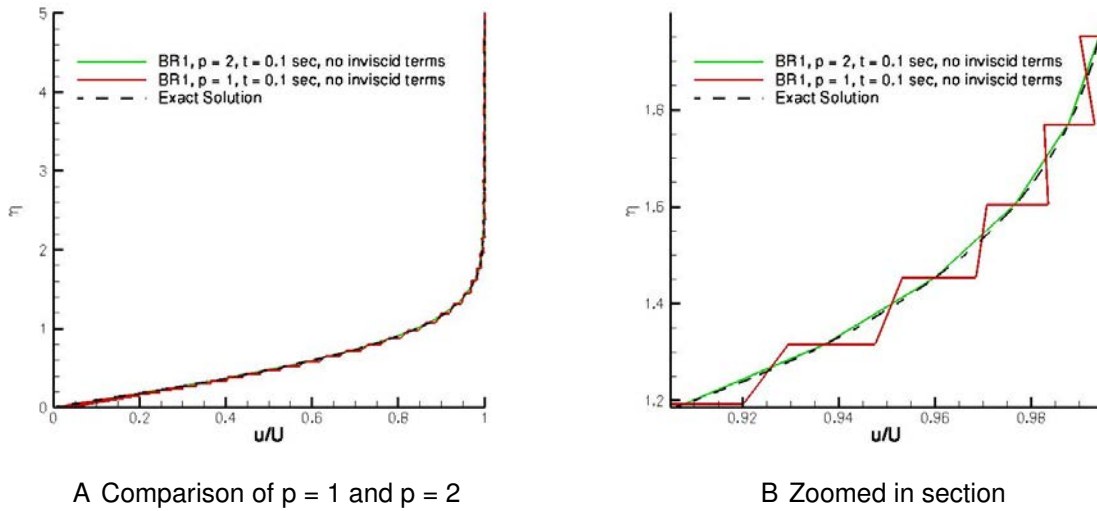


Figure 4-15. Rayleigh problem: Comparison of $p = 1$ and $p = 2$ using BR1 scheme. A) Comparison of solutions with $p = 1$ and $p = 2$. The simulation time is 0.1 sec. Inviscid terms are turned off in this case to isolate the effect of BR1 scheme on the solution. Inter-element jumps observed with $p = 1$ are no longer observed with $p = 2$. (B) Zoomed in section provides a more clear picture of this effect.

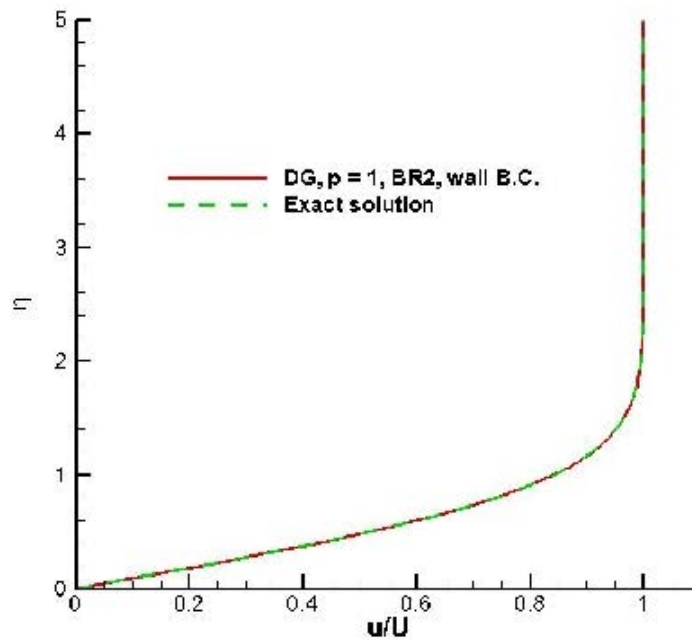


Figure 4-16. Rayleigh problem using BR2 and $p = 1$. Inter-element jumps are no longer visible.

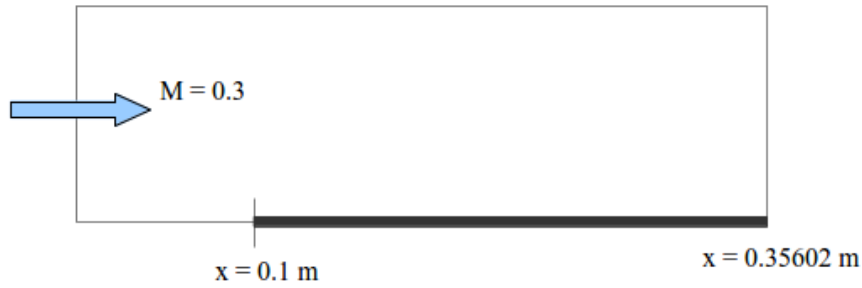


Figure 4-17. Schematic of flat plate problem. Flow Mach number is 0.3. Total domain size is 0.35602 m, the plate begins at $x = 0.1 \text{ m}$, and the total plate length is 0.25603 m.

This is Mach 0.3 flow over the flat plate. The freestream density is 1.17659 kg/m^3 and the freestream velocity is 104.165 m/s . The boundary conditions are as follows,

Left side: Freestream inlet boundary condition.

Top side and right side: Pressure outflow condition, with fixed freestream pressure = 101325 Pa .

Bottom side (before plate): symmetric in y direction.

Bottom side (after plate): Wall boundary with $u = v = 0$ and density taken from inside element and total energy fixed at $P/(\gamma - 1)$

For inviscid terms at the bottom boundary, pressure normal contribution is used. We present results with both BR1 and BR2 schemes. If we do not use pressure normal contribution for the inviscid flux, but instead use $\alpha (U_b - U_n)$ for the inviscid flux at the bottom boundary, we get results that do not match up with Blasius profile given in Figure 4-18.

Using correct application of boundary conditions at the wall for inviscid terms, we get more accurate comparisons of C_f profiles shown in Figure 4-19.

Using BR2 scheme, we obtain much accurate C_f profiles (Figure 4-20).

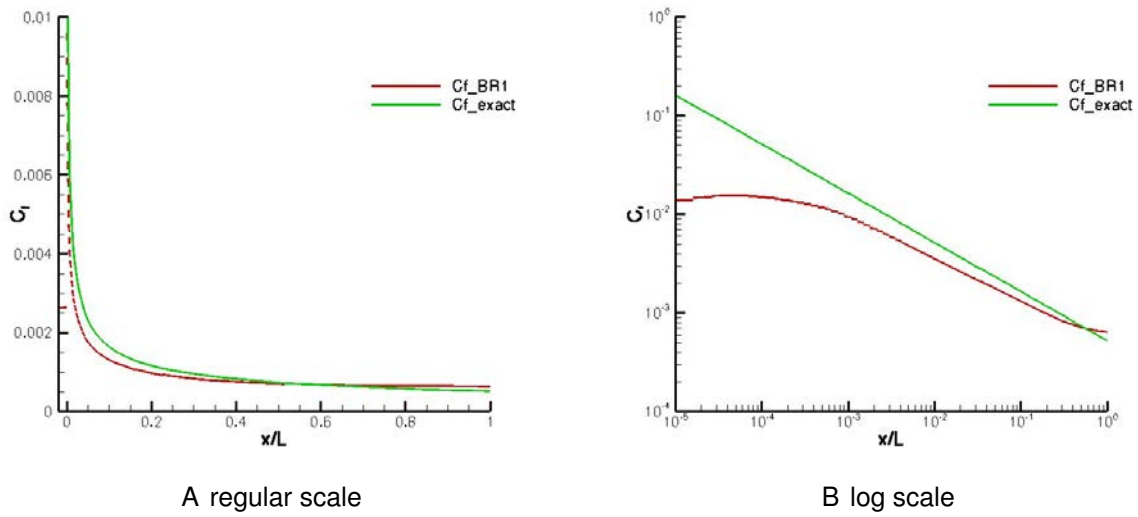


Figure 4-18. Flat plate solution with BR1 scheme and incorrect boundary condition. A) C_f plot in regular scale. B) C_f plot in log scale. MIG solution is compared to the exact Blasius profile. Deviation from exact solution is significant because of incorrect application of boundary condition for the inviscid terms.

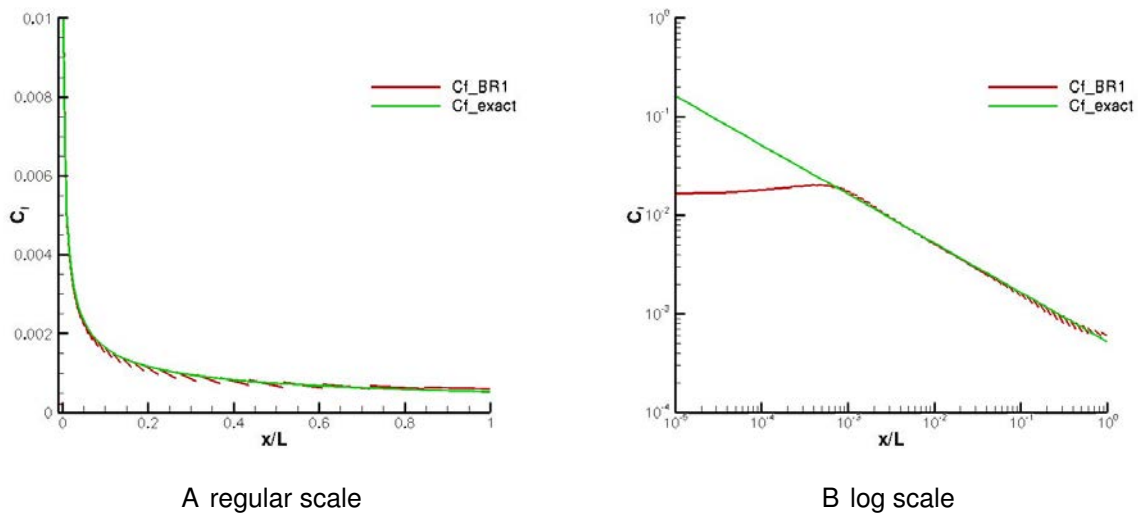
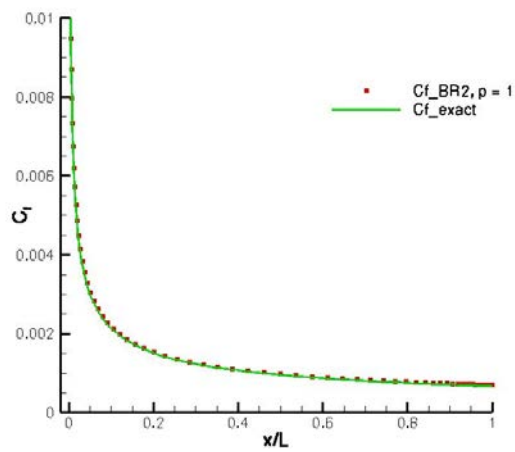
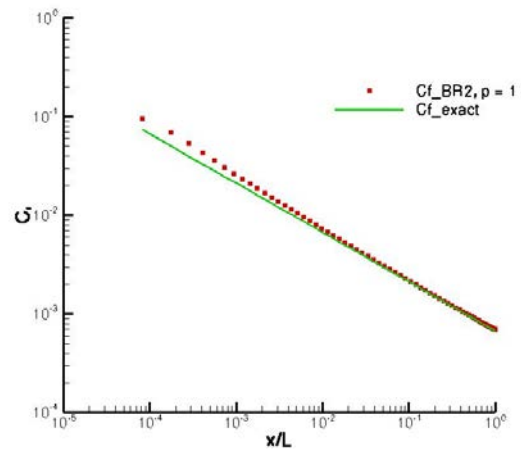


Figure 4-19. Flat plate solution with BR1 and correct boundary conditions for inviscid terms. A) C_f plot in regular scale. B) C_f plot in log scale. MIG solution compares well to the exact Blasius profile.



A regular scale



B log scale

Figure 4-20. Flat plate solution with BR2 and correct boundary conditions for the inviscid terms. A) C_f plot in regular scale. B) C_f plots in log scale. MIG solution compares very accurately to the exact Blasius profile.

CHAPTER 5

THERMAL ABLATION TEST CASES

In this chapter, we present some test cases that were attempted with DG method after having demonstrated solution capability for inviscid and viscous flow problems in Chapter 4. Our attention herein, is on solving the thermal response of a charring ablator. We choose three test cases,

- An arc-jet case by Ahn & Park [15], with carbon phenolic as TPS material
- Ablation test sample from 4th AF/SNL/NASA Ablation Workshop, Albuquerque, NM
- Langley arc-jet test case

A charring ablator like carbon phenolic leads to generation of pyrolysis gases, which flows through the porous ablating material and affects overall heating of the material.

As mentioned earlier, one of the first material thermal response codes, CMA, does not take into account the flow of pyrolysis gas through the ablating material. This assumption is valid for high heating rate entries, but not for low to moderate heating rate environments. This was the case for Pioneer Venus probes which went on their mission in 1978 [15]. This mission had four probes, which all entered into the atmosphere of Venus, sending back the data of thermocouple temperatures to Earth. Wakefield and Pitts, 1980 [15] tried to reconstruct this data using CMA. They first tested the code with some arc jet cases, which accurately matched the experiment results.

However, when an attempt was made to reconstruct the temperature plots, their results showed very high temperature rise for the thermocouples. This was contrary to the flight data obtained from the thermocouples (Figure 1-5). This anomaly in the results was attributed, in 1998 by Ahn et al. [36], to the lack of modeling of the flow of the pyrolysis gas through the ablating media. As already noted, the codes like CMA considered the pyrolysis gas to leave the material instantly, upon its production. Their

thermocouple temperature reconstruction were closer to the actual data points received from the probes.

We try to compare our results with 1-D arc jet data that was obtained experimentally by Wakefield and Pitts and numerically solved by both [15] and [36].

5.1 1D Arc Jet Cases from Ahn & Park

Wakefield and Pitts, tested CMA code for carbon phenolic material by running some test cases in an arc jet heating facility, also known as Ames Advanced Entry Heating Simulator [84]. In this test facility, a test sample is exposed to a combined, yet mutually independent convective and radiative heating. Test sample is placed in centerline of a supersonic flow heated by an electric arc, and radiative heating is focused at the test sample by using argon arc radiation source and arc-imaging optics. A schematic from [84] is shown in Figure 5-1.

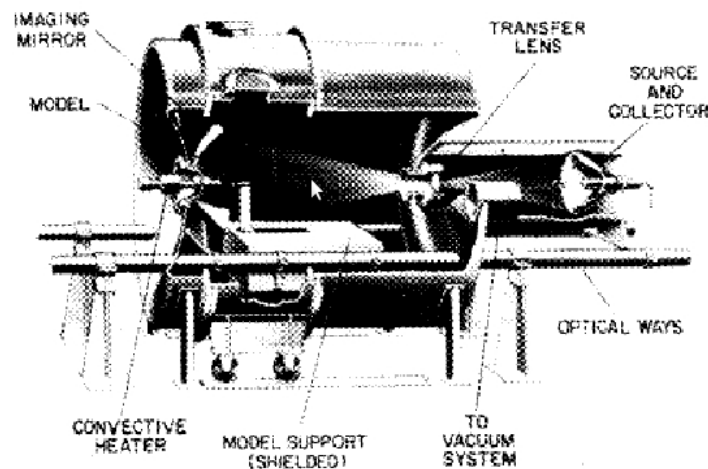


Figure 5-1. Advanced Entry Heating Simulator. Test sample is placed in the center line of supersonic flow from left side, heated by electric arc, and radiative heating from right side is focused on test sample using argon arc radiation source and arc-imaging optics [84].

Here, the test sample is made of carbon phenolic and is exposed to a series of tests, (i) convective heat transfer of 1400 W/cm^2 , (ii) combined convective heat transfer of 1400 W/cm^2 and radiative heat transfer of 2300 W/cm^2 , and (iii) radiative heat

transfer alone of 600 W/cm^2 . Total time for exposure for these tests is 4-5 sec. For convective heating of 1400 W/cm^2 , surface pressure on the test sample is 0.22 atm and flow enthalpy is 23.3 KJ/g. These tests were close to actual flight heat fluxes and served to test the working of the code by Wakefield and Pitts.

5.1.1 Material Properties of Carbon-Phenolic

Carbon phenolic has two components, phenolic resin and graphitic carbon. The resin component undergoes decomposition with rise in temperature, and releases a mixture of gases called pyrolysis gas. The rate of decomposition of the resin component, R , expressed as an Arrhenius equation is written in terms of temperature, T and resin density, ρ_r in Eq. (5-1),

$$R = \sum_{k=1}^N \left(-\frac{B_k}{T} \right) \rho_v \left(\frac{\rho_r}{\rho_v} \right)^n \quad (5-1)$$

Here, ρ_v is the density of virgin material. This expression was evaluated in many previous works and also given in [36]. Here $N = 2$, and n is also taken to be a constant equal to 2. Activation Energy, B_k is taken to be 3544 and 19680 K for $k = 1$ and 2 respectively and constants A_k are 677 and $1.64 \times 10^9 \text{ s}^{-1}$ for $k = 1$ and 2 respectively.

Thermal conductivity and specific heat were measured experimentally in [15], and are given in Figure 5-2. The expressions were curve fitted, and are given in Eq. (5-4). As indicated in [15], these properties are measured for the virgin material from 250 K to 480 K and for the char material from 250 K to 3000 K. The temperature range for virgin material was taken before the onset of pyrolysis.

$$C_{p_c}(T) = c_1 z^4 + c_2 z^3 + c_3 z^2 + c_4 z + c_5 \text{ J/kg} - \text{K} \quad (5-2)$$

$$C_{p_r}(T) = 1174 \text{ J/kg} - \text{K} \quad (5-3)$$

$$\log_{10}(k(T)) = -6.5 \times 10^{-8} T^2 + 5 \times 10^{-4} T - 0.1 \quad (5-4)$$

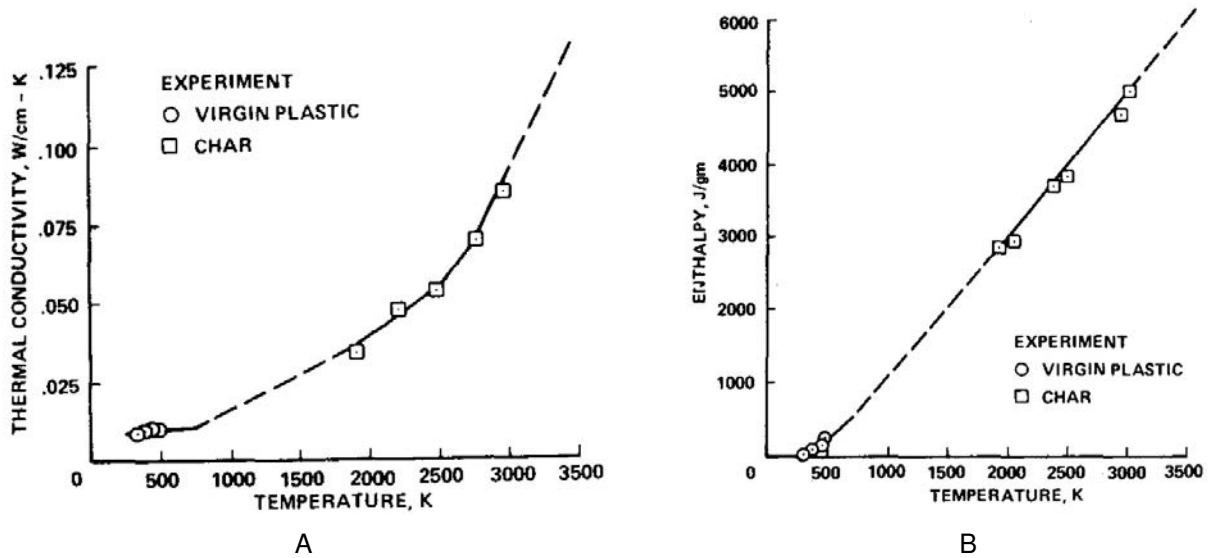


Figure 5-2. Material properties of carbon phenolic. A) Thermal conductivity of carbon phenolic for virgin plastic and char material as given in [15]. B) Enthalpy of carbon phenolic. Properties for virgin plastic were measured from 250 K to 480 K and for char from 250 K to 3000 K.

The virgin and char density are given to be 1490 kg/m^3 and 1240 kg/m^3 respectively. The elemental composition of the resin material is given as C: 1.3527, H: 6.4557, O: 1 by mole. Heat of formation for carbon-phenolic was given to be 372 J/g. Governing equations for 1-D thermal ablation are used for the results shown.

5.1.2 A Comment on Governing Equations Used in This Work

Here, we use governing equations used by Ahn et al. in their two papers [36] and [17]. We will refer to them as 1998 and 2002 paper respectively, in this work to highlight the modeling differences in both the papers. These equations include the decomposition of the resin material and the energy balance in both the char and resin material. This is the norm in many thermal response codes, as noted in Chapter 1. Most thermal response codes with the exception of SCMA (by Ahn et al.) and a series of papers by Martin et al. and Amar et al. [32, 33, 44, 53], do not take into account the flow of pyrolysis gas through the ablating medium.

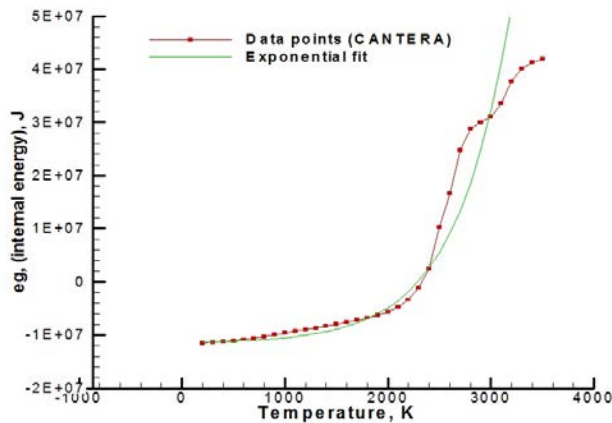
Hence, any cooling by flow of pyrolysis gas is neglected resulting in over-prediction of temperature distributions in the ablating material. This will result in a conservative design of TPS, which will not be cost effective. Papers by Martin et al., consider the role of pyrolysis gas in Energy equation, but the flow velocities are evaluated using Darcy's equation or Forchheimer correction (for non-Darcy flows). But, for our work, we solve for a conservation equation for mass, momentum and energy balance for the pyrolysis gas. The governing equations are given in Chapter 2.

5.1.3 Pyrolysis Gas Modeling

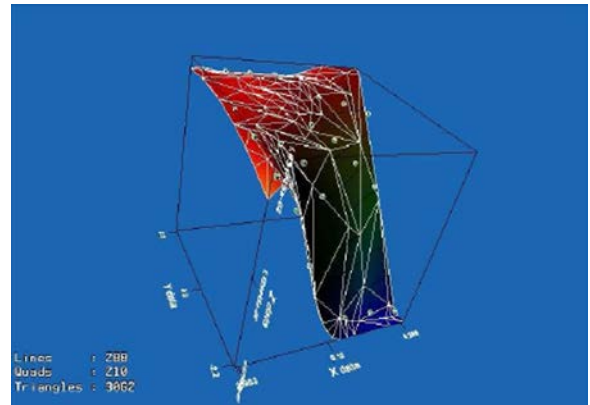
Resin material undergoes decomposition and produces a mixture of gases, known as pyrolysis gas. 14 gas species are considered, C, CH, CH₂, CH₃, CH₄, CO, CO₂, C₂, C₃, H, HO, H₂O, O, and O₂. These are assumed to be at thermal equilibrium at solid material's temperature and pressure inside, i.e. the gas gets sufficient time to absorb all possible energy from the solid, after it exits to atmosphere.

CANTERA [85], a thermochemical solver is used to evaluate thermodynamic properties of gas like molecular weight, internal energy, pressure etc as a function of temperature and gas density. Initial composition of the gas for calculation purposes is taken to be same as resin material, C: 1.3527, H: 6.4557, O: 1. The input to CANTERA for all thermodynamic calculations is through a CTI file, and properties like specific heat, enthalpy, and entropy are specified as functions of temperature, in terms of NASA polynomials, for each of the components of the pyrolysis gas. For non-equilibrium analyses, reactions and their rates (in Arrhenius coefficients) can also be specified in this CTI file. An equilibrium criterion is set to be at constant temperature and pressure. Figure 5-3 shows the plots of internal energy, e_g , as a function of temperature and molecular weight, MW, as function of gas density and temperature.

The data points for both e_g and MW are exponentially fitted and their expressions are given in Eq. (5-6). It is essential to get a plot that grows monotonically and avoid any discontinuity in the gradients of these properties. The expression of e_g , was obtained



A



B

Figure 5-3. CANTERA plots for the pyrolysis gas. A) Plots for internal energy, e_g , as a function of temperature, T . Red line indicates data points from CANTERA and green line is curve fitting using TECPLOT. B) Molecular weight of gas, MW represented by z -axis in terms of gas density, ρ_g , represented by y -axis and temperature, T , represented by x -axis. The data was obtained from CANTERA [85], and surface fitting was done through online software [86].

using TECPLOT, while 3D data for MW (in terms of temperature and density) was curve fitted using an online software [86]. We used second order polynomial in logarithm (of base 10) in density and fourth order polynomial in temperature. X -axis, in Figure 5-3 B, is from 2.952 to 9.288, which stands for temperature, y -axis is from -2.2 to 2.2, which stands for $\log_{10}(\rho_g)$ and z -axis is from $4.872e-3$ to $1.8317e-2$, which is for molecular weight, MW of gas in kg/mol. CANTERA can also be used for including the effects of chemical reactions in the flow solver.

We have used two curve fits for internal energy, e_g . In Figure 5-3 A, we fitted the data points with one single exponential curve for whole range between temperatures of 200 K and 3400 K, but this curve underpredicts internal energy for the temperature range of 2400 K to temperature range of 3000 K and then overpredicts for the rest of the range. For temperature range below 3000 K, this underprediction of internal energy is significant, and will result in lower cooling provided by the flow of gas, therefore for more accurate prediction we choose second curve as shown in Figure 5-4.

$$e_g = \exp(A_1 T + A_2) - A_3 \quad (5-5)$$

$$MW = B_1 \exp(y) + B_2 \exp(x) + B_3 \exp(x) \exp(y) + B_4 \quad (5-6)$$

Here, $A_1 = 1.869 \times 10^{-3}$, $A_2 = 11.98$ and $A_3 = 1.156 \times 10^7$. For the expression of the molecular weight, MW in Eq. (5-6), x and y depend on the temperature and the gas density respectively as, $x = (T/1000)^2$ and $y = \log_{10}(\rho_g)$, and constants are $B_1 = 1.7981 \times 10^{-4}$, $B_2 = -1.333 \times 10^{-6}$, $B_3 = 2.0159 \times 10^{-7}$, and $B_4 = 1.678 \times 10^{-2}$.

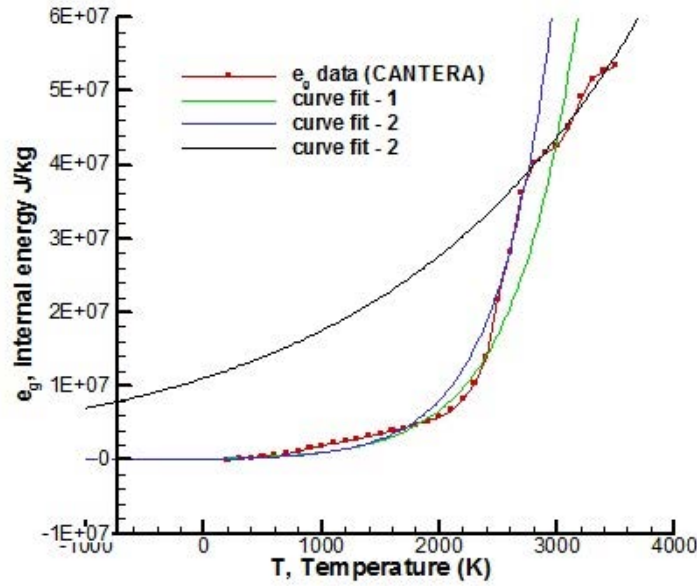


Figure 5-4. Second curve-fitting for internal energy of the pyrolysis gas. e_g is expressed in terms of temperature, T . Black curve is used from 2800 K to 3400 K and blue curve is used from 200 K to 2800 K.

5.1.4 Boundary and Initial Conditions

Total grid size is taken to be 1 cm, and the inner boundary is fixed at $x = 0$ cm and outer boundary at $x = 1$ cm. Boundary conditions are as follows. No boundary conditions are needed for the first equation of Eq. (2-64), since it is a pure unsteady differential equation. For the second equation of Eq. (2-64), no boundary conditions for $\epsilon \rho_g$ are specified at $x = 0$ cm. At $x = 1$ cm, $\epsilon \rho_g$ is found by solving the state equation, i.e.

molecular weight as a function of $\epsilon\rho_g$ and T , which basically relates pressure, gas density and temperature. Pressure at $x = 1$ cm, is given to be 0.22 atm (arc jet case in [15] and [36]), and temperature will be known by solid's temperature. For the third equation of Eq. (2–64), u is taken to be 0 m/s and adiabatic boundary condition for temperature exists at $x = 0$ cm for fourth equation.

At $x = 1.0$ cm, first equation of Eq. (2–64), as mentioned, does not need a boundary condition. Boundary condition for the second equation is already specified. No boundary condition is applied on velocity at $x = 1.0$ cm. For temperature, an incoming heat flux (in the negative X direction) of 1400 W/cm^2 is specified. Initial conditions are uniform throughout the domain for all 4 variables; ρ_r is 250 kg/m^3 , $\epsilon\rho_g$ is $6.05 \times 10^{-3} \text{ kg/m}^3$ (evaluated at $P = 0.22 \text{ atm}$, and $T = 300.0 \text{ K}$), u is 0 m/s and T is 300.0 K.

5.1.5 Results

Wakefield and Pitts conducted an arc jet wind tunnel experiment with the carbon-phenolic sample, which was exposed to a heat flux of 1400 W/cm^2 . They compared their results with CMA simulation, and these results were also published by Ahn and Park. Total run time for the problem is 5 sec, and surface pressure and enthalpy at the exit are 0.22 atm and 23300 J/g. Total thickness of model domain is 1 cm.

Here we consider two cases, by Ahn and Park in their 1998 and 2002 papers. Differences in both cases were noted in Chapter 1. First we present results for case with $D = 0$, which was considered in the 1998 paper. In Figure 5-5 A and B, we show spatial distribution of solution variables at a time of 4 sec. From Figure 5-5 B, we can see from plot of resin density that pyrolysis zone extends from 2 mm to 4 mm. Other two regions that can be identified are virgin plastic ($\rho_r = 250 \text{ kg/m}^3$) and char zone ($\rho_r = 0 \text{ kg/m}^3$).

Pressure varies from a value of nearly 8 atm in the region of virgin plastic, where it is flat, to as low as 0.1 atm on the right side of domain. High pressure gas gradient is observed at the pyrolysis zone, but the gas flow is actually driven by the gradient of product of gas pressure, P and void fraction, ϵ . This is seen in the jump of velocity

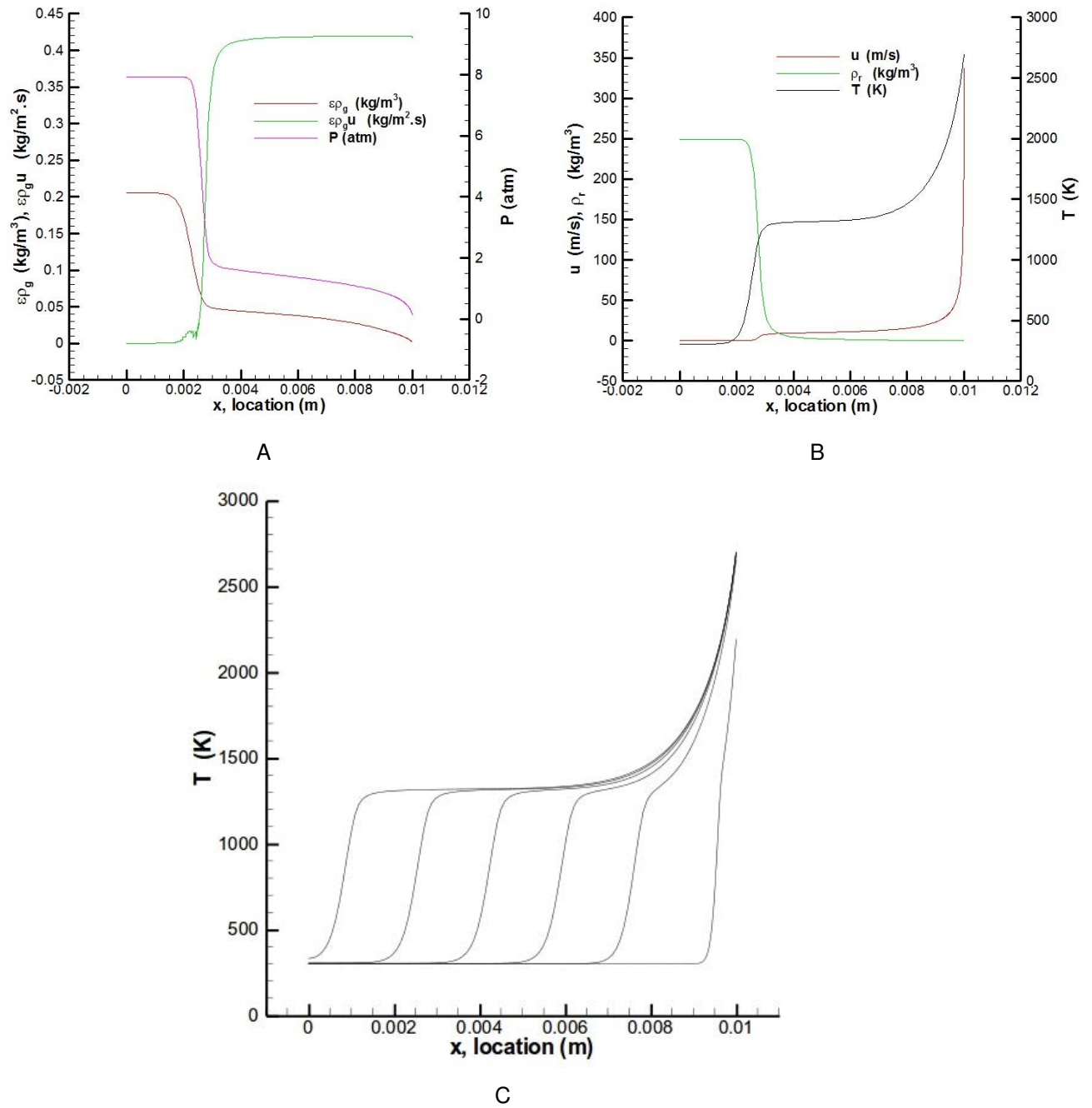


Figure 5-5. Results for thermal ablation with diffusion coefficient, $D = 0$. A) Plots of gas density, flux and pressure are shown at $t = 4$ sec. B) Plots of gas velocity, resin density and total temperature are shown at $t = 4$ sec. C) Temperature distribution plotted at time = 0.1, 1, 2, 3, 4, and 5 sec to show the cooling effect of pyrolysis gas.

magnitude at the pyrolysis zone, and higher velocities are attained at the right boundary due to a steeper gradient of ϵP . We also observe some numerical artifacts on solution of gas momentum, since gas momentum has friction which acts as a dominant source term. We also observe cooling effect of pyrolysis gas from these plots.

In Figure 5-5 B, temperature profile of the material has a steeper gradient at the beginning of pyrolysis zone at around 2 mm, as compared to elsewhere in domain. There are two heating mechanisms in the domain, thermal conduction and convection cooling. In beginning of pyrolysis zone, we only observe thermal conduction, whereas at other places we observe both convection cooling and conduction. This explains the observed temperature distribution and the trend of thermal response can be seen in Figure 5-5 C, where we see that a steep rise in temperature is slowed down by the convection cooling of the exiting pyrolysis gas.

And, based on our calculations, we observe that increase in the pyrolysis gas density in the virgin plastic zone is due to the resin decomposition term, R , which also leads to corresponding gas generation. But temperature at virgin zone is 300 K, so value of R should be very close to zero, which is not the case with model chosen in Ahn et al. This tells that gas generated due to pyrolysis primarily leaves out to the atmosphere.

Both friction and inertia terms in 2002 paper provide resistance to gas flow, so if their values are higher than in 2002 paper (this is exactly the case with 1997 paper) they would provide sufficient resistance to the flow, which would lead to significant rise in values for gas density in virgin plastic domain. We also observed a difference in results shown in Ahn and Park in their two papers for the result of gas pressure for the day probe. Pressure in the virgin plastic domain for 1997 paper is nearly 75.67 atm, and that in 2002 paper is nearly 30 atm at flight time = 27 sec. We investigate this difference in the two models between the two papers.

In Figure 5-6, we compare our results for temporal variation of the surface temperature (on the right side of the domain). We provide results for our simulation

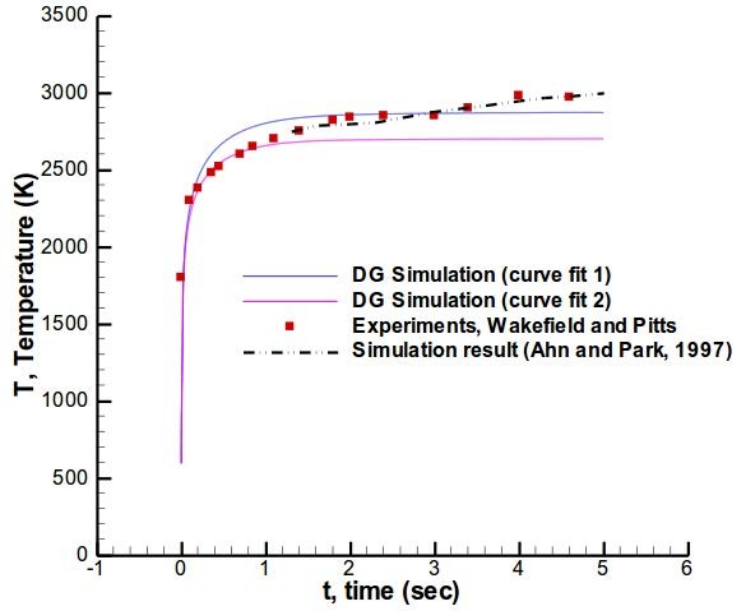


Figure 5-6. Temporal variation of surface temperature for $D = 0$. Comparison is made with Ahn and Park simulations [36] and experimental results [15].

for both curve fit - 1 and curve fit - 2 for internal energy, e_g . As already mentioned, curve fit - 2 is more accurate than curve fit - 1. Hence, we find our results to match the experimental results for initial 1 sec. After 1 sec, there is no further rise in the observed temperature due to high gas velocity, which leads to high cooling at the surface. This exactly balances out the net heat influx to the surface and thermal conduction.

Second case, we present is with nonzero diffusion term in Eq. (2-64). This case is exactly similar to Ahn and Park, 2002. Shown in Figure 5-7, are the results for solution variables at time of 4 seconds, to highlight the differences in both the models of 1998 and 2002 paper. Diffusion term, in the momentum equation, is related to the second derivative of pressure. This term results in more diffused profile for the gas density. Pressure is related to the gas density and the temperature, and both are more diffused out, which causes a lower pressure (actually ϵP) gradient that drives the flow. Therefore, we get lower gas momentum near the exit, as compared to the case with $D = 0$. Therefore, we find these results to be consistent with the basic gas dynamics.

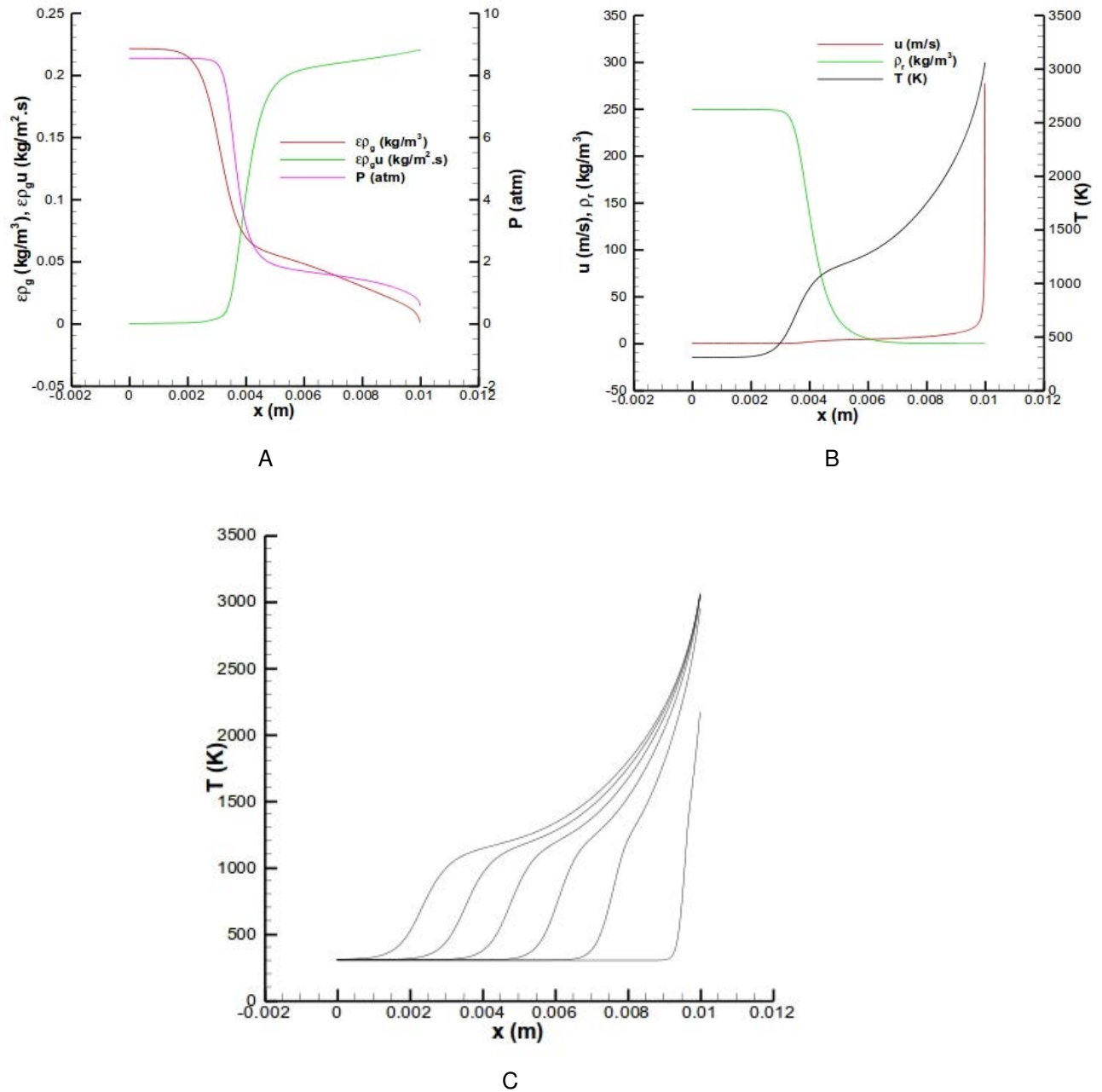


Figure 5-7. Results for thermal ablation and nonzero diffusion coefficient. A) Plots of gas density, flux and pressure are shown at $t = 4$ sec. B) Plots of gas velocity, resin density and total temperature are shown at $t = 4$ sec. C) Temperature distribution plotted at time = 0.1, 1, 2, 3, 4, and 5 sec to show the cooling effect of the pyrolysis gas. As compared to the case with $D = 0$, all the profiles are more diffused, and the pyrolysis front also travels with slower speed.

Due to the diffusion term, the gas velocity is lower. This causes lower cooling as compared to case with $D = 0$. Therefore, we observe diffused temperature profile in this case. This, in turn, affects the decomposition of the resin material and we see a broader pyrolysis zone in this case, which extends roughly from 3 mm to 7 mm. This diffusion mechanism is, in general, better for the vehicle's body, since it provides for more time that the vehicle gets before its temperature starts to increase. E.g. temperatures above 500 K are observed at location of 2.25 mm for earlier case ($D = 0$) and for this case at location of 3.17 mm at time of 4 sec. There is no significant difference in pressure for both cases, pressure in this case is approximately 0.5 atm higher than that of case-1. Velocities in the domain, for this case, are lower as compared to the case with $D = 0$. Therefore, we have lower cooling within the domain. Since, heat conduction is a diffusion mechanism, we also observe more diffused profiles for temperature. From temperature profiles, we can infer which effect is dominant, conduction or convective cooling.

In Figure 5-8, the temporal variation of surface temperature is compared from simulation results from MIG, Ahn and Park, 2002 and experimental results by Wakefield and Pitts, 1980. Again, the results are plotted for both curve fits-1 & 2 (for internal energy). Our surface temperature shoots to higher value, at a later time than the experimental results. Reason for this, as already explained, is lower cooling for this case. Given our lack of clarity about some aspects of their model, our plot is close to experiment results.

We also compare result for the mass loss of TPS material, with the simulation results shown in 2002 paper, and our results are close to their results with an over prediction error of 3.2 % . The experiment results differ from the simulation results by a constant. The reason for this is ascertained to be mass loss that occurred while the test sample was moved from edge of the stream (in arc jet wind tunnel) to center of the streamline and while removing the sample from the center of streamline. The fact that

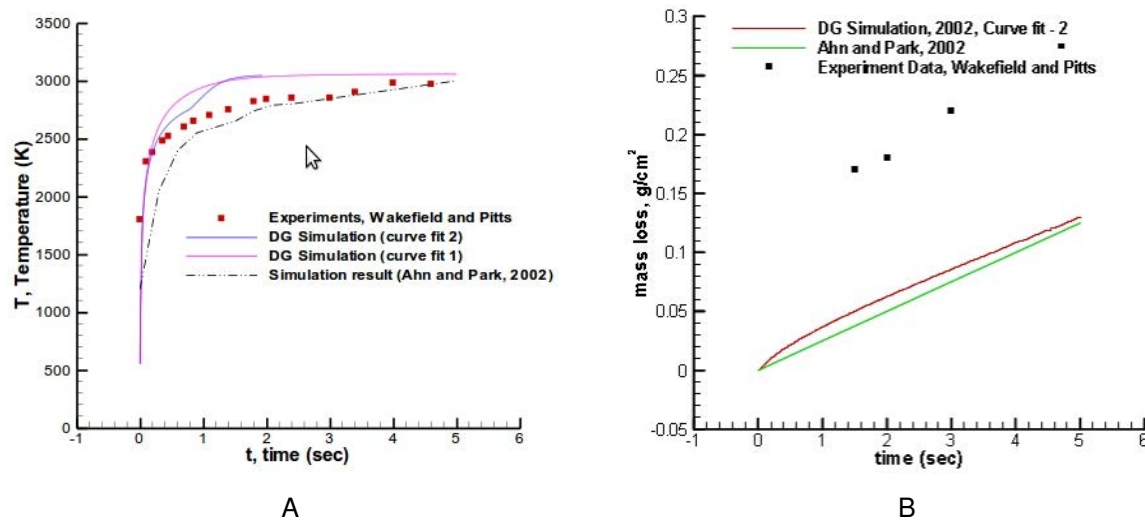


Figure 5-8. Surface temperature and mass loss comparison for non zero diffusion. A) Temporal surface temperature variation for non-zero D and 2002 paper. B) mass loss comparison with 2002 paper and experimental results. Mass loss in our simulations is over-predicted by an error of 3.2 %

both experiment and simulations have same slope, indicates that mass loss predicted by the model is accurate.

5.2 Ablation Workshop Cases

In this section, we present results for TACOT case, presented in 4th AF/SNL/NASA Ablation Workshop, Albuquerque, NM for an inter-code comparison exercise. In this workshop, an ablation test case was designed and compared on different ablation codes worldwide. The purpose of the exercise was two folds, to inter-calibrate the similar type codes (code types being identified as type 1, 2 and 3 in the workshop) to compare the numerical methods, their respective merits and weaknesses and how the same input data (provided by the organizers) is interpreted and fed into their respective codes, by the participants.

Second purpose was to compare the outcome of modeling differences used in the different types of codes. Three types of codes were identified as type 1, 2 and 3. Type 1 codes considered basic heat transfer analysis, decomposition of the resin,

equilibrium chemistry for pyrolysis gas and simplified transport for the gas. Type 2 added an average momentum equation for the pyrolysis gas, where type 3 considered high-fidelity physics like non-equilibrium thermochemistry for the gas, in-depth ablation etc.

A theoretical ablative model, titled, TACOT or Theoretical Ablative Composite for Open Testing, was developed with thermo-chemical properties close to those of low density ablators, for meaningful model comparison. Architecture of the material is chosen such that the material can be easily manufactured but is good only for ground testing, and not for actual re-entry flights, so that the scope of this exercise could be broadened to international participation. The material selected for the model was highly porous (80 % porosity), and consisted of 10 % (by vol. fraction) of ex-cellulose carbon fibers coated by a matrix of ex-novolac/formaldehyde polymer, which constitute another 10 % of the volume fraction.

The material densities for both carbon fibers as well as matrix are 1600 kg/m^3 and 1200 kg/m^3 respectively. Thermal conductivity and specific heat of the virgin and char materials, were taken from [34] in this exercise and are plotted with temperature in Figure 5-9. Enthalpies of the char and virgin materials can be calculated from integration of the specific heats, along with formation enthalpies of char and virgin material being 0 J/kg and $-2 \times 10^6 \text{ J/kg}$ respectively (at 298 K). Enthalpy of the material is calculated by considering the material to be mixture of both virgin and char at the temperature of the solid.

For type 2 codes, the porosity of the material is taken to be 0.8 for virgin and 0.85 for char material. Permeability for virgin and char are 1.6×10^{-11} and 2.0×10^{-11} respectively, and were evaluated from the DNS simulation. The products of pyrolysis gas from decomposition of phenolic were obtained from [87] by George F. Sykes, and elemental composition of C, H and O was determined to be, 0.206, 0.679 and 0.115 respectively (mole fractions). The elemental composition of the pyrolysis gas products is

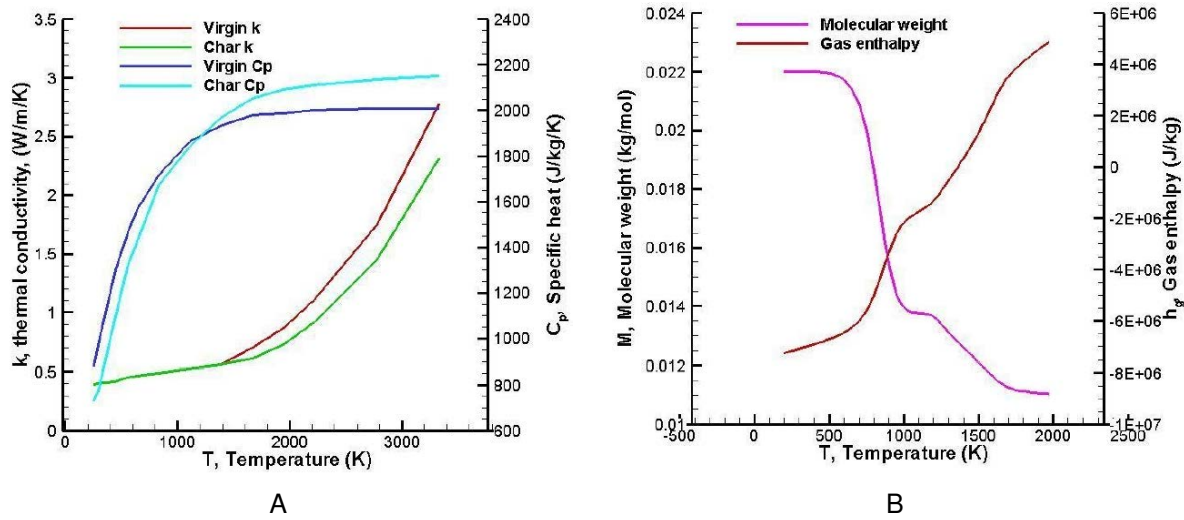


Figure 5-9. Material properties for TACOT. A) Thermal conductivity and specific heat for virgin and char material plotted with temperature. B) Molecular weight and gas enthalpy of the gas using thermo-equilibrium assumption.

used to evaluate the thermal properties of the pyrolysis gas, assuming thermo-chemical equilibrium of the gas at the temperature of the solid material. In Figure 5-9 B, we provide the plots for molecular weight, M and the gas enthalpy for the pyrolysis gas, h_g , based on the thermo-chemical equilibrium assumption. The pyrolysis gas properties are a function of temperature at the pressure of 1 atm.

The domain for the problem is 5 cm; Boundary conditions on right side are known temperature as a function of time, and outside pressure of 1 atm. The right side temperature as a function of time is given in Figure 5-10. Left side of the domain is adiabatic and no flow condition (i.e. $u = 0$) is also considered.

The total run time for simulation is 1 min, and the results from MIG-DG are plotted against the baseline case, run by FIAT, a commercially used NASA material response code. Figure 5-11 shows comparison of the temporal variation of temperatures at the surface and at hypothetical thermocouple locations at depths of 1, 2, 4, 8, 16 and 50 mm. We observe that temperature increases at all depths except 50 mm, which is the left end of the domain and is considered adiabatic. So, we observe that over a period of

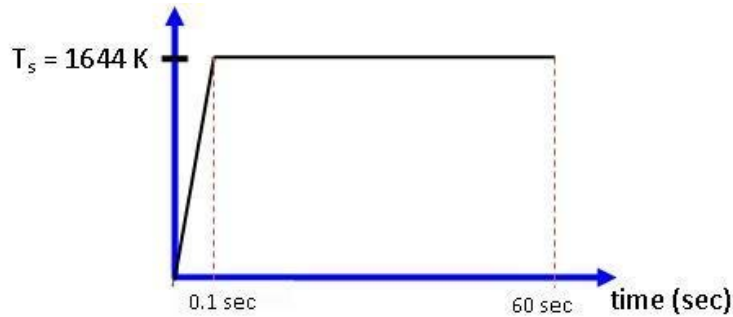


Figure 5-10. Boundary condition for TACOT. Temperature distribution varying as a function of time is applied at the right side of the solution domain.

1 min, the effect of high surface-temperature boundary condition does not reach the left end, which is assumed to be connected to the vehicle's body. Our results are very close to the results of FIAT, for outside thermocouple locations. However, we under-predict the temperatures by around 5 % errors at the more inside thermocouples (at 8 and 16 mm depths). We also show our results for the mass loss rate of the pyrolysis gas at the exit of the domain, and virgin and char depths with time in Figure 5-11 B.

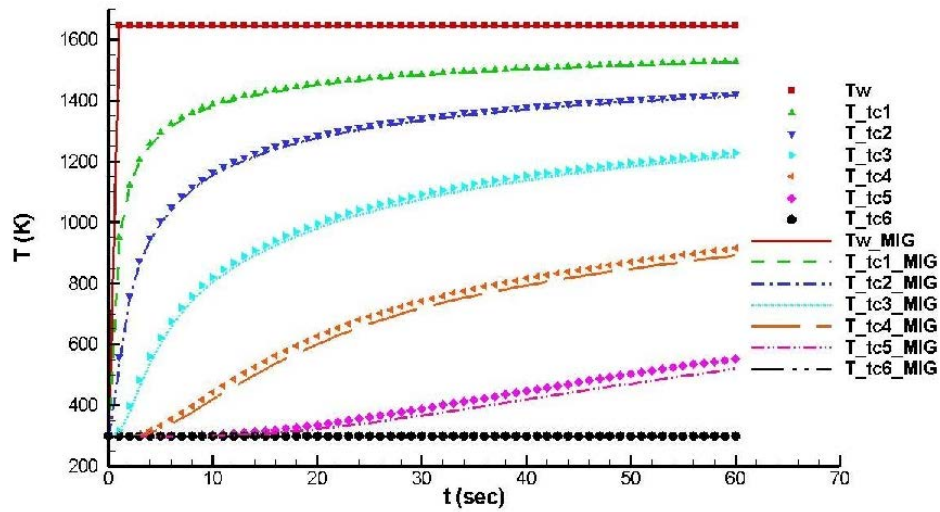
We solve Langley arc jet test case (in section 5.3) to match the experiment results given in [88]. This way, we demonstrate our capability to solve for both thermal ablation and hypersonic flow problems in one single framework.

5.3 Langley Arc Jet Test Case

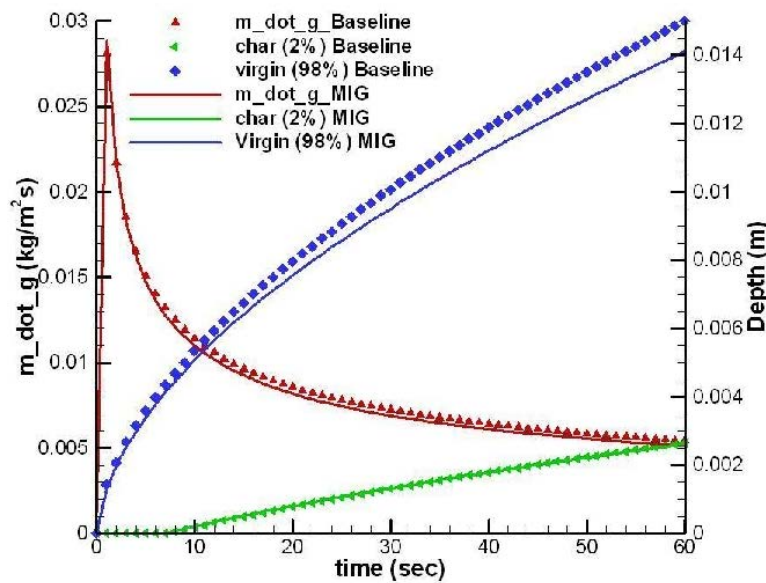
The test sample used in this work, is shown in Figure 5-12. The sample has 1.27 cm of thickness at its centerline, it is axisymmetric with nose radius of 7.98 cm at the stagnation point [88].

We have used different sources for identifying the material properties of the test sample and the pyrolysis gas. We setup this case by using Fay Riddell model, to find the heat flux at the surface, described in the section 5.3.1.

The test sample's geometry allows the problem to be analyzed as 1-D, 2-D and 3-D. The problem nature is essentially 2-D and 1-D is a good approximation as well.



A



B

Figure 5-11. Simulation results for TACOT. A) Comparison of temporal variation of temperature at the surface and at the thermocouple locations of 1 mm, 2 mm, 4 mm, 8 mm, 16 mm and 50 mm, with the reported results from FIAT (in the ablation workshop). Results from MIG agree very closely to the reported results from FIAT. B) Mass loss rate from the exit of the sample to the outside and comparison of char and virgin material depths with time varying from 1 sec to 60 sec.

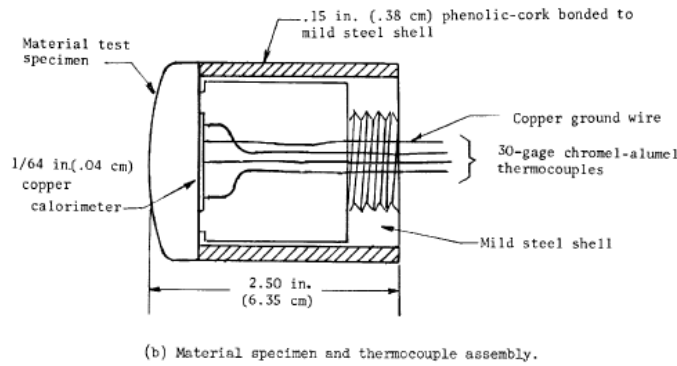
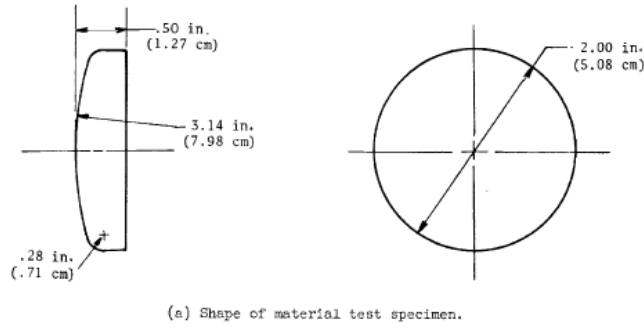


Figure 7.- Model design used in the evaluation of the thermal properties.

Figure 5-12. Langley arc-jet test sample [88].

5.3.1 1-D Ablation Test Case with Fay Riddell Model

For 1-D ablation test case, we take the sample size of 1.27 cm (size of the sample at the stagnation point). Fay Riddell model describes the surface heat flux for given amount of dissociation of the air at the boundary layer edge. Sutton [88] gives the cold heat wall stagnation surface heat flux for this particular test to be 1.45 MW/m^2 . The expression for surface heat flux is given in Eq. (5-7).

$$q''_s = \frac{0.768}{P_r^{0.6}} (\rho_e \mu_e)^{0.4} (\rho_w \mu_w)^{0.1} (H_e - H_w) \left(1 + (Le^{0.52} - 1) \frac{h_d}{H_s} \right) \left(\frac{du}{dx} \right)_e^{0.5} \quad (5-7)$$

The index 'e' denotes the edge of the boundary layer formed on the body in the hypersonic flow, and 'w' denotes the wall or the surface of the body at the stagnation

point. Fay Riddell model is only valid at the stagnation point, hence is useful to predict heat flux at the stagnation point when a flow solver to solve the hypersonic flow outside the body is not present. In our case, Fay Riddell model serves as a useful first step before doing both the flow solver and the ablation in a single framework.

To use the Fay Riddell model, our first objective is to predict the amount of dissociation present in the air at the boundary layer edge, after the flow has moved through the shock into the shock layer. This will be done by matching q_s'' found from Eq. (5-7) to the cold wall heat flux given from the experiment ($= 1.45 \text{ MW/m}^2$). It is also given that the wall is super-catalytic, hence all species present in the flow, close to the wall, must combine into free stream species. Hence at the wall, we will only have O_2 and N_2 . The cold wall temperature is 300 K. The temperature of the gas at the boundary layer edge is found by dividing the stagnation enthalpy by the specific heat for the composition of air at the boundary layer edge. Hence, we can find out the amount of composition of gas in the boundary layer edge for which the heat flux from the Fay Riddell model will match the cold wall heat flux provided from the experiments. Thus, knowing the air composition at the boundary layer, we can employ the Fay Riddell model to predict wall heat flux for the 1-D ablation test case.

Graphs of material properties for both solid and gas, and their curve fits are given in Figure 5-13 through 5-16.

5.3.2 Simulation Results

We present our results for thermal ablation problem for the Langley arc jet test case. We consider first data point in Table IV in Sutton's work [88]. Here, the pressure at the stagnation point of the test sample is 0.07 atm (7091 Pa) and the cold wall heat flux is 1.45 MW/m^2 . Mass fraction of atomic oxygen therein is given to be 0.23, which implies that all of O_2 in the boundary layer edge is oxidized to O. Using this information and varying the mass fraction of atomic N and N_2 at the boundary layer edge, we determine the amount of N in boundary layer edge that gives the Fay-Riddell heat flux at the

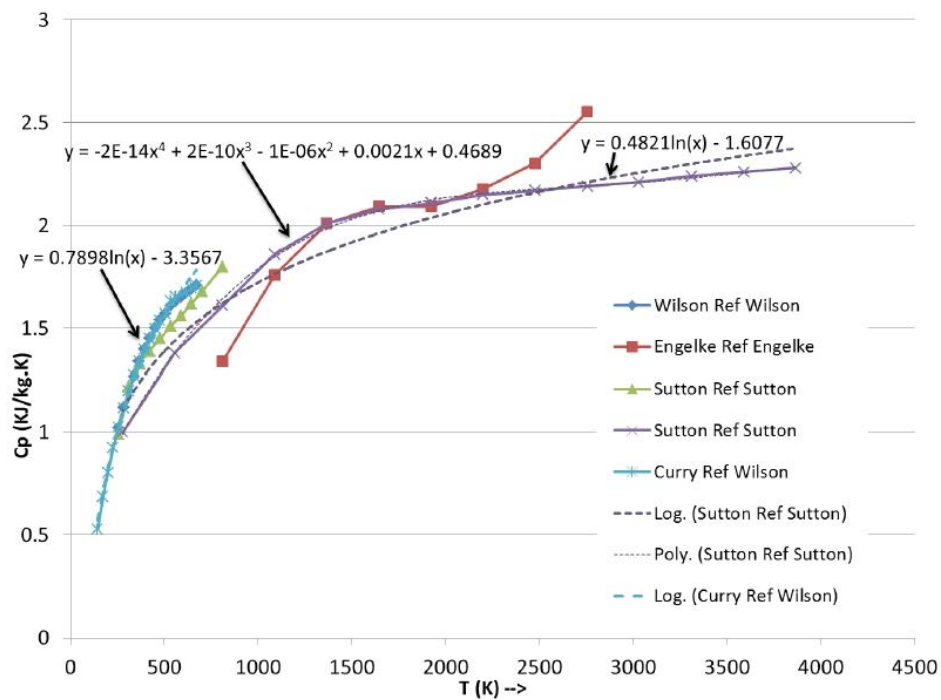


Figure 5-13. Specific heat plots for Narmco 4028. Curve equations are fitted to these data points for use in MIG.

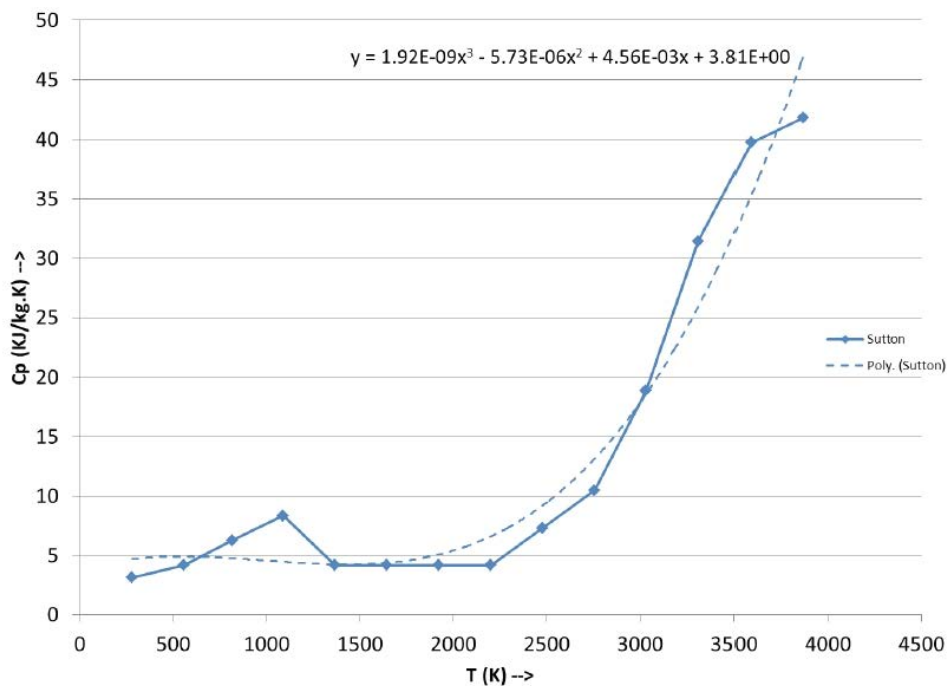


Figure 5-14. Specific heat plot for pyrolysis gas from Sutton. Curve equation is fitted to these data points for use in MIG.

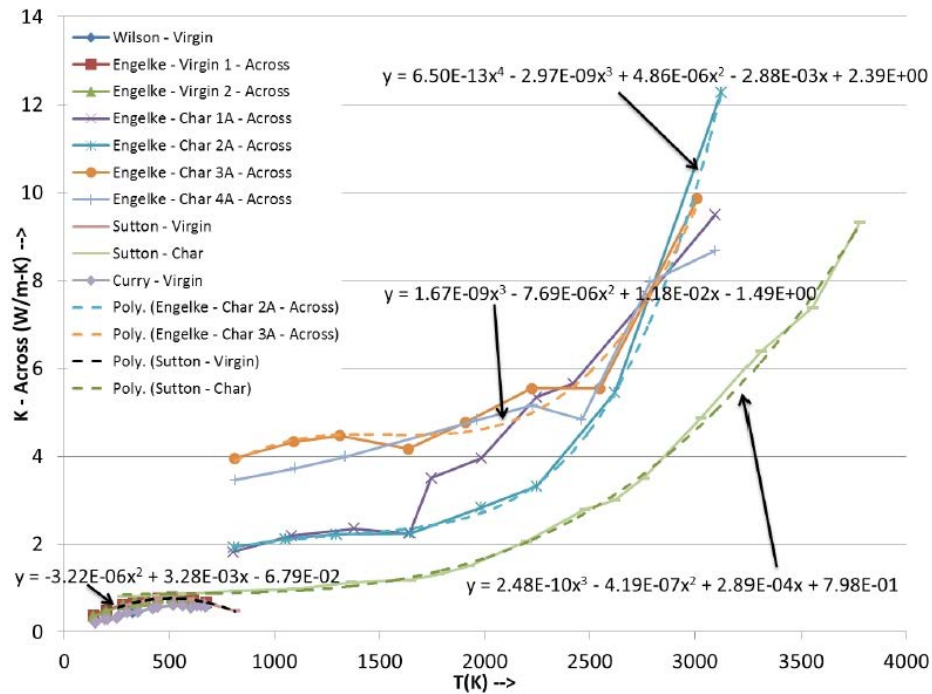


Figure 5-15. Thermal conductivity plots for Narmco 4028 with perpendicular fibers. Curve equations are fitted to these data points for use in MIG.

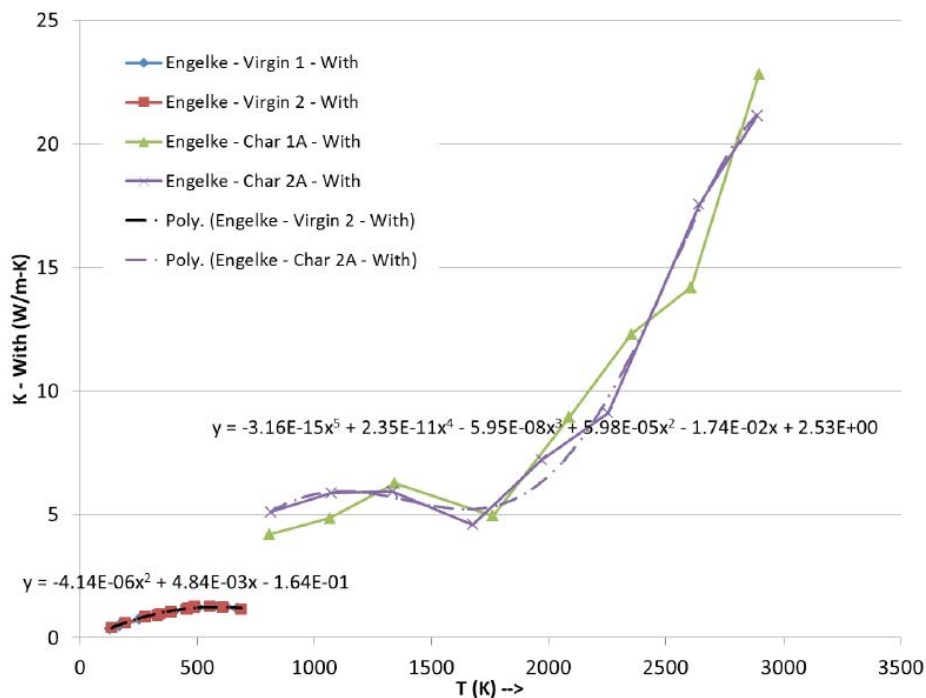


Figure 5-16. Thermal conductivity plots for Narmco 4028 with parallel fibers. Curve equations are fitted to these data points for use in MIG.

stagnation point (at 300 K surface temperature of the stagnation point) to be equal to the given value of the cold wall heat flux of 1.45 MW/m^2 . We get mass fraction of N and N_2 to be 0.47 and 0.3 respectively. Thus, for these given values of gas composition in the boundary layer, we can now use Fay-Riddell heat flux to provide for the heat flux, due to outside hypersonic flow, at the wall as a function of wall temperature.

Using this, we ran 1-D thermal ablation problem and got results shown in Figure 5-17. These are compared to experimental temporal variation of the surface and back-surface temperatures published in [88].

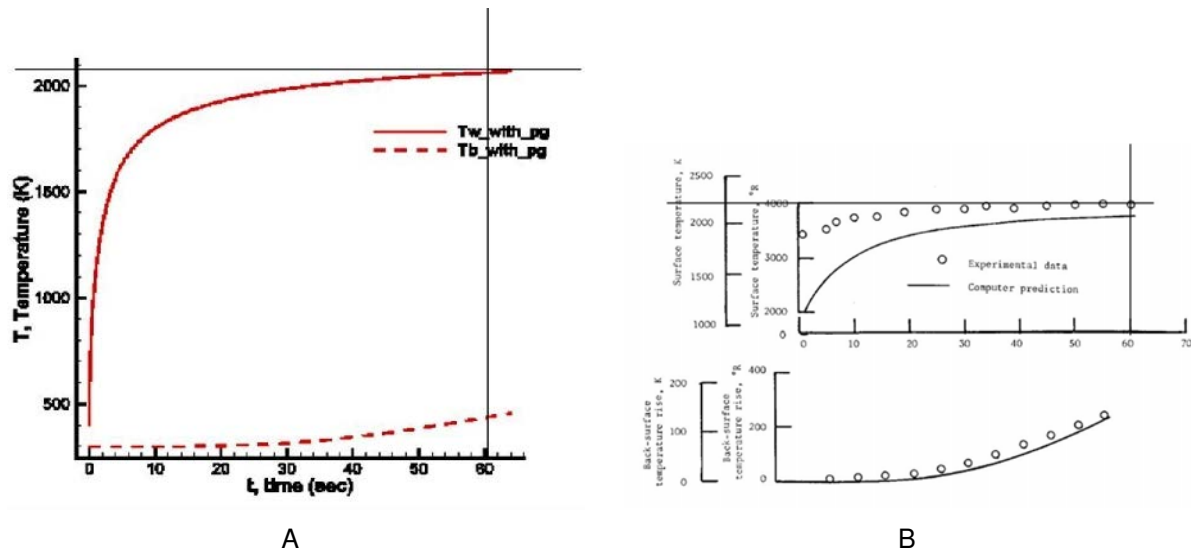


Figure 5-17. Simulation results for Langley arc jet test case. A) Temporal variation of surface and back-surface temperatures using MIG. B) Temporal variation of surface and back-surface temperatures from [88].

We see that the results, from MIG, for the temporal variation of the surface and back-surface temperatures for the Langley arc jet test case match very closely to the experiments [88] (Figure 5-17).

CHAPTER 6

HYPERSONIC FLOW CASES

This chapter focuses on hypersonic flow simulation outside a given body. Even though, numerical effort at simulating hypersonic flows began a few decades before, this is still a challenging problem, as has been demonstrated from examples presented in Chapter 1. In this chapter we consider, hypersonic flow over cylinder and demonstrate solution capability for inviscid and viscous hypersonic flows, followed by hypersonic flows with full thermo-chemical non-equilibrium.

As mentioned in Chapter 3, we employ two methods to capture shocks in the hypersonic flows, r-p adaptivity with $p = 0$ for shock regions and r-p adaptivity along with slope limiter (used for the results in Chapter 7) to capture the shock with higher (≥ 1) order of accuracy. We also implement time-implicit solutions for higher CFL numbers and hence faster solution turn around time.

Previous applications of DG method were limited to viscous hypersonic flows [2, 10]. Here, we extend DG to chemically reacting hypersonic flows with thermal non-equilibrium. Use of p-adaptive method, allows us to interpolate non-smooth shock region with piecewise element-averaged polynomial ($p = 0$) and with higher order polynomials ($p \geq 1$) where the flow features are mathematically smooth.

Also by redistributing (r) elements in critical regions about shock, we get accurate solutions without employing excessive mesh elements (h). Specifically, we study the flow over a stationary cylinder using (i) inviscid, (ii) viscous, and (iii) thermo-chemical non-equilibrium flow regimes. We compare our simulations with the published results.

Approaches, available in the literature, have so far focused on using either the slope limiters [59] or the artificial dissipation scheme [2, 79] to capture the shocks especially for the hypersonic flows. An approach to capture the shocks, without using either a slope limiter or artificial dissipation was attempted in [10]. We think that this approach

is useful and more convenient to use in the case of DG methods and further explore its application to the viscous and thermo-chemical nonequilibrium hypersonic flows.

It is well known, that $p = 0$ (the first order accurate method) is sufficient to capture a shock of any strength. Hence, using an effective shock indicator technique, we can apply $p = 0$ in the shock regions and higher order polynomial accuracy, $p \geq 1$ in the smooth flow regions. We can focus on reducing the mesh size in the shock and increasing the order of accuracy in the smooth flow regime to increase the over all accuracy of the solution.

A recent work in DG methods, [2] has demonstrated that the sub-cell shock capturing (i.e. capturing the shock within an element using the artificial dissipation and a shock sensor) lacks robustness and may not be more accurate than super-cell shock capturing or refinement (capturing the shock within few elements of reduced size for more accurate shock capturing).

We also look into the shock refinement option rather than the shock capturing for high order DG method. We employ p-adaptivity to use $p = 0$ for shock region and $p \geq 1$ for smooth flow. For refining the mesh near the shock, rather than opting for h-adaptivity, we choose r-adaptivity, in order to selectively refine only the cells near the shock. This can be implemented to hypersonic flow over any general body shape, with special interest for problems with detached shock.

In this work, we validate the steady state solutions, though for thermal ablation, its essential to obtain a time accurate solution response. Our implicit time scheme is first order accurate. We present validation of our results for inviscid, viscous and thermo-chemical non-equilibrium hypersonic flow problems. Here, we present results for $p = 0$ and 1.

Specifically, the three test cases for hypersonic flow over a circular cylinder are, (i) inviscid flow simulation for a freestream Mach number of 6 (compared with results from [10]), (ii) viscous hypersonic flow freestream Mach number of 17 (with results compared

from [2]), and (iii) flow with the thermo-chemical non-equilibrium for freestream Mach number of 17. These test cases serve as benchmark cases to validate our code for solution capability to solve hypersonic flow problems of varying degree of complexities.

6.1 Inviscid Hypersonic Flow

Here, we solve for inviscid hypersonic case using r-p adaptivity. First, we simulate the problem with $p = 0$ everywhere to steady state (Figure 6-1). Then this solution is taken, and by using shock sensor and p-adaptivity method, we apply $p = 1$ solution in regions with smooth flow features and $p = 0$ in regions of shock (Figure 6-2).

The jump indicator based on pressure jump values (section 3.7) over each edge of the element is used to distinguish between shock and smooth flow regions. This jump indicator [2, 10] is found to be more robust in comparison to the smoothness indicator in [79]. Also for time accurate simulations, starting from uniform flow as initial solution, when the shock moves along the elements, smoothness indicator fails to provide distinction between regions with $p = 0$ and $p \geq 1$. Shock indicator based on pressure jump does not face this issue.

After we obtain a steady state solution with $p = 0$ and $p = 1$ using p-adaptivity, we apply r-adaptivity, where using the shock location, we compress the domain bringing it closer to shock. This results in clustering of all the elements on domain outside shock and within shock, close to the shock. The elements can also be clustered in a fashion so that elements closer to shock are finer than elements away from the shock. Thus the shock can be accurately captured, with small mesh elements. This can be repeated several times to get shocks location accurately. After we obtain steady solution on this mesh, we can proceed to p-adaptivity method with $p = 2$ in smooth flow region and $p = 0$ in shock regions. This can be extended to higher values of p to increase order of accuracy within smooth region.

In Figure 6-1, we show steady state solution obtained with $p = 0$ for the inviscid hypersonic problem. We show density, pressure (P/P_∞) and Mach number contours.

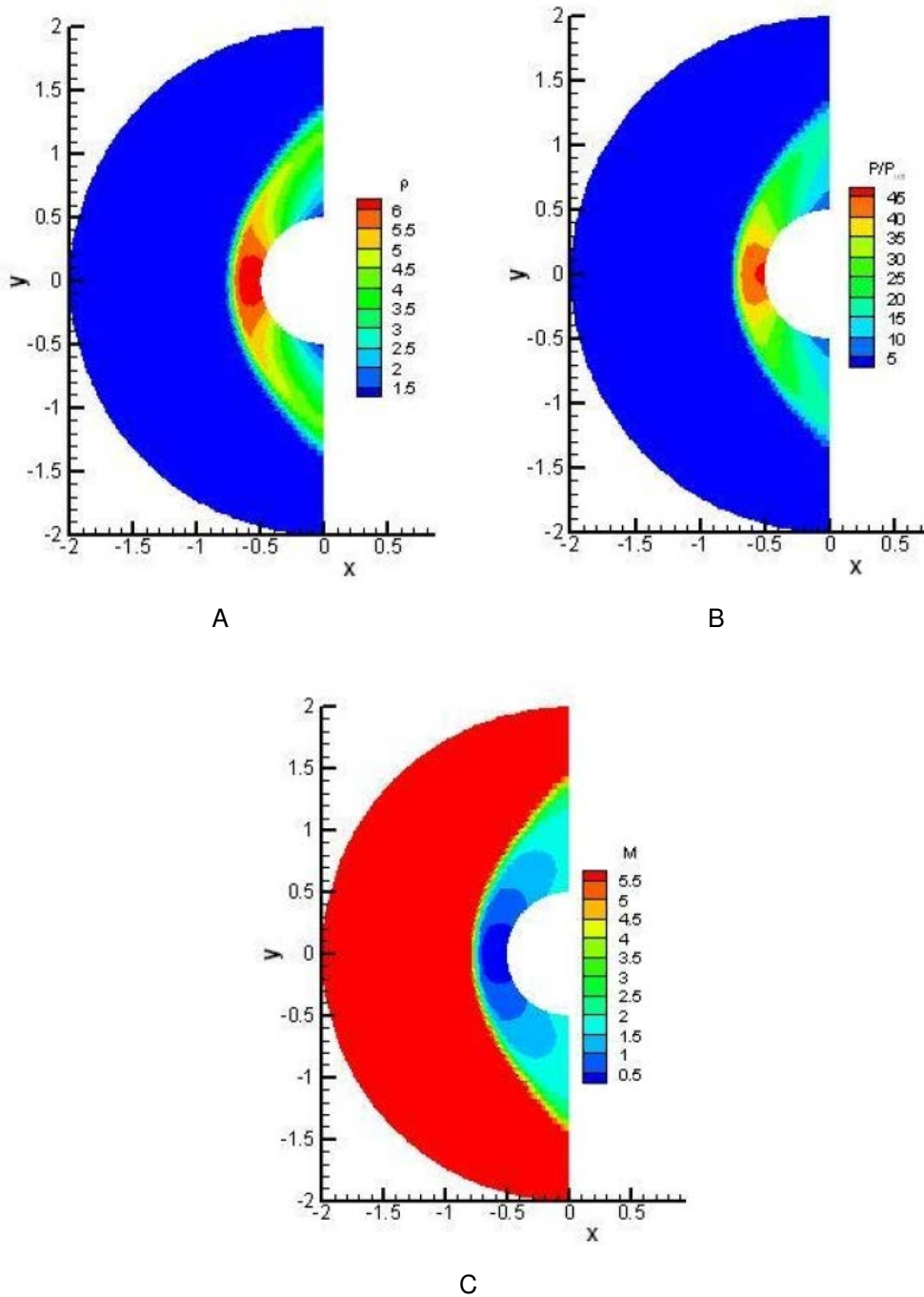


Figure 6-1. Results for inviscid hypersonic case ($M = 6$) with $p = 0$. A) Density contours. B) P/P_∞ contours. C) Mach number contours. Mesh is 128×100 elements, with 128 elements in the circumferential direction and 100 elements in the radial direction, with finer mesh close to the cylinder wall. Pressure and Mach contours compare well with results published in [10].

These contours are comparable to the contours given in [10]. Our next step is to obtain contours with p-adaptivity using $p = 1$ in regions of shock and $p = 0$ in smooth flow regions. For this, we take the steady state solution obtained from Figure 6-1, with $p = 0$ everywhere, and using shock detector based on pressure jump, apply $p = 1$ in smooth regions and $p = 0$ in shock regions. Shock location is evaluated at every time step, and $p = 0$ and $p = 1$ accordingly applied and the solution is run up to steady state. In Figure 6-2, density contours along with indicated shock is shown. Density contours are more stretched out in smooth flow regime due to using $p = 1$ there, but there is also some waviness in the solution near the shock. Reason for waviness is coarse mesh near the shock and higher threshold value used for shock indicator which shows some oscillations. These oscillations persist in solution, although not causing any stability problems. These oscillations in the shock region are shown in 3-D plot of density contours in Figure 6-3. We can get rid of the oscillations by lowering the shock indicator threshold value (Figure 6-3 B) or by refining the mesh by redistribution of elements in the rest of the domain outside the shock in close proximity to shock (Figure 6-4), thus reducing the mesh size. We do not see oscillations in Figure 6-3 B, but then the region of $p = 0$ is very wide and includes regions from top and bottom of cylinder as well in addition to shock. This may not be useful since we will have poor accuracy in regions above and below the shock. Shock indicator which exactly identifies shock and not other regions without shock, will be useful. For this purpose, value of 0.1 was seen to best serve the purpose with least oscillations for this particular mesh.

For finer shock resolution, we apply r-p adaptivity, bringing the domain elements close to shock region as shown in Figure 6-4. All the domain elements outside the shock are clustered into the shock uniformly. Thus, as we can see the mesh in Figure 6-4, we get finer elements within the shock region. It is clearly seen in Figure 6-5, that shock thickness has reduced as compared to results shown in Figure 6-1. We still observe some waviness in solution profiles. These solutions have not yet reached steady state

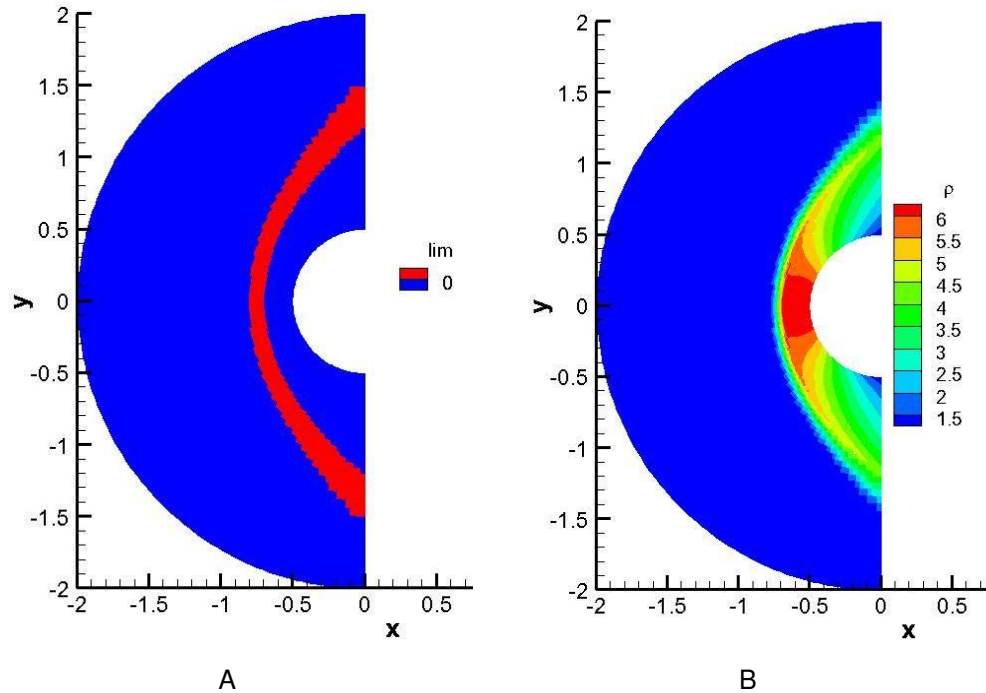


Figure 6-2. Shock indicator. A) Shock location as indicated from pressure jump shock indicator. Threshold value of 0.3 is used for the shock indicator. Red region indicates shock ($p = 0$ is used by setting the limiter to a value of 1) and blue region indicates smooth region ($p = 1$ is used by setting limiter to a value of 0). B) Density contours with levels set same as those with only $p = 0$. Density contours are more stretched out in comparison to $p = 0$, but some waviness in the solution is visible near the shock.

(from the perspective of norm of residual), but the shocks location is stationary. Solution seems to have effect of error wave propagation from shock to the flow in the shock layer, which can be very easily seen in contour plots of Mach number and density. This error wave may be due to difference in accuracy of scheme in shock with $p = 0$ and shock layer with $p = 1$. In these simulations, shock location is being evaluated at every time step, and thus this may cause delay for solution reaching steady state from residual perspective. It will be of interest to find out if the error waves go away when solution reaches steady state, or is it dependent on oscillations near shock which are controlled by adjusting threshold value for shock indicator and also by refining the shock region more and more.

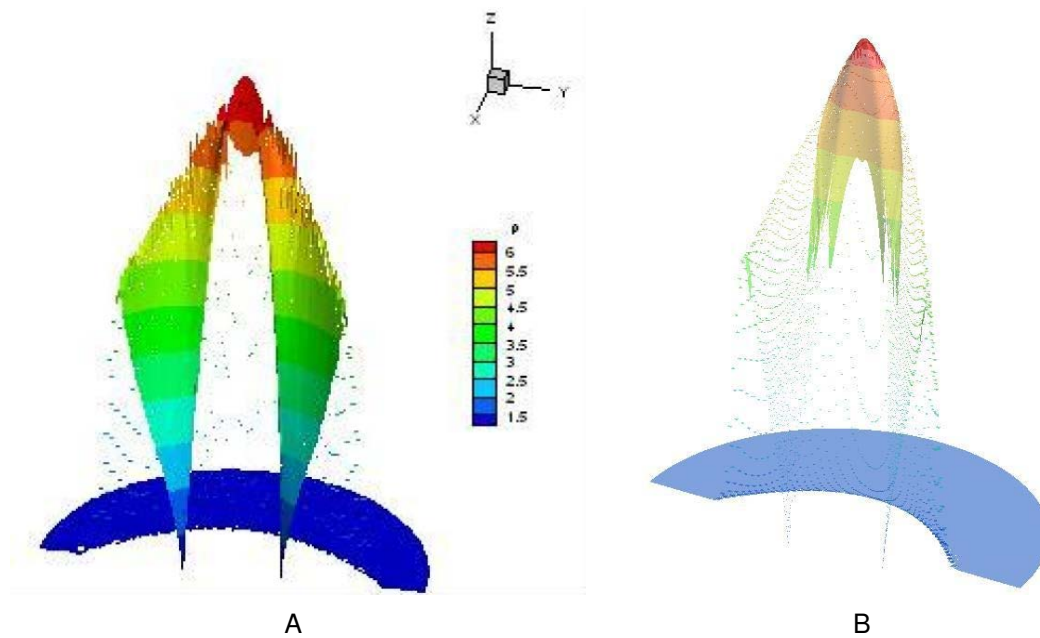


Figure 6-3. 3-D density contour plots for different shock indicator thresholds. A) Threshold value of 0.3. B) Threshold value of 0.04. Decreasing threshold value removes oscillations, but it does not serve the purpose for having high order approximation in the smooth flow region.

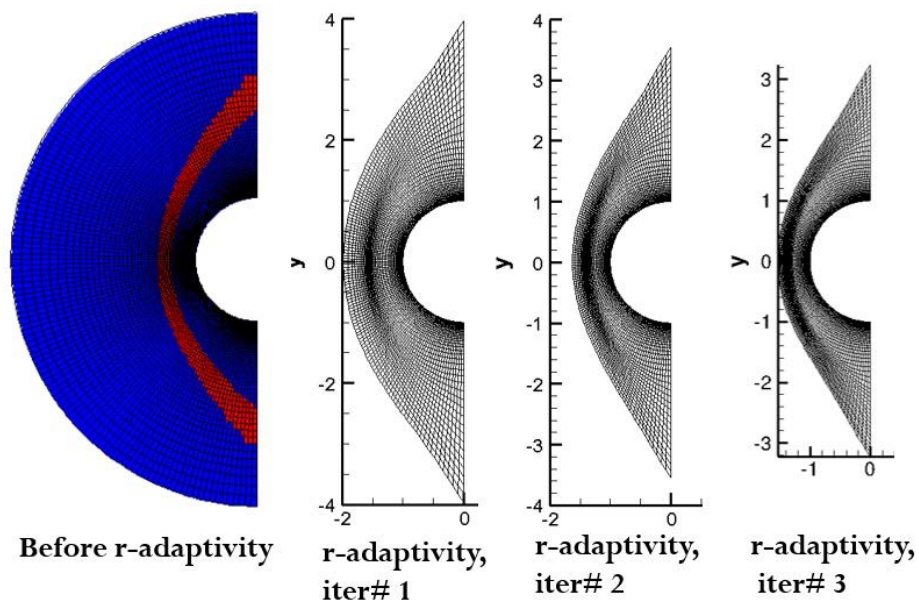


Figure 6-4. Shock-based r-p adaptivity mesh refinement. Successive application of r-p adaptivity to the original mesh, with shock location identified using the pressure based shock sensor, results in increasingly finer mesh at the shock.

Using r-p adaptivity, we get following results compared to results by Wang et al. (Figure 6-5).

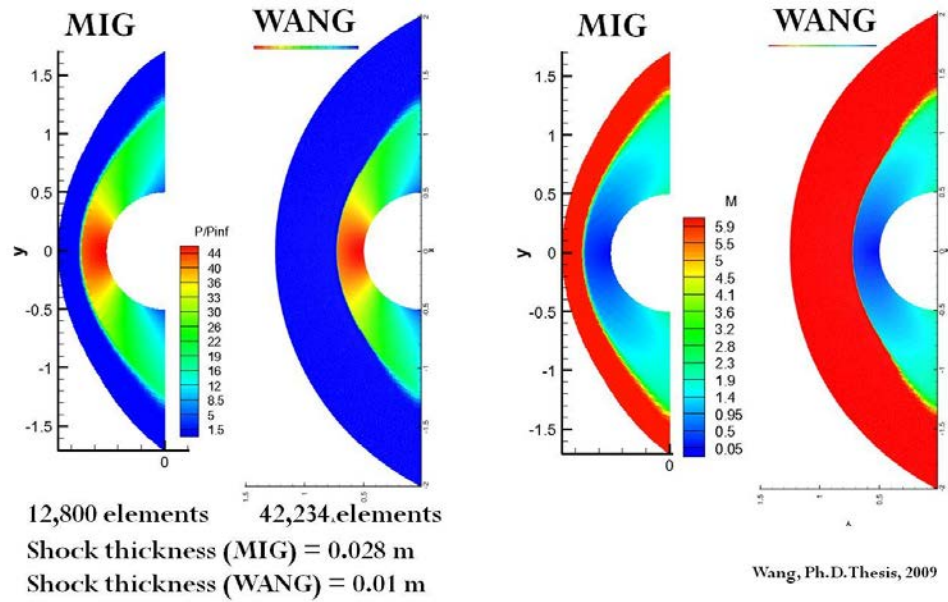


Figure 6-5. Solution comparison for inviscid hypersonic flow with r-p adaptive method. Better shock resolution is obtained, using r-p adaptivity and higher order polynomial approximation in MIG (DG method). Shock is finely captured, with approximately a third of the elements used in Wang. The solution method focuses on refining the mesh near the shock and increasing polynomial order of accuracy in smooth flow regions to improve solution resolution everywhere.

To finalize the accuracy of our inviscid hypersonic flow results we show the shock standoff distance as predicted by our code compared to that presented in Wang (Figure 6-6). We note that despite using $1/3^{\text{rd}}$ of number of elements in Wang, we accurately predict shock stand-off distance to be 0.726 m. This is due to using r-p adaptivity where the elements outside the shock are redistributed to cluster near the shock, thus providing enhanced mesh resolution at the shock.

The advantages of r-p adaptivity, over h-p adaptivity used in [10], is that it is more suitable for transient problems, and does not lead to the increase in number of elements. Hence this is very suitable for problems of coupled simulation of hypersonic flow and

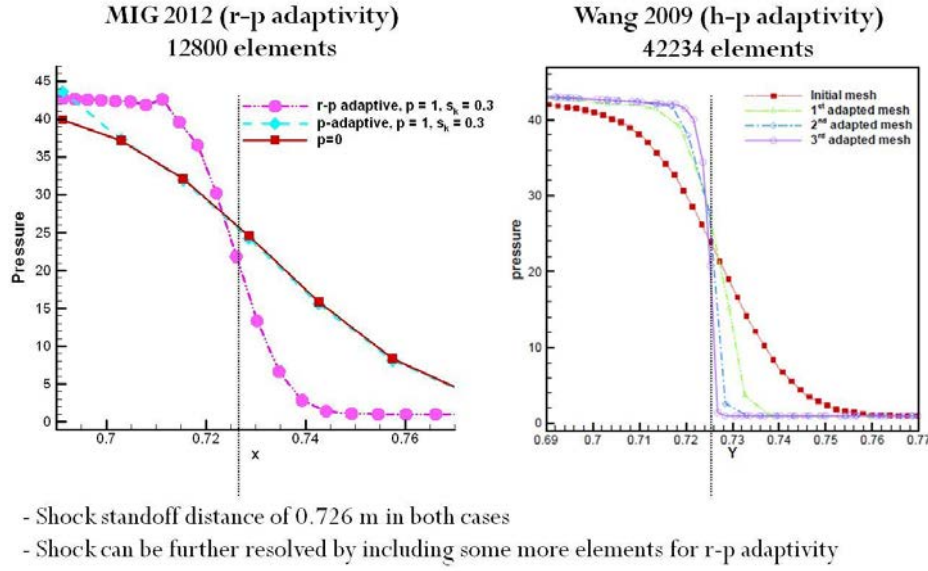


Figure 6-6. Stagnation line pressure comparison for Mach 6 inviscid hypersonic flow. Shock location is identified and the shock standoff distance is 0.726 m in both cases. These results are compared to Wang [10]. The method used in [10] is h-p adaptivity for refining the mesh close to the shock.

thermal ablation since shock's location can vary upon blowing of pyrolysis gases from solid domain into fluid domain. Hence this adjustment can be made using r-p adaptivity.

6.2 Viscous Hypersonic Flow

In this section, we present results obtained for viscous hypersonic flow. Here, the Mach number for the flow is 17, and the results are compared to one of the results given in [2]. As seen in Figure 6-7, temperature contours for both results match well. Shock standoff distance is also 0.4 m in both cases.

These results are again improved by further applying r-p adaptivity to the obtained solution and re-rerunning the simulations. This r-p adaptivity changes the mesh to readjust the elements outside the shock to in the shock (Figure 6-8).

The improved results for viscous hypersonic flow are hence seen in Figure 6-9,

We also conducted mesh convergence study, wherein, we refined the mesh both near the wall and in the θ direction. The plots for heat coefficient is given in Figure 6-10.

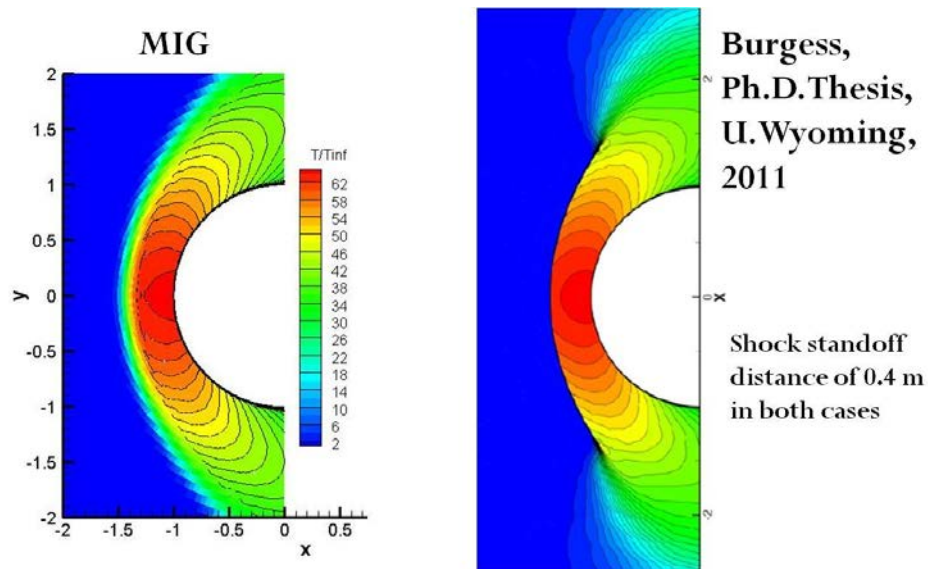


Figure 6-7. Mach 17 viscous hypersonic flow results. Results from MIG are compared to Burgess [2]. Both results show same shock standoff distance of 0.4 m.

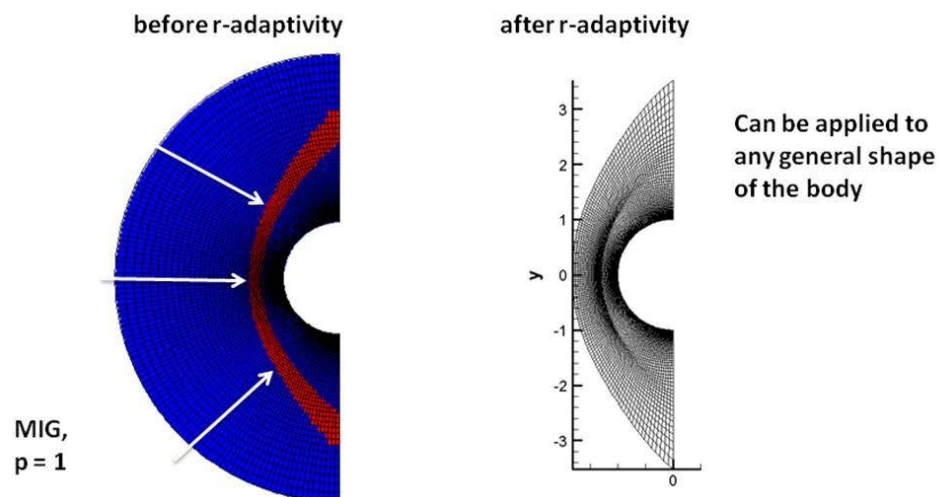


Figure 6-8. r-p adaptive solutions to viscous hypersonic flow. r-p adaptivity is applied to the steady state solution obtained from the initial mesh.

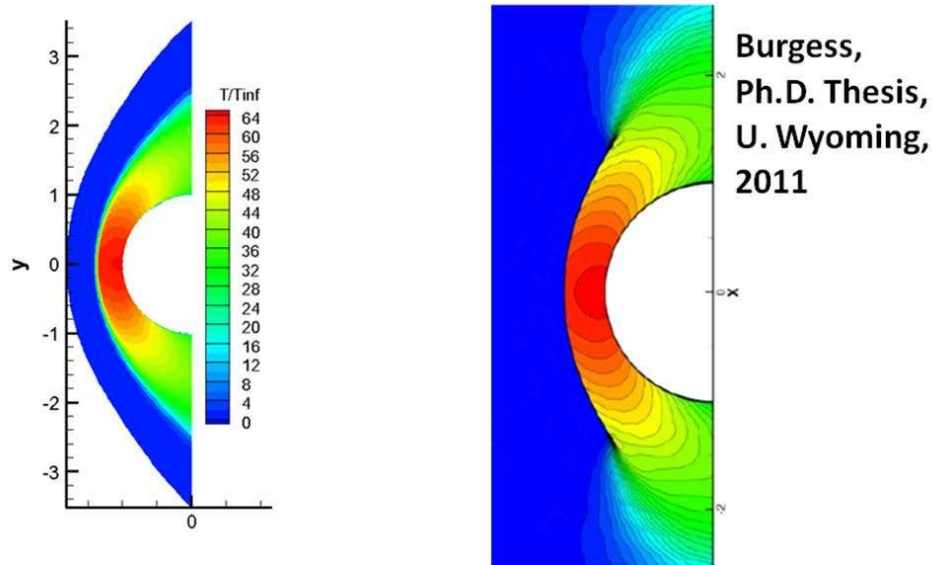


Figure 6-9. Viscous hypersonic flow result comparison. Results from MIG (after r-p adaptivity) are compared to [2]. Our code uses 12,800 elements as compared to 37,575 elements in [2].

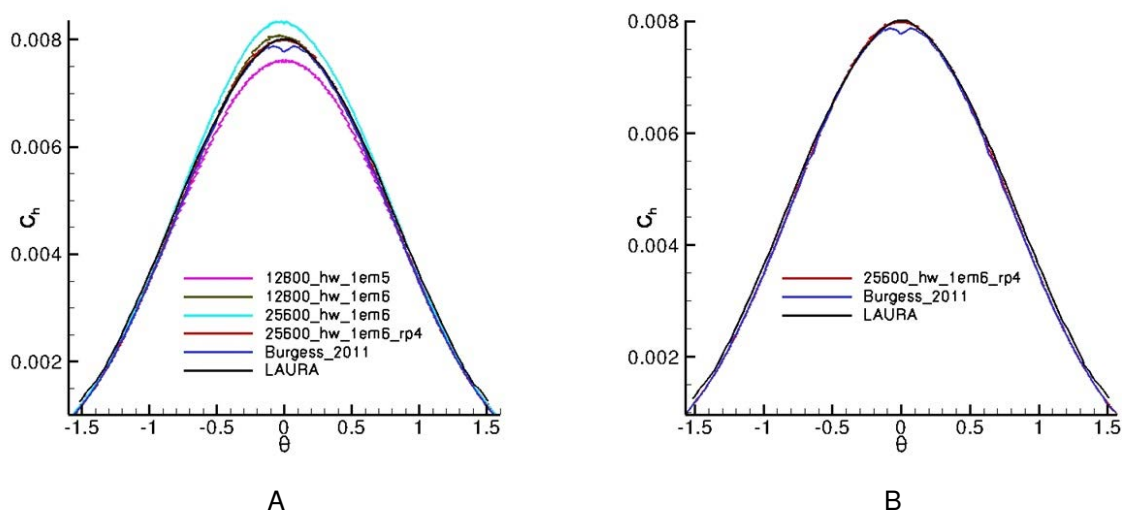


Figure 6-10. Surface heating coefficient profile for viscous hypersonic flow. A) Surface heating coefficient profile is shown for different meshes and r-adaptivity. Wall thickness certainly affects the results in addition to the refinement of the mesh in θ direction. But this is not sufficient, even r-adaptivity which refines the mesh in the shock is seen to affect the result significantly. B) Comparison of our best results with LAURA and Burgess [2].

Two meshes are used in Figure 6-10, base mesh of 128×100 elements and the mesh with twice the number of elements in θ direction, i.e. 256×100 elements. Two wall thicknesses are used in the simulations, 10^{-5} m and 10^{-6} m. A finer wall thickness certainly improves the results for C_h . We compare our results to Burgess, [2] and LAURA [89], and note that result reported in [2] has small kink in the profile at stagnation point which may be due to not having fine enough mesh for the shock. In Figure 6-10 B, we show our best case (with 4th r-adaptive iteration) to match the standard LAURA result very accurately.

6.3 Hypersonic Flow with Thermo-Chemical Non-Equilibrium

After benchmarking our results for inviscid ($M = 6$) and viscous ($M = 17$) hypersonic flows, we present the results for hypersonic flow in thermo-chemical non-equilibrium. We consider 5 species model with over all 5 chemical reactions (described in Chapter 2), and compare our results with those obtained from US3D by Dr. Gosse.

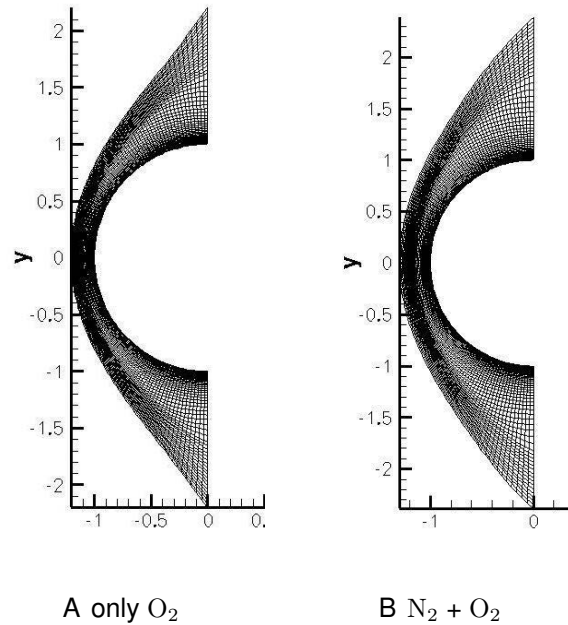


Figure 6-11. Final r-p adapted meshes for non-equilibrium cases. A) only O_2 in freestream. B) Both O_2 and N_2 in freestream. In the 4th and final iteration of r-p adaptivity, the meshes are fine at the identified shock locations of 0.15 and 0.2 m (away from cylinder's surface) respectively.

The governing equations for this problem are the multi-species Navier-Stokes equations with elaborate transport, chemistry and vibrational models, which requires diligent and tedious book keeping. First case is with only oxygen, O_2 in the freestream flow. This test case was crucial for us to debug the code, as the simulations for the full problem (the second test case), $N_2 + O_2$ in freestream with full thermo-chemical non-equilibrium, did not match in the initial attempt. Not being able to match MIG results for the full problem to US3D initially, we compared our code to US3D for models other than chemistry, i.e. viscous, inviscid and thermal non-equilibrium models. Each model was tested in isolation of other to find out the difference in models. Thus, we were able to eliminate all the models and only model that caused the difference was thermo-chemistry model.

For this purpose, we tested the first case with only O_2 in freestream. This case has only one reaction, i.e. dissociation of O_2 into O , and is much easier to debug than the second test with $N_2 + O_2$ in freestream and full thermo-chemical non-equilibrium. Thus we found the reason for the discrepancy in the results, to be in chemistry coefficients. Park's model provides values for coefficients for both forward and equilibrium rate constants. In this, the density and molecular weight are to be used in g/cm^3 and g/mol . Thus, the expressions for reaction rates given in Eq. (2-52) and Eq. (2-53), have to have a factor to properly account for using SI units for density and molecular weight.

For this simulation, a mesh with circular outer domain was taken for first set of runs and a steady state solution obtained with p-adaptivity (i.e. $p = 0$ in shock). Highest timestep that we used in this case was 10^{-6} sec, which corresponds to maximum CFL number of 500 at the wall where the wall thickness is 10^{-5} m. Then applying r-p adaptivity to this solution we rerun the simulation again to steady state. After 4 iterations, we achieve the final r-p adapted mesh with shock location identified at approximately 0.15 m and 0.2 m (for test-case 1 and 2 respectively) away from the cylinder at the stagnation line. Meshes for both the test cases are given in Figure 6-11.

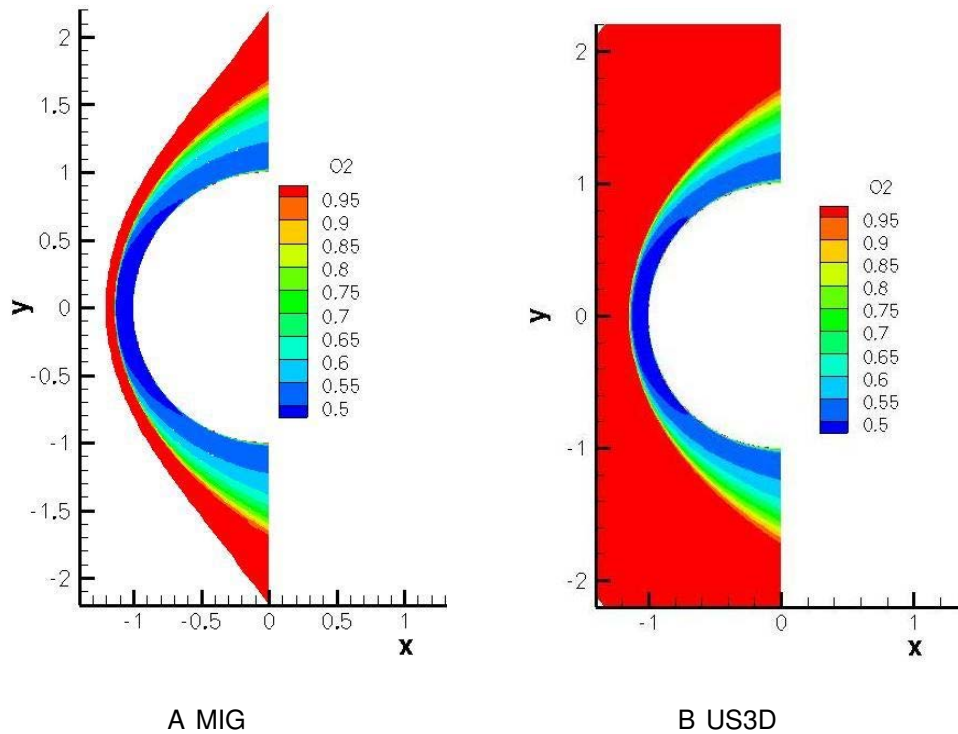


Figure 6-12. Mass fraction of O_2 for MIG and US3D for only O_2 test case. A) Contours from MIG. B) Contours from US3D. Both are steady state results. Significant dissociation of O_2 , nearly 55 %, is observed in both the cases. Dissociation follows immediately after the flow passes through the shock.

The final solution on these meshes are now presented. First for only O_2 case, the comparison is shown for MIG and US3D. Shock standoff distance in both cases is predicted to be 0.15 m, and other properties like density, pressure and velocity also compare well.

In Figure 6-12, significant dissociation of O_2 into O is observed. High temperatures in shock of nearly 5000 K are responsible for this dissociation, at which the forward reaction rates for $O_2 + M \rightleftharpoons 2O + M$ dominate the backward rates. Away from the stagnation region, temperatures in the shock are lower, hence lesser amount of dissociation is observed. Therefore, higher mass fraction of O_2 is seen in shock and shock layer away from the stagnation region. Based on same arguments, we can

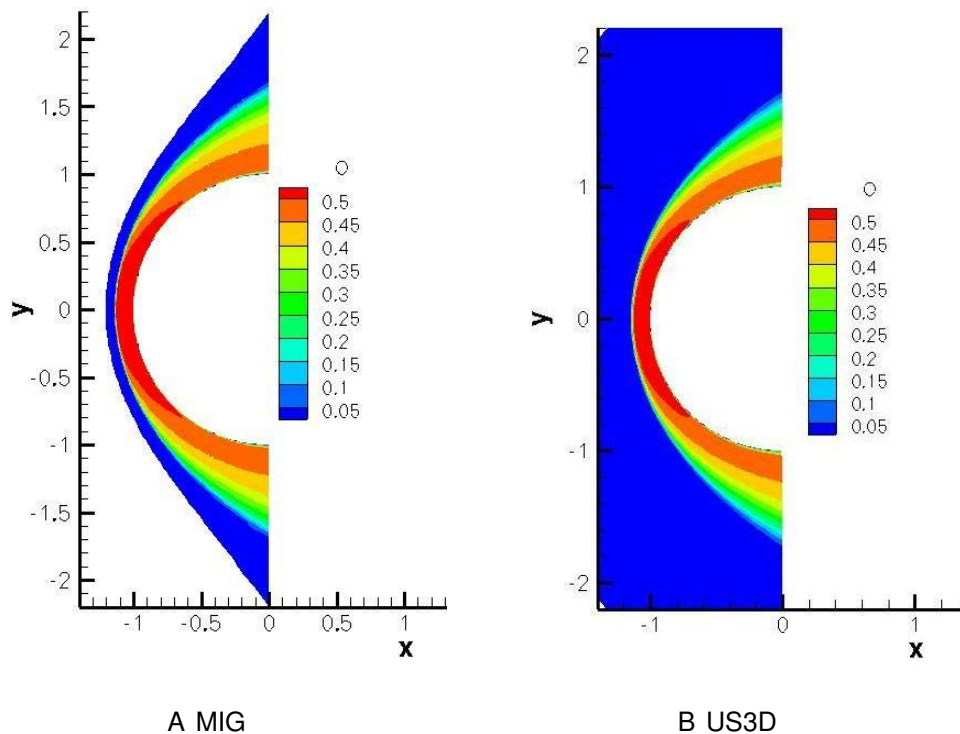


Figure 6-13. Mass fraction of O for MIG and US3D for only O_2 test case. A) Contours from MIG. B) Contours from US3D. Both are steady state results. Significant production of O, nearly 55 %, is observed in both the cases. Reason for this production follows exactly from the dissociation of O_2 , as explained in Figure 6-12.

explain the corresponding contours for mass fraction of atomic oxygen, O. Comparisons between MIG and US3D are very similar.

As can be seen in Figure 6-17, a significant drop in temperatures occur right after the shock, due to dissociation processes, which are endothermic in the forward direction. The species (both diatomic and monoatomic oxygen) equilibrate (on stagnation line), a small distance after the shock. Hence, no further drop in temperature is observed along the stagnation line after the initial drop. However, away from stagnation line, due to lower temperatures in shock, O_2 continues to dissociate causing further decrease in temperature as the flow moves closer to the cylinder surface.

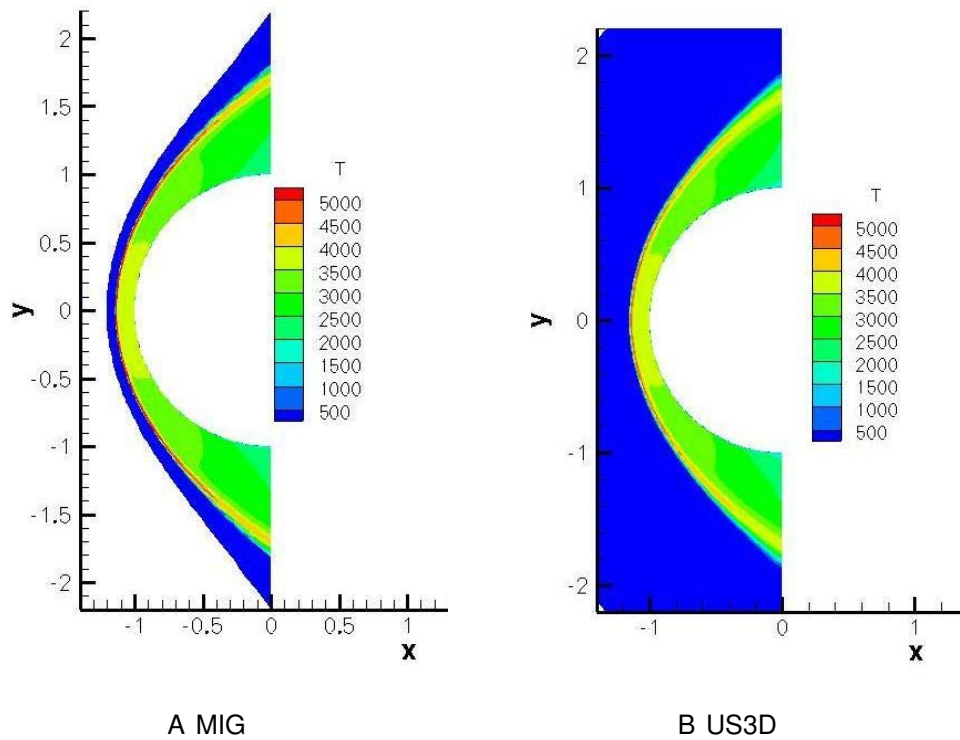


Figure 6-14. Contours for temperature, T for MIG and US3D for only O_2 test case. A) Contours from MIG. B) Contours from US3D. Both are steady state results. Contours match well for both MIG and US3D. Nature of temperature contours can be understood based on the amount of dissociation of O_2 observed in the shock.

This explains the nature of contours seen for both T and T_v in Figure 6-14 and 6-15 respectively.

Although the temperature contours in Figure 6-14 compare well, the maximum temperatures encountered in the shock in MIG and US3D are 6680 K and 5380 K respectively. This results from oscillations in temperature around the shock, as shown in Figure 6-16. Hence this difference is purely related to p-adaptivity approach employed in MIG to capture the shock and may be improved by the use of slope limiter.

The stagnation line properties are also plotted for mass fractions of O_2 and O , and T and T_v and compared for both MIG and US3D codes in Figure 6-17.

Stagnation plots, in Figure 6-17, show a higher temperature rise (for T) in the shock for MIG in comparison to US3D. This has already been discussed and may be

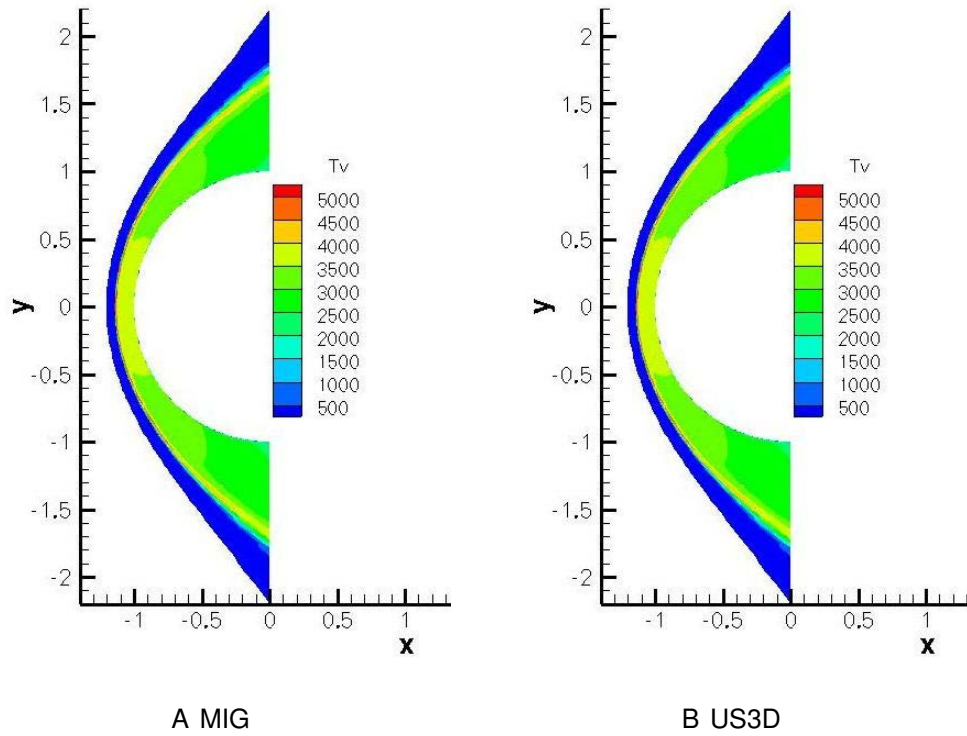


Figure 6-15. Contours for vibrational temperature, T_v for MIG and US3D for only O_2 test case. A) Contours from MIG. B) Contours from US3D. Contours compare well for both MIG and US3D. Nature of vibrational temperature contours can be understood similar to the explanation given in Figure 6-14 for translational-rotational temperature, T .

connected to p-adaptivity approach used in this work. Thermal non-equilibrium is seen to be predominant in the shock and some distance (nearly 0.02 m) after the shock. Elsewhere, thermal equilibrium is predominant.

Additionally, O_2 is seen to dissociate in the shock and the post-shock region, leading to formation of O. In the post-shock region, dissociation is prominent to a distance of 0.032 m away from the shock. In the rest of post-shock region, both the mass fractions of O_2 and O becomes almost constant, thus reaching chemical equilibrium. At the wall, which is fully catalytic having fixed temperatures of 500 K for both T and T_v , we find that O_2 and O go back to their freestream values. In comparison of MIG, and US3D, apart from the high rise in temperature observed in MIG, rest all values compare fairly well for both the codes.

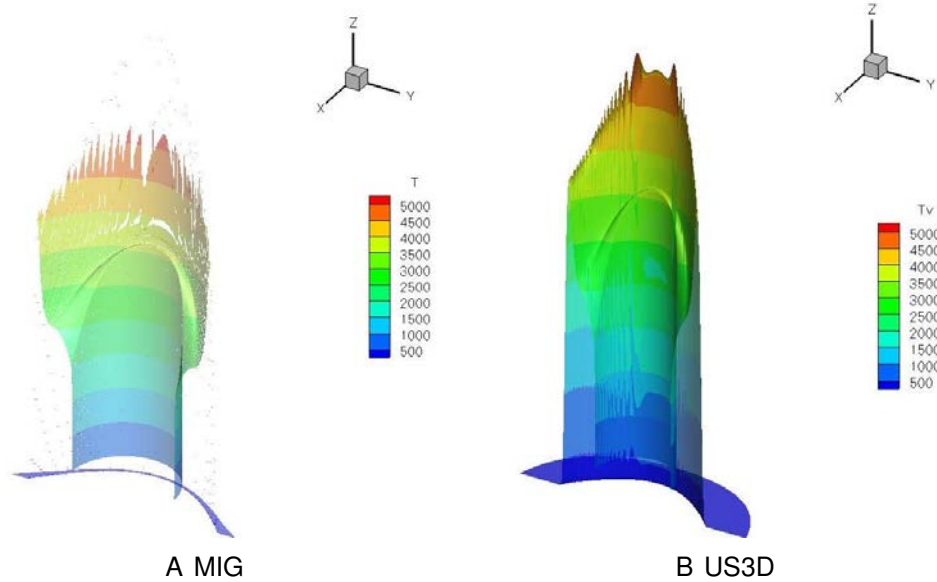


Figure 6-16. 3D contours for temperature, T for MIG and US3D for only O_2 test case. A) 3D contours for MIG. B) 3D contours for US3D. High temperature, observed in MIG, is at the shock and is due to the oscillations near the shock. Method, used in MIG, is r-p adaptivity with $p = 0$ for shock regions.

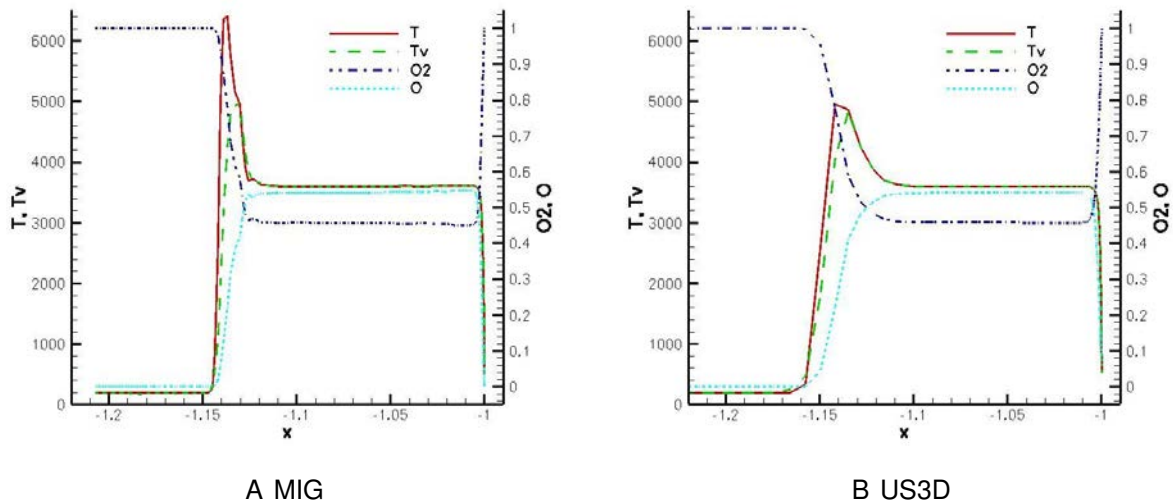


Figure 6-17. Stagnation line plots for only O_2 case. A) Stagnation line plots for MIG. B) Stagnation line plots for US3D. Plots for temperatures, T and T_v , and mass fractions of O_2 and O are shown. Higher temperature rise, at the shock, is observed in MIG in respect to US3D.

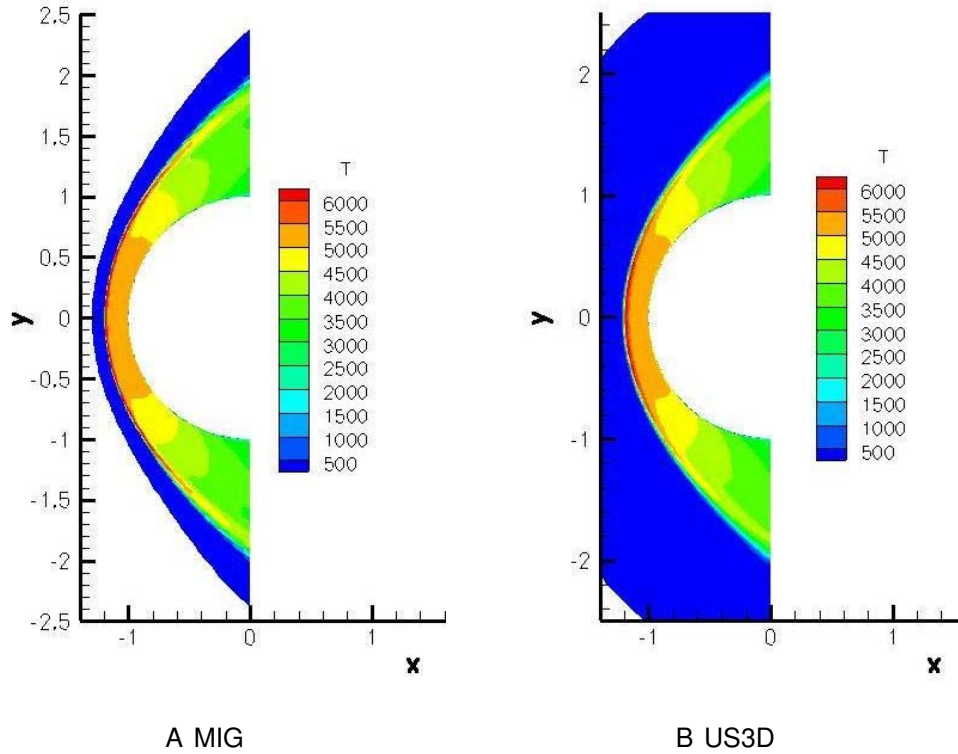


Figure 6-18. Temperature contours for $N_2 + O_2$ case. A) Contours for MIG. B) Contours for US3D. Both results compare very well to each other. Maximum temperature in MIG is 7700 K and in US3D is 6500 K, and the difference is attributed to p-adaptivity.

Next, we present results for second test case; with $N_2 + O_2$ in freestream in mass fraction ratio of 0.7562:0.2438. Freestream temperature is 200 K, and the wall, which is fully catalytic is again at a fixed temperature of 500 K. For this also, we compare our results from MIG to those from US3D.

Temperature contours for $N_2 + O_2$ case are shown in Figure 6-18 for both MIG and US3D. Both the results compare very well to each other. The maximum temperature in MIG is found to be 7700 K and in US3D to be 6500 K. This difference is due to p-adaptivity as has already been explained for the case of only O_2 .

Contours for vibrational temperature also compare very well for MIG and US3D (Figure 6-19). For T_v , maximum temperature in flow field for MIG is 6300 K and for US3D is 6550 K. Hence, the maximum values of vibrational temperature are much

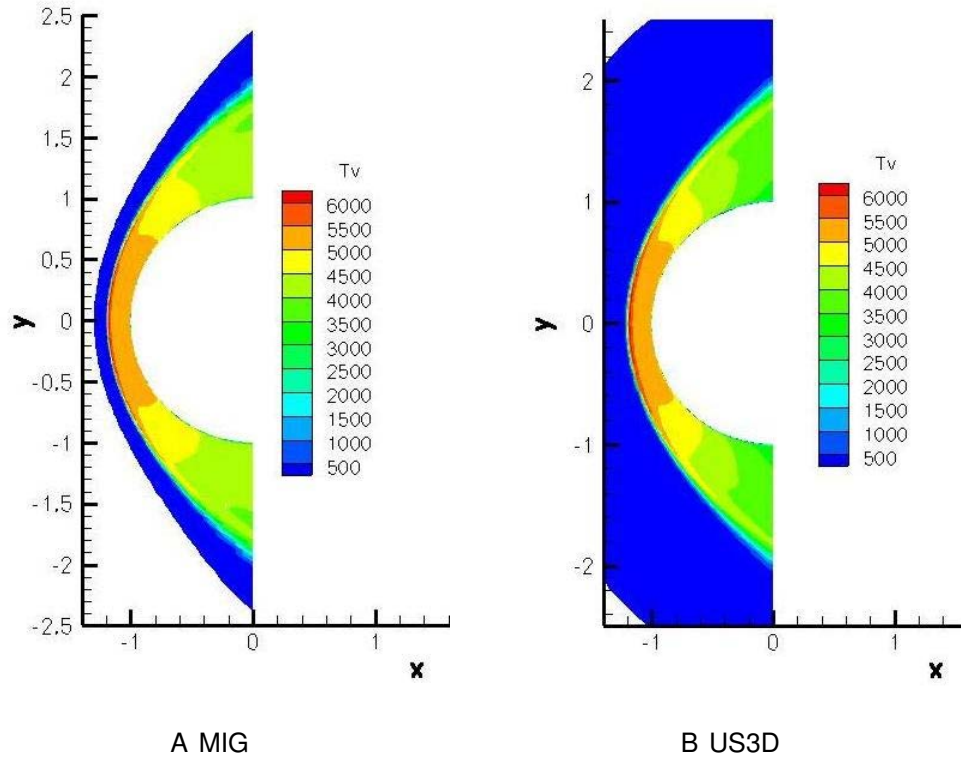


Figure 6-19. Vibrational temperature contours for $N_2 + O_2$ case. A) Contours for MIG. B) Contours for US3D. Both results compare well to each other. Maximum temperature in MIG is 6300 K and in US3D is 6550 K, and the difference is again attributed to p-adaptivity.

closer for both the codes than it is for the maximum values of translational-rotational temperature. Hence, the difference between the two simulations can more certainly be attributed to difference in shock capturing approaches in both the codes.

Contours for mass fraction of O_2 are seen in Figure 6-20, and again the excellent comparison is seen in both the codes. Complete dissociation of O_2 is seen in shock layer compared to only a partial dissociation of O_2 in the only O_2 case. This is explained by sensitivity of temperature contours and the shock standoff distance to the chemistry model. Results change significantly when the chemistry and thermal non-equilibrium models are turned on.

Shock standoff distance, for only O_2 and $N_2 + O_2$ cases, are 0.15 m and 0.2 m respectively, in comparison to 0.4 m and 0.3 m for full thermo-chemical equilibrium and

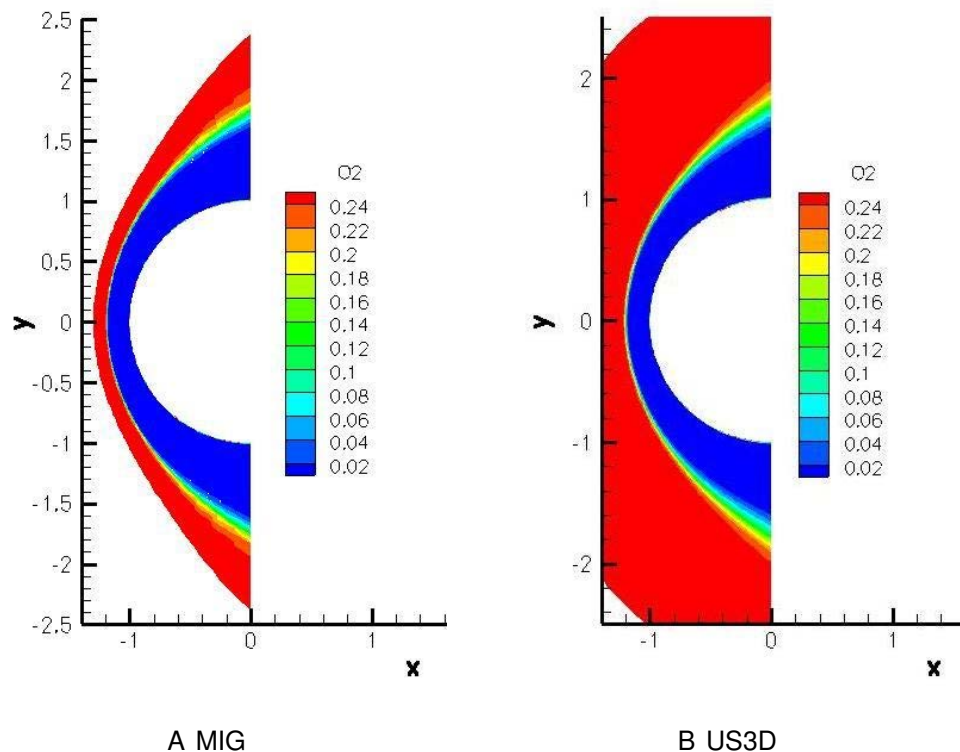


Figure 6-20. Mass fraction contours of O_2 for $N_2 + O_2$ case. A) Contours for MIG. B) Contours for US3D. Complete dissociation of O_2 occurs in the shock layer, as opposed to only partial dissociation in only O_2 case.

only thermal non-equilibrium. Due to higher temperatures observed in $N_2 + O_2$ case (6500 K maximum temperature in comparison to 5300 K for only O_2 case), complete dissociation of O_2 is observed. Dissociation of N_2 into N atoms is incomplete with maximum dissociation of nearly 0.07, (Figure 6-24) occurring just after the shock. As we observed in the case of only O_2 , the species are in thermo-chemical equilibrium in the shock layer at least close to stagnation region. This is due to increased value of density post-shock, that causes the species to equilibrate faster due to increased number of collisions.

A small portion of atomic nitrogen, N (produced by the dissociation), combines with atomic oxygen, O to form NO close to the shock region (Figure 6-22 and 6-25). Away from shock, in the shock layer, the temperatures are not high enough to sustain NO

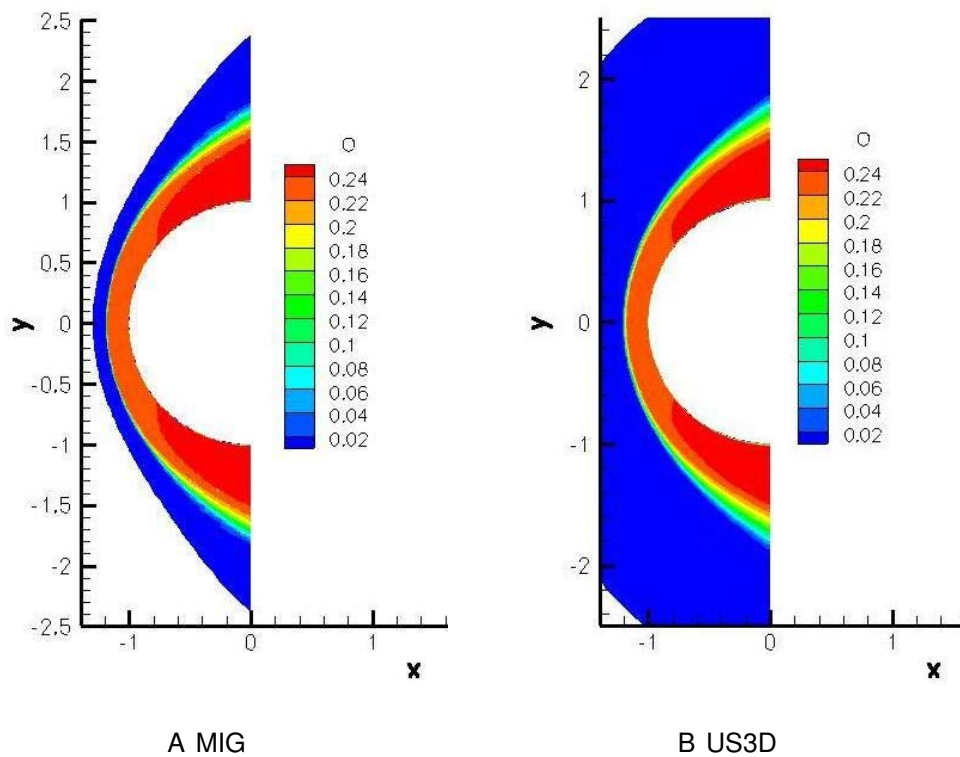


Figure 6-21. Mass fraction contours of O for $N_2 + O_2$ case. A) Contours for MIG. B) Contours for US3D. Maximum mass fraction for O, i.e. 0.2438 is found close to the top and bottom regions of the cylinder. This correlates to the mass fraction of NO. Maximum O occurs when NO (formed in the shock) dissociates back into N and O, giving extra O.

which again dissociates into atomic N and O. Thus in the contours of N, we see the maximum value of mass fraction being just after the shock rather than in the shock.

As N_2 and O_2 continue to dissociate for some distance even after the shock, the temperature contours which have maximum in the shock, continue to drop unlike purely viscous case, where the temperatures remain almost constant after the shock.

As we go away from the stagnation line towards either the top or bottom of cylinder, temperature values decrease, and hence the amount of NO also decrease, which is produced in shock region, and it again dissociates to N and O, thus we see that maximum mass fraction of O is at top and bottom regions of cylinder, not near stagnation line.

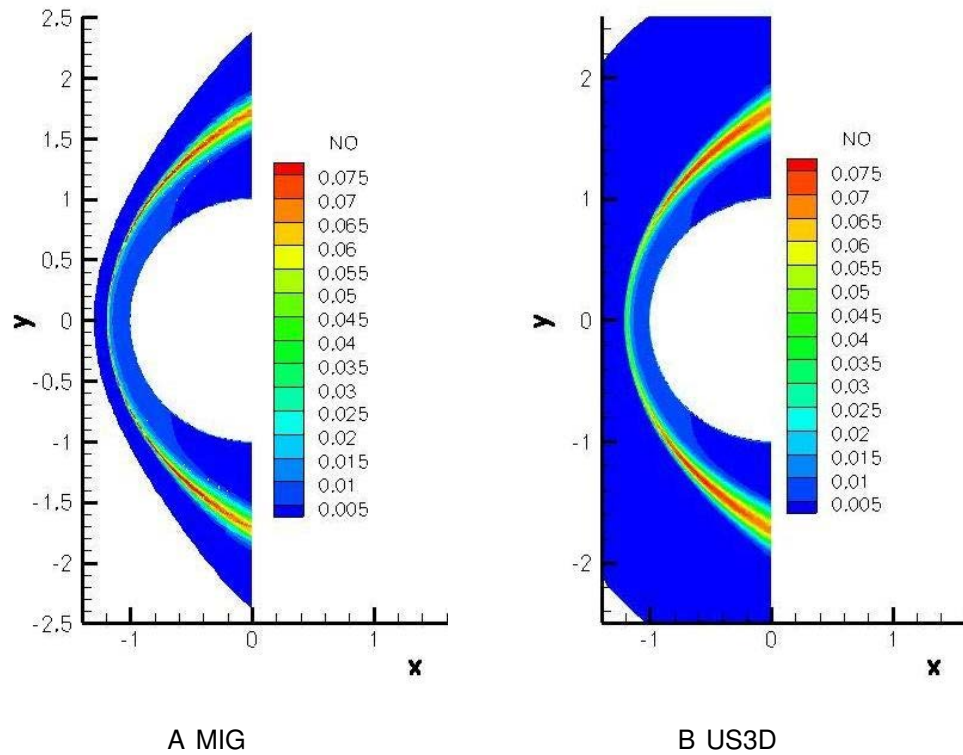


Figure 6-22. Mass fraction contours of NO for $N_2 + O_2$ case. A) Contours for MIG. B) Contours for US3D. Maximum mass fraction for NO, and also its production, occurs in the shock by combination of atomic N and O, produced by the dissociation reactions of N_2 and O_2 . As the temperatures (being maximum at the shock) drop down in the shock layer, NO (produced in the shock) again dissociates into N and O.

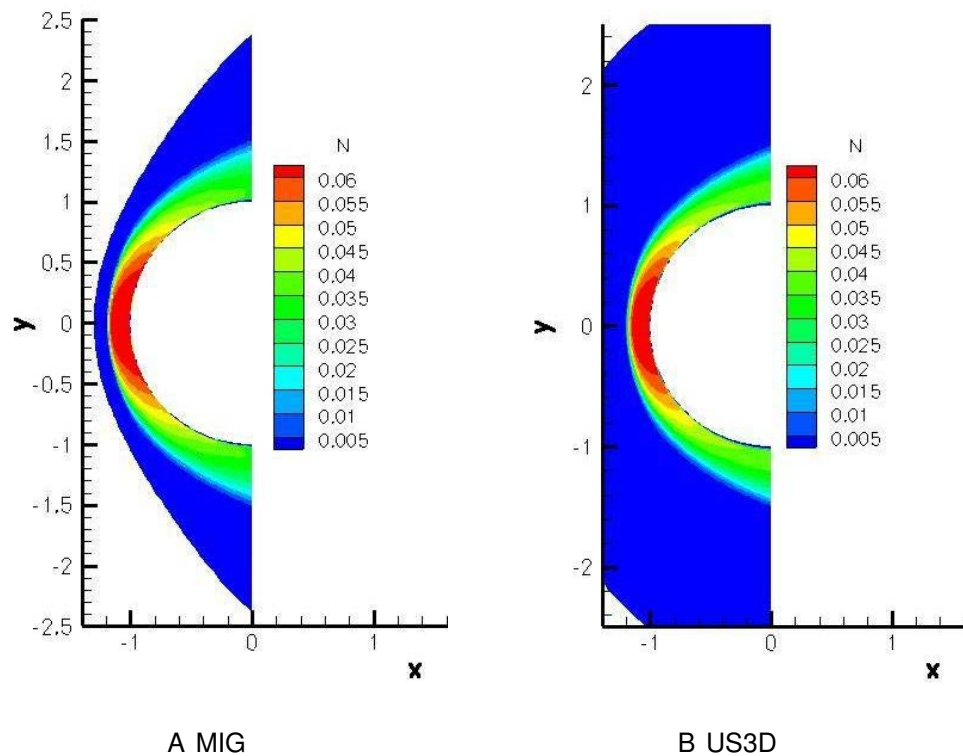


Figure 6-23. Mass fraction contours of N for $N_2 + O_2$ case. A) Contours for MIG. B) Contours for US3D. Maximum mass fraction for N occurs, close to the stagnation region just after the shock. N is formed by the dissociation of N_2 , and recombines (in the shock) with O to form NO.

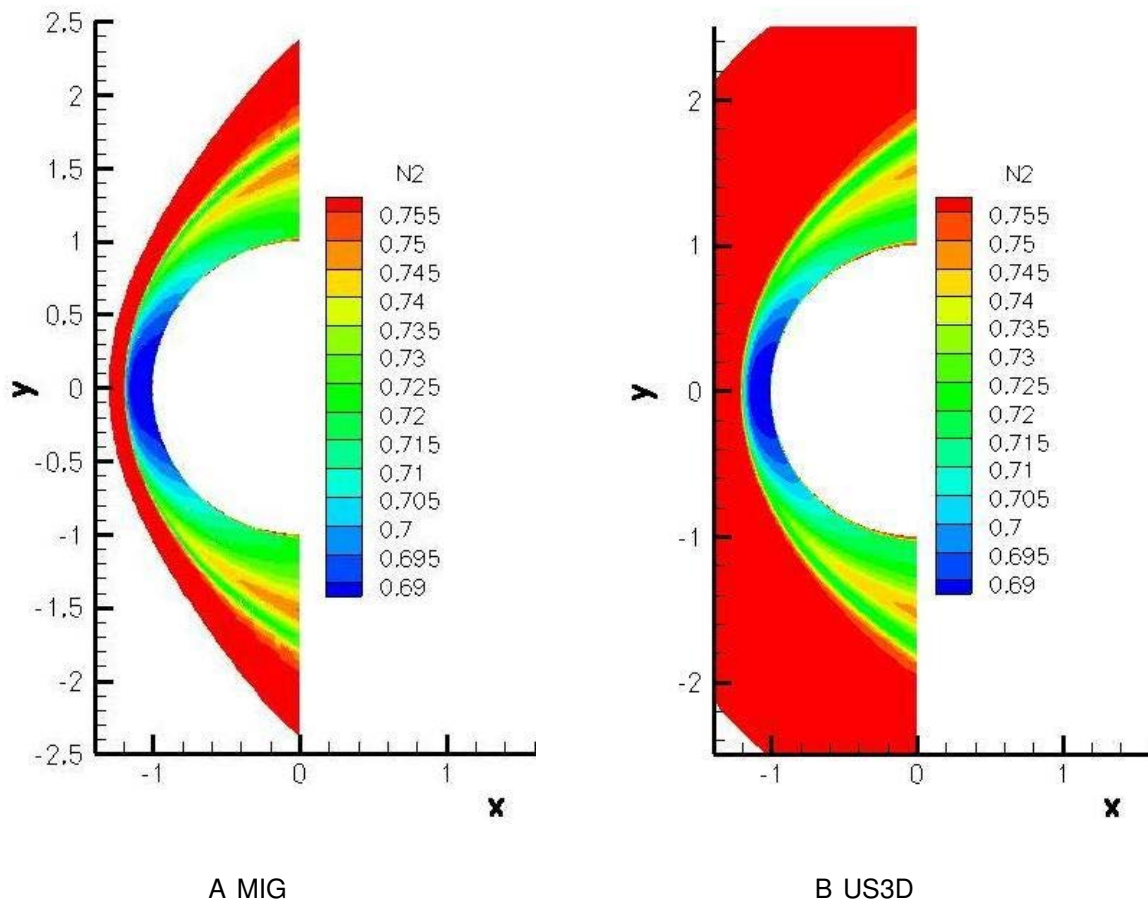
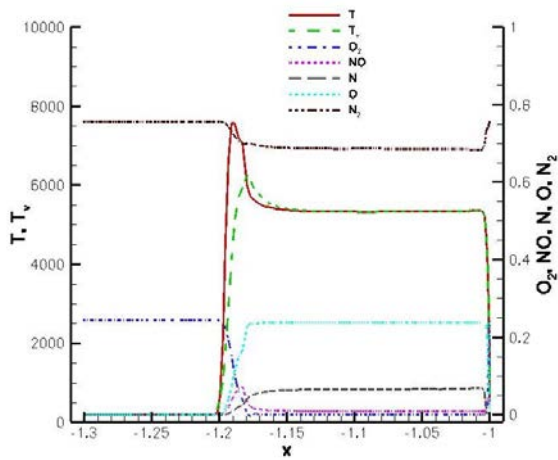
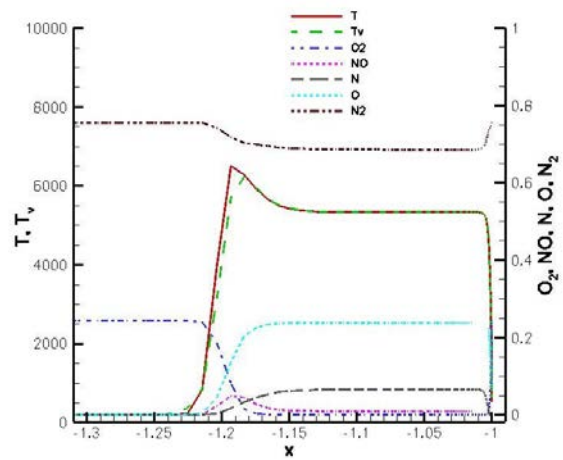


Figure 6-24. Mass fraction contours of N_2 for $N_2 + O_2$ case. A) Contours for MIG. B) Contours for US3D. Maximum dissociation of N_2 occurs near the stagnation region. Interestingly, increase in the N_2 mass fraction, occurs just after the shock, at the top and bottom of the cylinder.



A MIG



B US3D

Figure 6-25. Stagnation line plots for $N_2 + O_2$ case. A) Plots for MIG. B) Plots for US3D. Temperatures, T and T_v , and mass fractions of all the species are shown. High temperature rise at the shock (in MIG) is observed relative to US3D. N_2 dissociates only partially in the shock. Production of NO is seen only in the shock, after which it again dissociates back to N and O.

CHAPTER 7

EFFECT OF PLASMA DBD ACTUATORS ON HYPERSONIC FLOW CASES

Active flow control is a very expanding topic of research, due to its vast industrial applications. Out of all flow control methods, like mechanical flaps, wall synthetic jets or MEMS; plasma based flow control is very promising. This is due to their robustness, simple design, low power consumption and real time flow control with high frequency [90].

Non-thermal plasmas are known to create maximum air flow speeds of 8 m/s (at 0.5 mm distance from wall) in a quiescent flow and able to provide effective flow control for freestream flow velocities up to 30 m/s. Air flow control can have many applications. E.g., by increasing the turbulence (with a wall jet), one can enhance the flow mixing in the separation region of the wing. Thus delaying the flow separation on the wing, one can increase the lift obtained. On the other hand, by decreasing turbulence, one can reduce the noise of an aerodynamic system.

In hypersonic flow control, plasma actuators have been successfully used along with magnetohydrodynamics [91]. In addition to this, the use of nano-pulsed DBD plasma actuators [92] has allowed significant shift (around 20 %) in distance of the detached bow shock from the cylinder. Both these cases add pressure perturbation to the flow.

In [91], via the use of direct current surface plasma discharge, electromagnetic perturbation is added to the flow that results in the growth of displacement thickness of the shear layer, being amplified by the pressure interaction. This mechanism depends on triggering the flow instability without requiring to add huge amount of power to ionize the flow. Hence, the power requirement of this device is low. This has been demonstrated to deflect the freestream flow of Mach 5, by an angle of 5° . This effect is expected to increase with the increase of incoming flow Mach number.

According to [91], DBD plasma actuators are most effective at bifurcation points in the flowfield, where the flow velocities are low (≤ 30 m/s). However, an important feature of hypersonic flows is the strong inviscid-viscous interactions. Boundary layer in hypersonic flow is no longer negligible as it is in subsonic or supersonic flows. This large displacement thickness, in the boundary layer, displaces the incoming flow, thus producing outward flow deflection. This causes the compression waves to be produced, which coalesce into a shock wave. This shock wave then interacts with the boundary layer to close the interaction loop.

These inviscid-viscous interactions strengthen on the increase in Mach number of the incoming flow, hence this mechanism is exploited both in the case of adding electro-magnetic perturbation to the hypersonic flow [91] and in the case of nano-pulsed discharge by adding a pressure perturbation in the shear layer of the flow [92]. The former plasma case has been applied to a flat plate and to the geometric cowl of scramjet.

The surface DBD plasma actuators depend on electrohydrodynamic acceleration of wall jet to actuate the flow near the wall. But, this becomes exceedingly difficult to achieve at high speeds, since it becomes excessively difficult (because of large power requirements) to maintain the high space charge density and high electric field in the discharge.

An alternative to this is sought in [93] wherein a series of high voltage nanosecond pulses (producing very high electric fields for a very short duration of time) are used to reattach the flow for Mach 0.85. In this case, the main mechanism of flow control is rapid localized heat generation, rather than electrohydrodynamic force in the case of micro-second pulsed DBD actuators [94]. In quiescent flow, this nanosecond pulsed DBD plasma actuator is known to produce shock waves [93].

It is interesting to note that the energy responsible for plasma breakdown in one pulse for nanosecond plasma (lasting 10 ns) and microsecond plasma (lasting 10 μ s)

is almost same [95]. Various methods of flow control, used for bow shock control in supersonic flows, like pulsed DC arced discharge, pulsed microwave discharge and laser optical breakdown, use thermal heat addition to reduce wave drag and surface heat transfer.

But, since the nanosecond pulsed plasma, applied to increase the shock stand-off distance temporarily, is in cold flow ($T_{\infty} = 56$ K); the heat loss due to increased shock distance is seen to be countered by the net heat added by the nano pulse. In fact, the C_h profiles increase by two orders of magnitude [96]. It is not clear, if the same effect will be observed in the case of hypersonic flow over re-entry vehicles, wherein the maximum temperature in the flowfield is of order of 10,000 K? The maximum temperature of the flow-field in the case of [96] is 300 K.

Our main motive in the present work is to reduce the net surface heating coefficient, C_h at the surface of the vehicle. Nanosecond pulse, though promising to increase the shock stand-off distance, seems to add more heat during its duty cycle. Although, it is not clear if this will be beneficial for a re-entry vehicle or not.

Therefore as an alternative, we attempt to see the effect of micro-second pulsed DBD plasmas, wherein the power deposition is minimal (approximately 10 W/m^2 of the electrode).

The boundary layer for hypersonic flows (at the stagnation point) is few millimeters. In fact, the flow has very low velocity, close to the stagnation point. Hence, the localized body force of DBD plasma actuator can significantly affect the flow in this region, thus making significant changes in the C_h profile over the cylinder. We are interested in this application.

7.1 Effect of Plasma DBD Actuator on Surface Heating in Mach 17 Hypersonic Flow Over Cylinder

We look into the effect of micro-second pulsed DBD plasma actuators on hypersonic flows. As an example, we consider Mach 17 hypersonic flow over cylinder from Chapter

6. The cylinder radius is 1 m. The body force as a result of plasma actuation is taken from [97] and applied at the stagnation point on the cylinder surface. We first note the effect of this actuation, on the heat transfer coefficient, C_h , in order to enhance our understanding of the physics of this problem. Various designs for plasma actuators are then considered, by varying locations and polarity (i.e. direction of the force) of the plasma actuation.

We employ the grid given in Figure 7-1 for these results and use DG methods along with slope limiter to capture the shock. This grid has 256×100 elements in the domain, where the 256 elements are uniformly distributed in the θ direction and 100 elements, with varying sizes, are distributed along the radial direction.

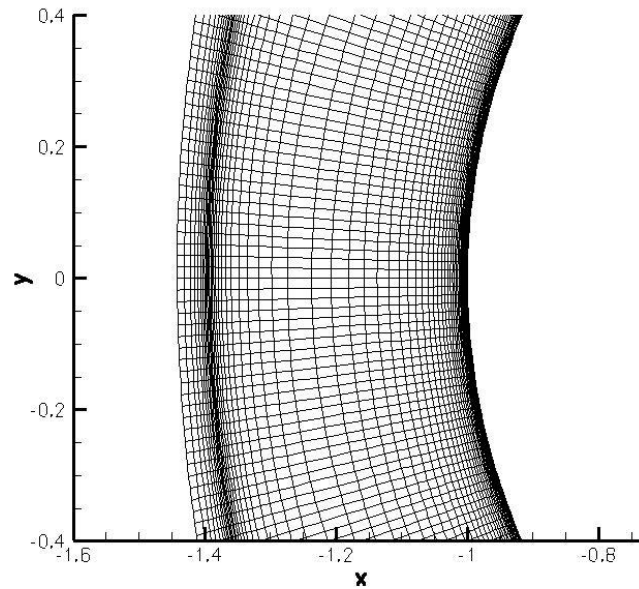


Figure 7-1. Mesh for plasma actuation of hypersonic flow. It has 256 X 100 elements.

The body force distribution, based on first principles simulation of plasma discharge [97], is described as,

$$f_x = \frac{F_{x,0}}{\sqrt{F_{x,0}^2 + F_{y,0}^2}} \exp \left(- \left(\frac{(x - x_0) - (y - y_0)}{y - y_0 + y_b} \right)^2 - \beta_x (y - y_0)^2 \right) \quad (7-1)$$

$$f_y = \frac{F_{y,0}}{\sqrt{F_{x,0}^2 + F_{y,0}^2}} \exp \left(- \left(\frac{(x - x_0)}{y - y_0 + y_b} \right)^2 - \beta_y (y - y_0)^2 \right) \quad (7-2)$$

Here, $F_{x,0} = 2.6$, $F_{y,0} = 2.0$, $\beta_x = 7.2 \times 10^4$, $\beta_y = 9.0 \times 10^5$ and $y_b = 0.00333$. x_0 and y_0 represent the edge location of electrodes. This body force is integrated over the whole domain, and is multiplied by a factor to give average force distribution of approximately 10 kN/m².

This body force distribution, when applied at the stagnation point of the cylinder surface, looks as given in Figure 7-2.

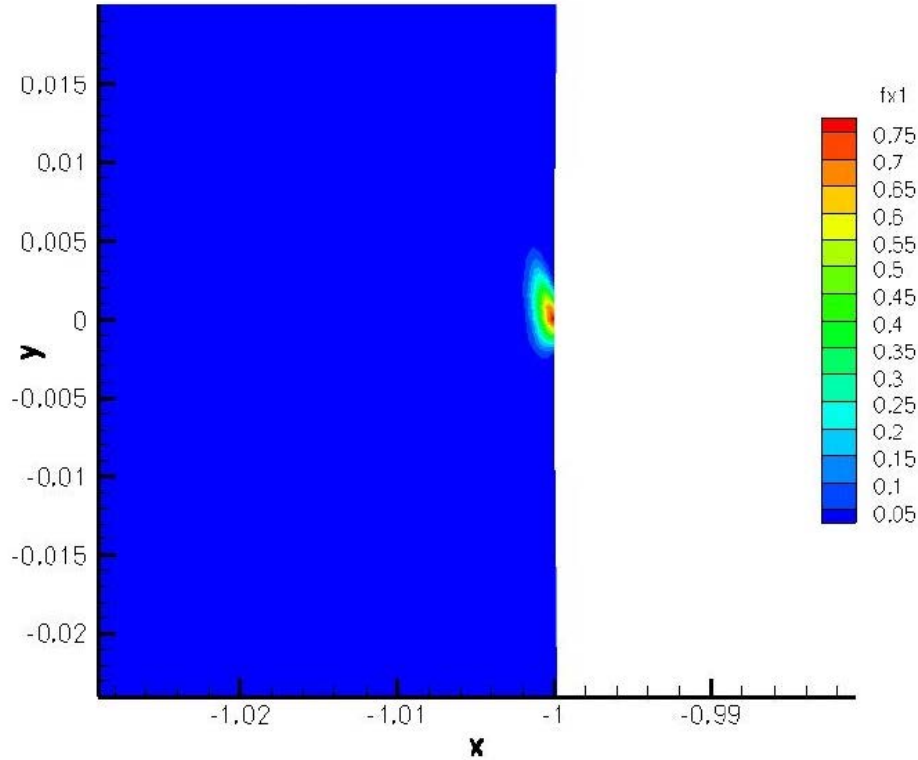


Figure 7-2. Plasma body force distribution in 'plasma1' configuration. Plasma actuator is applied at the stagnation point, with body force in the +y-direction.

We present the results for plasma actuation of hypersonic flows. Profiles for surface heat transfer coefficients, C_h , are shown for three different configurations of placement of DBD plasma actuators. 'plasma1' refers to the plasma actuator placed at the stagnation point, with body force in the +y-direction; 'plasma2' refers to two plasma actuators placed at 25 mm distance (measured along the circumference of the cylinder), away from the stagnation point. In this case, both plasma actuators apply body force away from each other, i.e. plasma actuator in positive part of y-axis, applies force in +y-direction and plasma actuator, in negative part of y-axis, applies force in -y-direction. In the third configuration, i.e. 'plasma3', the locations of plasma actuators is unchanged from 'plasma2' configuration, but the directions of both forces are reversed so that both the forces act towards each other. The schematic in Figure 7-3 illustrates the three configurations.

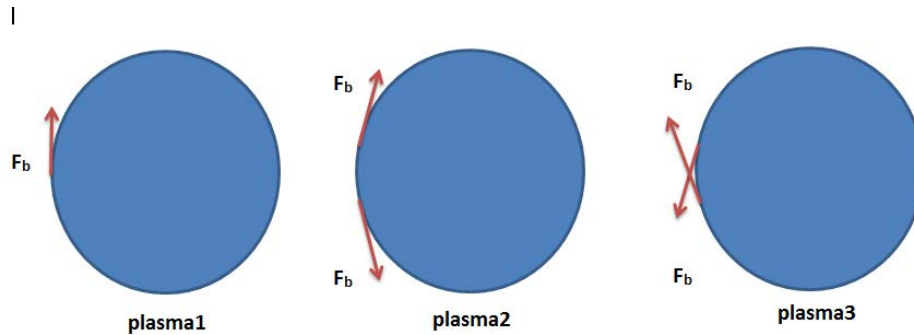


Figure 7-3. Three configurations of plasma DBD actuators. In the first configuration, plasma actuator is applied at the stagnation point, with flow forcing in positive y-direction. Second and third configurations have same placements of the actuators, i.e. ± 25 mm from stagnation point along cylinder circumference, but with reversed flow forcing. Second configuration has forces pointing away from each other and third configuration has forces pointing towards each other.

The effect of these three configurations on the C_h profile is summarized in Figure 7-4 .

Plasma1 configuration leads to both increase and reduction of C_h profile along the surface of the cylinder. Maximum value of C_h of 0.00846 occurs at $\theta = -0.0136$ (very

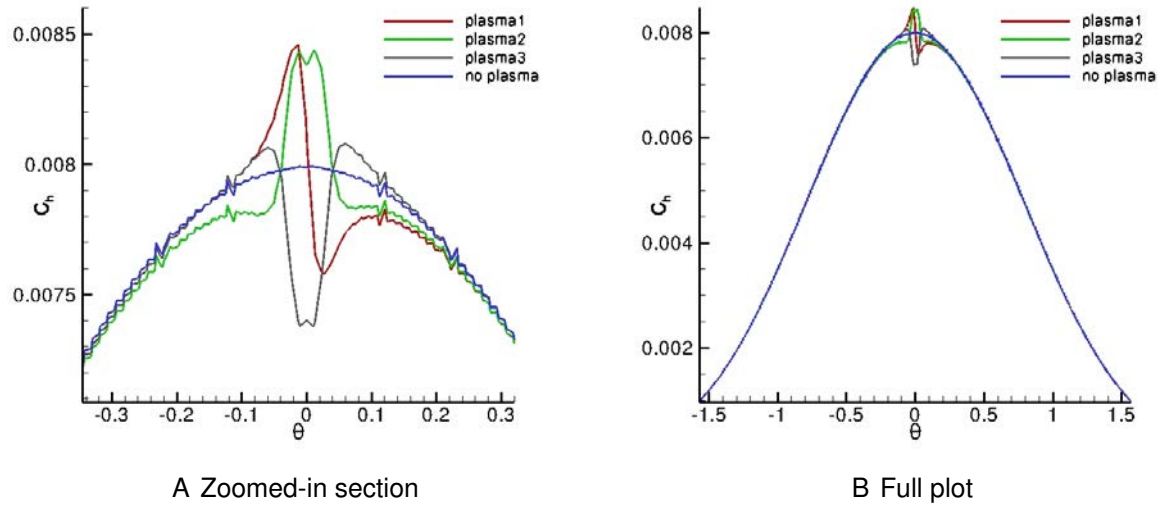


Figure 7-4. Effect of plasma on C_h profile for hypersonic flow over cylinder. (A) Zoomed in section of the C_h profile. (B) Full plot of C_h profile. The base case of 'no plasma' from MIG, compares well to C_h profile from LAURA. 'plasma3' gives the best possible C_h reduction.

close to stagnation point), and minimum value of C_h of 0.00758 occurs at $\theta = 0.025$.

Since radius is 1 m, these locations correspond to -13.6 mm and 25 mm distance away from stagnation point.

Upon performing integration under the curve, we can see that the plasma actuator provides net cooling effect. Other two configurations, plasma2 and plasma3 are similar to moving the plasma's effect on C_h profile (in plasma1) in ± 25 mm direction to the location of plasma actuator, and reversing the C_h profile based on the direction of plasma body force. Thus, the second and third configurations give overall heat transfer addition and reduction respectively.

To understand the flow physics, the effect of plasma actuator on the temperature and velocity profiles, near the wall (in direction normal to the wall), is analyzed, w.r.t. 'no plasma'. First, the effect of configuration1 is considered.

The effect of actuator is easily seen in temperature contours, both with and without plasma (Figure 7-5). Visually, the temperature contours (for 'plasma1') are moved

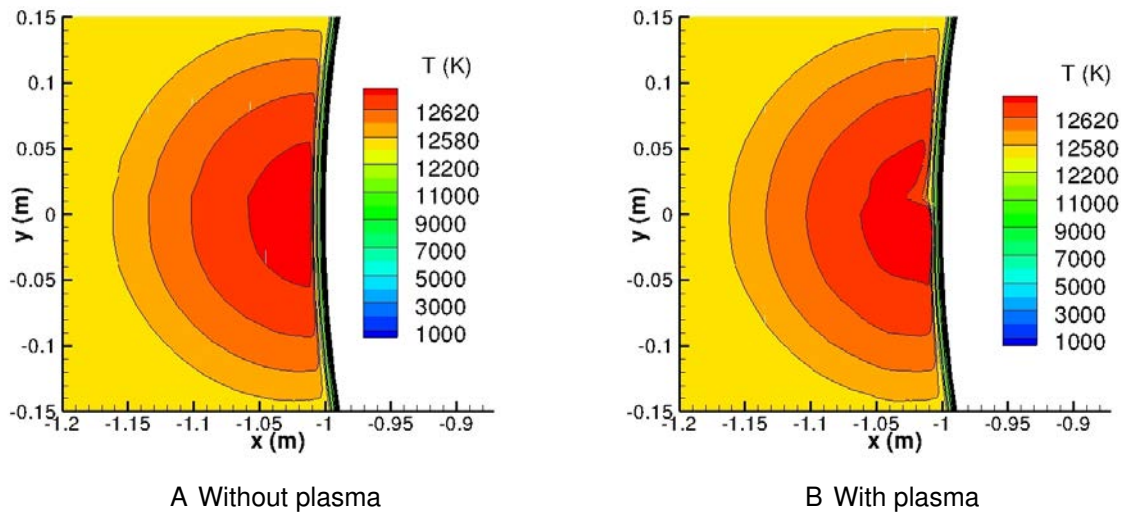


Figure 7-5. Effect of plasma actuator, in 'plasma1', on temperature contours. A) Temperature contours for 'no plasma' case. B) Temperature contours for 'plasma1' case.

closer to the cylinder surface for negative y-axis and away from the surface for positive y-axis, when compared to 'no plasma' case. Thus, the actuator reduces the C_h value at about 25 mm distance downstream from its actual location, by strongly pushing the temperature contours away from the cylinder surface.

It can therefore be seen that the micro-second pulsed plasma DBD actuator, which are generally considered only appropriate for subsonic flows, have significant effect on hypersonic flows (near the boundary layer), in terms of heating. This is due to large thickness of boundary layer encountered in hypersonic flows, which results in low magnitude of velocities for a significant distance near the cylinder surface, and hence allows the plasma actuator to make some significant effect on the surface heating in hypersonic flow.

We look at the temperature and velocity profiles, in Figure 7-6 and 7-7, near the cylinder surface, as we move away from the wall in the normal direction.

We notice from Figure 7-6, that all the temperature profiles fall into a single curve for the 'no plasma' case. For 'plasma1' case, the temperature profiles are higher

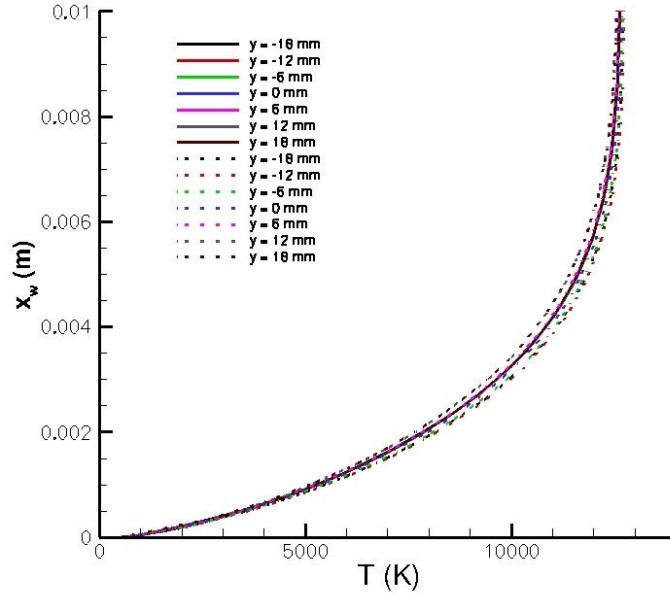


Figure 7-6. Temperature plots in 'plasma1' configuration. Temperature plots in the flow are shown with distance from the wall, denoted as x_w . Y locations correspond to the distances along the cylinder circumference, starting from the stagnation point. Solid lines refer to the results without plasma and dotted lines refer to the results with plasma (plasma1).

relative to the 'no plasma' case for locations closer to the actuation point in the positive y-direction; and below the temperature profile for 'no plasma' case for locations closer to the actuation point but in the negative y-direction. This corresponds to the increment and decrement observed in C_h profile in Figure 7-4. From Figure 7-5, we note that the maximum value of C_h is at -12.5 mm, close to -13.6 mm, seen in Figure 7-4.

Velocity profiles, in Figure 7-7, indicate that there is a significant increase of y-velocity, from 1 m/s to 8.5 m/s, at a distance of nearly 1 mm away from cylinder surface at stagnation point. Thus, a strong flow velocity is actuated, which is why the actuator causes significant effect in the C_h value at the stagnation point, in the positive y-direction.

Next, we look at flows in second and third configurations. Forces point away from each other in plasma2 and towards each other in plasma3. The temperature

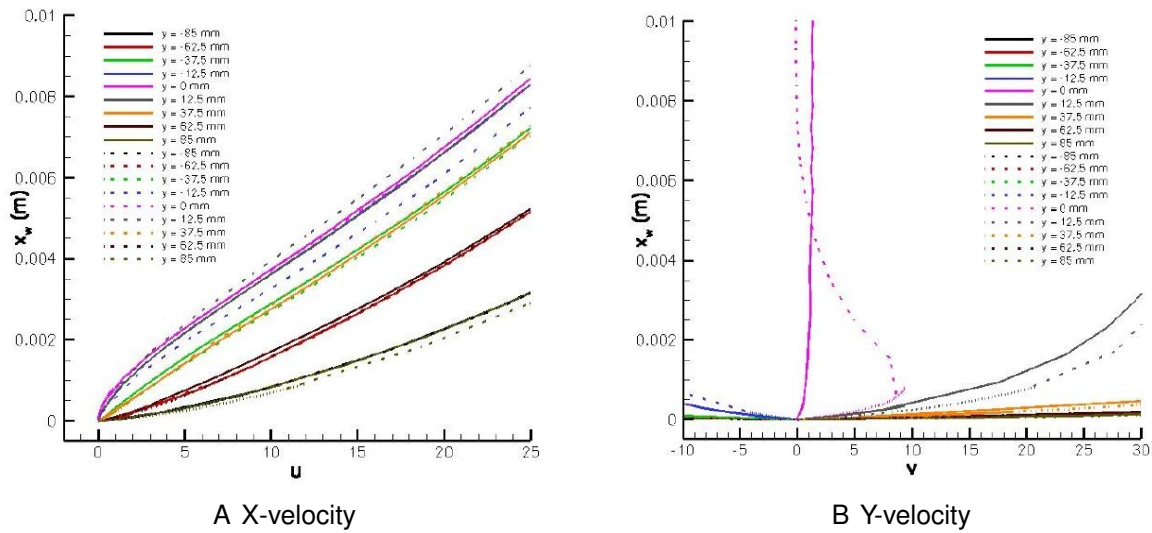


Figure 7-7. Velocity profiles in 'plasma1' configuration. A) X velocity profile shown with wall distance. B) Y velocity profile shown with the wall distance. x_w is the distance, measured in the normal direction, from the wall. Y-velocity is almost parallel to the cylinder surface, near the stagnation point, and is thus relevant to understand the cause of observed change in C_h value, near the stagnation point.

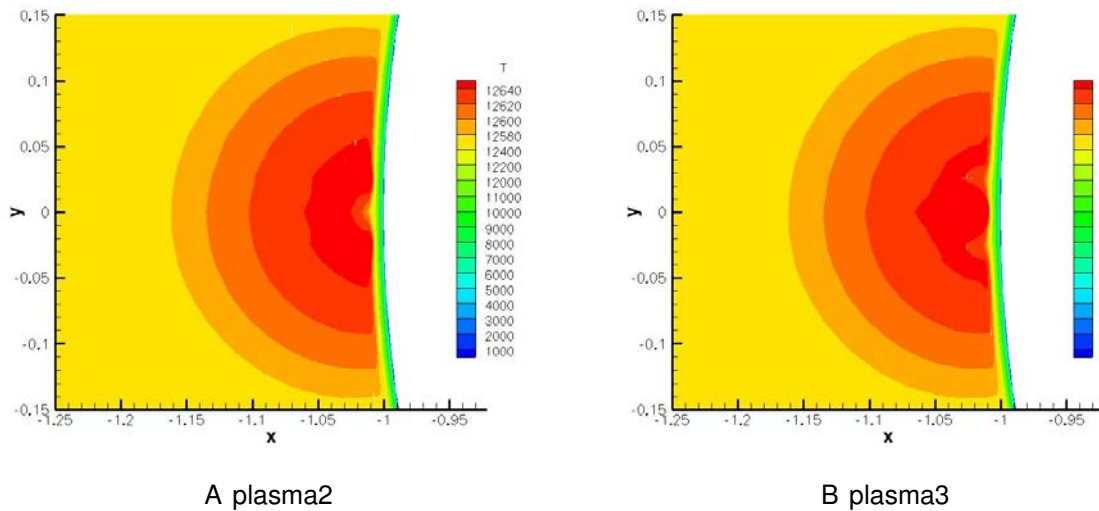


Figure 7-8. Temperature contours for plasma2 and plasma3 configurations. A) Temperature contours for plasma2 configuration. B) Temperature contours for plasma3 configuration.

contours close to the stagnation region are shown in Figure 7-8. It is clearly seen that in 'plasma2' configuration, the temperature contours are compressed relative to 'no plasma' case, from $y = -50$ mm to $+50$ mm. Thus, for $\theta = -0.05$ to 0.05 , we see that C_h value for plasma2 configuration is higher than 'no plasma' configuration. For rest of the region, C_h profile falls below the C_h profile for 'no plasma' case.

Correspondingly for 'plasma3' configuration, the temperature contours are pushed away from the cylinder wall, again from $y = -50$ mm to $+50$ mm, thus causing reduction in C_h value relative to 'no plasma' case.

What causes the temperature contours to be pulled into and pushed away from the wall in plasma2 and plasma3 configurations respectively? We will try to understand this from the velocity schematic given in Figure 7-9, for the 'plasma1' configuration. Plasma body force induces a flow (shown in red) in the direction of the force. The oncoming flow (shown in blue) hits the cylinder surface (approximated by a flat wall in black).

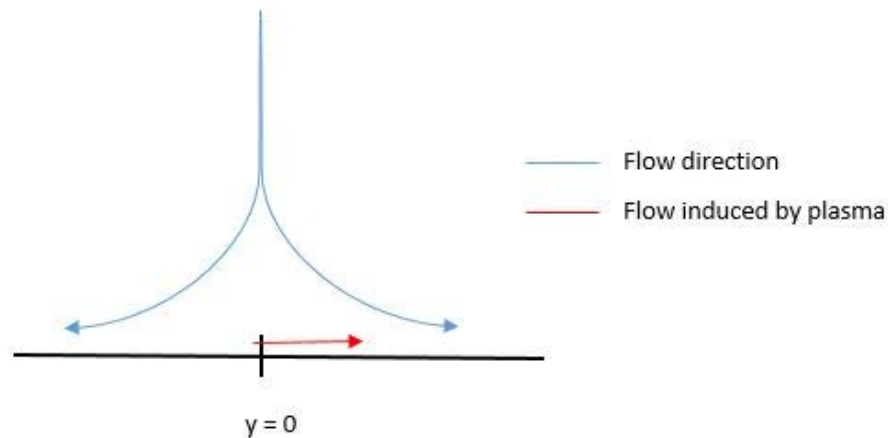


Figure 7-9. Schematic of flow induced by plasma body force. The force and the induced flow (in red) is in $+y$ direction. The oncoming flow (in blue) hits the wall (in black). The cylinder surface close to the stagnation region can be approximated by a flat wall.

Without the plasma body force, the flow has zero tangential velocity (along y -axis) a few mm distance away from the wall, and hence maximum value of C_h is experienced

at the stagnation region. The flow induced, by the plasma, causes a leftward shift (from stagnation point) of the point of zero tangential velocity. This causes the maximum in C_h to shift slightly to the left in Figure 7-4. The question, that arises, is why C_h profile shoots above the maximum value of C_h at the stagnation point for the 'no plasma'?

This is answered when looking closely (near the region of stagnation point), at the changes in velocity profiles, induced by the plasma in the 'plasma1' configuration, relative to 'no plasma' case in Figure 7-10.

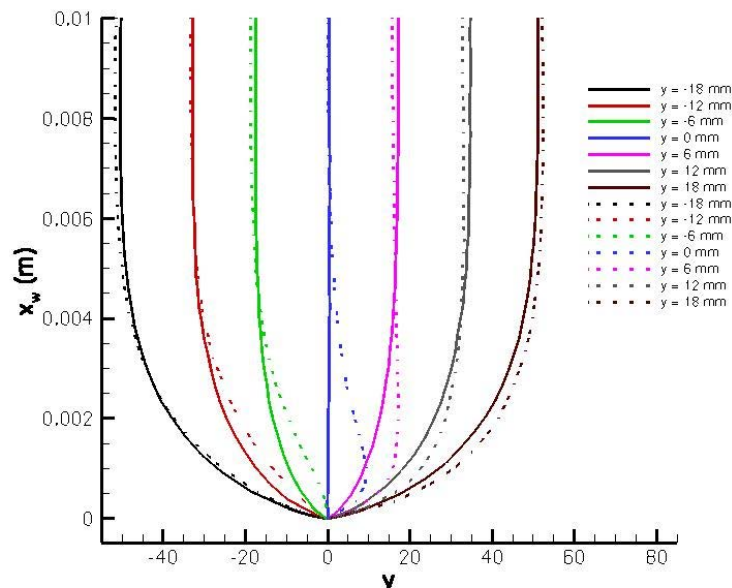


Figure 7-10. Y-velocity profile in 'no plasma' and 'plasma1' configurations. Y-velocity (parallel to the wall) is generated for several locations, to the left and right of the stagnation point. Dotted and solid lines are used for plots with and without plasma actuators.

From Figure 7-10, we notice that plasma actuator decelerates the flow (going in negative direction, to the left of the stagnation point), hence causing increased heating at the surface, to the left of the stagnation point, and accelerates flow from stagnation point to approximately 18 mm to the right of the stagnation point, hence reducing heat transfer to that surface. Plasma actuator sucks in fluid at high temperature, from the bottom of the cylinder stagnation point and makes it flow over the cylinder surface to the

top of the cylinder stagnation point. Thus, it increases the heat transfer to the bottom of the cylinder stagnation point, by pushing the high temperature fluid closer to the wall. It decreases the heat transfer to the top of the cylinder by generating a wall jet to the top of the cylinder, that pushes away the temperature contours from the wall.

Temperature profiles for plasma2 and plasma3 configurations in comparison to 'no plasma' case, can be summarized in following way.

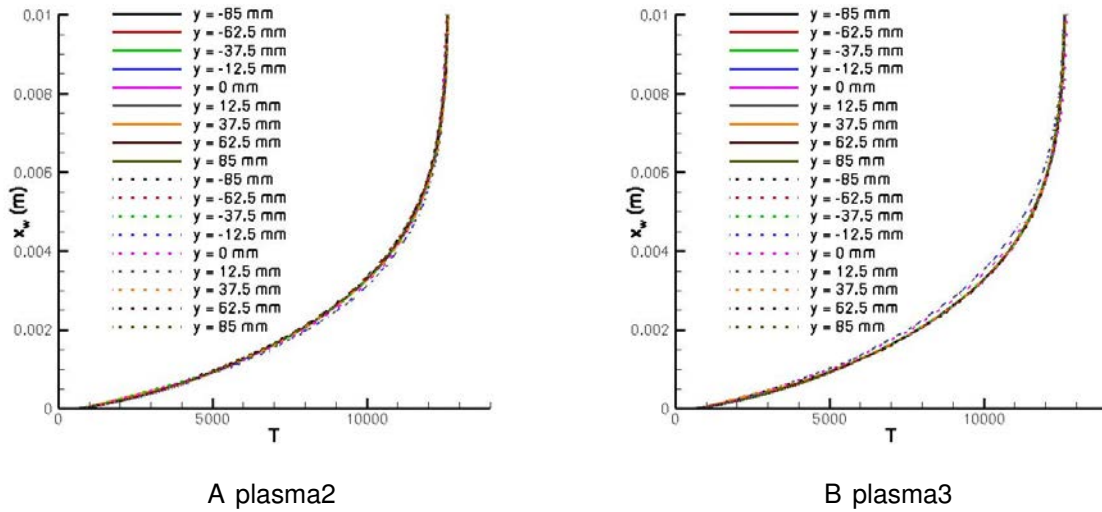


Figure 7-11. Temperature profiles for 'plasma2' and 'plasma3' configurations. A) 'plasma2' configuration. B) 'plasma3' configuration. Results are shown in comparison to 'no plasma' case.

It can be seen in Figure 7-11 that temperature profiles for 'plasma2' case, primarily lie below temperature profile for 'no plasma' case and that for 'plasma3' case, primarily lie above 'no plasma' case, thus being consistent with higher and lower C_h profiles observed for 'plasma2' and 'plasma3' cases respectively in reference to 'no plasma' case.

Same observation is also made in the velocity profiles for y-velocity, for 'plasma2' and 'plasma3' cases (Figure 7-12). Here, the plasma DBD actuator located in positive y-axis, introduces a wall jet in the direction of the fluid flow in plasma2 configuration and in opposite direction of fluid flow in plasma3 configuration. By increasing the flow

velocity next to wall, plasma actuator is able to entrain more of high temperature fluid, thus producing more surface heating for plasma2 configuration, and by decreasing the flow velocity next to wall, it is able to push the high temperature fluid away from the wall, thus reducing heating next to the wall for plasma3 configuration.

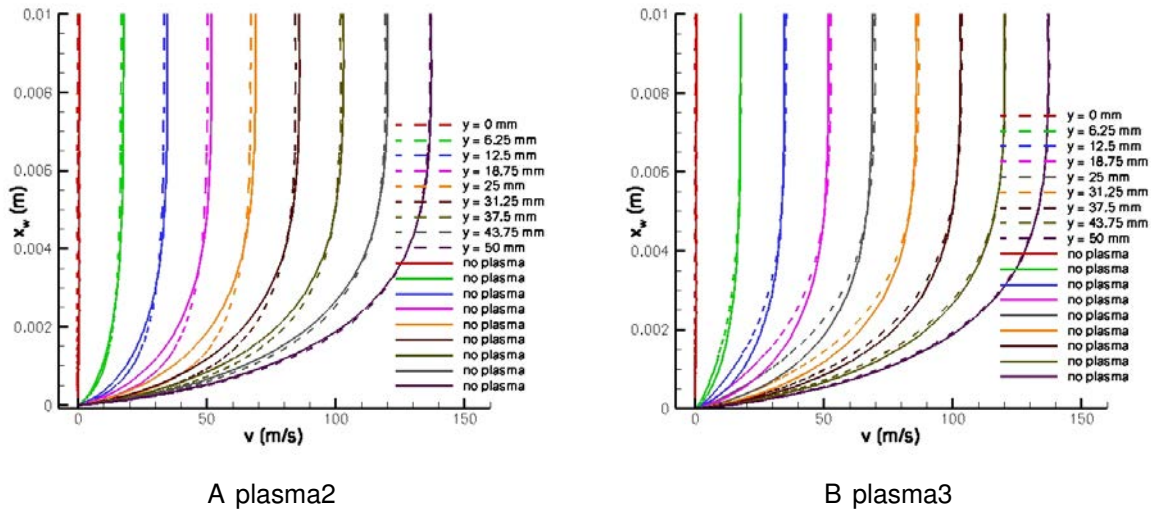


Figure 7-12. Y-velocity profiles for 'plasma2' and 'plasma3' configurations. A) 'plasma2' configuration. B) 'plasma3' configuration. Results are shown in comparison to 'no plasma' case.

7.2 Effect of Plasma DBD Actuator on Surface Heating in Mach 17 Non-equilibrium Hypersonic Flow Over Cylinder

After successfully looking into the effect of plasma DBD actuator on the Mach 17 flow over hypersonic flow, we investigate its effect on a cylinder in hypersonic flow with thermo-chemical non-equilibrium. Applying the plasma actuators in the three configurations described in the section 7.1, we observe a similar effect on the surface heating in Figure 7-13.

When comparing plasma3 configuration to the base case, reduction of temperature gradient next to wall (at stagnation line) is observed (Figure 7-14). This is true for both translational-rotational temperature, T and vibrational temperature, T_v . The effect is dominant to within 10 mm distance away from wall.

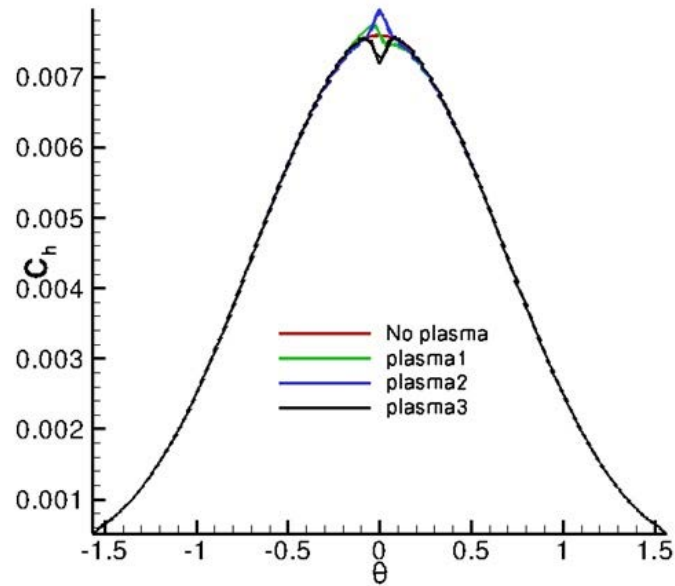


Figure 7-13. Effect of plasma actuator on C_h profile for NEQ hypersonic flow. In reference to the 'no plasma' case, 'plasma1' case gives both increase and decrease in C_h value, 'plasma2' case gives overall increase in C_h value and 'plasma3' case, as expected, gives overall reduction of heating.

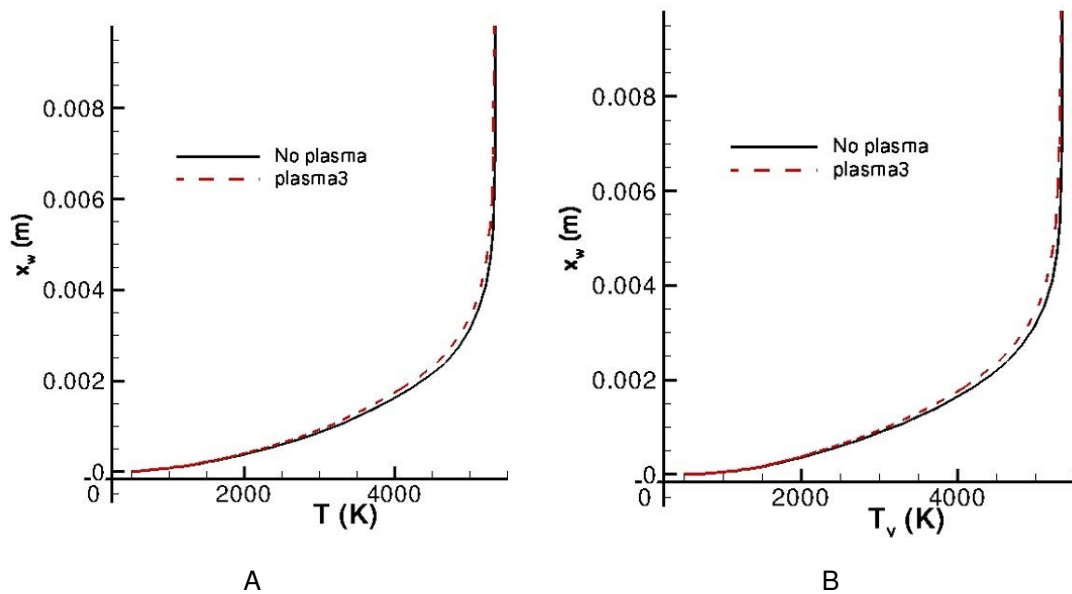


Figure 7-14. Effect of plasma3 configuration on stagnation line plots of T and T_v . A) Plot of T . B) Plot of T_v . Effect is shown in reference to 'no plasma' case. Only a minor effect is seen in the temperature plots for distance up to 10 mm away from cylinder wall.

In addition to temperature profiles, the application of plasma DBD actuator is also seen to have effect on species mass fractions. This effect is not so pronounced for O_2 and O, as can be seen in Figure 7-15.

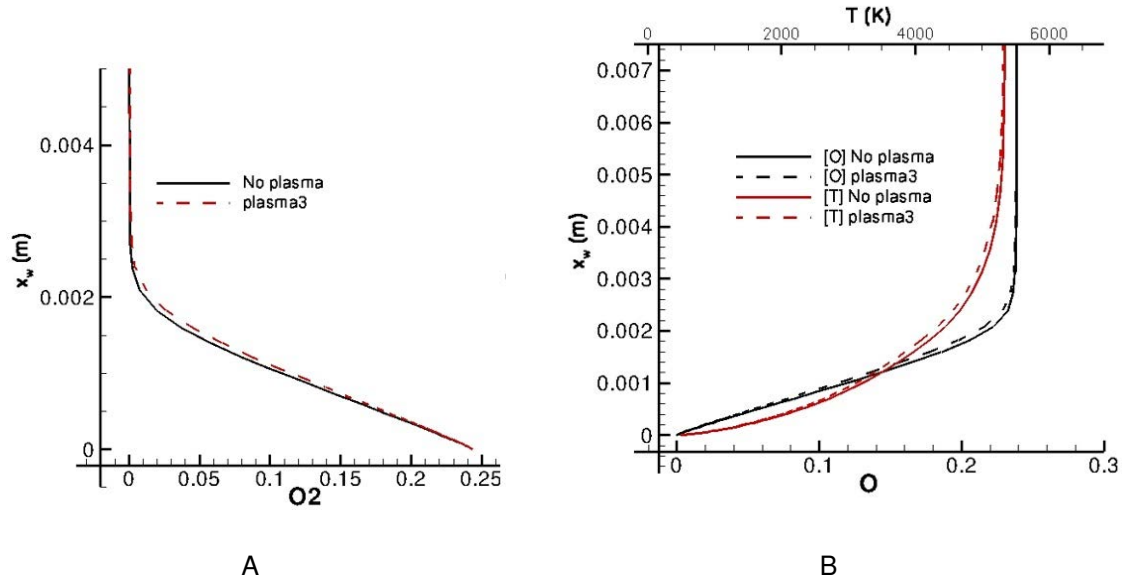


Figure 7-15. Effect of plasma3 configuration on stagnation line plots of O_2 and O. A) Plot of O_2 . B) Plot of O. This effect is shown in reference to 'no plasma' case. Only a minor effect is seen in the plots for distance up to 6 mm away from cylinder wall.

However, more significant effect is seen on stagnation line plots for N and NO (Figure 7-16). The difference of plasma3 case, w.r.t. the base case is seen up to 25 mm distance away from the wall. In Figure 7-16 A, we notice sudden reduction of N, close to the wall, for both with and without plasma actuator. This happens due to reduction in temperature, close to the wall (due to the boundary condition). At lower temperatures, nitrogen can not sustain in the atomic form, and hence recombines to N_2 (primarily) and NO near the wall. This recombination releases large amount of heating to the wall. A minor change in temperature, because of plasma, causes significant variation in mass fraction of N, up to distance of 25 mm away from wall.

For NO, there is increase in mass fraction, close to the wall (from 4 mm to 2 mm next to the wall). This is due to atomic N and O recombining into N_2 , O_2 and

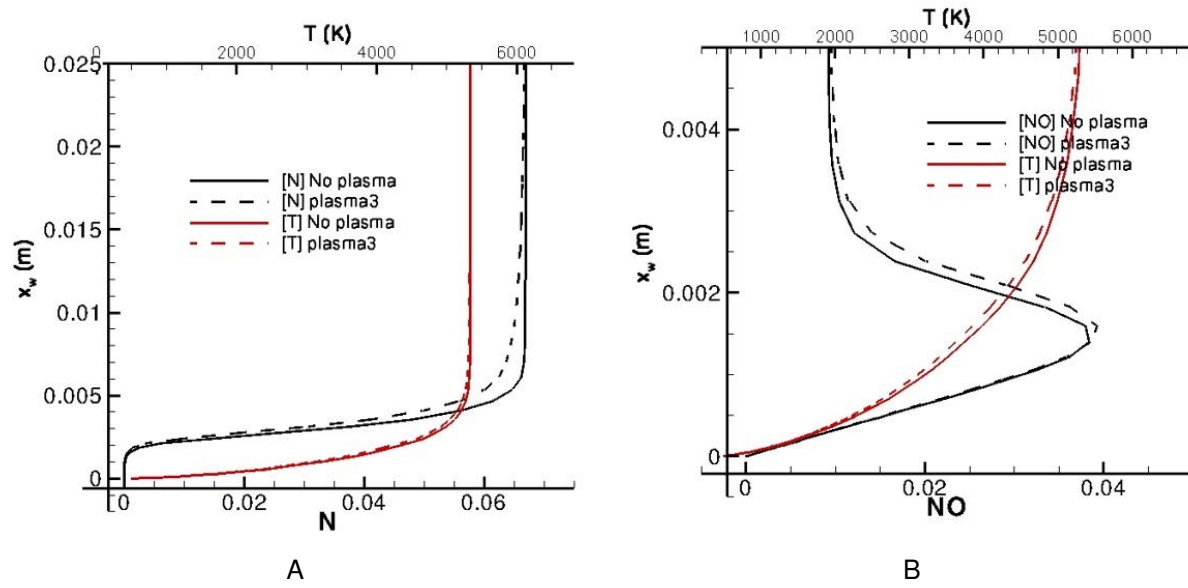


Figure 7-16. Effect of plasma3 configuration on stagnation line plots of N and NO. A) Plot of N. B) Plot of NO. This effect is shown in reference to 'no plasma' case. Significant difference is noted, in the mass fractions of N and NO, due to plasma DBD actuator in plasma3 configuration. For N, the effect is seen up till 25 mm distance away from wall.

NO. For distance of 2 mm away from the wall, even NO species vanishes due to the super-catalytic wall boundary condition. Hence a small peak for NO is observed in Figure 7-16 B.

Plot of N_2 in Figure 7-17 shows that its mass fraction increases in two phases when approaching wall. From 30 mm to 2 mm distance from the wall, N_2 monotonically increases, after which there is a dip in its mass fraction. This is due to mass fraction of NO increasing at a distance of 2 mm close to wall. When NO start decreasing at approximately 1.5 mm distance away from wall, N_2 again begins to increase in its mass fraction. Thus, significant effect of plasma DBD actuators is noted on hypersonic flows, both with and without thermo-chemistry.

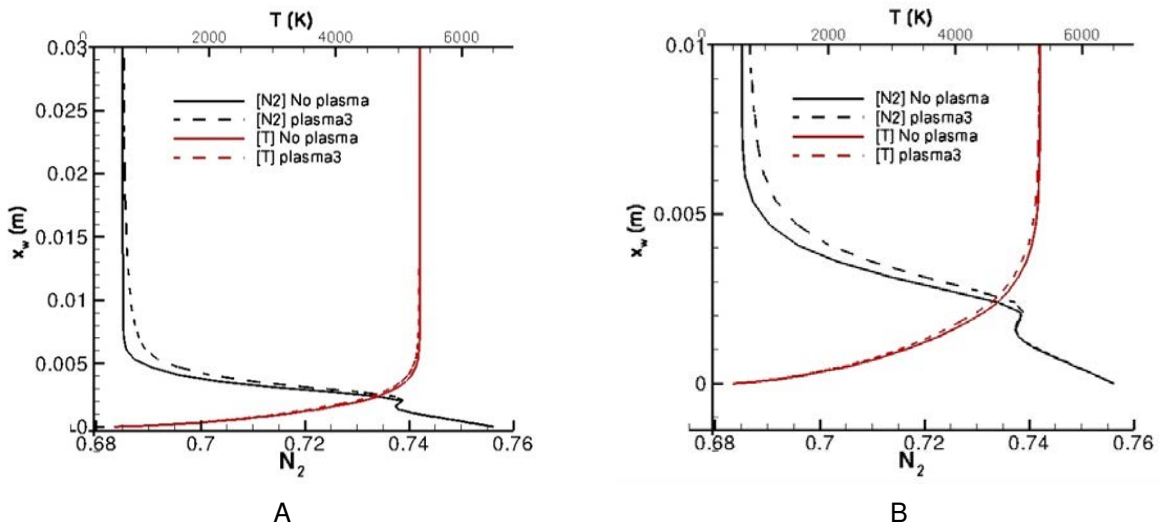


Figure 7-17. Effect of plasma3 configuration on stagnation line plots of N_2 . A) Stagnation line plot of N_2 near the wall. B) Zoomed-in section. A significant difference is seen in curves for N_2 up to 30 mm distance away from wall

CHAPTER 8 CONCLUSION

In this work, we have successfully introduced discontinuous Galerkin (DG) methods to the fields of thermal ablation and hypersonic non-equilibrium flows. These two areas are characterized by highly non-linear, fully coupled and multi-physics problems. The challenges in thermal ablation include, unsteady flow of pyrolysis gases (which is a mixture of 14 gas species considered in chemical and thermodynamics equilibrium) flowing through a porous media, which is undergoing charring and ablation phenomena. For hypersonic flows with thermo-chemical non-equilibrium, the challenges are chemically reacting gas species (5 species model of N_2 , O_2 , NO , N and O was used) undergoing convection and diffusion processes in thermal non-equilibrium (we considered a two-temperature, $T-T_v$ model).

Because of their complex governing equations, these problems are hard to analyze for their physics and thus difficult to debug as well. In addition, for an efficient solution process, a fully implicit method is indispensable. Without a fully implicit approach, the solution process is severely constrained with the time step restriction. This is due to high valued source terms occurring in both thermal ablation and hypersonic non-equilibrium flows. However, a fully implicit method requires the formulation of the jacobian matrices. This is a difficult task as the jacobian matrix is complex due to the complexity of the governing equations, and has to be re-tailored at the boundary for specific set of boundary conditions used. A small human error can significantly affect the convergence of the solution procedure. For this purpose, we implemented numerical evaluation of these jacobians, and carefully tailored them to the boundary conditions applied. We were able to get very good convergence rates for both problems, using CFL numbers of 10,000 and 5,000 for thermal ablation and hypersonic flow problems respectively. Herein, no approximations were assumed and the full set of governing equations were used.

We also demonstrated high-order accuracy and mesh convergence for the validation cases, shown in this work. Problems ranging from low speeds ($M = 0.01$), to moderate ($M = 0.3, 0.38$ and 0.5) and high speeds ($M = 6, 10$ and 17) were solved. In summary, we covered a wide range of flows varying from subsonic, transonic, supersonic and hypersonic flows.

In the field of hypersonic flows, both with and without thermo-chemistry, we demonstrated the application of r-p adaptivity method for capturing solutions with shock. With $p = 0$ used in the shock region, we captured shocks successfully without the use of slope limiters or artificial viscosity methods. r-adaptivity was used to selectively refine the elements in the shock, bringing in elements from outside the shock. Thus, extra number of elements, employed in the case of h-adaptivity, were not needed. This saves significant computational effort. Essentially, we successfully demonstrated the use of r-p adaptivity for hypersonic flows with inviscid, viscous and thermo-chemical non-equilibrium formulations. A good agreement for shock stand-off distance, surface heating coefficient and the temperature and species mass fractions was made for inviscid, viscous and non-equilibrium hypersonic flows respectively.

In addition to above, we also simulated the effect of micro-second pulsed, sinusoidal Dielectric Barrier Discharge (DBD) plasma actuators on the hypersonic flow over cylinder. A significant effect, on the heating on the cylinder surface, was noted. This has been possible due to the large boundary layer and small velocities, especially in the stagnation region, where the plasma actuators are able to actuate a wall jet close to cylinder surface. For the basic setting of the plasma actuator placed at the stagnation point of the cylinder, this wall jet pushes the fluid (close to the stagnation point) in the positive y-direction. This brings the high temperature gas, below and above the actuator, closer to and away from the cylinder surface respectively. Thus, the application of plasma actuator results in higher heating rate for surface below the stagnation point, and lower heating rate for surface above stagnation point.

In the two different configurations tried with two plasma actuators used on the cylinder surface at a distance of 50 mm from each other, the second configuration gives overall reduction in surface heating coefficient. Thus, we have demonstrated, that micro-second plasma DBD actuators, though conventionally thought of as being ineffective for high speed flows, do have significant effect on the heating distribution on the cylinder. We can work on more designs in future for even better performance of plasma DBD actuators for heating reduction in hypersonic flows.

The challenging area, that is yet unresolved, is the heating prediction for the hypersonic flow for locally refined mesh. The DG code is not free from residual effects coming from abruptly changing mesh elements, especially near stagnation line. Some residual differences between the surface heating plots, for locally refined mesh and the expected profile, are produced. This problem is, however, not unique to the DG methods or to the r-p adaptivity approach, but prevalent among all the methods (in the published literature). The results for surface heating predictions have, in general, been found to be very sensitive to the mesh.

In the field of thermal ablation, we find that much advancement in the understanding of the thermal ablation phenomena has occurred from the 1960's, when the work in numerical simulation of thermal ablation began. Simulations at that time began with very simplifying assumptions, like thermally ablating media without any flow of pyrolysis gas being considered. CFD approximation methods were used to provide for net heating rates at the surface of the vehicle instead of solving flow outside the vehicle. At the same time, developments in CFD were also taking place, where full 3-D Navier Stokes was solved. Problem however, was the use of simple boundary conditions for CFD methods and simple governing equations for material thermal response, which did not take the unsteady nature of flow of pyrolysis gas within the porous ablating material. With the exception for Ahn et al and Dr Gosse's work, the pyrolysis gas motion is still considered to be steady at a particular instant.

We have demonstrated capability to solve thermal ablation problems, with the unsteady flow of pyrolysis gas through the porous charring ablator, using DG methods, with high order accuracy. DG method, used specifically for thermal ablation problems, was 3rd order accurate in space. For two test cases, namely TACOT test case from Ablation workshop and for the Langley arc-jet test sample, we have demonstrated accurate solution comparisons to the experimental results. The cases from Ahn et al, however do not match well with the experimental predictions. This is expected to be connected to the thermodynamic properties of pyrolysis gas in this case. The thermodynamic properties for the pyrolysis gas were provided in the two test cases (TACOT and Langley arc-jet case, where we accurately matched our results to the published and experiment), but not for Ahn et al., where we used CANTERA to generate thermodynamic properties for the gas.

We have even attempted to solve 2-D thermal ablation problem. In this we, however, ran into convergence issues, due to the condition number of the jacobian matrix being very high (approximately 10^{13}). This causes y-velocity to grow unboundedly (for a problem with flow only in x-direction) and become unstable. Therefore, our future step in the field of thermal ablation will be to resolve the convergence issue with the 2-D thermal ablation and run it in single framework with hypersonic flow.

Two alternatives to solving the 2-D thermal ablation problem, in case the problem still persists, are as follows. First option is to approximate 2-D thermally ablating geometry as a stack of 1-D grids aligned parallel to the normal at the exit of the 2-D geometry (where the pyrolysis gas leaves the 2D domain). Thus, we will attempt to run the Langley arc-jet test case in a loosely coupled fashion with the hypersonic flow solver. Second option is to use Darcy's law to evaluate the velocity profile, based on pressure distribution inside the porous material. As already mentioned, many papers in literature for thermal ablation, do not solve for unsteady momentum equation, and use Darcy's law instead. This approach is more stable, as it does not have the time term

for momentum equation in the Darcy's law and can thus be used if the 2D unsteady momentum equation for the pyrolysis does not work.

If the single framework solution or the loosely coupled solution is successfully implemented, it will open, for us, new avenues for different types of multi-physics problems.

APPENDIX A FLUID PROPERTIES

Table A-1. Blottner coefficients for species viscosity

Species	A_s	B_s	C_s
O ₂	4.49290x10 ⁻²	-8.26158x10 ⁻²	-9.20195
NO	4.36378x10 ⁻²	-3.35511x10 ⁻²	-9.57674
N	1.15562x10 ⁻²	6.031679x10 ⁻¹	-1.24327x10 ¹
O	2.03144x10 ⁻²	4.29440x10 ⁻¹	-1.16031x10 ¹
N ₂	2.68142x10 ⁻²	83.17738x10 ⁻¹	-1.13156x10 ¹

Table A-2. Coefficients for forward reaction rates

Reaction	$C_{f,r,m}$	$\eta_{f,r,m}$	$\theta_{f,r,m}$
N ₂ + M \longleftrightarrow N + N + M	3.70x10 ¹⁸	-1.6	113,200
O ₂ + M \longleftrightarrow O + O + M	2.75x10 ¹⁶	-1	59,500
NO + M \longleftrightarrow N + O + M	2.30x10 ¹⁴	-0.5	75,500
N ₂ + O \longleftrightarrow NO + N	3.18x10 ¹⁰	0.1	37,700
NO + O \longleftrightarrow O ₂ + N	2.16x10 ⁵	1.29	19,220

Table A-3. Equilibrium constant coefficients

Reaction	$A_{1,m}$	$A_{2,m}$	$A_{3,m}$	$A_{4,m}$	$A_{5,m}$
1	0.98499x10 ¹	-0.11314x10 ²	-0.32028x10 ⁻²	0.55205x10 ⁻⁴	-0.63738x10 ⁻⁷
2	0.88695x10 ¹	-0.53794x10 ¹	-0.88234x10 ⁻¹	0.47129x10 ⁻²	-0.63470x10 ⁻⁴
3	0.80072x10 ¹	-0.73520x10 ¹	-0.26707x10 ⁻¹	0.12446x10 ⁻²	-0.15780x10 ⁻⁴
4	0.86594x10 ¹	-0.71680x10 ¹	-0.24999	0.15237x10 ⁻¹	-0.21498x10 ⁻³
5	0.88464x10 ¹	-0.41842x10 ¹	-0.37449	0.22172x10 ⁻¹	-0.31042x10 ⁻³

APPENDIX B BASIS FUNCTIONS

Table B-1. Basis functions for 2D discontinuous Galerkin

Basis/Order	1	2	3	4
1	1	1	1	1
1		$-1 + 2x$	$-1 + 2x$	$-1 + 2x$
1		$-1 + 2y$	$-1 + 2y$	$-1 + 2y$
1			$1 - 6x + 6x^2$	$1 - 6x + 6x^2$
1			$1 - 2y - 2x + 4xy$	$1 - 2y - 2x + 4xy$
1			$1 - 6y + 6y^2$	$1 - 6y + 6y^2$
1				$-1 + 12x - 30x^2 + 20x^3$
1				$-1 + 2y + 6x - 12xy - 6y^2 + 12xy^2$
1				$-1 + 6y - 6y^2 + 2x - 12xy + 12yx^2$
1				$-1 + 12y - 20y^2 + 20y^3$

REFERENCES

- [1] Dec, J. A., Braun, R. D., and Lamb, B., "Ablative thermal response analysis using the finite element method," *Journal of Thermophysics and Heat Transfer*, Vol. 26, No. 2, 2012, pp. 201–212.
- [2] Burgess, N. K., *An adaptive discontinuous Galerkin solver for aerodynamic flows*, Ph.D. thesis, University of Wyoming, 2011.
- [3] Yoon, S., Gnoffo, P. A., White, J. A., and Thomas, J. L., "Computational challenges in hypersonic flow simulations," *AIAA Paper*, Vol. 4265, 2007, pp. 2007.
- [4] Bhatia, A., Roy, S., and Gosse, R., "Pyrolysis gas flow in thermally ablating media using time-implicit discontinuous Galerkin methods," *49th AIAA Aerospace Sciences Meeting including the New Horizons Forum and Aerospace Exposition*, , No. AIAA 2011-145, 2011.
- [5] Bhatia, A. and Roy, S., "Modeling the motion of pyrolysis gas through charring ablating material using Discontinuous Galerkin finite elements," *SIAM journal on numerical analysis*, , No. AIAA 2010-982, 2010.
- [6] Bhatia, A., Roy, S., and Gosse, R., "2-D Hypersonic Non-equilibrium Flow Simulation using rp Adaptive Time-Implicit Discontinuous Galerkin Method," *51st AIAA Aerospace Sciences Meeting including the New Horizons Forum and Aerospace Exposition*, 2013.
- [7] Sinha, K., "Computational Fluid Dynamics in Hypersonic Aerothermodynamics." *Defence Science Journal*, Vol. 60, No. 6, 2010.
- [8] Gnoffo, P. A., "Updates to multi-dimensional flux reconstruction for hypersonic simulations on tetrahedral grids," *Proceedings of the 48th AIAA Aerospace Sciences Meeting*, 2010.
- [9] Barter, G. E. and Darmofal, D. L., "Shock capturing with PDE-based artificial viscosity for DGFEM: Part I. Formulation," *Journal of Computational Physics*, Vol. 229, No. 5, 2010, pp. 1810–1827.
- [10] Wang, L., *Techniques for High-Order Adaptive Discontinuous Galerkin Discretizations in Fluid Dynamics*, Ph.D. thesis, University of Wyoming, 2009.
- [11] Gnoffo, P. A., "Planetary-Entry Gas Dynamics 1," *Annual Review of Fluid Mechanics*, Vol. 31, No. 1, 1999, pp. 459–494.
- [12] Gosse, R., *Ablation Modeling of Electro-magnetically Launched Projectile for Access to Space*, Ph.D. thesis, University of Minnesota, Minnesota, WI, October 2007.

- [13] Gogu, C., Matsumura, T., Haftka, R. T., and Rao, A. V., "Aeroassisted orbital transfer trajectory optimization considering thermal protection system mass," *Journal of Guidance, Control, and Dynamics*, Vol. 32, No. 3, 2009, pp. 927–938.
- [14] Braun, R. D., "Aeroassist systems: An important element in NASA's new era of planetary exploration," *Journal of Spacecraft and Rockets*, Vol. 36, No. 3, 1999, pp. 297–297.
- [15] Pitts, W. and Wakefield, R., "Performance of entry heat shields on Pioneer Venus probes," *Journal of Geophysical Research: Space Physics (1978–2012)*, Vol. 85, No. A13, 1980, pp. 8333–8337.
- [16] Park, C. and Ahn, H.-K., "Stagnation-point heat transfer rates for Pioneer-Venus probes," *Journal of thermophysics and heat transfer*, Vol. 13, No. 1, 1999, pp. 33–41.
- [17] Ahn, H.-K., Park, C., and Sawada, K., "Response of heatshield material at stagnation point of Pioneer-Venus probes," *Journal of thermophysics and heat transfer*, Vol. 16, No. 3, 2002, pp. 432–439.
- [18] Seiff, A., Kirk, D. B., Young, R. E., Blanchard, R. C., Findlay, J. T., Kelly, G., and Sommer, S., "Measurements of thermal structure and thermal contrasts in the atmosphere of Venus and related dynamical observations: Results from the four Pioneer Venus probes," *Journal of Geophysical Research: Space Physics (1978–2012)*, Vol. 85, No. A13, 1980, pp. 7903–7933.
- [19] Zhong, J., Ozawa, T., and Levin, D. A., "Modeling of Stardust Reentry Ablation Flows in the Near-Continuum Flight Regime," *AIAA journal*, Vol. 46, No. 10, 2008, pp. 2568–2581.
- [20] Boyd, I. D., Zhong, J., Levin, D. A., and Jenniskens, P., "Flow and radiation analyses for stardust entry at high altitude," *AIAA Paper*, Vol. 1218, 2008.
- [21] Ozawa, T., Zhong, J., Levin, D., Boger, D., and Wright, M., "Modeling of the stardust reentry flows with ionization in dsmc," *AIAA paper*, Vol. 611, 2007.
- [22] Anderson, J. D., *Hypersonic and high temperature gas dynamics*, Aiaa, 2000.
- [23] Ayasoufi, A., Rahmani, R., Cheng, G., Koomullil, R., and Neroorkar, K., "Numerical simulation of ablation for reentry vehicles," *9th AIAA/ASME Joint Thermophysics and Heat Transfer Conference*, 2006, pp. 5–8.
- [24] Reynier, P., "Convective Blockage during Earth Re-entry. A review." 2008.
- [25] R, T., "Thermal Diffusivity of POCO Graphite and Stainless Steel SRM 735-5," *Thermal Conductivity, Plenum Press*, Vol. 17, 1982, pp. 753–7621.
- [26] Kendall, R., Rindal, R., and Bartlett, E., "Thermochemical ablation," *AIAA Paper*, Vol. 642, 1965, pp. 13–15.

- [27] Moyer, C. B. and Rindal, R. A., "An analysis of the coupled chemically reacting boundary layer and charring ablator. Part 2- Finite difference solution for the in-depth response of charring materials considering surface chemical and energy balances(Computer program for finite difference equation analysis of in-depth response of materials exposed to high temperature environment)," 1968.
- [28] Maruyama, S., Viskanta, R., and Aihara, T., "Active thermal protection system against intense irradiation," *Journal of Thermophysics and Heat Transfer*, Vol. 3, No. 4, 1989, pp. 389–394.
- [29] Chen, Y.-K. and Milos, F. S., "Ablation and thermal response program for spacecraft heatshield analysis," *Journal of Spacecraft and Rockets*, Vol. 36, No. 3, 1999, pp. 475–483.
- [30] Potts, R. L., "Hybrid integral/quasi-steady solution of charring ablation," 1990.
- [31] Potts, R. L., "Application of integral methods to ablation charring erosion-A review," *Journal of spacecraft and rockets*, Vol. 32, No. 2, 1995, pp. 200–209.
- [32] Martin, A. and Boyd, I. D., "Simulation of pyrolysis gas within a thermal protection system," *40th AIAA Thermophysics Conference*, 2008, pp. 23–26.
- [33] Amar, A. J., Blackwell, B. F., and Edwards, J., "Development and Verification of a One-Dimensional Ablation Code Including Pyrolysis Gas Flow," *Journal of Thermophysics and Heat Transfer*, Vol. 23, No. 1, 2009, pp. 59–71.
- [34] Lachaud, J., Martin, A., Cozmata, I., and Laub, B., "Ablation workshop test case - Version 1.1 - Feb. 2, 2011," 2011.
- [35] Gaitonde, D. V., Visbal, M. R., and Roy, S., "A coupled approach for plasma-based flow control simulations of wing sections," *AIAA paper*, Vol. 1205, 2006, pp. 2006.
- [36] Ahn, H.-K., Park, C., and Sawada, K., "Dynamics of pyrolysis gas in charring materials ablation," *36th Aerospace Sciences Meeting & Exhibit*, 1998.
- [37] Candler, G. and McCormack, R., "Hypersonic flow past 3-D configurations," *AIAA, Aerospace Sciences Meeting, 25 th, Reno, NV*, 1987, p. 1987.
- [38] Chen, Y.-K., Henline, W., Stewart, D., and Candler, G., "Navier-Stokes solutions with surface catalysis for Martian atmospheric entry," *Journal of Spacecraft and Rockets*, Vol. 30, No. 1, 1993, pp. 32–42.
- [39] Version, G., "3, The General Aerodynamic Simulation Program, Computational Flow Analysis Software for the Scientist and Engineer, User's Manual," *Aerosoft Co., Blacksburg*, 1996.
- [40] Olynick, D. and Tam, T., "Trajectory-based validation of the shuttle heating environment," *Journal of spacecraft and rockets*, Vol. 34, No. 2, 1997, pp. 172–181.

- [41] Blackwell, B., "Numerical prediction of one-dimensional ablation using a finite control volume procedure with exponential differencing," *Numerical Heat Transfer, Part A: Applications*, Vol. 14, No. 1, 1988, pp. 17–34.
- [42] Blackwell, B. and Hogan, R., "One-dimensional ablation using Landau transformation and finite control volume procedure," *Journal of thermophysics and heat transfer*, Vol. 8, No. 2, 1994, pp. 282–287.
- [43] Hogan, R., Blackwell, B., and Cochran, R., "Application of moving grid control volume finite element method to ablation problems," *Journal of thermophysics and heat transfer*, Vol. 10, No. 2, 1996, pp. 312–319.
- [44] Martin, A. and Boyd, I. D., "Non-Darcian behavior of pyrolysis gas in a thermal protection system," *Journal of Thermophysics and Heat Transfer*, Vol. 24, No. 1, 2010, pp. 60–68.
- [45] Scalabrin, L. C. and Boyd, I. D., "Numerical simulations of the FIRE-II convective and radiative heating rates," *AIAA Paper*, Vol. 4044, 2007, pp. 2007.
- [46] Scalabrin, L. C., *Numerical simulation of weakly ionized hypersonic flow over reentry capsules*, Ph.D. thesis, The University of Michigan, 2007.
- [47] Chen, Y.-K. and Milos, F., "Two-dimensional implicit thermal response and ablation program for charring materials," *Journal of Spacecraft and Rockets*, Vol. 38, No. 4, 2001, pp. 473–481.
- [48] King, H., Muramoto, K., Murray, A., and Pronchick, S., "ABRES Shape Change Code (ASCC86): Technical Report and Users Manual," *Acurex Corporation, FR-86-24/ATD, Mt View, CA*, 1986.
- [49] Chen, Y. and Milos, F., "Thermal Response Modeling System for a Mars Sample Return Vehicle," *Thermal and Fluid Analysis Workshop, NASA CP-2002-211783*, Sept, 2001.
- [50] Manuals, M. and Volumes, A., "Marc Analysis Research Corporation," *Palo Alto, CA USA*, 1997.
- [51] Hassan, B., Kuntz, D. W., and Potter, D. L., "Coupled fluid/thermal prediction of ablating hypersonic vehicles," *AIAA paper*, Vol. 168, 1998, pp. 1998.
- [52] Kuntz, D. W., Hassan, B., and Potter, D. L., "Predictions of ablating hypersonic vehicles using an iterative coupled fluid/thermal approach," *Journal of Thermophysics and Heat Transfer*, Vol. 15, No. 2, 2001, pp. 129–139.
- [53] Martin, A., Boyd, I. D., and Poggie, J., "Strongly coupled computation of material response and nonequilibrium flow for hypersonic ablation," *41th AIAA Thermophysics Conference*, 2009, pp. 22–25.

- [54] Kitamura, K. and Shima, E., "Towards shock-stable and accurate hypersonic heating computations: A new pressure flux for AUSM-family schemes," *Journal of Computational Physics*, Vol. 245, 2013, pp. 62–83.
- [55] Barter, G. E., "Shock capturing with PDE-based artificial viscosity for an adaptive, higher-order discontinuous Galerkin finite element method," Tech. rep., DTIC Document, 2008.
- [56] Reed, W. H. and Hill, T., "Triangular Mesh Methods for the Neutron Transport Equation," *Los Alamos Report LA-UR-73-479*, 1973.
- [57] Cockburn, B., Lin, S.-Y., and Shu, C.-W., "TVB Runge-Kutta local projection discontinuous Galerkin finite element method for conservation laws III: one-dimensional systems," *Journal of Computational Physics*, Vol. 84, No. 1, 1989, pp. 90–113.
- [58] Cockburn, B. and Shu, C.-W., "TVB Runge-Kutta local projection discontinuous Galerkin finite element method for conservation laws. II. General framework," *Mathematics of Computation*, Vol. 52, No. 186, 1989, pp. 411–435.
- [59] Cockburn, B., Hou, S., and Shu, C.-W., "The Runge-Kutta local projection discontinuous Galerkin finite element method for conservation laws. IV. The multidimensional case," *Mathematics of Computation*, Vol. 54, No. 190, 1990, pp. 545–581.
- [60] Cockburn, B. and Shu, C.-W., "The Runge–Kutta discontinuous Galerkin method for conservation laws V: multidimensional systems," *Journal of Computational Physics*, Vol. 141, No. 2, 1998, pp. 199–224.
- [61] Cockburn, B. and Shu, C.-W., "The Runge-Kutta local projection P1-discontinuous Galerkin finite element method for scalar conservation laws," *RAIRO Modél. Math. Anal. Numér.*, Vol. 25, No. 3, 1991, pp. 337–361.
- [62] Bassi, F. and Rebay, S., "A high-order accurate discontinuous finite element method for the numerical solution of the compressible Navier–Stokes equations," *Journal of computational physics*, Vol. 131, No. 2, 1997, pp. 267–279.
- [63] Cockburn, B. and Shu, C.-W., "The local discontinuous Galerkin method for time-dependent convection-diffusion systems," *SIAM Journal on Numerical Analysis*, Vol. 35, No. 6, 1998, pp. 2440–2463.
- [64] Bassi, F., Crivellini, A., Rebay, S., and Savini, M., "Discontinuous Galerkin solution of the Reynolds-averaged Navier–Stokes and $k_i/\epsilon_i - \omega_i/\epsilon_i$ turbulence model equations," *Computers & Fluids*, Vol. 34, No. 4, 2005, pp. 507–540.
- [65] Douglas, J. and Dupont, T., "Interior penalty procedures for elliptic and parabolic Galerkin methods," *Computing methods in applied sciences*, Springer, 1976, pp. 207–216.

- [66] Peraire, J. and Persson, P.-O., "The compact discontinuous Galerkin (CDG) method for elliptic problems," *SIAM Journal on Scientific Computing*, Vol. 30, No. 4, 2008, pp. 1806–1824.
- [67] Persson, P.-O. and Peraire, J., "Newton-GMRES preconditioning for discontinuous Galerkin discretizations of the Navier-Stokes equations," *SIAM Journal on Scientific Computing*, Vol. 30, No. 6, 2008, pp. 2709–2733.
- [68] Nastase, C. R. and Mavriplis, D. J., "High-order discontinuous Galerkin methods using an $i\epsilon$ hp/ $i\epsilon$ -multigrid approach," *Journal of Computational Physics*, Vol. 213, No. 1, 2006, pp. 330–357.
- [69] Gopalakrishnan, J. and Kanschä, G., "A multilevel discontinuous Galerkin method," *Numerische Mathematik*, Vol. 95, No. 3, 2003, pp. 527–550.
- [70] Fidkowski, K. J., Oliver, T. A., Lu, J., and Darmofal, D. L., " $i\epsilon$ p/ $i\epsilon$ -Multigrid solution of high-order discontinuous Galerkin discretizations of the compressible Navier–Stokes equations," *Journal of Computational Physics*, Vol. 207, No. 1, 2005, pp. 92–113.
- [71] Wilke, C., "A viscosity equation for gas mixtures," *The Journal of Chemical Physics*, Vol. 18, 1950, pp. 517.
- [72] Blottner, F. G., Johnson, M., and Ellis, M., "CHEMICALLY REACTING VISCOUS FLOW PROGRAM FOR MULTI-COMPONENT GAS MIXTURES." Tech. rep., Sandia Labs., Albuquerque, N. Mex., 1971.
- [73] Vincenti, W. G. and Kruger, C. H., "Introduction to physical gas dynamics," *Introduction to physical gas dynamics, by Vincenti, Walter Guido; Kruger, Charles H. New York, Wiley [1965]*, Vol. 1, 1965.
- [74] PARK, C., "Assessment of two-temperature kinetic model for dissociating and weakly-ionizing nitrogen," 1986.
- [75] McBride, B. J., Zehe, M. J., and Gordon, S., *NASA Glenn coefficients for calculating thermodynamic properties of individual species*, National Aeronautics and Space Administration, John H. Glenn Research Center at Lewis Field, 2002.
- [76] Millikan, R. C. and White, D. R., "Systematics of vibrational relaxation," *The Journal of chemical physics*, Vol. 39, 1963, pp. 3209.
- [77] Lax, P. D., "Weak solutions of nonlinear hyperbolic equations and their numerical computation," *Communications on Pure and Applied Mathematics*, Vol. 7, No. 1, 1954, pp. 159–193.
- [78] Falgout, R., Cleary, A., Jones, J., Chow, E., Henson, V., Baldwin, C., Brown, P., Vassilevski, P., and Yang, U., "HYPRE: High Performance Preconditioners," *Users Manual. Version*, Vol. 1, No. 0, 2010.

- [79] Persson, P.-O. and Peraire, J., "Sub-cell shock capturing for discontinuous Galerkin methods," *AIAA paper*, Vol. 112, 2006, pp. 2006.
- [80] Parmar, M., *Unsteady forces on a particle in compressible flows*, Ph.D. thesis, University of Florida, 2010.
- [81] Bassi, F. and Rebay, S., "High-order accurate discontinuous finite element solution of the 2D Euler equations," *Journal of Computational Physics*, Vol. 138, No. 2, 1997, pp. 251–285.
- [82] Botta, N., "The inviscid transonic flow about a cylinder," *Journal of Fluid Mechanics*, Vol. 301, 1995, pp. 225–250.
- [83] Colella, P. and Glaz, H. M., "Efficient solution algorithms for the Riemann problem for real gases," *Journal of Computational Physics*, Vol. 59, No. 2, 1985, pp. 264–289.
- [84] D.L. Peterson, F. G. and Richardson, C., "Design and Performance of a Combined Convective and Radiative Heating Facility," *AIAA Paper 71-255, San Antonio, Texas*, 1971.
- [85] Goodwin, D., "Cantera users guide," *Division of Engineering and Applied Science, California Institute of Technology, Pasadena, CA*, 2001.
- [86] Philips, J., "ZunZun.com Online Curve Fitting and Surface Fitting Web Site," 2011, <http://zunzun.com>.
- [87] Sykes, G. F., "Decomposition Characteristics of a Char-Forming Phenolic Polymer Used for Ablative Composites," 1967.
- [88] Sutton, K., "An Experimental Study of A Carbon-Phenolic Ablation Material," , No. NASA-TN-D-5930, 1970.
- [89] Gnoffo, P. A. and Cheatwood, F., "User's Manual for the Langley Aerothermodynamic Upwind Relaxation Algorithm(LAURA)," 1996.
- [90] Moreau, E., "Airflow control by non-thermal plasma actuators," *Journal of Physics D: Applied Physics*, Vol. 40, No. 3, 2007, pp. 605.
- [91] Shang, J. S., Kimmel, R. L., Menart, J. A., and Surzhikov, S. T., "Hypersonic flow control using surface plasma actuator," *Journal of Propulsion and Power*, Vol. 24, No. 5, 2008, pp. 923–934.
- [92] Nishihara, M., Takashima, K., Rich, J., and Adamovich, I., "Mach 5 bow shock control by a nanosecond pulse surface dielectric barrier discharge," *Physics of Fluids (1994-present)*, Vol. 23, No. 6, 2011, pp. 066101.

- [93] Roupasov, D., Nikipelov, A., Nudnova, M., and Starikovskii, A. Y., "Flow separation control by plasma actuator with nanosecond pulsed-periodic discharge," *AIAA journal*, Vol. 47, No. 1, 2009, pp. 168–185.
- [94] Riherd, M. and Roy, S., "Serpentine geometry plasma actuators for flow control," *Journal of Applied Physics*, Vol. 114, No. 8, 2013, pp. 083303.
- [95] Kim, J.-H., Nishihara, M., Adamovich, I., Samimy, M., Gorbатов, S., and Pliavaka, F., "Development of localized arc filament RF plasma actuators for high-speed and high Reynolds number flow control," *Experiments in fluids*, Vol. 49, No. 2, 2010, pp. 497–511.
- [96] Bisek, N. J., Poggie, J., Nishihara, M., and Adamovich, I., "Computational and Experimental Analysis of Mach 5 Air Flow over a Cylinder with a Nanosecond Pulse Discharge," *AIAA Paper*, Vol. 186, 2012, pp. 2012.
- [97] Singh, K. P. and Roy, S., "Force approximation for a plasma actuator operating in atmospheric air," *Journal of Applied Physics*, Vol. 103, No. 1, 2008, pp. 013305.

BIOGRAPHICAL SKETCH

Ankush Bhatia was born in 1983 in Delhi, India. He earned his B. Tech. degree in Mechanical Engineering from Indian Institute of Technology, Delhi in 2006. During 2006-2007, he worked as a design engineer in Hindustan Petroleum Corporation Ltd. Since 2007, he has been working towards the doctorate here at the University of Florida under Dr. Subrata Roy. His research areas are computational fluid dynamics (CFD) simulations of thermal ablation and non-equilibrium hypersonic flows, and he specializes in finite element and discontinuous Galerkin methods.